IMPLOSION DYNAMICS, RADIATION CHARACTERISTICS, AND SPECTROSCOPIC MEASUREMENTS OF WIRE-ARRAY Z-PINCHES ON THE CORNELL BEAM RESEARCH ACCELERATOR (COBRA)

A Dissertation

Presented to the Faculty of the Graduate School

of Cornell University

in Partial Fulfillment of the Requirements for the Degree of

Doctor of Philosophy

by

Ryan David McBride

January 2009

IMPLOSION DYNAMICS, RADIATION CHARACTERISTICS, AND SPECTROSCOPIC MEASUREMENTS OF WIRE-ARRAY Z-PINCHES ON THE CORNELL BEAM RESEARCH ACCELERATOR (COBRA)

Ryan David McBride, Ph.D.

Cornell University 2009

This dissertation presents the results of two experimental studies of wire-array z-pinches on the 1-MA, 100-ns rise-time Cornell Beam Research Accelerator (COBRA).

In the first study, results are presented which characterize the implosion dynamics and radiation output of wire array z-pinches on COBRA. Here the load geometries investigated include 10- and 20-mm tall cylindrical arrays ranging from 4 to 16 mm in diameter, and consisting of 8, 16, or 32 wires of either tungsten, aluminum, or Invar (64% iron, 36% nickel). Diagnostics fielded include an optical streak camera, a time-gated extreme-ultraviolet framing camera, a laser shadowgraph system, time-integrated pinhole cameras, an x-ray wide-band focusing spectrograph with spatial resolution, an x-ray streak camera, a load voltage monitor, a Faraday cup, a bolometer, silicon diodes, and diamond photoconducting detectors. The data produced by the entire suite of diagnostics are analyzed and presented to provide a detailed picture of the overall implosion process and resulting radiation output on COBRA. The highest x-ray peak powers (300–500 GW) and total energy yields (6–10 kJ) were obtained using 4-mm-diameter arrays that stagnated before peak current. Additional findings include a decrease in soft x-ray radiation prior to stagnation as the initial wire spacing was changed from 1.6 mm to 785 μm, and a timing correlation between the onset

of energetic electrons, hard x-ray generation, and the arrival of trailing current on axis—a correlation that is likely due to the formation of micro-pinches. The details of these and other findings are presented and discussed.

In the second study, a new diagnostic setup was developed to record the visible-light spectra emitted from aluminum wire-array plasmas as a continuous function of time. To accomplish this, a half-meter Czerny-Turner spectrometer was used in conjunction with the existing visible light streak camera system. The emitted spectra was seen to consist solely of continuum radiation. This continuum data is now being used to determine electron density. To determine electron density from the continuum data, an absolute calibration of the detection system was required. The details of these experiments, and the absolute calibration technique are presented.

BIOGRAPHICAL SKETCH

Ryan David McBride was born in Johnson City, NY on February 21, 1978, to Richard and Cathy McBride. He has one sister, Ashley Raba, and is married to Rebecca Osterhout. He is also fortunate to have a wonderful extended family, including his loving grandparents John and Olga Warski.

Ryan grew up in Endwell, NY, and graduated from Maine-Endwell High School in 1996. He completed his undergraduate studies at the State University of New York, Binghamton, where he earned a BS degree in electrical engineering in May of 2000. It was during his senior year at Binghamton that Ryan met the love of his life, Rebecca Osterhout (whom he married in July of 2006). In May of 2001, Ryan earned an MEng degree in electrical engineering from Cornell and subsequently began working for IBM in Endicott, NY (which later became Endicott Interconnect Technologies, Inc. in November of 2002). After nearly two years of corporate woes, Ryan decided he had enough of industry, and returned to Cornell to begin his MS and PhD studies in the School of Electrical and Computer Engineering.

Entering the MS/PhD program in the Fall of 2003, Ryan joined the Space Plasma Physics group as a Graduate Research Assistant (GRA) for Dr. Wesley Swartz. During this first year, Ryan studied the plasma dynamics of the ionosphere along with plasma physics in general. Ryan found the study of the ionosphere intriguing, but was becoming more and more interested in the application of plasma physics to nuclear fusion energy.

Just before beginning his second year in the MS/PhD program, Ryan's interest in fusion energy inspired him to change course, and in the fall of 2004, he joined the Laboratory of Plasma Studies as a GRA for Professor David Hammer. Professor Hammer graciously allowed Ryan many academic freedoms,

enabling Ryan's studies in several areas of pure and applied physics, including: classical electrodynamics, quantum mechanics, thermodynamics, statistical mechanics, classical mechanics, non-linear dynamics & chaos, computational physics, advanced plasma physics, controlled fusion, mathematical methods, plasma spectroscopy, energy seminars, and so on. While wrapping up his coursework, and transitioning to full-time research in the lab, Ryan earned an MS degree in May of 2007 with a minor in applied physics.

Presently, it looks as though Ryan might finally break away from the 40-mile span that he has lived his entire life in. His plans upon completing his PhD include joining his wife in Albuquerque, NM, and starting his position as a high-energy-density physicist at Sandia National Laboratories. There he will be involved with experimental research conducted on the Z accelerator.

To my family, friends, and all other sources of inspiration

ACKNOWLEDGMENTS

This dissertation was made possible by the contributions of several individuals to whom I am deeply indebted.

Foremost, I thank my special committee chair and thesis advisor, David Hammer. His wisdom and guidance throughout my years with the Laboratory of Plasma Studies has been invaluable to me. He encouraged me to find research projects that I found interesting, and supported me when I desired to invest time in additional coursework. I sincerely appreciate having been given those freedoms, and I am absolutely certain that they have enabled my growth into a more mature and capable physicist. Additionally, I thank him and his wife, Tove Hammer, for their gracious hospitality for an extended period of time while completing this dissertation.

I also thank my additional special committee members, Charles Seyler and Richard Lovelace, for seeing me through this process, and for the knowledge they have shared with me, particularly while taking their courses in advanced plasma theory.

My deep gratitude goes out to Sergei Pikuz and Tania Shelkovenko for taking the time to teach me numerous experimental techniques in the laboratory, and for allowing me to collaborate with them on their projects while I learned. When the time came for me to lead my own research initiatives, they were always there to provide valuable assistance and advice, for which I am grateful.

The work presented in this dissertation benefited from the contributions of the talented faculty, staff, and students of the Laboratory of Plasma Studies. First, my deep appreciation goes out to Harry Wilhelm for his dedication in keeping our pulsed-power facilities up and running. His kindness, enthusiasm, and creative problem solving abilities have saved our research countless times.

I thank John Greenly for several valuable conversations regarding voltage and magnetic field measurements, as well as numerous other topics discussed in this dissertation. My sincere appreciation goes out to Todd Blanchard for his expertise as a machinist, his manufacturing of the custom-built hardware for these experiments, and for his assistance with the design of this hardware. I thank Joyce Oliver for handling the logistics of our funding and conference travel. I thank Bruce Kusse for serving as our laboratory director. Finally, I thank my fellow graduate students: Jonathan Douglass, Patrick Knapp, Kate Bell, Isaac Blesener, David Chalenski, and Wasif Syed for their various contributions to these experiments.

Many thanks also go out to Yitzhak Maron and his team for taking an interest in analyzing the continuum data presented in this dissertation, as well as for the numerous conversations and advice given in regards to the design of spectroscopy experiments.

I thank the U.S. Department of Energy, the National Nuclear Security Administration, and Sandia National Laboratories for their financial support of my graduate work. The projects presented in this dissertation were funded in part by Sandia National Laboratories Contract No. AO258 and in part by the Stewardship Science Academic Alliances program of the National Nuclear Security Administration under DOE Cooperative Agreement No. DE-FC03-02NA00057.

My sincere thanks to Wesley Swartz for his role in bringing me back to Cornell in the fall of 2003, and for providing funding for my first year of MS/PhD study.

My deep gratitude goes out to my roommate of three years, Michael Nicolls, for his encouragement and friendship. He kept me focused, made sure we started our homework on time, and, most importantly, made sure we got to

hockey on time!

Finally, I thank my family and friends for all of their love and support throughout my life. I am especially grateful to my wife, Rebecca, for her love and companionship throughout every day of this nearly half-decade process.

TABLE OF CONTENTS

Biographical Sketch . . . iii
Dedication . . . v
Acknowledgments . . . vi
Table of Contents . . . ix
List of Tables . . . xii
List of Figures . . . xiii

1 Introduction **1**
1.1 Motivation & Applications . . . 1
1.2 Brief Introduction to the Wire-Array Z-Pinch Process . . . 1
1.3 Pulsed-Power Generators . . . 2
1.4 The Use of Pulsed Power in Experiments Leading up to Wire-Array Z-Pinches . . . 6
1.5 Early Wire-Array Z-Pinch Research . . . 7
1.6 Resurgence in Wire-Array Z-Pinch Research . . . 8
1.7 Establishment of a National Center at Cornell . . . 11
1.8 Summary of Findings & Conclusions . . . 12

2 The COBRA Pulsed-Power Generator **15**
2.1 Overview of COBRA . . . 15
2.2 Diagnostics on COBRA . . . 16
2.2.1 Current Monitor . . . 16
2.2.2 Voltage Monitor . . . 16
2.2.3 Bolometer . . . 17
2.2.4 Photoconducting Detectors (PCDs) . . . 18
2.2.5 Silicon Diodes . . . 18
2.2.6 Time-Integrated Pinhole Cameras . . . 19
2.2.7 Laser Shadowgraph System . . . 20
2.2.8 Time-Gated Micro-Channel-Plate (MCP) Camera . . . 21
2.2.9 Streak Cameras . . . 22
2.2.10 Wide-Band Focusing Spectrograph with Spatial Resolution (WB-FSSR) . . . 25
2.2.11 Faraday Cup . . . 26
2.2.12 Other COBRA Diagnostics . . . 26

3 The Z-Pinch **28**
3.1 Streaming Filamentation in Nature . . . 28
3.2 Bennett Pinch Equilibrium . . . 28
3.3 Dynamics from Non-Equilibrium . . . 34
3.4 Pease-Braginskiĭ Current . . . 38

4 The Wire-Array Z-Pinch **42**
4.1 The Four Phases of a Wire-Array Z-Pinch 42
4.1.1 Current Initiation & Resistive Phase 42
4.1.2 Ablation Phase 44
4.1.3 Implosion Phase 45
4.1.4 Stagnation & Radiation Phase 46

5 Implosion Dynamics and Radiation Characteristics on COBRA **47**
5.1 Experimental Setup 48
5.1.1 Diagnostics 48
5.1.2 Wire-array loads 53
5.2 Experimental Results 56
5.2.1 Representative Tungsten Experiments 57
5.2.2 Representative Aluminum Experiments 66
5.2.3 Invar Experiment (64% iron, 36% nickel) 71
5.2.4 Electrical Power Into Load vs. Radiated Power Out 75
5.2.5 Implosion Models & Data Fitting 77
5.2.6 Hot Spot Observations 87
5.2.7 Sparse Wire-Array Experiments 89

6 Spectroscopic Measurements of Ablated Plasma in Aluminum Arrays **97**
6.1 Experimental Setup & System 102
6.2 Absolute System Calibration 118
6.2.1 Calibration from Source to Detector 119
6.2.2 Calibration of Streak-Camera Detector 122
6.2.3 Pixel-Value Calibration 124
6.2.4 Wavelength Calibration 131
6.2.5 Timing Calibration 135
6.2.6 Putting the Pieces Together 137
6.3 Continuum Results 140

7 Conclusions **144**
7.1 Summary & Discussion 144
7.2 Looking Forward 150

A Experimental Data from Implosion Dynamics and Radiation Characteristics Study **155**

B Code for Implosion Dynamics Study **197**
B.1 shot_info.m 197
B.2 didt_zero.m 198
B.3 RMAnalyze.m 202
B.4 ablation_snow_plow.m 223

C Code for Continuum/Spectroscopy Study **232**
C.1 Mathematica Notebook for Optics/Grating Selection 232
C.2 MATLAB M-Files for Streak Camera Calibration and Data Processing 236
C.2.1 efficiency.m 236
C.2.2 zero.m 239
C.2.3 cal_I.m 241
C.2.4 cal_I_avg.m 244
C.2.5 cal_curve_coords_avg.m 246
C.2.6 white.m 247
C.2.7 root.m 249
C.2.8 spectra.m 249
C.2.9 spectral_cal.m 260
C.2.10 drift_correction_AI.m 264
C.2.11 vert_curves_AI.m 267
C.2.12 wavelength_shifter.m 269
C.2.13 time_curves_I.m 271
C.2.14 scan_spectra.m 272
C.2.15 spectra_movie.m 274

Bibliography **280**

LIST OF TABLES

5.1 Wire-array configurations tested. 56

LIST OF FIGURES

1.1 (Color) Drawing of the COBRA pulsed-power generator. 4
1.2 (Color) Cross-section of the COBRA vacuum convolute and insulator stack. 6

2.1 (Color) Graphic of a generic visible light streak system illustrating the working principles. The components are: (A) wire-array z-pinch load (usually the self emission from the wire plasma is the source of visible light), (B) optical relay lens (this could be a system of relay optics), (C) streak camera entrance slit, (D) image of wire-array and load region at the entrance slit, (E) electron-emitting photocathode, (F) electron-accelerating grid, (G) electrostatic lens, (H) electron trajectories, (J) upper sweep bias plate, (K) lower sweep bias plate, (L) phosphor screen, (M) detector (film, CCD camera, etc.). (Figure courtesy of J. D. Douglass.) . . . 23

4.1 Transverse dimension of an imploding array imaged as a continuous function of time by the visible-light streak camera. The image was produced by self emission. The vertical axis is time, and the horizontal axis is radial extent. This image is particularly useful for illustrating the four phases of a wire-array z-pinch implosion. 43
4.2 Representative data plot of $V_{load} - L_0\dot{I}$ to show the various phases of the wire-array z-pinch process. Of particular importance here is the resistive voltage collapse taking place approximately 15 ns into the current pulse, which marks the transition from the initiation phase to the ablation phase. 44
4.3 Laser shadowgraph image taken during the ablation phase illustrating the presence of ablation streams, a precursor plasma column, and the early formation of gaps near the bottom/cathode end of the array. 45

5.1 (Color) Total x-ray power derived by the two methods described in the text showing reasonable agreement. 50
5.2 (Color) 32-wire W array on an 8-mm array diameter giving 785-μm wire spacing (wire diameters are 5 μm; array height is 20 mm). The anode plate (above the array) and four return current posts (surrounding the array) are shown in (a). 53
5.3 (Color) Visible streak camera image synchronized to various signals for a 16-wire W array on an 8-mm array diameter, with 1.6-mm wire spacing, 5-μm wire diameters, and $\Pi \approx 10$. 58

5.4 Time-gated XUV images (top row) and laser shadowgraph images (bottom row) of imploding 32-wire W arrays with 8-mm array diameters, 785-μm wire spacings, 5-μm wire diameters, and $\Pi \approx 5$. Frame times are relative to stagnation on the visible streak images. 61
5.5 (Color) Visible streak camera image synchronized to various signals for a 32-wire W array on an 8-mm array diameter, with 785-μm wire spacing, 5-μm wire diameters, and $\Pi \approx 5$. 62
5.6 (Color) Visible streak camera image synchronized to various signals for a 16-wire W array on a 4-mm array diameter, with 785-μm wire spacing, 5-μm wire diameters, and $\Pi \approx 40$. 64
5.7 Time-gated XUV images (top row) and laser shadowgraph images (bottom row) of imploding 16-wire W arrays with 4-mm array diameters, 785-μm wire spacings, 5-μm wire diameters, and $\Pi \approx 40$. Frame times are relative to stagnation on the visible streak images. 65
5.8 (Color) Visible streak camera image synchronized to various signals for a 16-wire Al array on a 9-mm array diameter, with 1.8-mm wire spacing, 10-μm wire diameters, and $\Pi \approx 14$. 67
5.9 (Color) Visible streak camera image synchronized to various signals for a 32-wire Al array on an 8-mm array diameter, with 785-μm wire spacing, 10-μm wire diameters, and $\Pi \approx 9$. 68
5.10 (Color) Visible streak camera image synchronized to various signals for a 16-wire Al array on a 4-mm array diameter, with 785-μm wire spacing, 12-μm wire diameters, and $\Pi \approx 48$. 69
5.11 Time-gated XUV images (top row) and laser shadowgraph images (bottom row) of imploding 32-wire Al arrays with 8-mm array diameters, 785-μm wire spacings, 10-μm wire diameters, and $\Pi \approx 9$ Frame times are relative to stagnation on the visible streak images. 70
5.12 (Color) Visible streak camera image synchronized to various signals for an 8-wire Invar array on a 4-mm array diameter, with 1.6-mm wire spacing, 10-μm wire diameters, and $\Pi \approx 48$. 72
5.13 Time-gated XUV images of an imploding 8-wire Invar array on a 4-mm array diameter, with 1.6-mm wire spacing, 10-μm wire diameters, and $\Pi \approx 48$. Frame times are relative to stagnation on the visible streak images. 72

5.14 XUV images of W arrays revealing the presence of unstable precursors, suggesting a significant amount of current leakage into the precursors. The wire spacings in (a) were 2.2 mm and in (b) it was 2.4 mm (i.e., greater than the 1.6-mm threshold described in the text). Part (b) also shows the similarity between the shape of the precursor column (-12 ns) and the shape of the stagnation column (+18 ns). Frame times are relative to stagnation on the visible streak images. 74
5.15 (Color) Plot of electrical power into load versus radiated power out for W and Al. The two loads are the 4-mm-diameter loads of Secs. 5.2.1 and 5.2.2, respectively. 76
5.16 Implosion trajectories produced by the thin-shell, ablation-snowplow, and inductance unfold models for the 32-wire W (a) and Al (b) arrays of Sections 5.2.1 & 5.2.2, respectively. Both were on 8-mm array diameters and had 785-μm wire spacings. The wire diameters were 5 μm for W and 10 μm for Al, giving them $\Pi \approx 5$ and $\Pi \approx 9$, respectively. 82
5.17 Thin-shell trajectories overlaying the visible streaks of two Al experiments. The ablation-dominated trajectory from the 32-wire array of Sec. 5.2.2 is shown in (a) while a thin-shell-like trajectory from a 16-wire array with 17-μm wire diameters is shown in (b). The wire spacing was 785 μm in (a) and 1.6 mm in (b). Both arrays were on 8-mm diameters. Note the slower current rise in (b). The thin-shell trajectories were generated using Eqn. 3.36 with respective array masses and load current data. Thin-shell stagnation times were scaled to streak stagnation times by using 80% of the load current for (a) and 90% of the load current for (b). 85
5.18 Time-integrated, unfiltered, 50-μm pinhole images of imploding arrays for W, Al, and Invar, all revealing the presence of localized hot spots. The first layer of film (DR50) filters wide-spread soft radiation, while the second film (Biomax) typically shows the localized hot spots with greater contrast. 88
5.19 Time-integrated x-ray spectra with vertical and horizontal spatial resolution produced by the WB-FSSR, and revealing the continuum nature of the localized hot spots for W, Al, and Invar. . . 89
5.20 X-ray streak camera image of the top half of the pinch axis of an Invar array revealing the formation of discrete hot spots at various times and locations. 90
5.21 XUV image of an imploding sparse W array showing nonuniform implosion (8 wires on a 16-mm array diameter giving 6.3-mm wire spacing). 91
5.22 XUV (a) and laser (b) shadowgraph images of an imploding sparse Al array showing nonuniform implosion (8 wires on a 16-mm array diameter giving 6.3-mm wire spacing). 91

5.23 (Color) Visible streak camera image synchronized to various signals for a sparse W array showing nonuniform implosion (8 wires on a 16-mm array diameter giving 6.3-mm wire spacing). . 92
5.24 (Color) Visible streak camera image synchronized to various signals for a sparse Al array showing nonuniform implosion (8 wires on a 16-mm array diameter giving 6.3-mm wire spacing). . 93
5.25 Laser shadowgraph showing the axially nonuniform expansion rates of Al wires. 94
5.26 (a) Optical streak camera and XUV images for a 16-wire W array on a 16-mm array diameter showing that the precursor started just after the implosion phase began, but prior to stagnation. This should be compared to the corresponding images in (b), where the array was half the mass/wire-number (therefore imploded earlier) and no precursor was present. The implosions in (a) and (b) were produced by similar current pulses, which allowed the streaks to be synchronized, and thus share the same time scale relative to the start of current. 95

6.1 (Color) Illustration of setup for streaking visible-light spectra. . . 98
6.2 (Color) Graphic of the Czerny-Turner spectrometer configuration illustrating the working principles. 99
6.3 (Color) Spectral streak revealing only continuum emission. . . . 100
6.4 (Color) Streak of 16-wire array with 12-μm wire diameters. Resistive voltage collapse occurs earlier in the current pulse and at less current per wire than the experiment shown in Fig. 6.3, but still only continuum emission is observed. 101
6.5 (Color) Illustration of relay optics from source to spectrometer, and from spectrometer to streak camera. 104
6.6 (Color) Geometrical illustration of the light paths through lens L3 of Fig. 6.5, through the spectrometer to lens L4 of Fig. 6.5, and on into the streak camera (top-down view). 116
6.7 (a) Single streak image of CW HeNe laser source focused onto streak input slit. (b) Sum of all calibration streak images showing all calibration locations. 124
6.8 Images of laser spots taken in focus mode superimposed on images of same laser spots being streaked. This illustrates how streak trajectories can significantly miss their corresponding focus-mode positions. 133

6.9 Diagnostic laser configured to illuminate entire streak input slit. The short 150-ps pulse provides an effectively instantaneous flash, producing an image of the input slit at one moment in time. The result of this for one laser pulse is shown in (a). In (b), several of these images have been superimposed to illustrate the different times at which constant-time-curve calibration data has been taken. 136
6.10 (Color) Four spectral movie frames taken from the same shot at different times. The time of the spectrum in a given frame relative to the current pulse is also indicated. 141
6.11 Examples of the XUV framing camera images and laser shadowgraphs used to determine plasma thicknesses in the continuum/spectroscopy experiments. 142

7.1 (Color) Two time-gated XUV frames and their timings relative to various signals for an Al implosion. The very fast spike-like burst at the beginning of this particular x-ray pulse (which occurs rarely) is similar to the fast pulses produced by X pinches. The XUV frames show two dominant micro-pinch regions—one half way up the array and one at the bottom/cathode end of the array. The later XUV frame shows that these two neck-down regions have opened up after the fast initial x-ray burst, forming mini-diode-like gaps. The onset of electron-beam detection by the Faraday cup occurs at a time between these two frames (likely at the time when the neck-down regions first begin to open), suggesting that the energetic electrons detected are the result of electron acceleration across these mini-diode-like gaps. The vertical positions of these micro-pinch regions correspond to the vertical positions of continuum on the WB-FSSR images and to the vertical positions of bright spots on time-integrated pin-hole camera images. 151

A.1 (Color) Visible streak, XUV framing camera, laser shadowgraph, and various signal data for shot 766. 156
A.2 (Color) Visible streak, XUV framing camera, laser shadowgraph, and various signal data for shot 767. 157
A.3 (Color) Visible streak, XUV framing camera, laser shadowgraph, and various signal data for shot 768. 158
A.4 (Color) Visible streak, XUV framing camera, laser shadowgraph, and various signal data for shot 769. 159
A.5 (Color) Visible streak, XUV framing camera, laser shadowgraph, and various signal data for shot 770. 160
A.6 (Color) Visible streak, XUV framing camera, laser shadowgraph, and various signal data for shot 771. 161

A.7 (Color) Visible streak, XUV framing camera, laser shadowgraph, and various signal data for shot 772. 162
A.8 (Color) Visible streak, XUV framing camera, laser shadowgraph, and various signal data for shot 773. 163
A.9 (Color) Visible streak, XUV framing camera, laser shadowgraph, and various signal data for shot 774. 164
A.10 (Color) Visible streak, XUV framing camera, laser shadowgraph, and various signal data for shot 775. 165
A.11 (Color) Visible streak, XUV framing camera, laser shadowgraph, and various signal data for shot 776. 166
A.12 (Color) Visible streak, XUV framing camera, laser shadowgraph, and various signal data for shot 777. 167
A.13 (Color) Visible streak, XUV framing camera, laser shadowgraph, and various signal data for shot 778. 168
A.14 (Color) Visible streak, XUV framing camera, laser shadowgraph, and various signal data for shot 779. 169
A.15 (Color) Visible streak, XUV framing camera, laser shadowgraph, and various signal data for shot 873. 170
A.16 (Color) Visible streak, XUV framing camera, laser shadowgraph, and various signal data for shot 874. 171
A.17 (Color) Visible streak, XUV framing camera, laser shadowgraph, and various signal data for shot 875. 172
A.18 (Color) Visible streak, XUV framing camera, laser shadowgraph, and various signal data for shot 876. 173
A.19 (Color) Visible streak, XUV framing camera, laser shadowgraph, and various signal data for shot 877. 174
A.20 (Color) Visible streak, XUV framing camera, laser shadowgraph, and various signal data for shot 878. 175
A.21 (Color) Visible streak, XUV framing camera, laser shadowgraph, and various signal data for shot 879. 176
A.22 (Color) Visible streak, XUV framing camera, laser shadowgraph, and various signal data for shot 880. 177
A.23 (Color) Visible streak, XUV framing camera, laser shadowgraph, and various signal data for shot 881. 178
A.24 (Color) Visible streak, XUV framing camera, laser shadowgraph, and various signal data for shot 882. 179
A.25 (Color) Visible streak, XUV framing camera, laser shadowgraph, and various signal data for shot 883. 180
A.26 (Color) Visible streak, XUV framing camera, laser shadowgraph, and various signal data for shot 885. 181
A.27 (Color) Visible streak, XUV framing camera, laser shadowgraph, and various signal data for shot 950. 182
A.28 (Color) Visible streak, XUV framing camera, laser shadowgraph, and various signal data for shot 951. 183

A.29 (Color) Visible streak, XUV framing camera, laser shadowgraph, and various signal data for shot 952. 184
A.30 (Color) Visible streak, XUV framing camera, laser shadowgraph, and various signal data for shot 953. 185
A.31 (Color) Visible streak, XUV framing camera, laser shadowgraph, and various signal data for shot 954. 186
A.32 (Color) Visible streak, XUV framing camera, laser shadowgraph, and various signal data for shot 955. 187
A.33 (Color) Visible streak, XUV framing camera, laser shadowgraph, and various signal data for shot 956. 188
A.34 (Color) Visible streak, XUV framing camera, laser shadowgraph, and various signal data for shot 957. 189
A.35 (Color) Visible streak, XUV framing camera, laser shadowgraph, and various signal data for shot 958. 190
A.36 (Color) Visible streak, XUV framing camera, laser shadowgraph, and various signal data for shot 959. 191
A.37 (Color) Visible streak, XUV framing camera, laser shadowgraph, and various signal data for shot 960. 192
A.38 (Color) Visible streak, XUV framing camera, laser shadowgraph, and various signal data for shot 962. 193
A.39 (Color) Visible streak, XUV framing camera, laser shadowgraph, and various signal data for shot 974. 194
A.40 (Color) Visible streak, XUV framing camera, laser shadowgraph, and various signal data for shot 975. 195
A.41 (Color) Visible streak, XUV framing camera, laser shadowgraph, and various signal data for shot 977. 196

CHAPTER 1

INTRODUCTION

1.1 Motivation & Applications

Wire-array z-pinches are presently the most powerful and efficient laboratory x-ray sources available, achieving x-ray powers of >200 TW, x-ray energies ~2 MJ, and conversion efficiencies from stored electrical energy to radiated x-ray energy of $\gtrsim$15% [1, 2, 3]. They are also now allowing us to create and study, in the laboratory, magnetized plasmas of extremely high temperatures and densities. Thus, wire-array z-pinches are highly attractive for applications in both direct and indirect drive inertial confinement fusion (ICF) [4, 5, 6, 7, 8, 9, 10], high-energy-density physics (HEDP) [11, 12, 10], laboratory astrophysics [13, 14, 15], and radiation science [16].

1.2 Brief Introduction to the Wire-Array Z-Pinch Process

The wire-array z-pinch phenomenon begins with a large-amplitude electrical current pulse running through an array of wires (typically metal wires arranged in a cylindrical pattern with constant spacing between the wires). Early in the current pulse, the wires are rapidly vaporized and ionized into current-carrying plasma channels. The electromagnetic forces (i.e., Lorentz forces) between these parallel current channels are attractive and sufficient to accelerate the wire plasma toward the axis of symmetry. When the wire plasma reaches the axis of symmetry it stagnates due to the counter balancing forces of the op-

posing streams, and causes the multiple current-carrying channels to merge into a single current-carrying channel. The initial mass of the wire-array is typically tuned such that stagnation and channel merger occur at about the time when the current pulse reaches its peak amplitude. This results in an intense burst of electromagnetic radiation (mostly in the form of x-rays).

The energy source(s) for the resulting radiation burst is (are) still the subject of much debate, and we will discuss this more throughout the remainder of this thesis. However, for now, we simply note that this energy must come from one or more of the following three mechanisms. The first is the kinetic energy of the plasma streams thermalizing at the point of stagnation on axis. The second is magnetic compressional heating due to electromagnetic pinch-effects that occur whenever a single current-carrying plasma channel is established. The third is ohmic heating due to electrical current running through any resistance that may arise within the single current-carrying plasma channel (this resistance being the result of the increased density and/or turbulent structure within the plasma channel).

1.3 Pulsed-Power Generators

To obtain substantial radiation yield from a wire-array z-pinch, large-amplitude, fast-rising electrical current pulses must be generated—usually requiring more than a million amperes to be delivered in less than a few hundred billionths of a second (i.e., >1 MA in ~100 ns). Also, to maintain such current pulses as they are pushed through the dynamic impedances of wire-array z-pinch loads, voltages on the order of hundreds of thousands to millions of volts are required

(i.e., 0.1–10 MV). This requires machines with electrical powers on the order of a terawatt (i.e., 1 MA x 1 MV = 10^{12} W = 1 TW). To put this in perspective, at the time of this writing, 1 TW is about the peak average power level of the entire U.S. electrical grid. Thus, to produce such powerful electrical pulses, the wire-array z-pinch community (amongst other communities) relies on pulsed-power technology.

The concept of pulsed power can be summarized as the gradual accrual of stored energy over a long period of time, followed by a rapid delivery of the stored energy over a much faster period of time. As power is the rate at which energy is delivered, this simple pulse-compression principle can be applied to achieve substantial power gains, especially when chaining together a series of pulse-compression stages, as is typically done in large pulsed-power systems.

The methods used to store and later compress the energy vary from one pulsed-power device to another, but typically, in the z-pinch community, the pulsed-power drivers consist of Marx generators used in conjunction with pulse-forming transmission lines (see Fig. 1.1).

The Marx generator is a bank of storage capacitors arranged such that they are charged slowly in a parallel configuration over a long period of time, and discharged rapidly in a series configuration. This results in a voltage gain effectively equal to the number of capacitors. The rapid reconfiguration from parallel to series connections is accomplished using spark-gap switches.

Spark-gap switches consist of two electrodes separated by ~1 cm and are typically filled with a gas such as SF_6 (sulfur hexaflouride). With a large enough voltage applied across the gap, the breakdown potential of the gas (or vac-

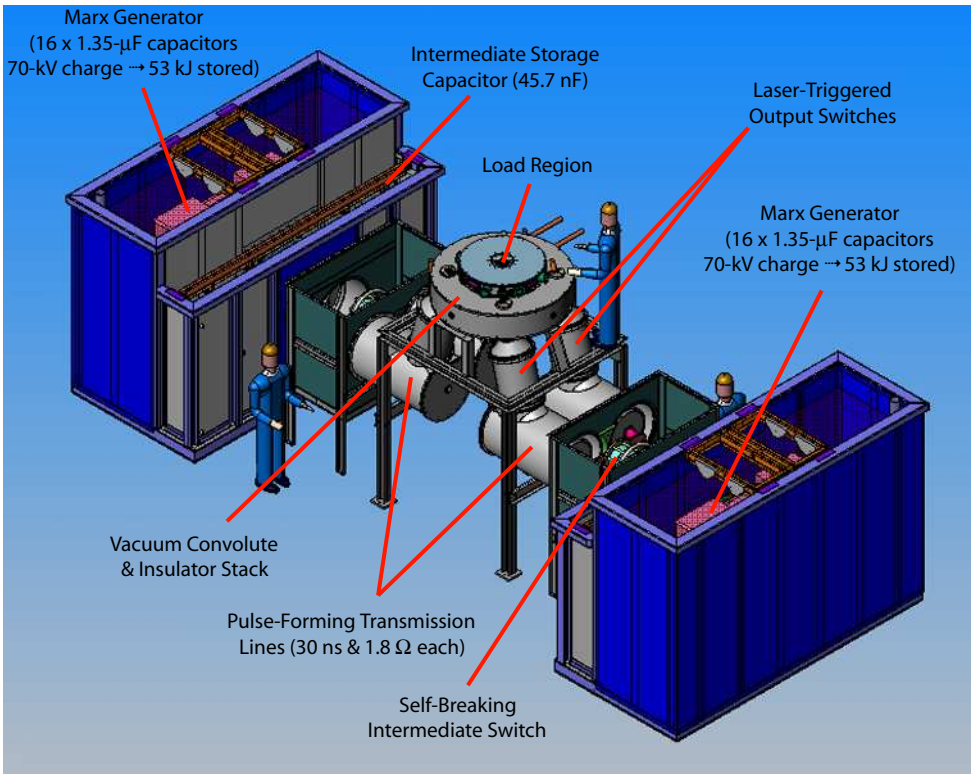

Figure 1.1: (Color) Drawing of the COBRA pulsed-power generator.

uum) can be exceeded, resulting in a plasma arc from one electrode to the other. This arc establishes the electrical connection necessary for current to flow in the Marx's series configuration. Spark-gap switches are also used to transfer energy from one pulse-compression stage to the next. To get spark-gap switches to close at desirable times, various triggering methods are used. In one method, a trigger pulse from an auxiliary voltage source is applied to an intermediate electrode between the two charged main electrodes of the switch. This quickly alters the gap potential, which can initiate breakdown, and thus establish switch closure. In another method, the beam of a laser is focused to a point between the two charged main electrodes. With a high enough laser intensity, electrons can be stripped from gas molecules in the gap, which can initiate breakdown, and thus establish switch closure.

The high voltage produced at the output of a Marx generator is typically fed into a large intermediate storage capacitor (ISC), which effectively lowers the output impedance of the Marx generator. The output of an ISC is usually spark-gap switched into one or more pulse-forming transmission lines. While a pulse line charges, its output spark-gap switch is in an open state. Once the pulse line charges to the desired voltage, V_0, the output switch is closed, and a current pulse flows into the load region of the machine. Theoretically, if the output of the pulse line is connected to a short circuit load, then a peak current of V_0/Z_0 results, where Z_0 is the impedance of the pulse line [17]. If the load is a resistor matched to the impedance of the pulse line, then a peak current of $V_0/(2Z_0)$ results—this is an important point to keep in mind later when we discuss the results of wire-array z-pinch implosions.

With the pulse-line output switches closed, the current pulse is finally delivered to the wire-array load, often by way of a vacuum convolute. As the current pulse approaches the wire array load in a typical convolute, the anode-cathode feed gap decreases (see Fig.1.2). The large voltages applied across the smaller and smaller gap size can lead to electron emission from the metal surface of the cathode feed. Electron emission crossing the anode-cathode feed gap can become a problematic source of current loss prior to reaching the wire array. This problem is mitigated however by magnetic insulation. Here the self-produced magnetic field lines of the current pulse are oriented perpendicular to the voltage drop across the anode-cathode feed gap. Since electrons are impeded from flowing across magnetic field lines by the Lorentz force, the electrons emitted from the cathode feed are partially restricted from flowing across the gap to the anode feed. The current pulse is then successfully delivered to the wire-array load.

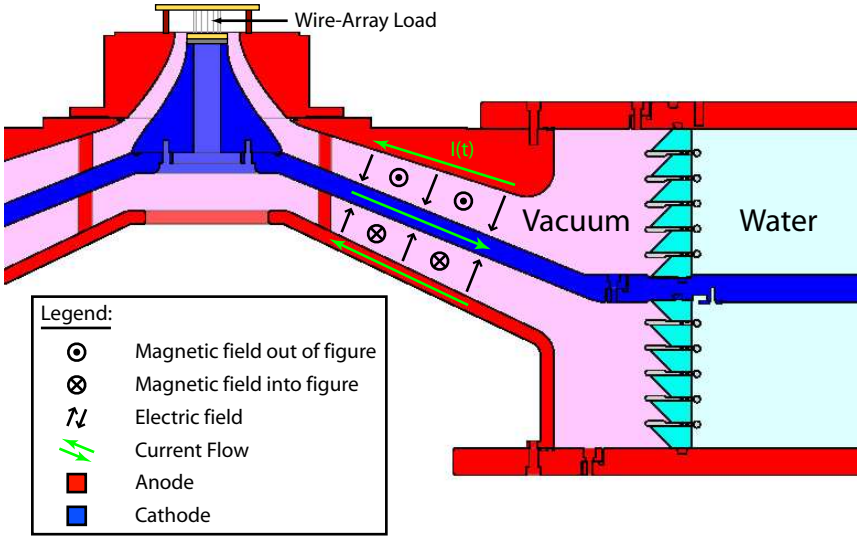

Figure 1.2: (Color) Cross-section of the COBRA vacuum convolute and insulator stack.

1.4 The Use of Pulsed Power in Experiments Leading up to Wire-Array Z-Pinches

Pulsed-power systems such as that described above existed prior to their use in wire-array z-pinch experiments. (For a nice review on the history and evolution of these machines up to their present use in wire-array z-pinch research, see the Ph.D. thesis by J. D. Douglass [18].) Following Douglass, the 1960s and 70s saw the use of such pulsed-power systems for generating relativistic electron beams (REBs) across anode-cathode gap diodes in the load region. These REBs were focused onto high-Z materials to generate intense hard x-ray sources for radiography. In the early to mid 70s, it was discovered that by stringing a single fine wire across the anode-cathode gap diode, plasmas with high temperatures and densities could be produced from the wire material, and that these plasmas radiated appreciable amounts of soft x-rays [19, 20].

1.5 Early Wire-Array Z-Pinch Research

To the author's knowledge, the first use of multiple wires arranged in a configuration that resulted in what would be known today as a wire-array z-pinch experiment did not come along until the work by Stallings *et al.* in 1976 conducted on the OWL II' generator at Physics International in California [21]. Here the authors began by presenting measurements from single-wire experiments showing that a significant fraction of the total load current flows outside of the wire material by way of vacuum electron flow from cathode to anode. They stated that this was a result of the high self-inductance of the single wire in the load region of the generator. Thus the main purpose of their study was to test whether decreasing the initial wire inductance would increase the electrical current flowing within the wire material, and therefore increase the energy coupling from the generator to the wire material. They reduced the initial wire inductance by changing from a single-wire configuration to a multi-wire configuration where either four or six aluminum wires were arranged as a cylindrical array 3–12.5 mm in diameter. To account for more wires being used, the individual wire masses were reduced from that of the single-wire configuration. These multi-wire experiments resulted in x-ray powers and yields significantly higher than those produced by single-wire experiments. Stallings *et al.* also observed that the wire material imploded during these experiments causing "bright spots" to be emitted from the array axis rather than the initial wire positions, and noted that it was unclear whether the high x-ray powers and yields were due to electrical resistivity and current on axis or to the kinetic energy of the implosion thermalizing on axis (or both).

The pioneering work by Stallings *et al.* spawned an abundance of wire-array

z-pinch research, which took place throughout the 1980s and into 90s. Much of this early work was carried out on the BLACKJACK 3, 4, and 5 generators at the Maxwell Laboratories [22, 23, 24], and later reviewed by Pereira and Davis [25]. Many of the observations and questions discussed in Ref. [25] are still relevant today, particularly those related to bright and/or hot spots, radiation transport effects, and early plasma blow-off and precursor radiation (these topics will be discussed later in this thesis). During this era from 1976 to the early 90s, the wire-arrays almost exclusively consisted of six wires, as six were theoretically shown to be stable against perturbations that destroyed cylindrical symmetry [26]. Also, experiments with 12 and 24 wires did not show an increase in x-ray yield [25].

1.6 Resurgence in Wire-Array Z-Pinch Research

The wire-array z-pinch community received a jolt of excitement in 1996 when Sanford *et al.* used the 8-MA Saturn generator at Sandia National Laboratories to conduct the first systematic study on the effect of increased wire number (or quasi-equivalently, the effect of decreased wire spacing) [27]. Here it was experimentally shown that decreasing the wire spacing from 5.8 mm to 393 μm, while keeping the array radius and mass constant, increased the total x-ray power by a factor of about 20. This was done by increasing the number of wires from 10 to 192, while correspondingly decreasing the wire diameter (i.e., the mass per wire). Also noted in this study was an apparent transition between a slow linear rise in x-ray power as wire spacing decreased from 5.8 to 1.4 mm, and a rapid non-linear rise as the wire spacing decreased from 1.4 mm to 393 μm. The transition found at the 1.4-mm wire spacing is likely material dependent, and in this

case, due to the expansion rate of the aluminum wires being used.

The success of the experiments conducted on Saturn was the impetus for converting Sandia's more powerful light-ion accelerator PBFA-II (Particle Beam Fusion Accelerator II) to drive wire-array z-pinch loads, becoming known as PBFA-II Z—a pulsed-power device capable of producing 20 MA in about 100 ns. Results of wire-array z-pinch experiments on the reconfigured accelerator were extraordinary. The use of 240, 7.5-μm-diameter tungsten wires (520-μm wire spacing) achieved an x-ray power of about 200-TW and an x-ray energy of nearly 2 MJ [2]. (To put this x-ray yield in perspective, 2 MJ is approximately equal to the kinetic energy of your average mid-size car racing down the highway at about 115 miles per hour—only this 2 MJ of x-ray energy is originating from a volume on the order of 50 mm^3 and being released in less than 10-billionths of a second.) For these experiments, the accelerator was discharging a total of only 11 MJ of stored electrical energy per shot [2], thus achieving the aforementioned conversion efficiency of $\gtrsim$15%. It should also be noted that even more powerful implosions have been achieved using nested wire array configurations, where multiple cylindrical arrays with different array diameters are arranged in a concentric fashion [1].

Due to the success of these experiments, and to the fact that light-ion experiments were terminated at the facility, PBFA-II Z simply became known as Z. In fact, Z has recently been upgraded to drive wire-array z-pinch loads at 26 MA in just over 100 ns (sometimes being referred to as Z*R* for Z-*Refurbished*). At the time of this writing, however, preliminary tests/experiments have only just begun [28, 29].

Today, the wire-array z-pinch community continues to try to increase x-ray

power, energy yield, and quality, as well as to understand how x-ray power and energy scale with the amplitude and rise time of the driving current pulse. The quest for this understanding is largely application driven. For example, experiments on Z have demonstrated that wire-array z-pinches (using the dynamic hohlraum approach) are capable of driving thermonuclear deuterium-deuterium fusion reactions [30]. In fact, recent experiments have achieved the indirect-drive ICF record for the production of thermonuclear neutrons (up to 3.5×10^{11} neutrons) [31]. In spite of these achievements, however, present x-ray powers and energies are not sufficient for high-yield ICF, and driver currents on the order of 60 MA are thought to be necessary [5]—although this scaling remains uncertain.

In attempts to better determine scaling laws, several paths are being taken. One route is to develop a deeper understanding of wire-array z-pinch processes through theory and simulation [32, 12], along with efforts to improve experimental data for code validation [33, 34, 35, 36, 3]. Another approach is to run experiments with different driver currents. Hence the Z accelerator upgrade to 26 MA, as well as research activity on lower-current machines such as the previously-mentioned 8-MA Saturn accelerator at Sandia [27, 37], the 4-MA Angara-5-1 facility in Russia [38, 39], and 1-MA machines found at universities, such as the MAGPIE facility at Imperial College, London [33, 40], the Zebra facility at the University of Nevada, Reno [41, 42], and the COBRA facility here at Cornell [43, 35, 44, 45, 34]. Remarkably, many of the wire-array z-pinch phenomena observed at 1 MA, such as wire ablation, a delayed implosion of the bulk of the wire mass, and the presence of trailing mass [45, 46, 41] (all topics that will be discussed later in this thesis), are also seen at 20 MA [47, 3].

1.7 Establishment of a National Center at Cornell

Partially due to the successes of preexisting university facilities, and partially due to recent community excitement in high-energy-density physics, a national center for the study of pulsed-power-driven high-energy-density plasmas has been established here at Cornell. In addition to Cornell, the center includes participants from the Lebedev Institute in Russia, Imperial College in London, the Weizmann Institute in Israel, the University of Rochester in New York, and the University of Nevada in Reno. The center was created at least in part to be a user facility, and has been utilized by visiting researchers from Sandia, the University of Michigan, the University of California, San Diego, and Idaho State University. In order to facilitate wire-array z-pinch research at Cornell, the Cornell Beam Research Accelerator (COBRA) was reconfigured to drive wire-array z-pinch loads at 1 MA, and now simply goes by the name COBRA. (Like the evolution of PBFA-II into the present Z machine, COBRA's history involves a reconfiguration from driving light-ion beams to driving wire-array z-pinches.) With the construction of the new driver, however, came the need to characterize the driver and the z-pinch processes that ensued. The results presented in this thesis constitute just such a characterization.

1.8 Summary of Findings & Conclusions

Throughout this thesis, we will be discussing the experimental techniques and results that led to the following findings and conclusions:

1. The highest peak radiated powers and total radiated energy yields were obtained using 4-mm-diameter arrays that stagnated before peak current
    - Measured up to 10 kJ of total radiated energy
        - A conversion efficiency of about 10% from stored electrical energy
        - An increase of 1.5–2× relative to other loads tested
    - Measured 300–500 GW of peak radiated power
        - An increase of 1.5–2× relative to other loads tested
    - Physical reasons for this enhanced radiation:
        - The Poynting flux is directed into the pinch prior to peak current, and is maximum at 2/3 of the time to peak current, which is similar to the stagnation times of these light, 4-mm-diameter arrays
        - Small-diameter arrays transfer current to axis during implosion/stagnation more efficiently, thereby increasing compressional and/or resistive heating
        - The fast overall implosion phase for light, small-diameter arrays (found to be about 6 ns) mitigates the negative effects of Rayleigh-Taylor growth

  - The dynamic impedances of light, small-diameter arrays are better matched to COBRA, thus increasing energy coupling to these loads

2. Sub-keV radiation from the precursor column decreases significantly as wire spacing goes from 1.6 mm to 785 μm, and precursor columns are more unstable for wire spacing ≥1.6 mm, indicating that more current is transferred to the precursor column for wire spacing ≥1.6 mm
3. From trajectory fits, ablation velocities were in the range of 110–170 km/s and trailing masses were in the range of 20–40% (although the fits were not unique)
4. A greater number of hot-spots were observed for all materials tested when stagnation occurred before peak current and 4-mm-diameter arrays were used
5. Hot spot formation was observed to have a transient and discrete nature similar to micro-pinch processes in x-pinches
6. During the radiation pulse of an experiment, a transition to higher-energy x-rays was observed, and can be explained by an effective current sheath arriving on axis, compressing the plasma column, and driving micro-pinches
7. The driving electrical power pulse into the load closely resembles the radiated power pulse out of the load

    - Indicates that resistive and/or magnetic compressional heating contribute directly and significantly to the total radiated power on COBRA

- Supports arguments regarding the relevance of Poynting flux and hot spots

8. Spectroscopic measurements of the coronal plasma in aluminum wire-array z-pinch experiments showed only continuum radiation in visible wavelengths

    - The continuum emission began at the time of wire breakdown for thick 134-μm wires
    - The volume continuum intensity was in the range of about 1–6 x 10^{17} photons/sec/sterad/cm^3/Å, with a nearly constant spectral dependence
    - The continuum intensity was proportional to the driving current

CHAPTER 2

THE COBRA PULSED-POWER GENERATOR

2.1 Overview of COBRA

The COBRA generator delivers 0.8–1.2-MA current pulses to wire-array z-pinch loads (see Fig. 1.1). Laser-triggered pulse-line output switches enable current pulse shaping, where the zero-to-peak rise time can be made to vary from just under 100 ns to more than 200 ns. COBRA is a negative-polarity machine consisting of two Marx generators, each with 16, 1.35-μF capacitors. These capacitors are charged to 70 kV for approximately 100 kJ of stored electrical energy. Each Marx generator discharges into its own large ISC. Subsequently, each ISC discharges into two pulse-forming transmission lines (i.e., four pulse-lines in total). The four parallel pulse-lines have an effective output impedance of about 0.45 Ω, and feed a magnetically insulated vacuum convolute (see Fig. 1.2). This convolute enables delivery of the current pulse to the wire-array load. The experiment chamber is large (about 1 m in diameter) and accessible making it easy to equip the chamber with diagnostics simply by placing them on custom-built breadboards which surround the load region. The chamber also includes 18 side-on ports for radial viewing and two end-on ports for axial viewing (one above and one below). With vacuum pump times on the order of one hour, several shots can be made per day. For a detailed description of COBRA, see Refs. [48, 49].

2.2 Diagnostics on COBRA

2.2.1 Current Monitor

The main load current on COBRA is monitored by a large Rogowski coil. This is essentially a helical coil of wire, where the lead at one end is passed back through the coil to the other end. The helix is then wrapped around a point external to the coil forming a torus. The torus is then installed in COBRA's anode-cathode feed structure such that the torus encircles the cathode feed. As a current pulse flows into the load region, magnetic flux is generated around the cathode feed. The voltage across the two leads of the Rogowski coil is then proportional to the time-rate-of-change of the magnetic flux within the helical coil, which is of course proportional to the time-rate-of-change of the load current that generated the magnetic flux. Thus, to actually determine the load current, we must integrate the raw dI/dt signal that is recorded. The beauty of the Rogowski coil, however, is that it is insensitive to positioning, and only depends on the total current encircled by the torus [50].

2.2.2 Voltage Monitor

COBRA is equipped with an inductive load voltage monitor, which is essentially a long, high-inductance wire that makes a connection between the high-voltage cathode near the base of the wire array and the grounded chamber wall deep within the vacuum stack. This makes a long enough path length to limit inductively the current through the wire to less than 3% of the main load current. The current driven by the load voltage through the high-inductance wire is

measured by an adjacent $\dot{B}$ probe. Aside from a calibration factor, this measures voltage directly.

2.2.3 Bolometer

A bolometer is a device that allows one to measure directly the total radiated energy assuming it is protected from particle energy and debris. It is typically comprised of a thin metallic element that is exposed to the incident photon flux. The incident photon flux heats the element, causing a corresponding change in the element's resistivity and thus total resistance. The element's resistance is determined simply by Ohm's law, where one monitors an auxiliary current that is passed through the element for the duration of the experiment while simultaneously monitoring the voltage drop across the element (i.e., the voltage drop responsible for driving this current through the element). By knowing the temperature coefficient of the element resistivity, the specific heat of the material, and the area of the element exposed to the incident photon flux, one can determine a calibration factor for a bolometer in joules of x-ray energy deposited on the element per volt recorded on the oscilloscope. The COBRA diagnostics suite includes one bolometer with the calibration factor 0.55 J/V.

The bolometer provides a time-dependent measure of deposited x-ray energy with better than 3-ns resolution. This is because the element's temperature responds quickly to incident radiation (i.e., less than 3 ns), while it cools very slowly (i.e., much longer than the time-scale of the experiment). Thus one actually records the integrated history of the instantaneous radiation flux or power.

Finally, the element material of the COBRA bolometer is nickel, which effec-

tively provides a flat spectral response from zero eV out to a few keV. Bolometer elements are made from other materials as well, such as aluminum or gold. One can use different materials to provide slightly different spectral responses. These spectral differences are most noticeable above a few keV.

2.2.4 Photoconducting Detectors (PCDs)

COBRA is equipped with several Photoconducting Detectors (PCDs), which are simple devices used to measure instantaneous x-ray powers. PCDs are essentially two-electrode devices, where the electrodes are approximately 3-mm in length and separated by about 1 mm. The space between the two electrodes is filled with diamond, and the electrodes are typically biased to 300 V. When exposed to x-rays, electrons are produced in the diamond by photoelectric absorption. These electrons are accelerated by the bias voltage, and collected by the positively biased electrode. The result is a signal that is monitored by an oscilloscope. The x-ray power is determined by the calibration factors, typically in the range of 20–100 W/V. This calibration is possible due to the flat spectral response of a PCD (at least up to photon energies of a few keV), and the fast on/off response times (~1 ns or better). Various filters can be placed in front of the exposed PCD to measure x-ray powers in various photon energy ranges.

2.2.5 Silicon Diodes

COBRA is also equipped with several silicon diodes (SiDs). These are similar to PCDs, but with several differences. First, the active element in an SiD is, as its

name would suggest, silicon. The spectral response of these devices is far from flat. Moreover, the response at any given wavelength is largely non-linear. For these reasons, SiDs are difficult, if not impossible, to calibrate. However, their response times are fast, and they are much more sensitive and less expensive than PCDs. Thus we typically use SiDs for simple detection and timing purposes (e.g., we may filter and bias them appropriately for detecting low levels of hard x-ray radiation).

2.2.6 Time-Integrated Pinhole Cameras

Several time-integrated pinhole cameras are available for use on COBRA with various x-ray films. Pinhole cameras can be understood by simple ray-tracing arguments. The radiating source emits varying levels of light intensity from different spatial points. Each emission point maps uniquely to a corresponding point on the film through the camera's single small pinhole. Ideally, this pinhole would be infinitesimal for perfect resolution, however this would cut off all light entirely. Thus a trade-off must be made between resolution and the intensity required to expose the film. Also, the size of the pinhole determines the lower energy threshold for the transmission of light through the pinhole (i.e., only photons with energies above the diffraction limit are effectively transmitted). Additionally, various filters can be applied to provide still greater control over the transmission of various photon energies. Thus with these cameras one can obtain time-integrated images of the radiating plasma source in various energy ranges.

2.2.7 Laser Shadowgraph System

On COBRA, three Canon digital EOS cameras with high resolution CCD chips, are used in conjunction with a frequency-doubled Nd:YAG laser (532 nm) to produce 150-ps time-resolved laser shadowgraph images. The main beam of the laser source is split into three channels to provide various frame times (about 10 ns between frames). This is accomplished simply by varying the path lengths of the three beams prior to their passage through the experiment chamber.

The images produced are due to a schlieren-like process [50], where parts of the imaging beam are refracted by density gradients in the plasma. The rays that are refracted only slightly by relatively mild density gradients are collected and focused by imaging optics, while rays that are refracted to larger angles by sharper density gradients are scattered out of the collection cone of the imaging optics. This process is not properly called schlieren imaging, however, as there is no beam stop at the focal point of the unperturbed rays. Also, it should be mentioned that complete reflection of an imaging photon will occur wherever the plasma density is high enough such that the electron plasma frequency exceeds the laser frequency. As the frequency of a 532-nm laser is 5.6×10^{14} Hz, the corresponding electron density is $3.9 \times 10^{21}/\mathrm{cm}^3$. The non-uniform plasma stagnating on the array axis in a wire-array z-pinch experiment can exceed this cutoff density, but only in some small localized regions. Therefore any contribution to the shadow image from this mechanism is most likely very small compared to that caused by refraction.

From these images, it is difficult to obtain quantitative information about actual plasma state parameters such as density. This is because a given ray may actually refract multiple times due to interactions with various density gradi-

ents as it traverses the plasma. It is then difficult, if not impossible, to unfold this history from the net refraction. On the flip side, these images do provide a qualitatively valuable picture of what is going on with the bulk mass of the plasma. Also, some geometrical quantities, such as implosion convergence ratios, axial periodicity of ablation streams, and the size of implosion bubbles can be determined. (Ablation streams and implosion bubbles are discussed in Chapters 4 and 5.)

2.2.8 Time-Gated Micro-Channel-Plate (MCP) Camera

COBRA is equipped with a time-gated MCP camera suitable for imaging with photon energies ranging from extreme-ultra-violet (XUV) to >1 keV. The camera can take up to four frames, and is set up for better than 4-ns time resolution. The use of pinholes (one pinhole per frame channel) enables 2D spatial imaging similar to that described in Ref. [51]. Again, various filters and pinhole sizes can be used to look at various photon energy ranges. After the pinholes, a photocathode converts incident photons to electrons via the photoelectric effect. The electrons are then accelerated and photomultiplied within small capillaries by a bias voltage applied along the capillaries. At the end of the capillaries, the accelerated and multiplied electrons impact a phosphor screen. The resulting phosphorescence exposes visible-wavelength-sensitive film. Time gating is accomplished by applying the accelerating bias voltage to the capillaries of a given frame channel only during the time of interest for that channel. Thus the minimum time resolution is determined by how short one can make the bias pulse width together with the capacitive limitations of the MCP circuit. Currently, the Blumlein transmission lines in the MCP's pulse generator produce about 4-ns

pulse widths.

2.2.9 Streak Cameras

Two streak cameras are available on COBRA. One is a Hamamatsu visible-light streak camera and the other is a Kentech x-ray streak camera. Both work fundamentally the same—i.e., they both "streak" a single dimension of incident photon intensity as a continuous function of time (see Fig. 2.1). This single dimension can, for example, be either a spatial dimension (as in a dynamics study) or a wavelength dimension (as in a spectroscopic study).

Photons from the single dimension chosen must be incident on the entrance slit of the given streak camera. In the case of the visible light streak camera, the photons are imaged onto the entrance slit and this image is then transferred by the camera's internal relay optics to a photocathode. In the case of the x-ray streak camera, the x-rays are transmitted directly to the photocathode (without imaging) through a cross slit. For both cameras, the photons reaching the photocathode are converted to electrons via the photoelectric effect. These electrons are accelerated longitudinally within the streak camera by a biases grid. At the end of this longitudinal acceleration, the electrons are focused by an electrostatic lens.

After the electrons have been accelerated longitudinally and focuses, they are deflected laterally by a time-varying transverse electric field. This field is created by discharging a bias potential across two plates (one plate on each side of the electron stream). This effectively paints the electron stream onto the phosphor screen in a single sweeping motion (similar to a cathode-ray tube televi-

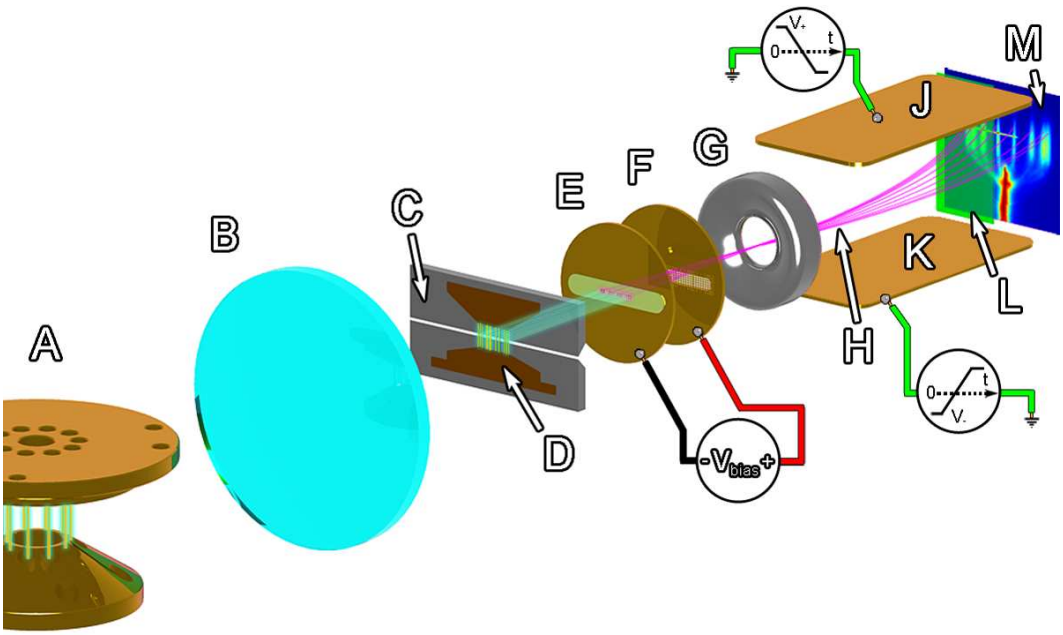

Figure 2.1: (Color) Graphic of a generic visible light streak system illustrating the working principles. The components are: (A) wire-array z-pinch load (usually the self emission from the wire plasma is the source of visible light), (B) optical relay lens (this could be a system of relay optics), (C) streak camera entrance slit, (D) image of wire-array and load region at the entrance slit, (E) electron-emitting photocathode, (F) electron-accelerating grid, (G) electrostatic lens, (H) electron trajectories, (J) upper sweep bias plate, (K) lower sweep bias plate, (L) phosphor screen, (M) detector (film, CCD camera, etc.). (Figure courtesy of J. D. Douglass.)

sion). The phosphorescence from the phosphor screen is then recorded by film or a digital CCD camera, or it is further intensified by use of an MCP (see 2.2.8 for a description of MCP operation). The visible streak system on COBRA, for example, uses an MCP to intensify the streak camera's phosphor image, and then digitally records the luminescence from the MCP's phosphor screen via a CCD camera. The digital image is then easily viewable with varying contrast using Hamamatsu's pre-packaged image software, as well as easily saved for post-processing.

The transverse bias voltage versus time waveform in a streak camera is a non-linear "S" curve. Thus one only uses the approximately linear region in the middle of this curve as the streak time window so that there is a linear relationship between a position in an image and the time of that position. Also, varying streak speeds and time windows can be obtained by making adjustments to this discharge waveform (this is automated for the visible streak camera by the Hamamatsu software, but must be done manually for the x-ray streak camera).

The time resolution of a streak image depends on the streak speed, the input slit width, and the streak camera's internal magnification. For example, if an instantaneous flash of light occurs during a streak, then an image of the input slit will be produced at that particular moment in time. This flashed slit image will then take up some finite fraction of the total streak image in the time direction (based on the slit width and the internal magnification within the streak camera). In other words, if the streak window is 100 ns, and a flashed slit image takes up 5% of the total streak image in the time direction, then the time resolution is 5 ns.

It should also be mentioned that the visible light streak camera can be put into "live mode" (also known as "focus mode"), which allows an experimenter the ability to make optical alignment and focusing adjustments to their system while continually monitoring the effects of those adjustments. Live mode is a system state where the streak camera has no transverse bias potential applied. Thus the electrons stream straight through to the phosphor screen, producing a stationary image of the streak camera input slit (i.e., with a small ~100-μm slit width, live mode will result in a thin horizontal line across the middle of the image). To allow the nearly real-time adjustment-monitoring capability, the

system's CCD camera continually takes pictures and sends them to the system's PC. The PC then continually updates the image on the computer monitor with the most current one taken by the CCD camera (the image is usually updated every half second or so). Also, by opening the slit wide (i.e., on the order of millimeters), 2D imaging can be accomplished in live mode, which helps when trying to focus an image onto the input slit/plane of the streak camera as well as when trying to align a particular part of an object's image onto the input slit.

2.2.10 Wide-Band Focusing Spectrograph with Spatial Resolution (WB-FSSR)

The WB-FSSR is a spherical-crystal x-ray spectrograph. What sets it apart from other similar spectrographs is the use of three spherically bent mica crystals that enable the simultaneous viewing of a much wider band of wavelengths than is typically available (the bandwidth usually being limited by how large one can make the bent spherical crystals). On COBRA, the WB-FSSR utilizes multiple-order reflections to view photon energies from about 670 eV all the way up to 9 keV or even higher.

The beauty of this device lies in the fact that essentially three dimensions of information are imaged onto a two-dimensional piece of film. This is because the images produced by this device have 2D spatial resolution, as well spectral resolution (i.e., the typical setup is such that the spectral and horizontal spatial dimensions share a direction on the film).

A thorough explanation of this device is cumbersome and beyond the scope

of this thesis, but is described nicely by S. A. Pikuz *et al.* [44]. The basic idea, however, is that there is a trade-off between spectral and spatial resolution. In the ideal sense, there is only one wavelength (or point on the film) with perfect spectral resolution (and hence no spatial resolution). As you move away from this point, the spectral resolution degrades slightly, but horizontal spatial resolution is acquired as the image of any horizontal spatial extent begins to magnify. In the practical sense, one essentially gets the best of both worlds.

2.2.11 Faraday Cup

The Faraday cup on COBRA is a simple device consisting of a small metal disc (about 1 cm in diameter) connected to ground via a resistive network. This disc becomes charged when placed in a stream of charged particles (e.g. electrons). The degree to which this disc becomes charged is dependent on how many electrons are incident on the disc. Thus the greater the electron intensity, the greater the voltage drop across the resistive network, which is monitored by an oscilloscope. The Faraday cup on COBRA is used to determine the electron beam intensity above the anode (the anode has a hole on axis to allow electron beams to pass). Finally, various filters can be placed in front of the disc to allow only higher energy electrons to be collected.

2.2.12 Other COBRA Diagnostics

Many of the diagnostics highlighted above are discussed further in Ref. [43]. However, the time-gated XUV/MCP camera, the two streak cameras, the Fara-

day cup, and the bolometer are new additions to the COBRA diagnostics suite since Ref. [43] was published. Also new, though not used in the experiments of this thesis, is a five-channel point projection x-ray back-lighting system by the name of STAR (sequential trans-axial radiography). This is a new x-pinch-based imaging system that has been developed at Cornell, and is currently operational (see Ref. [34]). Other recent developments worthy of mention are micro-$\dot{B}$ probes that have been deployed for measuring magnetic field penetration into the interior of the arrays prior to implosion, and an end-on/axial laser-interferometry system.

CHAPTER 3

THE Z-PINCH

3.1 Streaming Filamentation in Nature

Wherever there is an electrical current, there are streaming charge carriers, whether they be electrons, ions, positrons, or what have you. These streaming charged particles tend to self focus due to electromagnetic forces. If considering a bulk material such as an ionized gas or plasma, the self focusing of the constituent charge carriers results in the formation of a predominant current filament, as is readily observed in nature (e.g., lightning bolts, welding arcs, etc.). The streamers from a lightning discharge often branch off in a seemingly haphazard manner. However if you look at any one branch, you will see the same phenomenon, namely a self-confined electrical current channel. The radii of these current channels are often more-or-less constant in time suggesting that some kind of equilibrium has been achieved. It turns out that one can solve for this equilibrium, as was originally shown by W. H. Bennett [52], and later supplemented with power input/output considerations by R. S. Pease [53] and S. I. Braginskiĭ [54].

3.2 Bennett Pinch Equilibrium

As stated, electromagnetic forces cause streams of charged particles to self focus. The electromagnetic force on a charged particle is the well known Lorentz force

[55]

$$\mathbf{F} = q\left(\mathbf{E} + \mathbf{v} \times \mathbf{B}\right), \tag{3.1}$$

where $\mathbf{E}$ is the electric field intensity, $\mathbf{v}$ is the charged particle velocity, $\mathbf{B}$ is the magnetic flux density, q is the charge of the particle, and boldface Roman font represents vector fields in three dimensional space. The electric and magnetic fields must always satisfy Maxwell's equations [55]

$$\nabla \cdot \mathbf{E} = \frac{\rho}{\epsilon_0} \tag{3.2}$$

$$\nabla \cdot \mathbf{B} = 0 \tag{3.3}$$

$$\nabla \times \mathbf{E} = -\frac{\partial \mathbf{B}}{\partial t} \tag{3.4}$$

$$\nabla \times \mathbf{B} = \mu_0 \mathbf{J} + \mu_0 \epsilon_0 \frac{\partial \mathbf{E}}{\partial t}, \tag{3.5}$$

where ρ is the volume charge density, $\mathbf{J}$ is the electrical current density, t is time, and ϵ_0 and μ_0 are the permittivity and permeability of free space, respectively. In theory we can solve Maxwell's equations and the Lorentz equation self-consistently for any number and variety of charged particles [56]. However, in practice this is essentially impossible. Thus we are forced to make assumptions based on the system of interest. For wire-array z-pinch work, we are often dealing with plasmas that can be treated quasi-neutrally using a simple collisionless two-fluid model. The equations of motion for a two-fluid plasma are [57]

$$m_i n_i \dot{\mathbf{v}}_i = q_i n_i (\mathbf{E} + \mathbf{v}_i \times \mathbf{B}) - \nabla p_i \tag{3.6}$$

$$m_e n_e \dot{\mathbf{v}}_e = q_e n_e (\mathbf{E} + \mathbf{v}_e \times \mathbf{B}) - \nabla p_e, \tag{3.7}$$

where $m_{i,e}$ are the particle masses, $n_{i,e}$ are the particle volume densities, $q_{i,e}$ are the particle charges, $p_{i,e}$ are the thermal partial pressures, and the subscripts i and e denote ions and electrons, respectively. However, since $\mathbf{v}_{i,e}(t)$ describes

the bulk motion of the fluid, and since we are seeking a steady-state equilibrium solution, we can set $\dot{\mathbf{v}}_{i,e} = 0$, and thus the left-hand sides of Eqns. 3.6 and 3.7 are zero. Also, as ions in real experiments will have varying degrees of ionization, we must use the average ionic charge, $\bar{Z}$, in a two-fluid approximation. Thus with the assumption of quasi-neutrality, $n_e = \bar{Z} n_i$, $q_i = -\bar{Z} q_e$, and $q_i n_i = -q_e n_e$. Putting all of this together, we can sum Eqns. 3.6 and 3.7, giving

$$0 = (q_i n_i \mathbf{v}_i + q_e n_e \mathbf{v}_e) \times \mathbf{B} - \nabla(p_i + p_e). \tag{3.8}$$

But $(q_i n_i \mathbf{v}_i + q_e n_e \mathbf{v}_e)$ is the very definition of the current density $\mathbf{J}$, and the sum of the partial pressures, $(p_i + p_e)$, is just the total pressure p. So Eqn. 3.8 becomes

$$0 = \mathbf{J} \times \mathbf{B} - \nabla p, \tag{3.9}$$

or,

$$\nabla p = \mathbf{J} \times \mathbf{B}. \tag{3.10}$$

This simply states that the force density due to the gradient in the thermal pressure is balanced by the "$\mathbf{J} \times \mathbf{B}$ force" density. This is essentially the Bennett pinch equilibrium. Bennett was able derive the current at which this equilibrium should occur, I_B, as follows. Since we are seeking a steady-state solution, we can set $\partial \mathbf{E}/\partial t = 0$ in Eqn. 3.5, and thus we can replace $\mathbf{J}$ in Eqn. 3.10 with $\nabla \times \mathbf{B}/\mu_0$, giving

$$\nabla p = \frac{1}{\mu_0} (\nabla \times \mathbf{B}) \times \mathbf{B}. \tag{3.11}$$

Using a well known vector identity, this becomes

$$\nabla p = \frac{1}{\mu_0} \left[(\mathbf{B} \cdot \nabla)\mathbf{B} - \frac{1}{2} \nabla(\mathbf{B} \cdot \mathbf{B}) \right] \tag{3.12}$$

$$= \frac{(\mathbf{B} \cdot \nabla)\mathbf{B}}{\mu_0} - \frac{\nabla B^2}{2\mu_0} \tag{3.13}$$

At this point we make the assumption that our plasma has the form of a long cylindrical column (as is typically the case for the z-pinches/filaments we

are trying to model). The letter z in *z-pinch* comes from the fact that we align the axis of the plasma column with the z-axis of a cylindrical coordinate system, and choose the polarity such that the electrical current runs in the positive z-direction (i.e., $\mathbf{J} = J_z\hat{z}$, where $J_z > 0$). In this case, $\mathbf{B}$ has only a positive azimuthal component (i.e., $\mathbf{B} = B_\phi\hat{\phi}$ where $B_\phi > 0$), and therefore the $\mathbf{J} \times \mathbf{B}$ force density, $\mathbf{F}_{\mathbf{J}\times\mathbf{B}}$, is radially inward everywhere (i.e., $\mathbf{F}_{\mathbf{J}\times\mathbf{B}} = -J_z B_\phi \hat{r} = F_{\mathbf{J}\times\mathbf{B},r}\hat{r}$ where $F_{\mathbf{J}\times\mathbf{B},r} < 0$). In equilibrium, it is this radially-inward force density that balances the radially-outward force density of the particle thermal pressure. Additionally, this symmetry implies that the only variation is in the r-direction, so that $\nabla \rightarrow \partial/\partial r$ in Eqn. 3.13, and thus the first term on the right-hand side of the same equation becomes $-(B^2/\mu_0 r)\hat{r}$. Finally, we will take this plasma column to have a radius a, such that the particle density, and hence particle pressure, go to zero for $r \geq a$. With all of this in mind, we can multiply Eqn. 3.13 by r^2 and integrate from 0 to a (integrating by parts where needed), to get

$$\int_0^a \frac{\partial p}{\partial r} r^2 dr = -\int_0^a \frac{B^2}{\mu_0} r dr - \int_0^a \frac{\partial B^2}{\partial r}\frac{r^2}{2\mu_0} dr \tag{3.14}$$

$$pr^2\Big|_0^a - \int_0^a 2pr dr = -\int_0^a \frac{B^2}{\mu_0} r dr - \left(\frac{B^2 r^2}{2\mu_0}\Big|_0^a - \int_0^a \frac{B^2}{\mu_0} r dr\right) \tag{3.15}$$

$$\cancelto{0}{p(a)a^2} - \frac{1}{\pi}\int_0^a p 2\pi r dr = -\frac{B^2(a)a^2}{2\mu_0} \tag{3.16}$$

$$\frac{\int_0^a p 2\pi r dr}{\pi a^2} = \frac{B^2(a)}{2\mu_0} \tag{3.17}$$

$$\frac{\int_0^a p 2\pi r dr}{\int_0^a 2\pi r dr} = \frac{B^2(a)}{2\mu_0} \tag{3.18}$$

$$\langle p \rangle = \frac{B^2(a)}{2\mu_0} \equiv p_{mag}(a). \tag{3.19}$$

Here we have made use of the definition of an average over a distribution to get $\langle p \rangle$, the average particle pressure in the column. Thus Eqn. 3.19 states that $B^2(a)/2\mu_0$ (which we have defined here to be the magnetic pressure at a) must equal the average particle pressure throughout the plasma column.

Now, since we have specified that the particle density goes to zero for $r \geq a$, there can be no charge carriers, and hence no electrical current density for $r \geq a$. Therefore, with all of the current contained to $r < a$, we know that $B(a) = \mu_0 I/2\pi a$ (or in other words, to generate a value of $B(a)$, the driving current must be $I = 2\pi a B(a)/\mu_0$). Plugging this value for $B(a)$ into Eqn. 3.19, we get

$$\langle p \rangle = \frac{\mu_0 I^2}{8\pi^2 a^2} \equiv p_{mag}(a), \tag{3.20}$$

or, rearranging and solving for I, we get

$$I = \left(\frac{8\pi^2 a^2}{\mu_0} \langle p \rangle \right)^{\frac{1}{2}} \equiv I_B. \tag{3.21}$$

Equation 3.21 defines the equilibrium current found by Bennett. However, to get it into his form, we must further manipulate. First, in Bennett's 1934 paper, he assumes only singly-charge ions, or $\bar{Z} = 1$, thus $n_e = n_i \equiv n$. Second, he uses transverse temperatures (i.e., the temperatures in the r-ϕ plane), and allows for the electrons and ions (or positives as he calls them) to have independent temperatures, T_1 and T_2. Now, since these temperatures assume two degrees of freedom, and the average particle energy per degree of freedom is $kT/2$, where k is the Boltzmann constant, we can write the average pressure as

$$\begin{aligned} \langle p \rangle &= \langle p_e \rangle + \langle p_i \rangle & (3.22) \\ &= \langle n_e \rangle k T_1 + \langle n_i \rangle k T_2 & (3.23) \\ &= \langle n \rangle k (T_1 + T_2), & (3.24) \end{aligned}$$

and thus,

$$I_B^2 = \frac{8\pi^2 a^2}{\mu_0} \langle n \rangle k (T_1 + T_2). \tag{3.25}$$

Further still, Bennett prefers a linear particle density, N, which is obtained by multiplying our average volume particle density $\langle n \rangle$ by the area of our plasma

column πa^2. This leads to

$$I_B^2 = \frac{8\pi}{\mu_0} Nk(T_1 + T_2). \tag{3.26}$$

Of course Bennett wrote his paper in 1934, so naturally he used c.g.s. units. For converting from m.k.s. to c.g.s., $4\pi/\mu_0 \rightarrow c^2$ in Eqn. 3.26, and the rest remains unchanged (in this case). Thus finally we have

$$I_B^2 = c^2 \cdot 2Nk(T_1 + T_2) \quad \text{[c.g.s]}. \tag{3.27}$$

[For the purist—To match Bennett's somewhat strange notation, we would have to make the following symbolic reassignments: $I_B \rightarrow i_0$, $k \rightarrow K$, and $N \rightarrow \lambda_0$. Also, Bennett writes his linear particle density (our N) as

$$\lambda_0 = [c^2 \cdot 2k(T_1 + T_2)]/e^2(u + v)^2 \quad \text{[c.g.s]}, \tag{3.28}$$

where e is the charge of an electron, and u and v are the velocities of the electrons and positives, respectively (see his Eqn. 12). With this then, the square-root of Eqn. 3.27 becomes

$$i_0 = [c^2 \cdot 2K(T_1 + T_2)]/e(u + v) \quad \text{[c.g.s]}, \tag{3.29}$$

which matches his result exactly (i.e., the equation immediately following his Eqn. 12).]

To put Eqn. 3.21 in more traditional form, such as that found in N. R. Pereira's 1990 paper [58], we assume the ions and electrons have the same transverse temperature (i.e., $T_i = T_e \equiv T$), and that the temperature is uniform throughout the column. In this case we can write the average particle pressure as

$$\begin{aligned} \langle p \rangle &= \langle p_e \rangle + \langle p_i \rangle & (3.30) \\ &= \langle n_e \rangle kT + \langle n_i \rangle kT & (3.31) \\ &= \langle n_e \rangle (1 + 1/\bar{Z}) kT. & (3.32) \end{aligned}$$

Plugging $\langle p \rangle$ into the square of Eqn. 3.21, we have

$$I_B^2 = \frac{8\pi^2 a^2}{\mu_0} n_e (1 + 1/\bar{Z}) kT \tag{3.33}$$

$$= \frac{8\pi}{\mu_0} N_e (1 + 1/\bar{Z}) kT, \tag{3.34}$$

where this time we have made use of the linear electron density $N_e \equiv \pi a^2 \langle n_e \rangle$. Finally, after some slight rearrangement, we get

$$\frac{\mu_0 I_B^2}{4\pi} = 2N_e (1 + 1/\bar{Z}) kT, \tag{3.35}$$

as stated in Ref. [58].

The Bennett current is an interesting figure of merit since currents less than I_B will allow the plasma column to expand radially due to the thermal pressure exceeding the magnetic pressure. Conversely, currents exceeding I_B will drive a radial contraction of the plasma column (hence the *pinch* in *z-pinch*). The dynamics of just such a system are the subject of the following section.

3.3 Dynamics from Non-Equilibrium

In the preceding section we considered a warm cylindrical plasma column with a radius $r = a$ and a uniform temperature and density throughout. In this section we will look at the dynamics that result from driving a current through a system initialized in a non-equilibrium configuration. Namely, we will consider a cold plasma ($T_e = T_i = 0$) with all of the mass (and thus current) confined to an infinitely thin cylindrical shell at a radius $r = r_s$. This thin-shell model has been around for several years [25, 12], but is illustrative and useful nonetheless.

When current starts to flow, and $T = 0$, there is no thermal pressure to balance the magnetic pressure. By confining all of the current and mass to the

infinitely thin shell at $r = r_s$, the magnetic field is zero for $r < r_s$ and $\mu_0 I/2\pi r$ for $r > r_s$. Thus the magnetic field infinitesimally close to (but just outside of) the shell is essentially the same as in the preceding section at the outside edge of the Bennett equilibrium, namely $B(r_s) = \mu_0 I/2\pi r_s$. Thus there exists a large magnetic pressure gradient across the shell that accelerates the shell mass radially inward, and r_s becomes the dynamic variable $r_s(t)$.

The magnetic force per unit area (i.e., magnetic pressure) is $p_{mag} \equiv B^2(r_s)/2\mu_0 = \mu_0 I^2/8\pi^2 r_s^2$. Due to the cylindrical symmetry, this pressure is uniform over the entire shell surface. Thus the total force on the shell (directed radially inward everywhere) is the magnetic pressure times the surface area of the shell, $p_{mag} \cdot 2\pi r_s \cdot l$, where l is the length of the shell in the z-direction. This leads to the following equation of motion for a thin shell of unit length (i.e., $l = 1$):

$$\hat{m}\ddot{r_s} = -\frac{\mu_0 I^2}{4\pi r_s}, \tag{3.36}$$

where $\hat{m}$ is the mass of the shell per unit length.

This differential equation can be integrated numerically for any given $I(t)$ to predict implosion/stagnation times for the various initial masses and driving current pulses of real experiments. Examples of hollow cylindrical systems for which this model might apply include annular gas puff z-pinches [59], thin foil z-pinches [60], and the wire-array z-pinches discussed in this thesis. However in each of these cases there are differences between the idealizations of this model and reality. In the case of gas puffs, the initial mass distribution is difficult to control. The gas-injection process into the anode-cathode gap prior to the application of the current pulse leads to shell thickness and non-uniformity from the start. Likewise, with foil experiments, the thin foils used can become creased

during hardware and load assembly prior to an experiment. Also, foil experiments reveal that a small amount of ionized material blows off and assembles on the cylindrical axis much earlier than the bulk implosion [61]. This precursor implosion indicates that the foil material is not ionized uniformly from the start. Non-uniformities in foil implosions can result in current flows with azimuthal and radial components in addition to the axial component.

Early plasma blow-off and precursor implosion are also observed with wire-arrays. Additionally, wire-array z-pinch experiments show that most wire-array configurations preserve individual wire-plasma identity throughout the implosion (at least until the end of the implosion when all the current channels merge on axis). In other words, most wire-array configurations do not merge into a single thin plasma shell early in the process. These deviations of the wire-array z-pinch process from the thin-shell model above will be discussed more in Chapters 4 and 5. For now, though, we can continue to use this simple model to derive some useful relationships describing the energetics of a z-pinch implosion.

Following Ryutov *et al.* [12], we begin by multiplying Eqn. 3.36 by $\dot{r_s}$ and rearranging to get:

$$\hat{m}\ddot{r_s}\dot{r_s} = -\frac{\mu_0}{4\pi}\cdot I^2\cdot\frac{\dot{r_s}}{r_s} \tag{3.37}$$

$$\frac{d}{dt}(\frac{1}{2}\hat{m}\dot{r_s}^2) = -\frac{\mu_0}{4\pi}\cdot I^2\cdot\frac{d}{dt}(\ln(r_s)) \tag{3.38}$$

$$\frac{d}{dt}(W_{kin}) = -\frac{\mu_0}{4\pi}\cdot I^2\cdot\frac{d}{dt}(\ln(r_s)), \tag{3.39}$$

where W_{kin} is the kinetic energy of the shell. Integrating this expression (by parts on the right-hand side) from $t = 0$ ($r_s = r_{s0}$) to $t = t^*$ ($r_s = r_s^*$), we obtain

$$\int_0^{t^*}\frac{d}{dt}(W_{kin})dt = -\int_0^{t^*}\frac{\mu_0}{4\pi}\cdot I^2\cdot\frac{d}{dt}(\ln(r_s))dt \tag{3.40}$$

$$W^*_{kin} = -\frac{\mu_0}{4\pi}\left[\ln(r_s)I^2\Big|_0^{t^*} - \int_0^{t^*}\frac{dI^2}{dt}\ln(r_s)dt\right] \tag{3.41}$$

$$= -\frac{\mu_0}{4\pi}\left[\ln(r^*_s)I^2(t^*) - \cancelto{0}{\ln(r_s(0))I^2(0)} - \int_0^{t^*}\frac{dI^2}{dt}\ln(r_s)dt\right] \tag{3.42}$$

$$= -\frac{\mu_0}{4\pi}\left[\ln(r^*_s)\int_0^{t^*}\frac{dI^2}{dt}dt - \int_0^{t^*}\frac{dI^2}{dt}\ln(r_s)dt\right] \tag{3.43}$$

$$= \frac{\mu_0}{4\pi}\int_0^{t^*}\frac{dI^2}{dt}\left[\ln(r_s) - \ln(r^*_s)\right]dt \tag{3.44}$$

$$W^*_{kin} = \frac{\mu_0}{4\pi}\int_0^{t^*}\frac{dI^2}{dt}\left[\ln\left(\frac{r_s}{r^*_s}\right)\right]dt = \frac{1}{2}\hat{m}\dot{r}^2(t^*). \tag{3.45}$$

Now for a fixed current-pulse waveform $I(t)$, initial array radius r_{s0}, and final stagnated radius r^*_s, the mass per unit length alone determines the final implosion velocity just before stagnation. Thus we can seek the mass that maximizes energy transfer to the imploding shell by optimizing Eqn. 3.45 with respect to the mass while fixing $I(t)$ and r^*_s. This is done by taking the partial derivative of Eqn. 3.45 with respect to the mass and setting the resulting expression equal to zero:

$$\frac{\partial W^*_{kin}}{\partial\hat{m}} = \frac{\mu_0}{4\pi}\int_0^{t^*}\frac{dI^2}{dt}\frac{1}{r_s}\frac{\partial r_s}{\partial\hat{m}}dt = 0. \tag{3.46}$$

The differential $\partial r_s/\partial\hat{m}$ is positive definite (i.e., a more massive shell implodes slower and thus has a larger radius at a given time than a less massive shell). Therefore if t^* corresponds to the time of peak current or earlier, dI^2/dt will have only been positive (or zero), thus making the integrand positive over the entire integration, and resulting in a positive value for $\partial W^*_{kin}/\partial\hat{m}$. The expression can be zero only if t^* corresponds to some time after peak current, where negative dI^2/dt makes the integrand negative, thus gradually returning the integrated value $\partial W^*_{kin}/\partial\hat{m}$ back to zero. It turns out that for a current pulse of the form $I(t) = I_{peak}\sin^2(\pi t/2\tau_{peak})$, where $0 < t < 2\tau_{peak}$, the kinetic energy at stagnation is maximized when $\hat{m} = \mu_0 I^2_{peak}\tau_{peak}/16\pi r^2_{s0}$ [12]. This mass results in a stagnation time when the current has fallen to a level that is about 90% of its peak value.

This is an important figure of merit to keep in mind, as a sine-squared current pulse is a reasonable approximation for current generators such as COBRA and Z. We will revisit these ideas in Chapter 5.

3.4 Pease-Braginskiĭ Current

In the previous section we looked at the dynamics of kinetic energy transfer into an imploding cylindrical shell. In Sec. 3.2 we considered what the equilibrium of this imploding shell might look like once the shell has stagnated and thermalized on axis. However, one thing we have not considered yet is the fact that z-pinches are known to radiate intensely once they have stagnated on axis. Radiation is of course energy leaving the system, thus cooling the pinch column. If this energy loss is not replenished by the driving current, yet the current continues to flow, then the result is a drop in thermal pressure that allows for further radial contraction of the pinch column, a process called radiative collapse. (Note: Should radiative collapse occur, it will eventually stop due to the increasing plasma opacity and ohmic heating that result from the increasing particle and current densities of the radial contraction.) It is possible, however, that a Bennett-like equilibrium is established where the various energy input and output mechanisms are in balance. For an imploding thin shell that has stagnated and thermalized on axis, there are two possible energy input mechanisms: ohmic heating and magnetic compressional heating (i.e., "pdV work"). Likewise, there are multiple energy output (or radiative) mechanisms: bremsstrahlung, cyclotron, recombination, and line radiation.

Considering only ohmic heating and free-free radiation processes, R. S. Pease

in 1957 [53] and S. I. Braginskiĭ in 1958 [54] were able to derive an equilibrium current known as the Pease-Braginskiĭ current, I_{PB}. (Note: Since we are discussing an equilibrium condition, pdV work does not apply as it requires compressional motion of the plasma. Hence, only anomalous sources of resistivity and non-free-free sources of radiation were neglected.) A concise (one page) derivation of I_{PB} for ohmic and bremsstrahlung processes is found in N. R. Pereira's 1990 paper [58]. Here it is recognized that both ohmic heating and bremsstrahlung radiation are collisional processes, and thus I_{PB} can be expressed as a ratio of the relevant collisional cross sections. The result is:

$$I_{PB} = \left(\frac{8\ln\Lambda}{\alpha F_b}\right)^{1/2} 2\left(1+\frac{1}{\bar{Z}}\right) I_A, \tag{3.47}$$

where $\ln\Lambda$ is the Coulomb logarithm, α is the fine structure constant, F_b is a calculated factor equal to $(2\pi/27)^{1/2}$, and I_A is "nature's current scale, the Alfvén(-Lawson) current" (I_A being ec/r_e, where r_e is the classical electron radius). Equation 3.47 essentially states that the Pease-Braginskiĭ current is the natural current scale I_A times the square-root of the ratio of the ohmic-heating collisional cross section (i.e., $\sigma_\Omega \propto 8\ln\Lambda$) to the bremsstrahlung collisional cross section (i.e., $\sigma_b \propto \alpha_b F_b$)—times a correction for the ionization state. Clearly then, the bigger the bremsstrahlung cross section, the smaller the current and magnetic field need to be to confine the plasma (i.e., radiative collapse will assist the $\mathbf{J}\times\mathbf{B}$ force density). Conversely, the larger the ohmic-heating cross section, the more the plasma will heat up, increasing thermal pressure, thus requiring a larger current (i.e., a larger $\mathbf{J}\times\mathbf{B}$ force density) to maintain equilibrium and confine the plasma.

Pereira comments on the curious quantum-mechanical quantity α that appears in this classically derived I_{PB} of Eqn. 3.47. It turns out that in the bremsstrahlung calculation, where the radiation power due to Coulomb colli-

sions is integrated over all impact parameters, α comes from the lower limit imposed on the impact parameter. This lower limit keeps the integral finite, and was apparently an early triumph of quantum theory. Pereira also points out that the Coulomb logarithm, $\ln \Lambda$, is the result of the upper limit imposed in the integration (the result of a Debye shielding argument). Interestingly, these two limit factors end up in the final ratio of cross sections.

Equation 3.47 also states that I_{PB} is a constant for all materials with an average ionization $\bar{Z}$. However, it is important to note that for partially-ionized high-atomic-number plasmas, such as those often used/produced in wire-array z-pinch experiments (e.g. tungsten plasmas), the actual equilibrium current can differ significantly from that stated in Eqn. 3.47. For example, line and recombination radiation have been neglected in the derivation of Eqn. 3.47, while high-atomic-number plasmas have a plethora of atomic states available for line transitions and recombination. Hence in reality, the total cooling rate due to line, recombination, bremsstrahlung, and cyclotron radiation is considerably higher than that due to bremsstrahlung alone, and this lowers the equilibrium current. On the other hand, anomalous sources of resistivity (e.g., microturbulent structure) can lead to enhanced ohmic heating, and therefore increase the equilibrium current.

Discrepancies between experiment and theory can occur due to still more mechanisms not considered above. This is especially true for fast z-pinch experiments, where many processes in the rapidly evolving plasma might not establish an equilibrium state during an experiment. For example, the equilibrium current can be effectively lower if the plasma is not in ionization equilibrium, and the energy being deposited in the plasma by the current pulse is being used

for ionization rather than heating. Conversely, if the plasma is not yet in an equilibrium with regards to radiation transport and opacity, then the radiation being produced may actually be re-absorbed by the plasma, thus decreasing the cooling rate and increasing the effective equilibrium current.

In z-pinch experiments, discrepancies are apparent even for materials with atomic numbers in the range of 10–20, where I_{PB} is found to be much too low for the average conditions within stagnated pinch columns, and that only "micro-pinches" satisfy the Pease-Braginskiĭ condition due to their high densities [25] (we will discuss micro-pinches more in Chapter 5). It is possible to apply corrections to Eqn. 3.47 such that some additional mechanisms are accounted for. However, especially for high-atomic-number materials, these corrections almost certainly must be found numerically.

CHAPTER 4

THE WIRE-ARRAY Z-PINCH

4.1 The Four Phases of a Wire-Array Z-Pinch

As mentioned in Sec. 3.3, there are some significant differences between the idealizations of the thin-shell model and the realities of a wire-array z-pinch. Following Ref. [3], the essence of the overall wire-array z-pinch process can be broken down into four phases: (1) the current-initiation/resistive phase, (2) the ablation phase, (3) the implosion/run-in phase, and (4) the stagnation/radiation phase. These four phases are represented in Fig. 4.1.

4.1.1 Current Initiation & Resistive Phase

The current initiation phase is a short resistive heating period that takes place early in the current pulse. For example, in the experiments that we will be presenting in Chapter 5, the wire diameters used resulted in this period lasting from the start of the current pulse to approximately 5–20 ns into the current pulse.

During this phase, the ohmic-heating energy deposited into the wires causes them to melt and partially vaporize [62, 63]. This takes place until the driving voltage reaches a level sufficient to cause a breakdown from the anode to the cathode along the surface of the wires [62]. Once this occurs, each wire consists of a colder dense core, surrounded by a hotter, low-density coronal plasma [33, 45, 63]. The coronal plasma shunts current away from the dense cores, as the

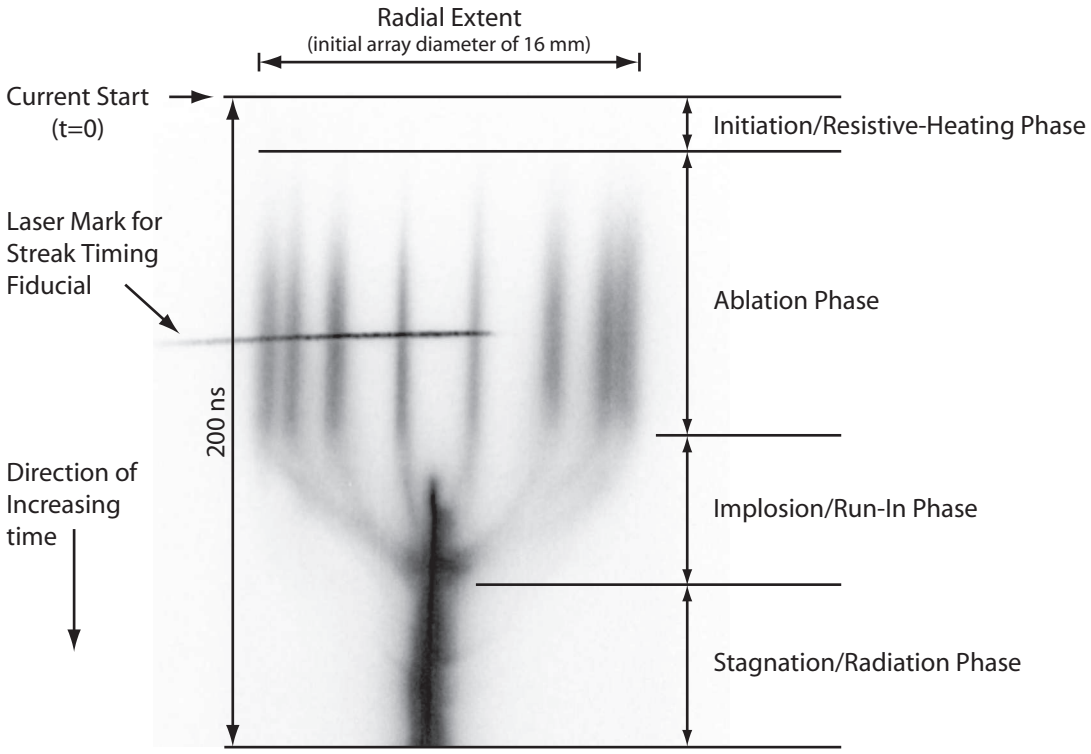

Figure 4.1: Transverse dimension of an imploding array imaged as a continuous function of time by the visible-light streak camera. The image was produced by self emission. The vertical axis is time, and the horizontal axis is radial extent. This image is particularly useful for illustrating the four phases of a wire-array z-pinch implosion.

resistance through the coronal plasma is negligible relative to that of the cores [62]. The resistance through the coronal plasma is also negligible relative to the wire as a whole prior to the breakdown [62], hence the breakdown transition is observed as a resistive voltage collapse by our load voltage monitor. This monitor measures $V_{load} = L\dot{I} + \dot{L}I + IR$. Since the wires remain stationary during this phase [63], we can make a reasonable assumption that $\dot{L} \rightarrow 0$ and $L \rightarrow L_0$, where L_0 is the initial load inductance. Thus if we plot $V_{load} - L_0\dot{I}$, we get the approximate resistive IR voltage. This is shown in Fig. 4.2, where one can note the resistive voltage collapse taking place near 15 ns. This is the moment that

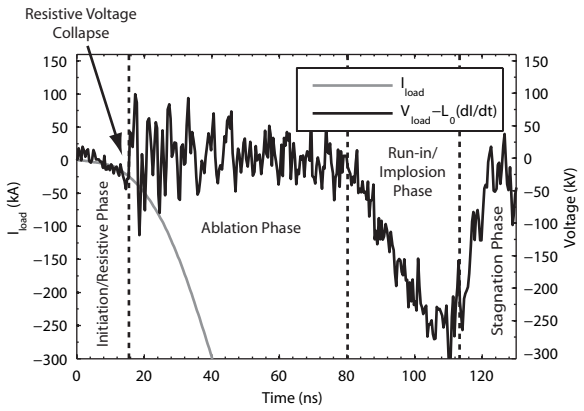

Figure 4.2: Representative data plot of $V_{load} - L_0\dot{I}$ to show the various phases of the wire-array z-pinch process. Of particular importance here is the resistive voltage collapse taking place approximately 15 ns into the current pulse, which marks the transition from the initiation phase to the ablation phase.

coronal plasma forms around the cores [62].

4.1.2 Ablation Phase

The ablation phase begins just after the resistive voltage collapse (see Fig. 4.2). During the ablation phase, mass is continually ablated from the dense wire cores, and becomes part of the lower-density coronal plasma [33]. As the coronal plasma is carrying most of the current, the wire cores are left force-free and stationary throughout the ablation phase [46] (also see Fig. 4.1). The coronal plasma is injected into the interior of the array by the $\mathbf{J} \times \mathbf{B}$ force. The injected plasma moves toward the array axis in discrete streams [33, 47], such as those shown in the laser shadowgraph image of Fig. 4.3. The streams eventually reach the array axis and are responsible for a steady accumulation of on-axis mass, commonly called the precursor column [64], which can also be seen in Fig. 4.3.

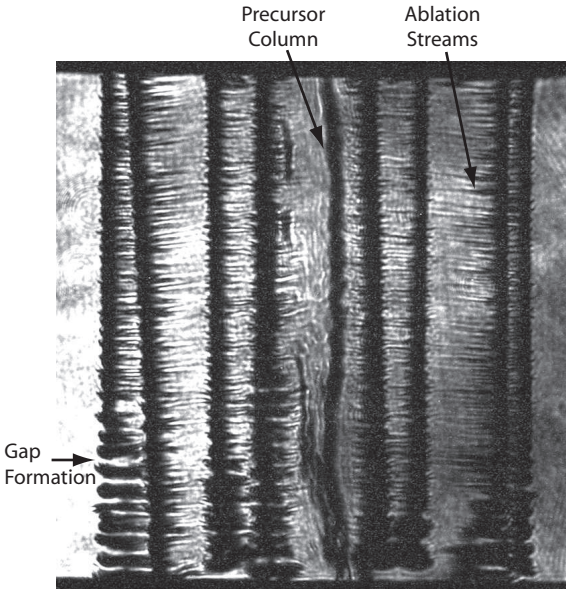

Figure 4.3: Laser shadowgraph image taken during the ablation phase illustrating the presence of ablation streams, a precursor plasma column, and the early formation of gaps near the bottom/cathode end of the array.

Recent work at Cornell shows that there is some magnetic field and current convected to the axis with the ablation streams, but most of the current remains in the coronal plasma at the initial wire-array radius [65].

4.1.3 Implosion Phase

The ablation phase is found to transition to the implosion phase when gaps form in the wire-cores [33]. These gaps are evident in Fig. 4.3 near the bottom of the array (i.e., near the cathode). Gap formation can either be due to the complete ablation of the wire core or to current penetrating the wire core sufficiently to accelerate what remains of the core toward the array axis. Either way, a large portion of the current and magnetic field now start to penetrate the interior of

the array and move toward the array axis [33].

During the implosion phase, a current-carrying plasma sheath forms a magnetic piston that sweeps up the previously injected coronal plasma in a snowplow-like fashion as it moves toward the array axis [33]. As this magnetic piston pushes on the plasma, small perturbations grow into larger magnetic bubbles due to the Rayleigh-Taylor instability. This nonuniformity results in a significant amount of trailing mass being distributed between the leading edge of the bubbles and the initial radius of the array [33, 3, 47]. We will present more evidence for these statements in Chapter 5.

4.1.4 Stagnation & Radiation Phase

The implosion phase transitions to the stagnation/radiation phase as the magnetic piston (i.e., the leading edge of the magnetic bubbles) reaches the array axis. The imploding plasma stagnating on axis is thermalized and perhaps compressed resulting in a burst of x-rays [33, 3, 46]. The duration and power of the x-ray burst can be significantly affected by the distribution of trailing mass imploding late relative to the leading edge of the bubbles, and/or not imploding at all. The experiments presented in Chapter 5 focus on the characteristics and timings of the implosion phase and the resulting x-ray bursts of the stagnation phase, as well as how these qualities change with various cylindrical wire-array loads on COBRA.

CHAPTER 5

IMPLOSION DYNAMICS AND RADIATION CHARACTERISTICS ON COBRA

Much of the early work on COBRA focused on diagnostic development and studies of the wire-array ablation process [43, 35, 44, 34, 45]. By contrast, the purpose of the experiments reported in this chapter was to characterize implosion dynamics and radiation production on COBRA, to identify similarities and differences relative to MAGPIE, Zebra, and Z, and to identify and study phenomena that can be seen as a result of the high-quality diagnostic suite and short (100-ns) current rise of COBRA. For this study, over 35 shots were taken to produce new data for 20 different load configurations. Analysis of this data set has revealed that the highest x-ray powers and total yields were obtained using 4-mm-diameter arrays that stagnated before peak current. Additional findings include a decrease in soft x-ray radiation prior to stagnation as the initial wire spacing is changed from 1.6 mm to 785 μm, and a timing correlation between the onset of energetic electrons, hard x-ray generation, and the arrival of trailing current on axis—a correlation that is likely due to the formation of micro-pinches. The details of these and other findings will be presented and discussed throughout the remainder of this chapter, which is organized as follows. In Sec. 5.1, we discuss the experimental setup, describing the diagnostics and the different wire-array configurations tested. In Sec. 5.2 we present our experimental results. We begin with representative tungsten (W) experiments in Sec. 5.2.1, where we first present detailed implosion and stagnation data from an experiment with 16-wires on an 8-mm array diameter to form a basis for comparison. We use this basis data to emphasize the presence and timing of significant features of the wire-array implosion process on COBRA before mov-

ing on to other W loads with closer wire spacings. Following the W results, we show similar data for aluminum (Al) and Invar (64% iron, 36% nickel) in Sections 5.2.2 and 5.2.3, respectively. In Sec. 5.2.4, we consider the electrical power into wire-array z-pinch loads relative to the total radiated power out. In Sec. 5.2.5, the results of parameter-tuned modeling of implosion trajectories are presented. Next, in Sec. 5.2.6, various imaging data are shown, revealing the presence of hot spots for all materials tested in our higher-yield implosions. Finally, in Sec. 5.2.7, we present data from experiments with very low wire numbers (8 wires) and large wire spacings (8 wires on a 16-mm array diameter for a 6.3-mm wire spacing), and consider questions regarding the relevance of low wire number experiments on COBRA ($\leq$32 wires) to high wire number experiments on Z (>100 wires).

5.1 Experimental Setup

5.1.1 Diagnostics

To measure total radiated energy as a function of time, where this energy range extends from the visible up through to $\gtrsim$5 keV, COBRA's calibrated nickel-element bolometer was used without filters. The bolometer was complemented by several calibrated and filtered PCDs put in place to measure the instantaneous x-ray power emitted at or above various photon energies. To measure >1-keV photons, 25-μm Beryllium (Be) and 12.5-μm titanium (Ti) filters were used, while 2 and 6-μm Mylar filters were used to measure sub-keV photons (along with the >1-keV photons). For detecting >5 keV radiation, multiple un-

calibrated silicon diodes (SiDs) were used with thick filters, such as 60-μm Al.

Two post-processing methods were employed to derive the absolute x-ray power. The first method simply takes the derivative of the smoothed and calibrated energy waveform produced by the bolometer assuming that virtually all of the energy is <5 keV. The second method begins with the assumption that the power waveform from the PCD with the lowest-energy filter (i.e., the 2-μm Mylar filter for >100 eV radiation) is representative of the absolute x-ray power waveform (i.e., same relative shape, but attenuated by some factor). To find the attenuation factor, we integrate the PCD waveform, giving the filtered x-ray energy as a function of time. We compare this energy waveform to the unfiltered energy waveform detected by the bolometer to find the approximate attenuation factor due to the filter. We then divide the original PCD waveform by the attenuation factor to get a waveform for the absolute x-ray power. Reasonable agreement between these two post-processing methods was achieved, thus increasing confidence in the results (see Fig. 5.1). However, errors can still be large due to noise on the bolometer signal and assumptions about the spectral content of the radiation. Thus, the values reported here are only to provide a rough estimate. It should also be noted that all powers and energies derived from these measurements were calculated assuming that the bolometer and PCDs have flat spectral responses and that the radiation source is an isotropic point source. If one considers an optically thick surface emitter with cylindrical symmetry instead, then the numbers reported here should simply be multiplied by $\pi/4$ [66].

A pinhole camera was used with no filter and a single, 50-μm pinhole to produce high-resolution time-integrated images. Two layers of film were used with this camera. The first layer was INDUSTREX DR50 (sensitive to and filtering

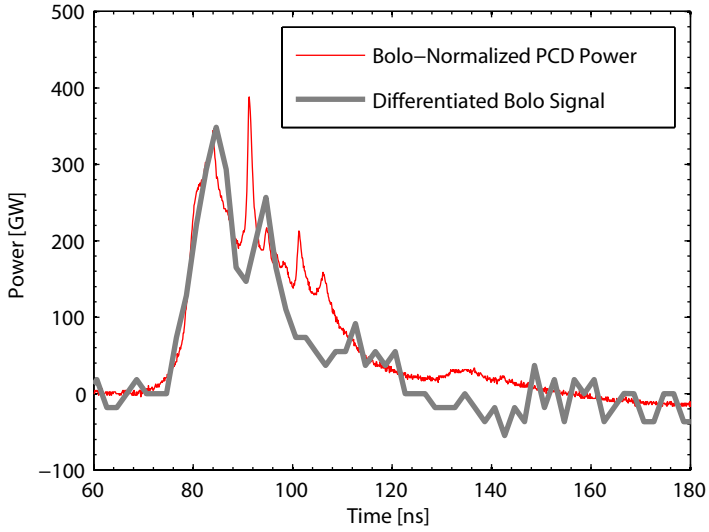

Figure 5.1: (Color) Total x-ray power derived by the two methods described in the text showing reasonable agreement.

out the <5-keV radiation) while the second layer consisted of Kodak BioMax MS, which was exposed by the remaining >5-keV radiation. Another camera was used with multiple larger ($\gtrsim$200-μm) pinholes. Each of these pinholes were filtered with various thicknesses of either aluminum or beryllium to produce time-integrated self-emission images of the pinch column in various energy ranges. Three layers of sensitive Kodak BioMax MS film were used with this camera.

The COBRA laser shadowgraph system was used to produce images such as the one shown in Fig. 4.3. The laser system was complemented by the time-gated MCP/XUV camera. As unfiltered 50-μm pinholes were used with the MCP camera, the diffraction limit resulted in images produced by >20-eV self emission.

To record implosion trajectories as a continuous function of time, the visible-light streak camera was used, producing images such as the one shown in

Fig. 4.1. For all of the experiments presented in this chapter, the streak window was 200-ns in duration and the entrance slit was opened to 100 μm. Due to the streak camera's internal magnification, this resulted in a time resolution of about 3 ns. Also, as the streak camera's photocathode is 17 mm wide, and as the camera's internal optics relaying images at the entrance slit to images at the photocathode have a magnification of 1:1, the usable dimensions for the entrance slit were 100 μm $\times$ 17 mm. Now, the optical system that was used to relay light from the wire-array source to the streak camera entrance slit had a magnification of 1.7:1. Therefore the image of the streak camera entrance slit at the array had dimensions of 170 μm $\times$ 29 mm. The optical relay system was also aligned such that the 29-mm extent of the slit image was oriented across the wires and transverse to the array axis, and so that the 170-μm extent of the slit image straddled the midpoint of the array's axial extent. Since the largest-diameter array used for these experiments was 16 mm, the 29-mm extent of the slit image sufficiently covered all array diameters. With the streak camera and relay optics set up in this way, we were able to recorded the radial extent of the visible-light self-emission from the midpoint of the array's axial extent over the course of the implosion (integrating over 170 μm in the axial direction). Also, since the 170-μm dimension is in the same direction as the time dimension on the resulting streak images, we consider 170-μm to be the axial resolution. We tested the imaging limitations of our relay optics in conjunction with our streak camera system by backlighting objects at the location of the wire-array loads with a white-light tungsten lamp source, and observing the resulting images produced by the streak camera system in focus/live mode (see Sec. 2.2.9 for a description of focus/live mode). We were able to image backlit objects down to just under 100-μm, and thus our radial resolution along the 29-mm dimension

was about 100 μm. The optical relay system and streak camera operation are discussed further in Chapter 6.

For time-integrated spectral imaging of the stagnated pinch column, the WB-FSSR was used. This spectrograph was complemented by the x-ray streak camera, which was used to image the axial extent of the pinch column as a continuous function of time (i.e., here we are *not* imaging the radial extent of the array as was the case with the visible-light streak camera just discussed in the paragraph above).

All of the above devices were positioned for side-on viewing. The axial position above the imploding wire-array was occupied by the Faraday cup, which was typically used with a 50-μm stainless-steel filter to monitor electron beam energies >130 keV, or with a 30-μm Al filter to monitor electron beam energies >60 keV.

Finally, the inductive load voltage monitor was also used. The signals from this monitor can be post-processed to determine two things: (1) the energy deposited in the wires during the resistive heating phase early in the current pulse (i.e., $\lesssim$5–20 ns into the current pulse), and (2) the change in inductance due to the collapsing geometry as the plasma accelerates inward during the implosion phase. From (2), we can estimate the centroid of a one-dimensional radial current distribution as a function of time. We shall refer to the position of this centroid as the position of the effective current sheath throughout the remainder of this study. This is similar to the voltage data processing scheme discussed in Ref. [3], and will be discussed more as the data is presented.

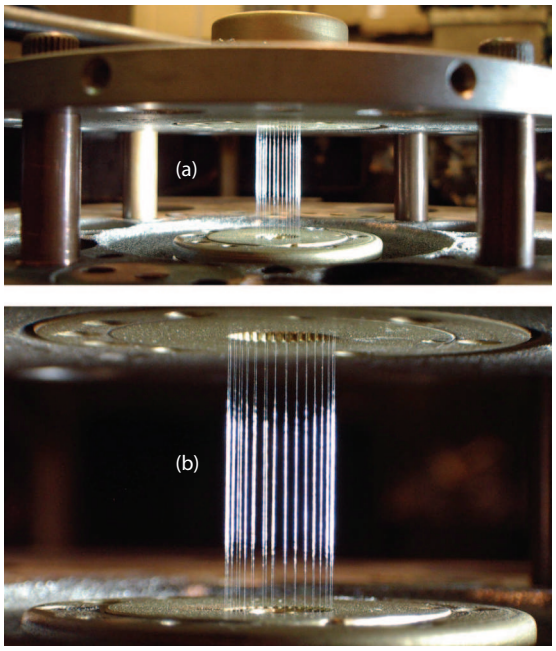

Figure 5.2: (Color) 32-wire W array on an 8-mm array diameter giving 785-μm wire spacing (wire diameters are 5 μm; array height is 20 mm). The anode plate (above the array) and four return current posts (surrounding the array) are shown in (a).

5.1.2 Wire-array loads

The advent of CNC-fabricated electrode inserts has enabled rapid hardware refurbishment, and wire spacings down to 785 μm for the first time on COBRA. Figure 5.2 shows photographs of a 32-wire array on an 8-mm diameter, giving 785-μm wire spacing. The four return current posts are equally spaced around the circumference of the anode plate, and are 45 mm from the array axis. This return-current arrangement allowed the diagnostics to have an unobstructed view of the entire array, and was the general setup used for all shots.

The load geometries investigated include 10- and 20-mm tall cylindrical arrays ranging from 4 to 16 mm in diameter, and consisting of 8, 16, or 32 wires

of either W, Al, or Invar. For one shot series, the stagnation time was held constant (about 120 ns into the current pulse) and the effects of varying wire material, wire number, wire diameter, array diameter, and wire spacing were investigated. In another shot series, the stagnation time was varied in addition to the other parameters listed above. To scale the wire-array loads to the appropriate stagnation time, the 0D model of Ref. [12] was used. The 0D model is simply the thin-shell model of Sec. 3.3 recast into dimensionless form. This is done to extract a useful scaling parameter. To non-dimensionalize the thin-shell model, we begin by making the following dimensionless assignments: $\tilde{r} \equiv r/r_0$, where r_0 is the initial array radius (and where we have dropped the subscript s for convenience), $\tilde{I} \equiv I/I_{peak}$, where I_{peak} is the peak amplitude of the current driver, and $\tilde{t} \equiv t/\tau_{peak}$, where τ_{peak} is the time to peak current (i.e., the zero-to-peak rise time of the current driver). Plugging these assignments into Eqn. 3.36 and rearranging, we obtain

$$\tilde{r}\tilde{r}'' = -\Pi\tilde{I}^2, \tag{5.1}$$

where the primes signify differentiation with respect to the dimensionless time $\tilde{t}$, and where

$$\Pi = \frac{\mu_0 I_{peak}^2 \tau_{peak}^2}{4\pi\hat{m}r_0^2} \tag{5.2}$$

is the desired dimensionless scaling parameter.

Despite the fact that the thin-shell model does not account for the ablation process known to occur in wire-array z-pinches, it does predict the time to stagnation reasonably well (to within about 90% accuracy). Also, the dimensionless scaling approach is useful to researchers discussing various loads on different machines. For example, a load with $\Pi \approx 8$ hints that stagnation should occur near peak current for a sine-squared pulse shape, regardless of a particular machine's peak current and rise-time, or a particular load's wire number, wire material,

wire diameter, or array diameter—all of which affect stagnation time. Note also that as Π increases, stagnation time moves earlier, and vice-versa.

As discussed in Sec. 3.3, the thin-shell model has been used to make a theoretical prediction that kinetic energy is maximized when stagnation occurs just after peak current [12]. The optimized mass per unit length found corresponds to $\Pi \approx 4$ (for a sine-squared pulse—which we will assume from here on). Thus, if one assumes that the thermalization of this kinetic energy is responsible for the x-rays radiated, then the maximum total x-ray energy yield should occur for loads scaled to $\Pi \approx 4$. For this reason, we ran a series of shots with $\Pi \approx 5$, while varying wire material, wire number, wire diameter, array diameter, and wire spacing, and then another series where we allowed Π to vary over the range 2–40. We will see from these results that loads scaled to $\Pi \approx 4$–5 do *not* yield the highest total x-ray energy on COBRA. Table 5.1 shows the various loads that were tested for the experiments reported in this study. The values for Π in Table 5.1 were calculated using a 1-MA peak current and a 100-ns zero-to-peak rise time. (Note: The peak currents and rise times varied somewhat in the actual experiments. In some cases the peak current was nearly 1.2 MA, thus Π would increase by almost 40% relative to the values recorded in Table 5.1. In other cases the peak current was reduced by almost 20% due to the large impedances of a fast implosions, and thus Π would decrease by almost 40% relative to the values recorded in Table 5.1. Similarly, the rise times varied by about $\pm$10% from shot to shot, and therefore Π would vary by about $\pm$20% from shot to shot relative to the values recorded in Table 5.1. However, the shot-to-shot variations in peak current and rise time tend to be anti-correlated. Thus to some degree their effects on Π tend to cancel each other out. Regardless, in keeping with the utility of this dimensionless scaling approach, the values in Table 5.1 are cal-

Table 5.1: Wire-array configurations tested.

Material	Π	Wire #	Wire ϕ (μm)	Array ϕ (mm)	Wire spacing (mm)	Array height (mm)	# of shots
W	2.5	16	5.1	16.0	3.142	20	2
W	5.1	8	5.1	16.0	6.283	10	1
W	5.1	8	5.1	16.0	6.283	20	3
W	5.1	8	10.2	8.0	3.142	20	3
W	5.1	16	5.1	11.3	2.219	20	3
W	5.1	32	5.1	8.0	0.785	20	2
W	10.2	16	5.1	8.0	1.571	10	1
W	10.2	16	5.1	8.0	1.571	20	2
W	36.1	8	5.1	6.0	2.356	20	1
W	40.6	16	5.1	4.0	0.785	20	2
Al	4.5	16	10.2	16.0	3.142	20	1
Al	5.8	8	12.7	16.0	6.283	20	1
Al	5.8	32	12.7	8.0	0.785	20	1
Al	6.5	16	17.0	8.0	1.571	10	3
Al	6.5	16	17.0	8.0	1.571	20	4
Al	9.0	32	10.2	8.0	0.785	20	2
Al	14.3	16	10.2	9.0	1.767	10	1
Al	14.3	16	10.2	9.0	1.767	20	1
Al	48.2	16	12.5	4.0	0.785	20	2
Invar	47.8	8	10.2	4.0	1.571	20	1

culated using the constant and nominal values of a 1-MA peak current and a 100-ns zero-to-peak rise time.)

5.2 Experimental Results

For all of the loads that we will be discussing here, the array heights were 20 mm. We did some experiments with 10-mm heights, but found no significant changes in the dynamics of implosion or the timing characteristics of the radiation. We also found that the x-ray peak power and total energy yield scaled

roughly linearly with array height (i.e., by reducing the array height from 20 mm to 10 mm, we reduced the emitting source size by one half, and thus reduced the total radiation power and energy yield by nearly one half). There are most likely exceptions to this scaling as we did not seek the optimum array height for x-ray production on COBRA during this study.

The data collected from all experiments and load configurations is included in Appendix A.

5.2.1 Representative Tungsten Experiments

All of the W loads discussed in this chapter used 5-μm wire diameter. Some experiments in other test runs used 10-μm wire diameter. However, the smaller wire diameter seemed to leave behind less trailing mass, and seemed to lead to more powerful implosions when compared to the results of the thicker wire diameter. Since we were usually constrained to keeping our arrays light in order to drive implosions in 100 ns at 1 MA, the smaller wire diameter also allowed more flexibility and closer wire spacings. Therefore, during the discussion that follows, the variable of wire diameter is fixed.

16 $\times$ 5-μm W wires, 1.6-mm wire spacing, 8-mm array diameter, $\Pi \approx 10$

Our "baseline case" with which we will compare other tests is a 16-wire W array on an 8-mm array diameter, providing 1.6-mm wire spacing and $\Pi \approx 10$. From our bolometer and PCD measurements, the x-ray peak power and total energy yield for this load were about 200 GW and 5 kJ, respectively. Figure 5.3 shows

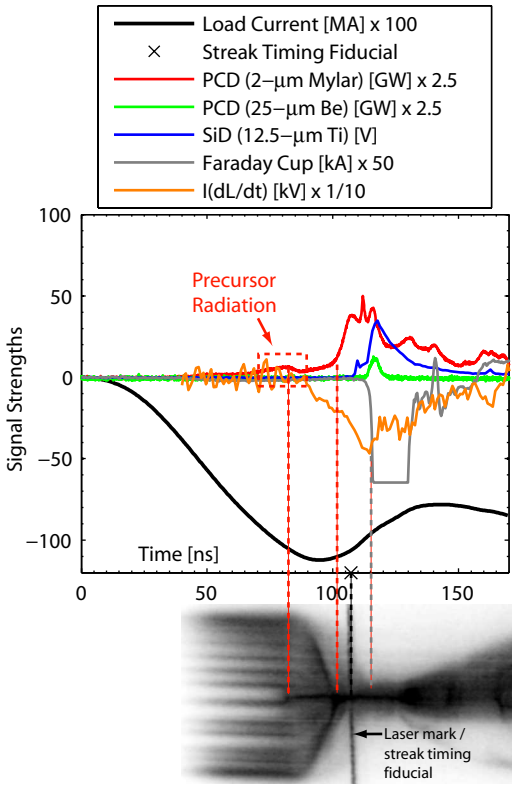

Figure 5.3: (Color) Visible streak camera image synchronized to various signals for a 16-wire W array on an 8-mm array diameter, with 1.6-mm wire spacing, 5-μm wire diameters, and $\Pi \approx 10$.

an optical streak camera image synchronized to a plot of electrical signals from various diagnostics. To obtain values for the signals in the units displayed in the plot legend, the multiplicative factors shown next to the respective trace names must be divided out.

From the streak image in Fig. 5.3, one can see that the visible-light self emission from the plasma near the wire cores remains stationary until about 85 ns into the current pulse, and that stagnation occurs at approximately 100 ns. We also see the onset of visible-light self emission from the precursor column on the axis of the array at about 82 ns. This onset of visible precursor light consistently corresponds to a short "pre-pulse" of sub-keV x-ray radiation detected by the

2-μm Mylar-filtered PCD (red). This correspondence agrees with observations made by Bott *et al.* [64].

Also in Fig. 5.3, we see that the Mylar-filtered PCD signal (red) rises rapidly at stagnation. (From here on we will refer to stagnation as the time when the most intense and well-defined implosion trajectory on the visible streak reaches the array axis.) Note that this rise precedes the rise of the Be-filtered PCD (green) and the Ti-filtered SiD (blue) by about 12 ns. Both the Be and Ti filters allow only >1-keV radiation to be detected, while, as previously noted, the Mylar filter includes sub-keV transmission windows.

Close inspection of the streak image in Fig. 5.3 reveals a barely visible trajectory trailing the most intense and well-defined trajectory. This secondary trajectory appears to be the implosion of trailing mass, with faint self-emission after the main implosion. (From here on we will refer to the most intense and well-defined implosion trajectory on the visible streak images as the *main* implosion trajectory, and the secondary, low-level emission implosion enveloped as the *trailing* implosion trajectory.) The trailing trajectory arrives on axis about 12 ns after the main trajectory, or in other words, at about the time when the >1-keV signals begin to rise rapidly.

The timing of the trailing trajectory's arrival on axis is also correlated with the gray trace in Fig. 5.3, representing the electron beam detected on axis above the array via the Faraday cup. Although the signal is clipped, the timing of the onset of electron beam detection is clear, and corresponds to that of the trailing trajectory's arrival on axis.

Next consider the orange trace in Fig. 5.3, representing $\dot{L}I$ voltage. This volt-

age provides a measure of the rate of increase of the load inductance due to the decreasing radius of the effective current sheath. That is, the global magnetic field surrounding the array must fill a larger volume as the radius of the effective current sheath collapses towards the axis, hence the load inductance increases. The $\dot{L}I$ values actually plotted were obtained from the load voltage measurement as follows. Assuming the resistive voltage to be negligible, the total load voltage measurement becomes $V_{load} \approx L\dot{I} + \dot{L}I \Rightarrow V_{load} - L\dot{I} \approx \dot{L}I$. This differential equation is solved numerically to evaluate $L(t)$ using time-dependent measurements of total load voltage and current. With $L(t)$ determined, we can then plot $V_{load} - L\dot{I} \approx \dot{L}I$, as in Fig. 5.3. Note the correspondence between the peak in the $\dot{L}I$ voltage and the arrival of the trailing trajectory on axis.

To summarize, the initial rise of the Mylar-filtered PCD signal corresponds to the arrival on axis of the main implosion trajectory, while the fast rise of the >1-keV signals, the onset of electron beam detection, and the peak in $\dot{L}I$ voltage, all correspond to the arrival on axis of the trailing trajectory. These timing correspondences are observed in essentially all of our W experiments, as we will see throughout this section.

32 × 5-μm W wires, 785-μm wire spacing, 8-mm array diameter, $\Pi \approx 5$

In order to test the applicability to COBRA of trends seen or predicted elsewhere that suggest higher x-ray powers and total yields may be obtained by using higher-wire-number arrays with more closely-spaced wires [67, 33], and loads with $\Pi \approx 4$ [12], we tested a 32-wire, 5-μm wire diameter, W array with an 8-mm diameter, providing 785-μm wire spacing and $\Pi \approx 5$. Results for this load are shown in Figs. 5.4 and 5.5.

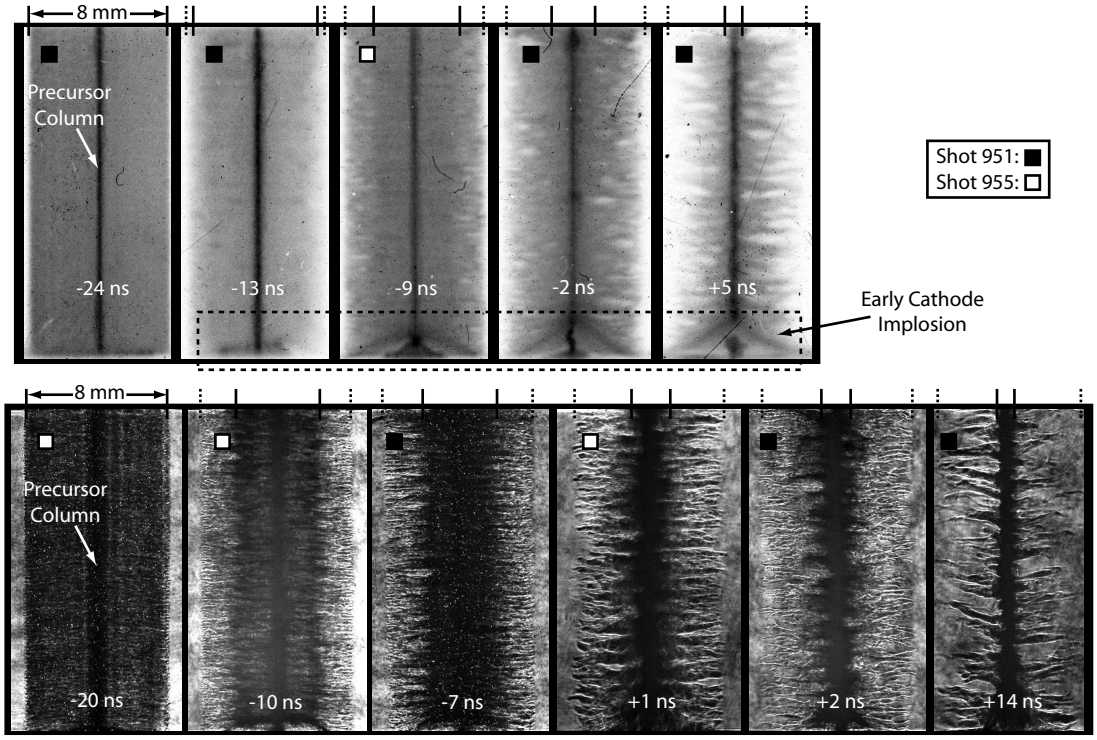

Figure 5.4: Time-gated XUV images (top row) and laser shadowgraph images (bottom row) of imploding 32-wire W arrays with 8-mm array diameters, 785-μm wire spacings, 5-μm wire diameters, and $\Pi \approx 5$. Frame times are relative to stagnation on the visible streak images.

From the XUV and laser shadowgraph images shown in Fig. 5.4, one can observe the shell-like magnetic piston moving radially inward in the two series of sequential frames. The time labels of these frames are relative to the stagnation time found in the corresponding streak image of Fig. 5.5. We can see from the XUV and laser images that plasma near the cathode-end of the array implodes before the rest, and that this early cathode implosion arrives on axis before the stagnation time found in the streak. This early cathode implosion affects the PCD signals shown in Fig. 5.5. Regardless of this distortion in the PCD signals, we can still see all of the timing correspondences that are related to the main and trailing implosion trajectories. In fact the trailing trajectory in the streak

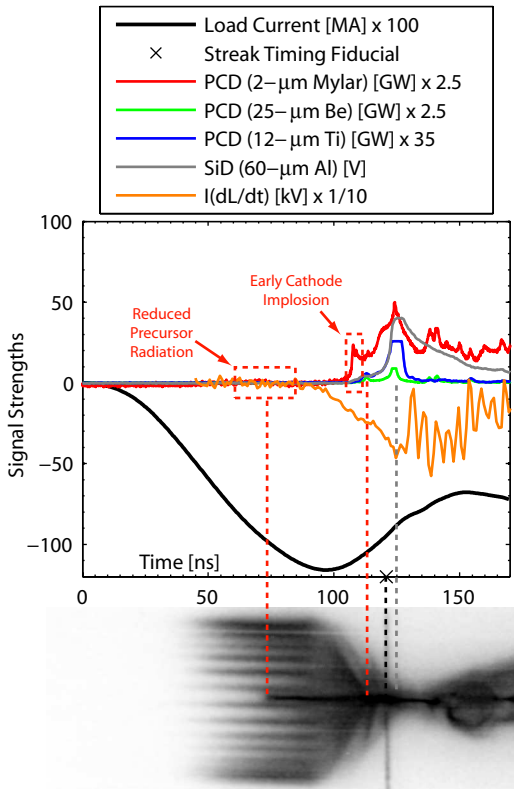

Figure 5.5: (Color) Visible streak camera image synchronized to various signals for a 32-wire W array on an 8-mm array diameter, with 785-μm wire spacing, 5-μm wire diameters, and $\Pi \approx 5$.

image of the present example is more apparent. Also, in comparing the peaks of the PCD signals of Fig. 5.5 with those of Fig. 5.3, we see that the amplitudes are very similar. Additionally, bolometer/PCD processing indicates that the absolute x-ray peak power and total energy yield were only slightly increased to about 250 GW and 6 kJ, respectively.

Relative to Fig. 5.3, the Mylar-filtered PCD signal in Fig. 5.5 shows a significant reduction in the sub-keV x-ray pre-pulse that corresponds in time to the first appearance of the precursor column on the streak (which occurs at about 72 ns). This could be due to less current transfer into the interior of the array (where less compression and heating of the precursor column could cause the

decrease in soft precursor radiation), or it could be a result of less sub-keV radiation escaping the array perimeter due to the optical depth of the more closely spaced wire cores and coronal plasmas. This characteristic of reduced precursor radiation in sub-keV x-rays as wire spacing decreases from ≥1.6 mm to ≤785 μm is consistent for all of the W (and Al) loads where 785-μm wire spacing was investigated.

16 × 5-μm W wires, 785-μm wire spacing, 4-mm array diameter, $\Pi \approx 40$

In order to test an array with a stagnation time before peak current while keeping the wire spacing at 785 μm, we tested 16, 5-μm wires on a 4-mm diameter. This increased Π to about 40, ensuring an implosion before peak current. The use of this load resulted in a substantial increase in both x-ray peak power and total yield. Bolometer and PCD measurements implied a peak x-ray power of about 400 GW and a total x-ray energy yield of about 10 kJ. For COBRA, this is an efficiency of about 10% for the conversion of stored electrical energy to radiated x-ray output energy. Figure 5.6 shows the high x-ray power detected through various filters. Note once again the decrease in sub-keV x-ray precursor radiation associated with the 785-μm wire spacing. Also, the aforementioned timing correspondences are present: the correspondence between the rapid rise of the sub-keV x-ray signals with the main implosion trajectory, and the correspondence between the rapid rise of the >1-keV x-ray signals with the trailing trajectory and the peak in the $\dot{L}I$ voltage.

A distinct feature of an implosion/stagnation before peak current is that the shape of the drive current waveform is severely affected, as can be seen in Fig. 5.6. This is because COBRA is a low impedance driver (≈0.45 Ω), requir-

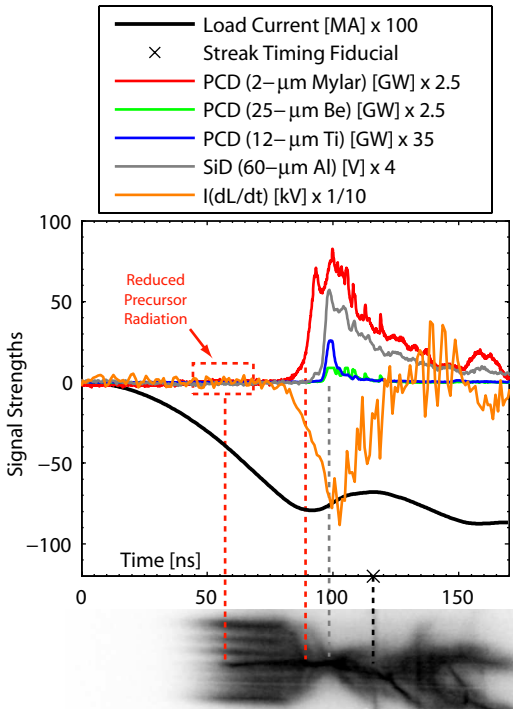

Figure 5.6: (Color) Visible streak camera image synchronized to various signals for a 16-wire W array on a 4-mm array diameter, with 785-μm wire spacing, 5-μm wire diameters, and $\Pi \approx 40$.

ing about 0.45 MV to drive 1 MA into a short circuit load. Thus, the increased impedance due to the rapidly rising load inductance as the array implodes can be significant relative to the small driver impedance, and acts to reduce the overall drive current. For example, the voltage driving the load is approximately equal to $\dot{L}I$ (the reason for this is discussed in Sec. 5.2.4). Now referring to Fig. 5.6, we see that this $\dot{L}I$ voltage rapidly increases to nearly 1 MV, while the current is limited to about 0.8 MA. Thus, roughly, we have 1 MV $\div$ 0.8 MA $\approx$ 0.45 Ω + $Z_{load} \rightarrow Z_{load} \approx 0.8\ \Omega$. Therefore, as stated, this $\approx$0.8-Ω load impedance is significant relative to COBRA's 0.45-Ω output impedance. Similar reductions in drive current have been observed on Z [68], while the effect is less noticeable on relatively higher-impedance drivers, such as Zebra at UNR [69].

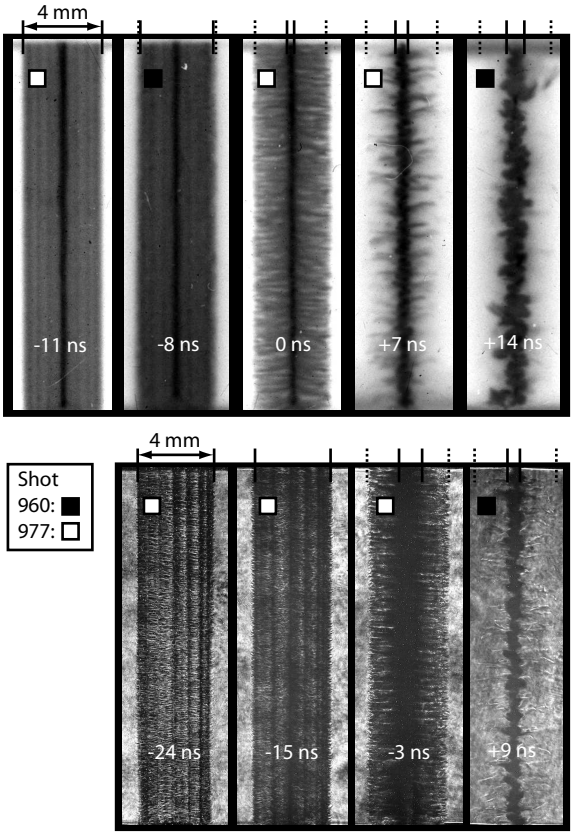

Figure 5.7: Time-gated XUV images (top row) and laser shadowgraph images (bottom row) of imploding 16-wire W arrays with 4-mm array diameters, 785-μm wire spacings, 5-μm wire diameters, and $\Pi \approx 40$. Frame times are relative to stagnation on the visible streak images.

In Fig. 5.7, we present XUV and laser shadowgraph images of this load as it imploded. The pinch column appears to remain stable and uniform well after the stagnation time found in the streak image. That is, the column appears to remain stable while trailing mass continues to implode. As can be seen in the last frames of each of these two sequences, the column does not appear to destabilize until nearly all of the trailing mass has imploded. This is perhaps related to the production higher-energy x-rays noted to occur when the trailing trajectory in a streak image arrives on the array axis.

The x-ray power and yield for this 16-wire, 4-mm-diameter array was greater than all other W loads tested.

5.2.2 Representative Aluminum Experiments

Figures 5.8, 5.9, and 5.10 display streak and signal data for three Al loads that are similar in mass, wire number, and array diameter to the three W loads presented in Section 5.2.1. For Al, we see the same trend in x-ray power and yield, namely the power and yield are the highest for a 16-wire array on a 4-mm diameter, where the stagnation time is prior to the time when the peak in drive current would have occurred had it not been for the increasing inductance of the imploding load. The peak x-ray powers for the loads shown in Figs. 5.8, 5.9, and 5.10 were about 200, 250, and 330 GW, respectively, while the total x-ray energy yields were about 4, 5, and 6 kJ, respectively. As was the case with the W arrays, the precursor radiation is reduced in the two loads with 785-μm wire spacing, relative to the load presented in Fig. 5.8 with 1.8-mm wire spacing.

There are some significant differences between the Al and W shots, however. First, for Al, the precursor radiation is less intense in visible wavelengths (from streak images) and in sub-keV x-rays (from Mylar-filtered signals). This is illustrated most clearly by comparing the larger 1.6/1.8-mm wire-spacing examples of W and Al in Figs. 5.3 and 5.8, respectively. Second, despite Al having larger Mylar-filtered PCD signals upon stagnation, the overall energy yields are considerably less than for W. In the most powerful Al case of the 16-wire array on a 4-mm diameter ($\Pi \approx 48$), the bolometer indicated approximately 6 kJ, as opposed to the nearly 10 kJ detected for the comparable W load of Sec. 5.2.1. Next, com-

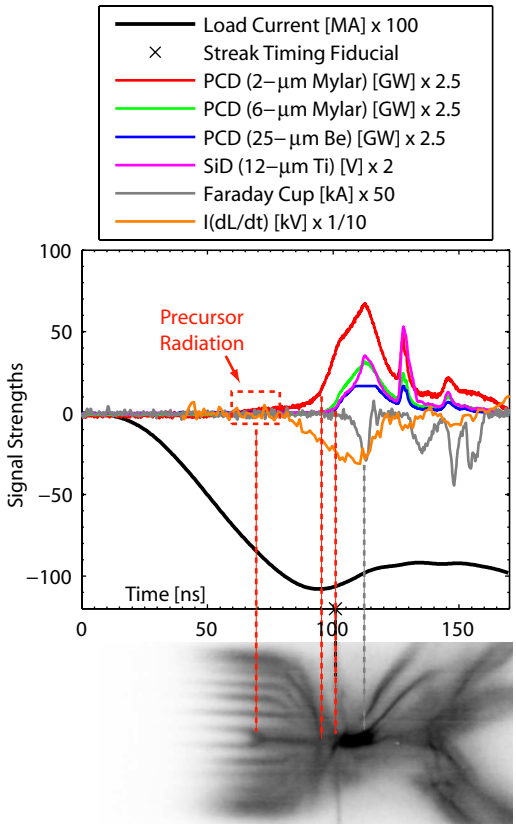

Figure 5.8: (Color) Visible streak camera image synchronized to various signals for a 16-wire Al array on a 9-mm array diameter, with 1.8-mm wire spacing, 10-μm wire diameters, and $\Pi \approx 14$.

paring the 25-μm Be-filtered PCD (>1 keV) with the Mylar-filtered PCDs (which include sub-keV and >1-keV transmission windows), we see similar x-ray pulse shapes and timing. This implies that a significant amount of the radiation upon stagnation for Al is >1 keV. Perhaps this is due to Al K-shell radiation ($\gtrsim$1.6 keV), as has been seen or discussed elsewhere [25, 37, 70, 33]. Also notice that the streak implosion trajectories are not as well defined for Al as they are for W, especially for the trailing trajectories. In fact, there are often several trailing trajectories apparent for Al, sometimes with later-starting trajectories catching up to earlier-starting trajectories in a convergence at stagnation (see Fig. 5.9).

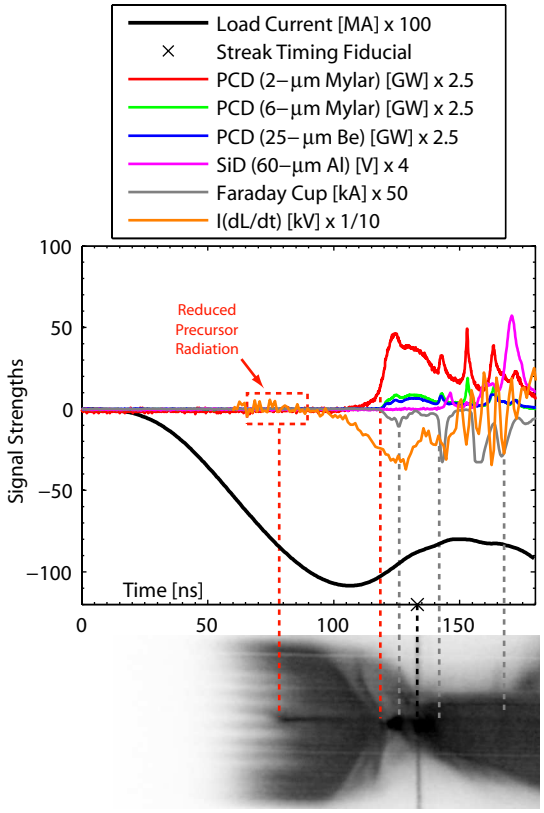

Figure 5.9: (Color) Visible streak camera image synchronized to various signals for a 32-wire Al array on an 8-mm array diameter, with 785-μm wire spacing, 10-μm wire diameters, and $\Pi \approx 9$.

Finally, we do see some late-time bursts of harder radiation in Al experiments, sometimes associated with trailing trajectories (see Fig. 5.9), but this radiation is substantially less intense than the late-time bursts of harder radiation produced by similar W experiments. Related to this is the fact that Faraday cup measurements show much more intense electron beam generation in W arrays.

Figure 5.11 shows time-gated XUV and laser shadowgraph images for one of the 32-wire Al configurations tested. In the XUV images, one can clearly see the imploding piston front, which consists of imploding bubbles of larger physical size than those seen in the W implosions (compare Figs. 5.4 and 5.11). The

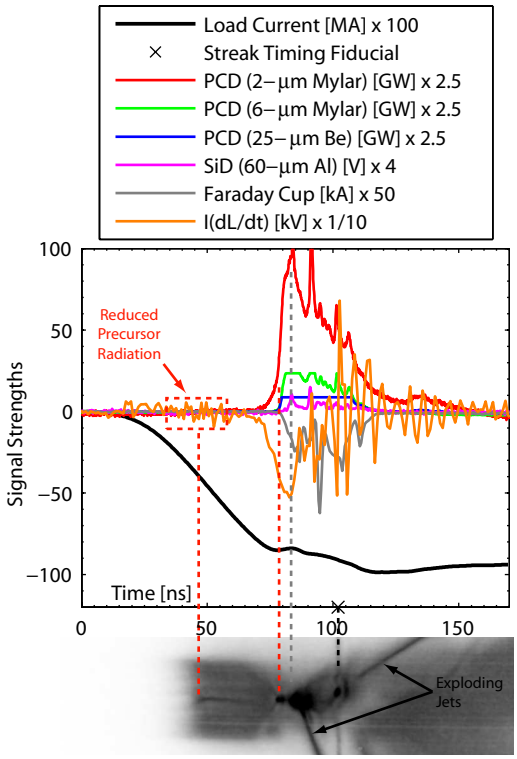

Figure 5.10: (Color) Visible streak camera image synchronized to various signals for a 16-wire Al array on a 4-mm array diameter, with 785-μm wire spacing, 12-μm wire diameters, and $\Pi \approx 48$.

larger-scale structure for Al is also seen in the laser shadowgraph images, and appears to be related to the larger fundamental wavelength for Al that occurs during the ablation phase. (The fundamental wavelength for Al is ~500 μm, while it is closer to 250 μm for W, as has been observed in Ref. [46], and later verified on COBRA as well.)

Summarizing the differences between the implosion/radiation characteristics of Al and W arrays, we have: (1) the overall x-ray energy yield is substantially less for Al (6 kJ versus 10 kJ for W); (2) upon stagnation, W produces a burst of sub-keV x-ray radiation while Al produces a burst of $\gtrsim$1-keV radiation (perhaps Al K-shell emission); (3) for W, shortly after the sub-keV x-ray burst

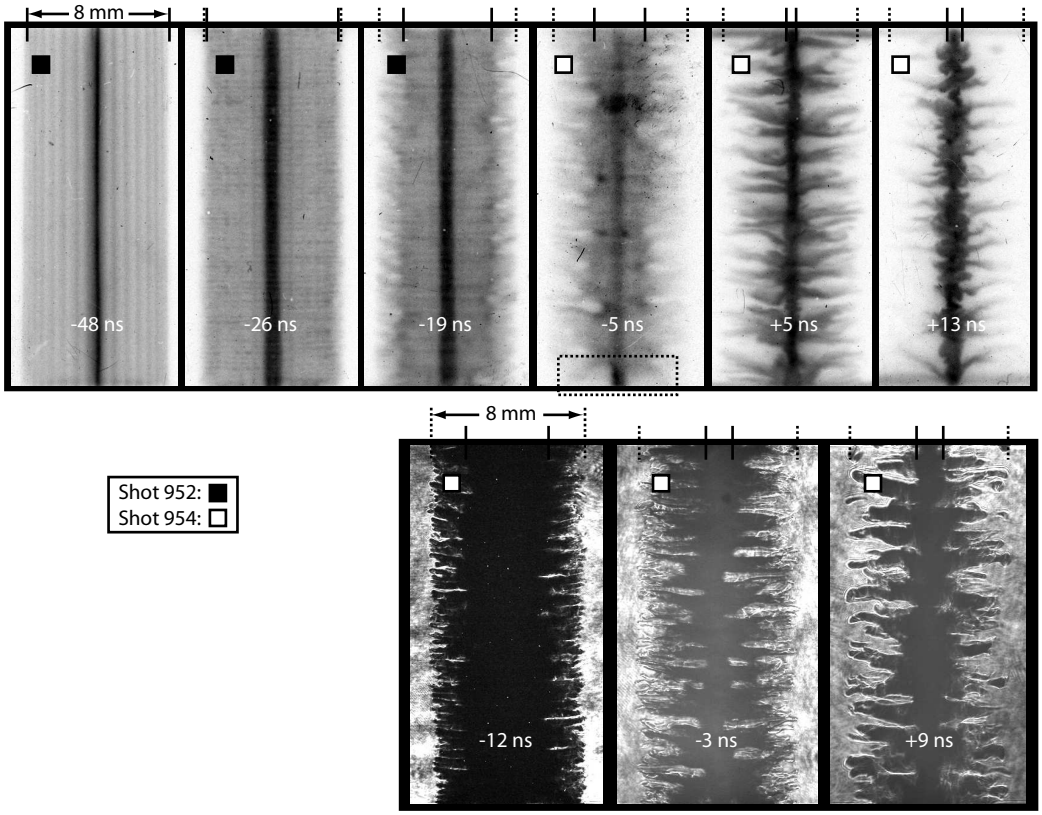

Figure 5.11: Time-gated XUV images (top row) and laser shadowgraph images (bottom row) of imploding 32-wire Al arrays with 8-mm array diameters, 785-μm wire spacings, 10-μm wire diameters, and $\Pi \approx 9$ Frame times are relative to stagnation on the visible streak images.

there is an intense burst of >1-keV radiation that is time-correlated with the onset of intense electron beam generation as well as the arrival on axis of the trailing trajectory in the visible streak; (4) for Al, late-time bursts of hard radiation and electron-beam generation are substantially less intense, often occur much later in time, and are more difficult to associate with trailing streak trajectories; (5) spatial scales observed during the ablation, implosion, and stagnation phases are seen to be larger for Al; (6) the streak images and x-ray pulses appear to be more consistent from shot to shot for W—although this difference may

only be slight for the loads presented throughout Sections 5.2.1 and 5.2.2. We should also point out that for these loads presented in Sections 5.2.1 and 5.2.2, the shot-to-shot consistency for both materials was relatively high compared to sparse wire-arrays (sparse wire-arrays are presented in Sec. 5.2.7).

5.2.3 Invar Experiment (64% iron, 36% nickel)

A single Invar experiment was performed using a 4-mm array diameter. The choice of Invar was made because it is known to produce line radiation that is useful for spectroscopic analysis. Based on our results using light, small-diameter W and Al arrays, we wanted to keep the stagnation time before peak current to produce an intensely radiating spectral source. However, our supply of Invar wires only went down to 10 μm in diameter. This, together with the mass density of Invar, forced us to use only 8 of these 10-μm wires, thus giving $\Pi \approx 48$, and ensuring a stagnation time before peak current. This also resulted in an initial wire spacing of 1.6 mm. Data from this experiment are shown in Figs. 5.12 and 5.13 (spectroscopic data from this experiment are presented in Sec. 5.2.6). From bolometer and PCD measurements, we found the peak x-ray power to be about 400 GW and the total x-ray energy yield to be about 8 kJ.

As with W arrays with 1.6-mm wire spacing, a sub-keV x-ray pre-pulse was generated at the time when the precursor first appeared on the streak (near 50 ns), which can be seen in the 2-μm polycarbonate-filtered PCD trace of Fig. 5.12. (Polycarbonate and Mylar filters have similar transmission properties.) Additionally, we can see from the XUV images in Fig. 5.13 that the precursor appears m=1 unstable. This suggests that some portion of the total current is flowing

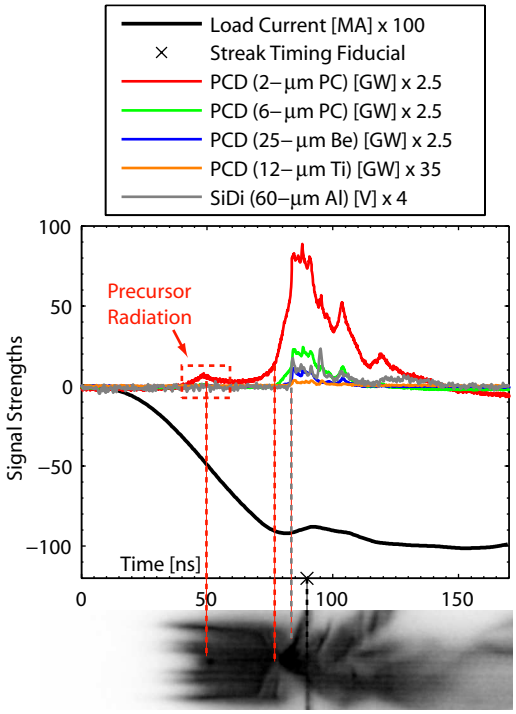

Figure 5.12: (Color) Visible streak camera image synchronized to various signals for an 8-wire Invar array on a 4-mm array diameter, with 1.6-mm wire spacing, 10-μm wire diameters, and $\Pi \approx 48$.

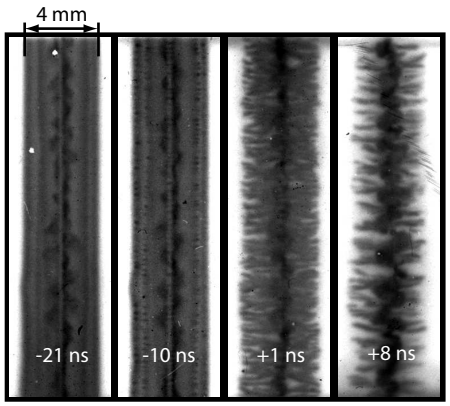

Figure 5.13: Time-gated XUV images of an imploding 8-wire Invar array on a 4-mm array diameter, with 1.6-mm wire spacing, 10-μm wire diameters, and $\Pi \approx 48$. Frame times are relative to stagnation on the visible streak images.

through the precursor column.

Precursor columns that are m=1 unstable have also been observed by Beg *et al.* [71], where nickel (Ni) wires were being tested. In this work they mention that W, Al, and copper (Cu) precursor columns are stable, and that current flow in the precursor column is likely enhanced for Ni, thus resulting in the m=1 structure. They attribute the enhanced current flow in Ni precursor columns to resistivity, citing that while Ni and Cu have similar atomic numbers (Ni=28, Cu=29) and radiative processes, the resistivity is higher for Ni at various phases (room temperature, melting point, boiling point). This argument could apply for Invar as well, since Invar is even more resistive than nickel at room temperature. However, we are unaware of Invar resistivity data at other phases.

Beg *et al.* also show that the x-ray pre-pulse that is time-correlated with precursor emission first appearing on the streak is reduced significantly as the wire number increases. Since they used a constant array diameter, their increased wire number resulted in a decreased wire spacing. Therefore their observation of decreased soft x-ray precursor emission with higher wire number is consistent with our observation of decreased soft x-ray precursor emission with smaller wire spacing. They mention that this decreased x-ray emission is perhaps due to less current in the precursor column, and therefore less compression of the precursor column, for higher-wire-number arrays (or quasi-equivalently, arrays with smaller wire spacing). We would like to extend this argument to include other materials, since W, Al, and Invar precursor columns on COBRA have appeared m=1 unstable for arrays with wire spacings ≥1.6 mm. Examples for W are shown in Fig. 5.14. It is interesting that in both Figs. 5.13 and 5.14, the morphology of the precursor column appears to determine the final morphol-

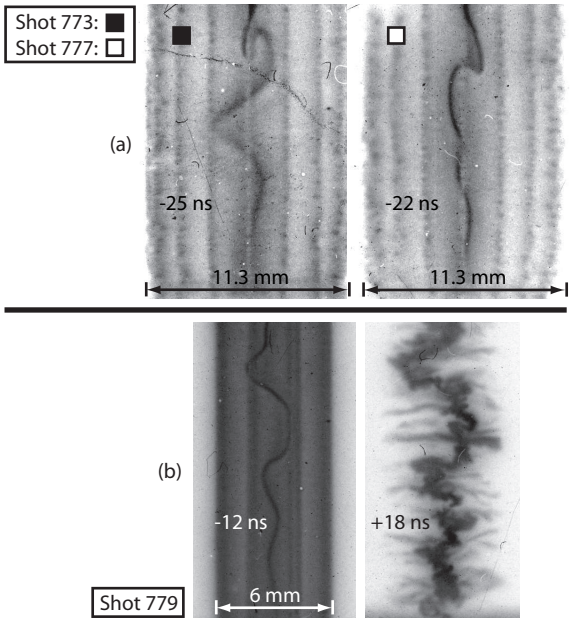

Figure 5.14: XUV images of W arrays revealing the presence of unstable precursors, suggesting a significant amount of current leakage into the precursors. The wire spacings in (a) were 2.2 mm and in (b) it was 2.4 mm (i.e., greater than the 1.6-mm threshold described in the text). Part (b) also shows the similarity between the shape of the precursor column (-12 ns) and the shape of the stagnation column (+18 ns). Frame times are relative to stagnation on the visible streak images.

ogy of the stagnation column.

A unique feature in the Invar streak image is that, prior to the abrupt turn in the main trajectory near 75 ns (marking the transition to the implosion phase), the brightest emission regions near the wire cores appear to be drifting radially inward as opposed to the more stationary emission observed in the W and Al streaks (compare Figs. 5.6 and 5.10 with Fig. 5.12, for example).

5.2.4 Electrical Power Into Load vs. Radiated Power Out

As mentioned in Sec. 1.2, disagreement persists within the community over the mechanisms responsible for transferring energy into the stagnated plasma column of a wire-array z-pinch, and thus over the mechanisms ultimately responsible for producing the intense burst of radiation. In the review paper by Pereira & Davis [25], it was briefly mentioned that the electrical power into a z-pinch load was of the same magnitude as the radiated power. To investigate this statement, we can plot both of these powers in absolute units and compare. To obtain the electrical power into the load, we make use of the load voltage monitor, which again measures $V_{load} = L\dot{I} + \dot{L}I + IR$. We can rewrite this as

$$V_{load} = [L_0 + \delta L(t)]\dot{I} + I(\dot{L} + R) \approx L_0\dot{I} + IZ_{load}, \tag{5.3}$$

where we took $\delta L(t) \ll L_0$, the validity of which has been verified numerically *a posteriori*. Now since power is voltage times current, the electrical power into the load is

$$P_{load} = I^2 Z_{load} = (V_{load} - L_0\dot{I})I, \tag{5.4}$$

where $V_{load}I$ is the total power delivered by the generator and $L_0\dot{I}I$ is rate at which energy is being stored in the magnetic field. The results of Eqn. 5.4 are shown in Fig. 5.15 for the 4-mm-diameter loads of Secs. 5.2.1 and 5.2.2, respectively. Also plotted in Fig. 5.15 are the bolometer-normalized PCD powers. Here we can see that the waveforms of the electrical input power and the radiated output power are of similar shape and magnitude for both W and Al when one averages through the large-amplitude oscillations that occur after stagnation. This suggests that the electrical power into the load contributes directly and significantly to the radiated power out on COBRA. Also, since $Z_{load} = (\dot{L} + R)$, this electrical power into the load can either be in the form of resistive/ohmic

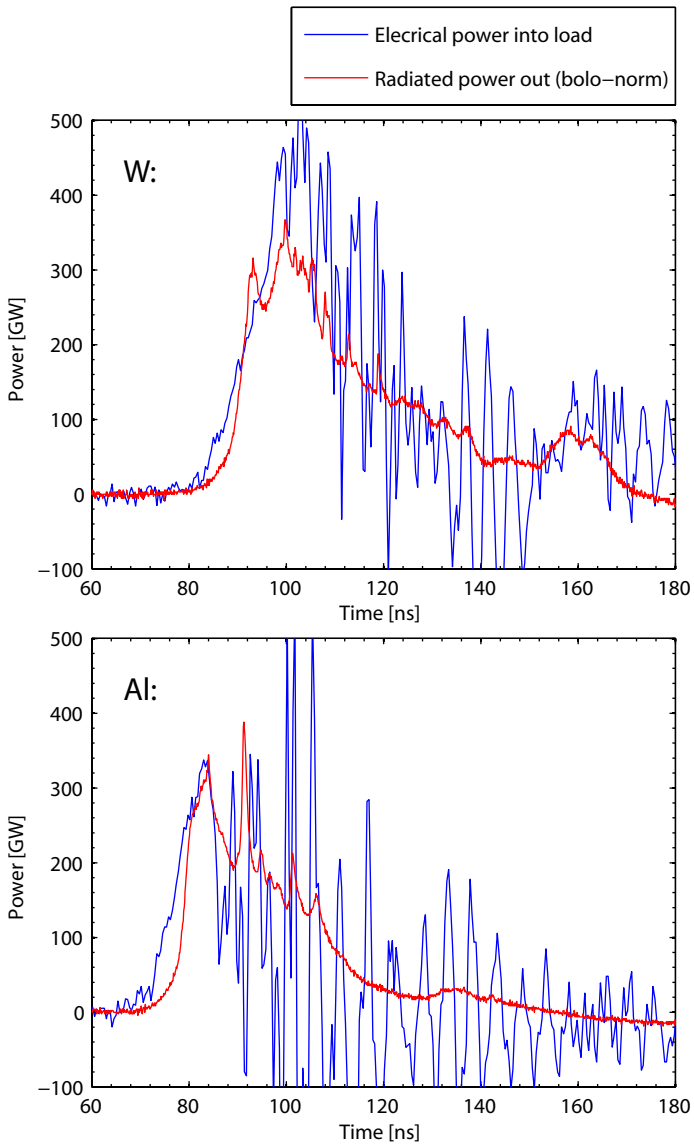

Figure 5.15: (Color) Plot of electrical power into load versus radiated power out for W and Al. The two loads are the 4-mm-diameter loads of Secs. 5.2.1 and 5.2.2, respectively.

heating, I^2R, or magnetic compressional heating, $\dot{L}I^2$ (i.e., pdV work). Unfortunately, the two mechanisms cannot be decoupled using this method.

It has been proposed by M. Haines [72] that two regimes exist for wire-array z-pinch implosions, one being a resistive/compressive regime and the other be-

ing a kinetic thermalization regime. Given the results plotted in Fig. 5.15, it seems likely that implosions on COBRA are dominated by the former. However, more investigation is required to support this more definitively.

5.2.5 Implosion Models & Data Fitting

As mentioned in Sections 3.3 and 5.1.2, and observed in the streak data shown throughout Sec. 5.2, the implosion trajectory of a wire-array z-pinch does not generally follow that predicted by the thin-shell model (i.e., Equation 3.36). As has been shown by others [46, 3], it is perhaps more accurate to use an ablation-snowplow model to represent the implosion trajectory.

For the ablation phase of the ablation-snowplow model, we use the rocket model of Lebedev *et al.* [46]. This model was introduced to account for the ablation streams and stationary wire cores observed during this phase of a wire-array z-pinch. It assumes that the current is confined to the coronal plasma near the stationary wire cores at the initial array radius $r = r_0$. Therefore, since the wire cores do not carry current, they are left force-free and stationary. This assumption also means that there is no electromagnetic force on the coronal plasma once it is injected into the array interior. Thus this model assumes that after a brief interval of acceleration near $r = r_0$, the injected coronal plasma coasts toward the array axis at the constant "ablation velocity", v_a. In approximation to these assumed phenomena, this model, like the thin-shell model of Sec. 3.3, distributes the current and mass uniformly around the azimuth of a cylindrical shell with an infinitesimal thickness. To clarify, there are not individual plasma current channels fixed near the initial wire locations at distinct

points around the azimuth, rather the current and mass are spread uniformly into sheet densities around the azimuth. Therefore we can use the same expressions as in Sec. 3.3 to relate the $\mathbf{J} \times \mathbf{B}$ force density and magnetic field pressure to the drive current.

With the assumptions above, the ablation of a wire core (i.e., the ablation of the infinitely thin cylindrical shell) will create an infinitesimal plasma element at $r = r_0$ with mass dm_a in the time interval dt (thus an ablation rate of dm_a/dt). This element is assumed to have zero initial momentum (i.e., $v_i = 0$). Now, the radially-inward $\mathbf{J} \times \mathbf{B}$ force density, $F_{\mathbf{J}\times\mathbf{B}}$, will act on this element only for the infinitesimal period of time dt in which the mass element is colocated with the driving current density at $r = r_0$ (i.e., in the time that it takes for the mass element to be created, it is driven off the shell at $r = r_0$ by the $\mathbf{J} \times \mathbf{B}$ force density, and thus begins its force-free coast toward the array axis). Therefore, by the fundamental relation between force and momentum, we have

$$F_{\mathbf{J}\times\mathbf{B}} = \lim_{\Delta t \to 0} \frac{\Delta P_a}{\Delta t} = \frac{P_a(t_i + dt) - P_a(t_i)}{dt} = \frac{dm_a v_a - dm_a \cancelto{0}{v_i}}{dt} = \frac{dm_a}{dt} v_a. \tag{5.5}$$

The mass of our system is either part of the ablation streams (with momentum per unit length $\hat{P}_a = \hat{m}_a v_a$) or part of the wire cores (with momentum per unit length $\hat{P}_c = \hat{m}_c v_c$). Neglecting any mass buildup in the precursor column, as well as any effects that this buildup might have on the ablation streams, the mass of our system will have the total radial momentum per unit length $\hat{P} = \hat{P}_a + \hat{P}_c$. However, our system mass is not isolated. The magnetic field is an external source that imparts momentum to our system mass. We denote the effective momentum per unit length of the magnetic field by $\hat{P}_{mag}$. Therefore, with the assumptions of the model described above, momentum conservation

gives

$$\dot{\hat{P}} = \dot{\hat{P}}_{mag} \tag{5.6}$$

$$\dot{\hat{P}}_a + \dot{\hat{P}}_c = \hat{F}_{\mathbf{J}\times\mathbf{B}} \tag{5.7}$$

$$\frac{d}{dt}(\hat{m}_a v_a) + \frac{d}{dt}(\hat{m}_c v_c) = p_{mag} \cdot 2\pi r_0 \tag{5.8}$$

$$\dot{\hat{m}}_a v_a + \hat{m}_a \cancelto{0}{\dot{v}_a} + \dot{\hat{m}}_c \cancelto{0}{v_c} + \hat{m}_c \cancelto{0}{\dot{v}_c} = \frac{B^2}{2\mu_0} \cdot 2\pi r_0 \tag{5.9}$$

$$\dot{\hat{m}}_a v_a = \frac{\mu_0 I^2}{4\pi r_0} \tag{5.10}$$

$$\Rightarrow \dot{\hat{m}}_a = \frac{\mu_0 I^2}{4\pi r_0 v_a}. \tag{5.11}$$

Recognizing that $\dot{\hat{m}}_a = -\dot{\hat{m}}_c$, we drop the subscript and define the ablation rate as the magnitude $\dot{\hat{m}} \equiv |\dot{\hat{m}}_a| = |\dot{\hat{m}}_c|$. (Note: The wire cores do not participate in this model mathematically, but physically they are needed to continuously supply the ablation streams with mass. Thus the wire cores impose an upper limit on the amount of mass that can be ablated.) Integrating Eqn. 5.11 up to a time of interest t, we obtain

$$\delta\hat{m} = \frac{\mu_0}{4\pi r_0 v_a} \int_0^t I^2 dt'. \tag{5.12}$$

As shown in Ref. [46], Equation 5.12 can be used to derive the following time-retarded expression for the mass density profile of the injected pre-fill plasma as a function of both radius and time:

$$\rho(r,t) = \frac{\mu_0}{8\pi^2 r_0 r v_a^2} \left[I\left(t - \frac{r_0 - r}{v_a} \right) \right]^2. \tag{5.13}$$

Equations 5.12 and 5.13 are the two fundamental relations applied when one uses the Lebedev rocket model for the ablation phase of an ablation-snowplow model. In this model, the ablation velocity is a parameter that must be determined from either experiment or simulation.

For the snowplow phase of an ablation-snowplow model, the current shell, including some fraction of the remaining mass in that shell (i.e., some fraction

of the non-ablated mass) are no longer fixed to $r = r_0$, and thus are allowed to be imploded by the $\mathbf{J} \times \mathbf{B}$ force density. Also for this phase of the model, one typically assumes that mass is no longer ablated out of the thin shell, rather mass is accumulated by the shell as it interacts with the pre-fill density $\rho(r, t)$ described by Eqn. 5.13. In other words, we have the thin-shell model of Sec. 3.3 with an added term to account for the change in momentum due to the accrual of in-flowing mass as the imploding shell sweeps up the pre-fill. The snowplow model as written in Ref. [46] is:

$$\hat{m}(t)\ddot{r} - 2\pi r\rho(r, t^*)\dot{r}^2 = -\frac{\mu_0 I^2}{4\pi r} \tag{5.14}$$

$$\dot{\hat{m}}(t) = -2\pi r\rho(r, t^*)\dot{r}. \tag{5.15}$$

However these equations only account for the interaction of the imploding shell with a *static* pre-fill, where this static pre-fill was determined in Ref. [46] by running the ablation model up to the moment where the snowplow implosion was initiated (i.e., integrating Eqn. 5.12 up to $t = t^*$, and using $\rho(r, t^*)$ in Eqn. 5.13). However, we know that the pre-fill is moving radially inward at the ablation velocity. This radial motion will affect the change in momentum as the snowplow sweeps up the pre-fill. To account for this dynamic pre-fill, we modify Eqns. 5.14 and 5.15 to read:

$$\hat{m}(t)\ddot{r} - 2\pi r\rho(r, t)(\dot{r} + v_a)^2 = -\frac{\mu_0 I^2}{4\pi r} \tag{5.16}$$

$$\dot{\hat{m}}(t) = -2\pi r\rho(r, t)(\dot{r} + v_a) \tag{5.17}$$

$$\rho(r, t) = \rho(r', t^*) \tag{5.18}$$

$$r' = r + v_a(t - t^*). \tag{5.19}$$

Similar modifications were implemented in the models of Ref. [73].

In practice, the models described above are numerically integrated and take the drive current data as inputs. Also, the ablation model and the snowplow model are used together in a piece-wise fashion. First, the ablation model is run until a certain percentage of the initial array mass has been ablated, then the snowplow model is initiated. In our case, we calculate the instantaneous pre-fill density and its interaction with the snowplow front at every time-step in the integration to account for the pre-fill moving radially inward at the ablation velocity. Since the ablation velocity is assumed to be constant in this model, the calculation is done in the simple time-retarded manner shown above in Equations 5.16–5.19. We would also like to mention, as was similarly noted in Ref. [73], that there is indeed some ambiguity as to how to proceed with initiating the snowplow model during the period of time when the initial mass of the snowplow front, which starts from rest, has not yet been accelerated up to the ablation velocity. Specifically, there is a question as to whether to allow ablation to continue during this period or to shut off the ablation completely, and allow the shell to accelerate drag-free until it catches up to the ablated pre-fill. For our purposes of obtaining simple estimates, we implemented the latter. The MATLAB functions written for this analysis, along with the functions that handle the processing and plotting of all the signals shown throughout this chapter, are included in Appendix B.

The ablation-snowplow model described above was parameter-tuned to produce trajectories that matched the main implosion trajectories in the streak images for all experiments. Free parameters included the ablation velocity, the percentage of mass ablated by the ablation model (Eqns. 5.12 and 5.13) prior to the initiation of the snowplow model (Eqns. 5.16–5.19), the percentage of non-ablated mass acted on at the initiation of the snowplow model, and the

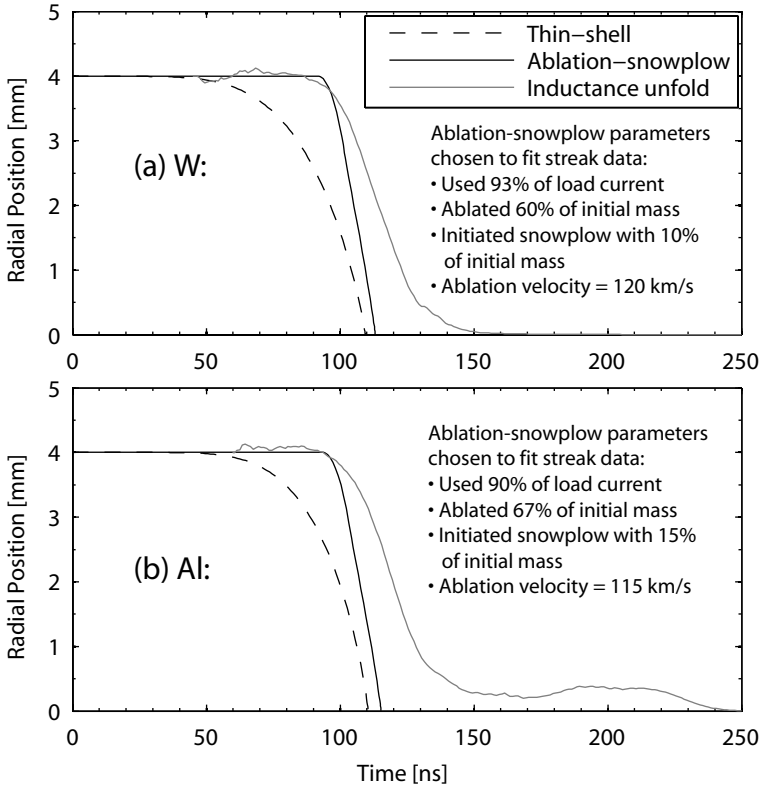

Figure 5.16: Implosion trajectories produced by the thin-shell, ablation-snowplow, and inductance unfold models for the 32-wire W (a) and Al (b) arrays of Sections 5.2.1 & 5.2.2, respectively. Both were on 8-mm array diameters and had 785-μm wire spacings. The wire diameters were 5 μm for W and 10 μm for Al, giving them $\Pi \approx 5$ and $\Pi \approx 9$, respectively.

percentage of load current used (as some fraction of the load current could be distributed throughout the interior of the array, and thus would not contribute to wire ablation or snowplow acceleration). Examples of this parameter fitting, along with the thin-shell trajectories, are shown for representative W and Al loads in Fig. 5.16.

The four free parameters used to give a good fit to the streak trajectory varied from shot to shot and from one array configuration to the next. Typically the percentage of initial array mass ablated prior to starting the snowplow was

in the range of about 45–70%, while the initial mass in the snowplow was usually 6–20% (the resulting trailing mass was typically 20–40%). The percentage of load current used was 90–95%, and the ablation velocities used were typically in the range of 110–170 km/s, with the apparent trend of increasing ablation velocity with decreasing wire number and initial wire diameter (or alternatively, increasing ablation velocity with increasing inter-wire gap). It is important to note, however, that these parameter fits are not unique, as more than one combination of parameters can be used to produce a trajectory that is similar to that on the streak. Nevertheless, the parameters chosen seem to agree reasonably well with those found elsewhere using a similar procedure [46].

In general, for the non-sparse arrays such as those presented in Sections 5.2.1 and 5.2.2, the streak trajectories for Al were more thin-shell-like than those for W. That is, for Al, the implosion phase started at an earlier fraction of the stagnation time, and the initial acceleration was more gradual. (In Sec. 5.2.7, however, sparse Al arrays are presented in which abrupt accelerations do occur.) W arrays, on the other hand, produced trajectories that started inward at a later fraction of the stagnation time, and accelerated very quickly to a nearly constant radial velocity.

In designing these experiments, we anticipated a change from an ablation dominated trajectory to a thin-shell trajectory for Al as the wire spacing decreased from 1.6 mm to 785 μm, as was observed in Ref. [46]. However, referring to the three Al streaks in Sec. 5.2.2 (where wire spacing was either 1.6 mm or 785 μm), we see only ablation-dominated trajectories. Possible reasons are COBRA's 100-ns rise time versus the 240-ns rise time used in Ref. [46], and the smaller wire diameters (10 μm instead of 15 μm), lower wire numbers (16 or 32

instead of 64), and smaller array diameters (4 or 8 mm instead of 16 mm) used here to achieve the 785-μm wire spacings. Also, in one shot with a slower current rise (which occurred by accident due to a machine misfire) we did observe a thin-shell-like trajectory using 17-μm Al wires in a 16-wire array with an 8-mm diameter. This is shown in Fig. 5.17(b). However as this gives a 1.6-mm wire spacing, we would not have expected a thin-shell trajectory in this case based on the observations in Ref. [46]. Perhaps the combination of thicker wire and a slower current rise result in more thin-shell-like trajectories. Thicker initial wire diameters can expand to greater final diameters [63], thus increasing plasma merger between wires, and the slower current rise can allow more time for the process of wire plasma expansion to occur. Also, the time for wire expansion is a smaller fraction of the overall time to stagnation for a slower current rise, making this period less noticeable in the longer overall trajectory, and hence the trajectory would appear more thin-shell-like. When the same load that produced the thin-shell-like trajectory in Fig. 5.17(b) was repeated with faster rising current pulses (95–100 ns), it did not produce thin-shell-like trajectories.

Returning now to Fig. 5.16, we see that also plotted are the effective current sheath trajectories by way of the inductance unfold described in Sec. 5.2.1. Here the time-dependent radius of the effective current sheath was calculated by inverting the expression for the inductance of a coaxial transmission line, giving

$$r_{Ieff}(t) = r_{ret} e^{-2\pi L(t)/\mu_0}, \tag{5.20}$$

where we have taken the radial position of the effective current sheath, r_{Ieff}, as the radius of the inner conductor and the radial position of our return current posts, r_{ret}, as the radius of the outer conductor. This method is not without its faults, however. As our geometry is not truly coaxial, tuning is required to find initial effective inductances. Another issue is when to initiate the integration

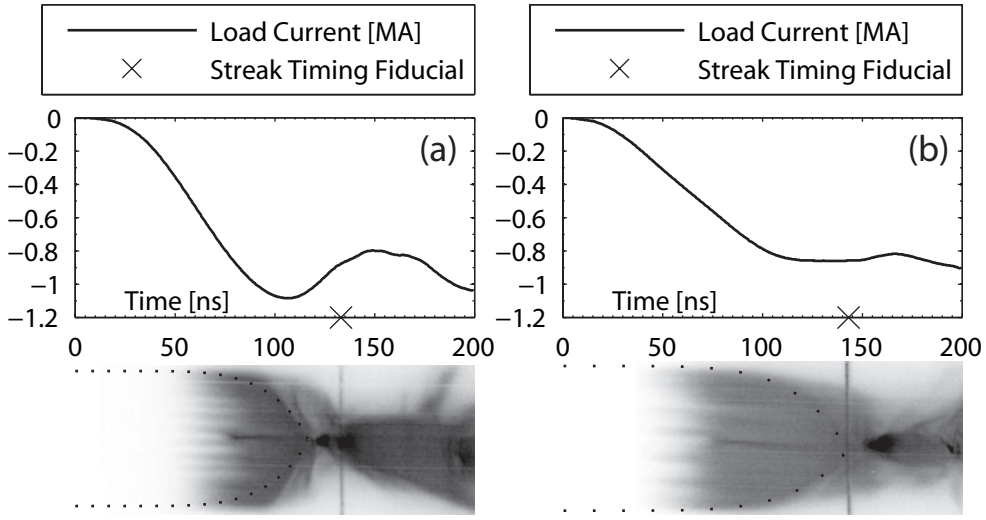

Figure 5.17: Thin-shell trajectories overlaying the visible streaks of two Al experiments. The ablation-dominated trajectory from the 32-wire array of Sec. 5.2.2 is shown in (a) while a thin-shell-like trajectory from a 16-wire array with 17-μm wire diameters is shown in (b). The wire spacing was 785 μm in (a) and 1.6 mm in (b). Both arrays were on 8-mm diameters. Note the slower current rise in (b). The thin-shell trajectories were generated using Eqn. 3.36 with respective array masses and load current data. Thin-shell stagnation times were scaled to streak stagnation times by using 80% of the load current for (a) and 90% of the load current for (b).

for calculating $L(t)$. It must be started after the resistive voltage collapse, since the relatively large IR term during the resistive phase invalidates our simplified differential expression for $L(t)$. However, the voltage collapse initiates a ringing in our voltage signal requiring that the start time during this ringing period be chosen judiciously. For these reasons, the effective current radius calculated by this method has considerable uncertainty. However, these plots are useful for their qualitative and timing information. For example, we have reasonable confidence in the time when the bulk of the current begins moving inward during the implosion phase, and when it later stagnates on axis.

Figure 5.16 shows that the trajectory of the effective current sheath trails the trajectory obtained from the ablation-snowplow model, and thus also trails the main implosion trajectory on the corresponding streak image. The trajectory of the effective current sheath therefore seems to correspond to the trailing trajectories mentioned throughout Sec. 5.2 for W. Hence it appears that the onset of intense hard x-rays and electron beams are correlated with the arrival of the effective current sheath on axis. This could correspond to the arrival of the remaining trailing mass on axis as well, given the fact that plasma channels at larger radii provide lower-inductance paths for the current to follow.

[Two Possible Scenarios: Considering the position of the effective current sheath, one can imagine the fronts of the imploding bubbles arriving on axis at the time when the main streak trajectory arrives on axis, and that these bubble structures connect back to the trailing mass that has remained stationary at the initial array radius. Thus the current path could be weaving in and out between the initial array radius and the array axis as it traverses the vertical extent of the array. The average radial position of such a weaving current channel would then be about half way between the array axis and the initial array radius. Referring now to Fig. 5.16 at the stagnation time of the ablation-snowplow trajectory (i.e., the stagnation time on the corresponding streak image), we see that the position of the effective current sheath is indeed about half way between the array axis and the initial array radius. On the other hand, the current could simply be distributed throughout the interior of the array, and follow an essentially vertical path. More experiments are needed to answer this, however, such as experiments where the magnetic field within the array is measured.]

5.2.6 Hot Spot Observations

For all materials tested, strongly radiating loads were accompanied by the presence of several bright spots in x-ray pinhole photographs, as have been reported elsewhere [25, 33]. These are small discrete points along the vertical pinch column that are intense and found to be relatively hot and dense when the radiation is analyzed spectroscopically [74].

In Fig. 5.18, we present time-integrated, unfiltered, 50-μm pinhole images of the imploding 4-mm-diameter W, Al, and Invar arrays discussed throughout Sec. 5.2. The first film (DR50) absorbs much of the wide-spread <5 keV radiation, while higher energies pass through to the second film (Biomax), which is more sensitive. Hence the second film typically reveals the presence of hot spots with greater contrast.

For the same three 4-mm-diameter loads, we present time-integrated spectral images produced by the x-ray WB-FSSR in Fig. 5.19. These images incorporate both vertical and horizontal spatial resolution with their spectral content. One can observe the pinch column imaged repeatedly at several discrete wavelengths and in various reflection orders of the crystal spectrograph. For example, the Al spectrum shows the pinch column imaged from anode to cathode in various Al XII and XIII lines in both second and third order. This should be contrasted with the observation of continuum components located at discrete vertical points, and spanning the horizontal extent of the film. The vertical positions of the continuum components correspond to the vertical positions of the bright spots in the pinhole camera images. Similar observations were made for Al implosions in Ref. [33]. From the W and Invar spectra, however, we find that high-energy inner-shell transitions (e.g. W-L_α) can be excited throughout

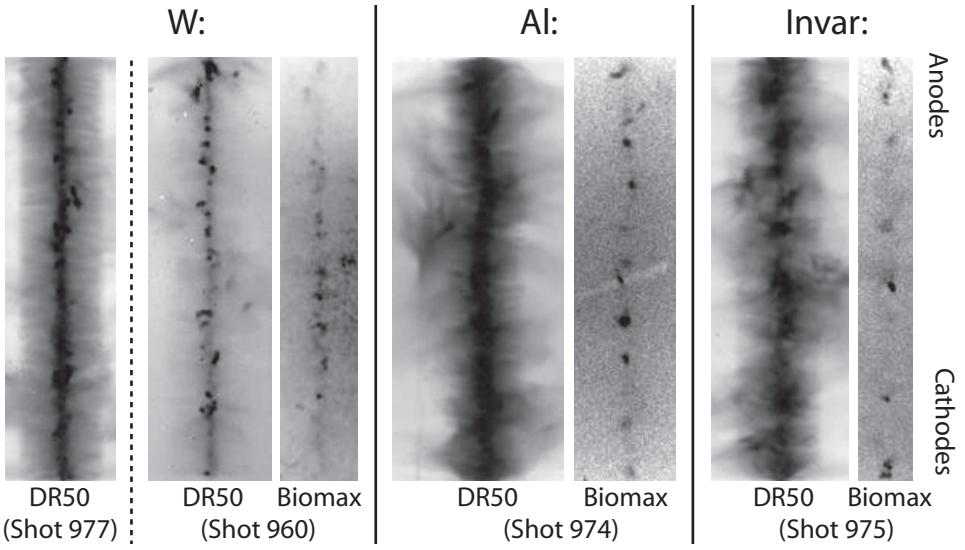

Figure 5.18: Time-integrated, unfiltered, 50-μm pinhole images of imploding arrays for W, Al, and Invar, all revealing the presence of localized hot spots. The first layer of film (DR50) filters widespread soft radiation, while the second film (Biomax) typically shows the localized hot spots with greater contrast.

the pinch column on the anode side of very intense hot spots. This suggests that energetic electrons are being generated near the hot spots, and that these electrons are knocking out the inner-shell electrons of partially ionized atoms on the anode side of the hot spots in the stagnated pinch column.

In Fig. 5.20, we present x-ray streak results for the Invar experiment. In this case the upper half of the pinch column was imaged as a continuous function of time. The various formation times of the localized hot spots correspond well with the bursts of radiation detected by PCDs with >1-keV filters. Also, the brightest emission from a given spot is seen to begin suddenly and last only a few nanoseconds, while less intense radiation can persist for longer. Similar results have been obtained for W and Al.

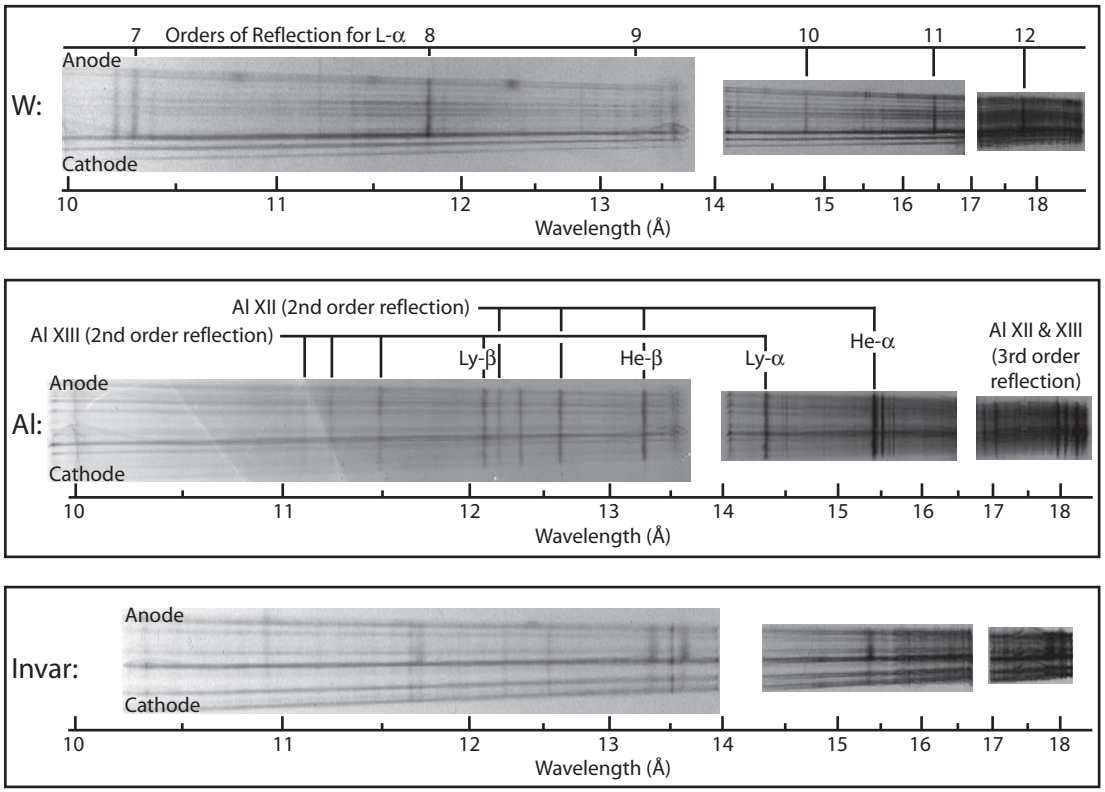

Figure 5.19: Time-integrated x-ray spectra with vertical and horizontal spatial resolution produced by the WB-FSSR, and revealing the continuum nature of the localized hot spots for W, Al, and Invar.

5.2.7 Sparse Wire-Array Experiments

In this section we consider the relevance of lower-current, lower-wire-number experiments (i.e., ~1 MA; ≤32 wires) to higher-current, higher-wire-number experiments (i.e., ~20 MA; ≥100 wires). Observations such as those presented in Ref. [33] show that with sparse array configurations (e.g., 8 wires on a 16-mm diameter), the wires appear to act in an independent/uncorrelated fashion. This mode of operation is observed on COBRA as well, as shown in Figures 5.21 and 5.22 for W and Al, respectively. These are 8-wire arrays on a 16-mm array diameter, giving a 6.3-mm wire spacing. Notice that the Al exam-

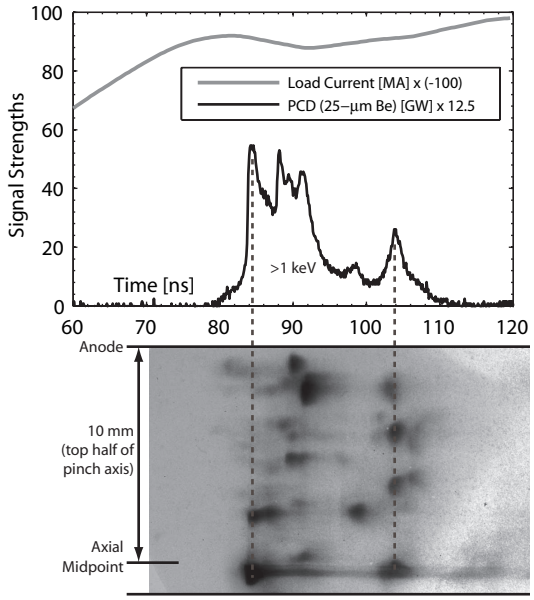

Figure 5.20: X-ray streak camera image of the top half of the pinch axis of an Invar array revealing the formation of discrete hot spots at various times and locations.

ple displays an extreme case of nonuniformity, where we can clearly distinguish individual bubbles protruding from a single wire.

The corresponding streaks and x-ray pulses are shown in Figures 5.23 and 5.24, respectively. We can see especially from the Al streak that the wires seem to implode almost independently, that the trajectory of a given wire seems to bifurcate at the start of the implosion, leaving material behind at the original wire location, and that this left-behind material often implodes at a later time. All of this leads to several different implosion trajectories arriving on axis at different times. The result is a very broad, low-power x-ray pulse. Also notice that for this sparse array case, the Al trajectory has a more abrupt transition to implosion, as opposed to the more rounded transitions for Al trajectories shown in Sec 5.2.2.

Figure 5.21: XUV image of an imploding sparse W array showing nonuniform implosion (8 wires on a 16-mm array diameter giving 6.3-mm wire spacing).

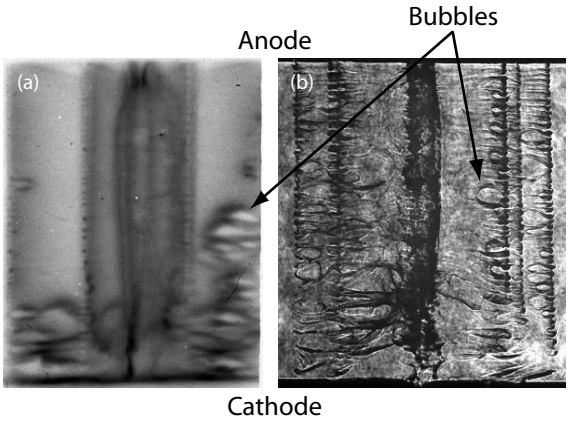

Figure 5.22: XUV (a) and laser (b) shadowgraph images of an imploding sparse Al array showing nonuniform implosion (8 wires on a 16-mm array diameter giving 6.3-mm wire spacing).

Based on the data set discussed here, as well as the data from several additional sparse array experiments acquired on COBRA, it appears that sparse W arrays implodes more uniformly and with better shot-to-shot consistency than sparse Al arrays despite having the same large inter-wire gaps. For example, from streak images, the individual wires in sparse W arrays transition to implosion and stagnate on axis more simultaneously than the wires in sparse Al

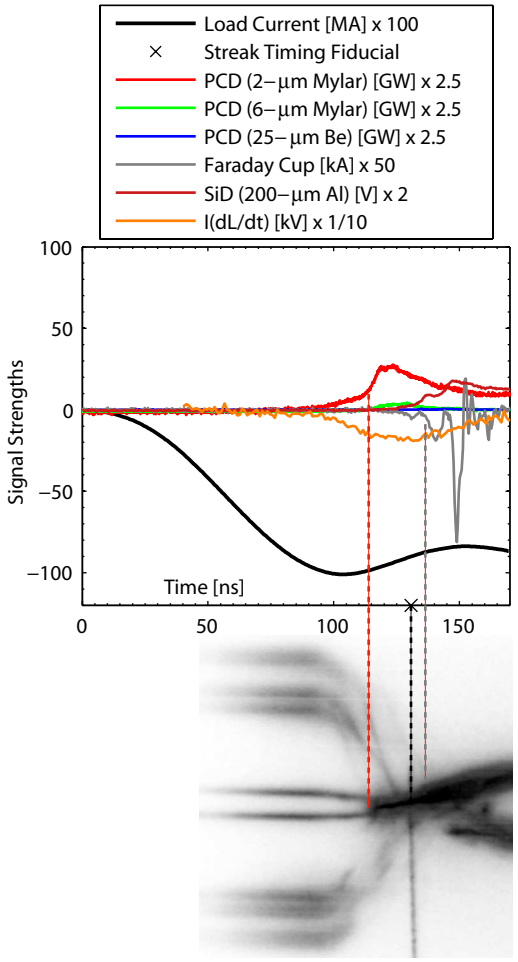

Figure 5.23: (Color) Visible streak camera image synchronized to various signals for a sparse W array showing nonuniform implosion (8 wires on a 16-mm array diameter giving 6.3-mm wire spacing).

arrays. Also, the axial nonuniformity of the implosion is more mild for sparse W arrays, as can be seen by comparing Figs. 5.21 and 5.22, where in the case of Al, the cathode end of the array has already imploded and stagnated while the anode end has not even begun to implode. This difference between W and Al in the axial nonuniformity of the implosion could be related to differences in the energy deposited in the wire cores during the resistive heating phase, which in turn could be due to contact and/or electric field effects. Evidence for this is

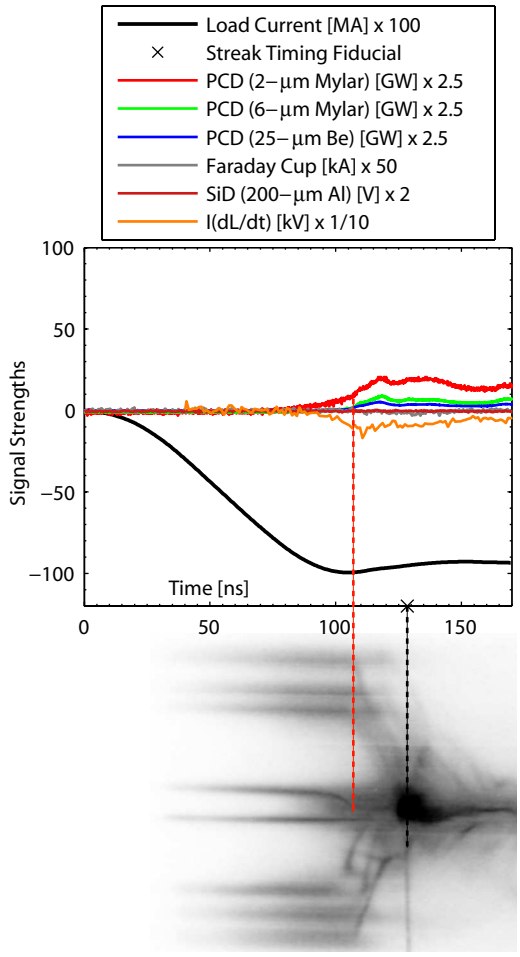

Figure 5.24: (Color) Visible streak camera image synchronized to various signals for a sparse Al array showing nonuniform implosion (8 wires on a 16-mm array diameter giving 6.3-mm wire spacing).

seen in laser shadowgraphs taken during the ablation phase, such as that shown in Fig. 5.25. Here, along a given Al wire, one can see evidence of two different expansion rates, with an abrupt transition between the two. This transition often occurs at a location about 20–40% of the array height up from the cathode for sparse Al arrays. For the region near the cathode, the Al wires are often expanded to about twice their diameter in the region near the anode. This region of greater wire expansion seems to correlate with the regions first imploding in

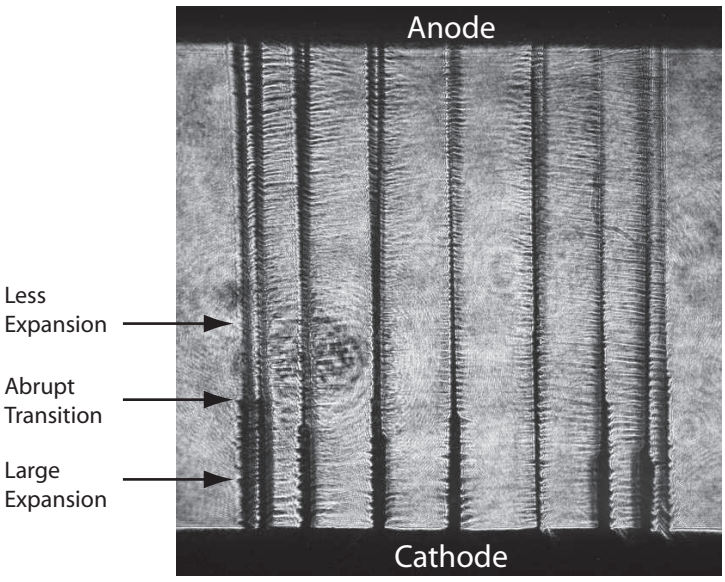

Figure 5.25: Laser shadowgraph showing the axially nonuniform expansion rates of Al wires.

Fig. 5.22. This extreme difference in the expansion rate along a given wire is not observed in sparse W arrays.

Regardless of these difference between sparse Al and W arrays, the shot-to-shot repeatability for any sparse array is poor. By contrast, the loads presented in Sections 5.2.1, 5.2.2 do seem consistent from shot to shot. In each case where we repeated a particular configuration, the results were reasonably similar when comparing streak images, framing camera images, laser shadowgraphs, bolometer yields, and x-ray pulse shapes and amplitudes. The increased consistency of x-ray pulse shapes and amplitudes are expected since we can clearly see that non-sparse arrays have greater axial uniformity during the implosion and greater wire-to-wire correlation. Therefore, since we were operating in a well correlated regime (for the data presented in the previous sections), and since our closest wire spacings (i.e., 785 μm) are comparable to at least the larger wire spacings used on Z (e.g., 530 μm) [3], it would seem that the

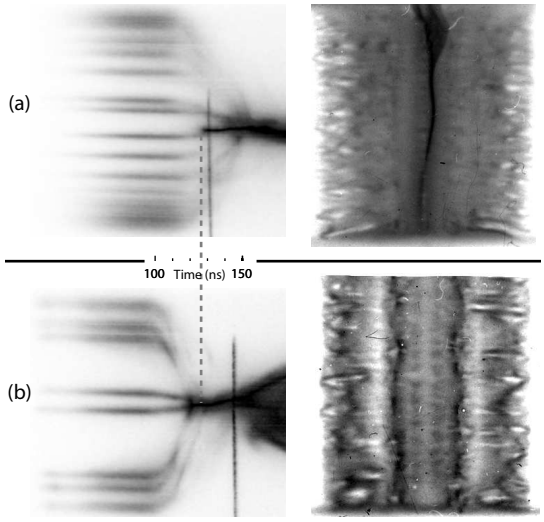

Figure 5.26: (a) Optical streak camera and XUV images for a 16-wire W array on a 16-mm array diameter showing that the precursor started just after the implosion phase began, but prior to stagnation. This should be compared to the corresponding images in (b), where the array was half the mass/wire-number (therefore imploded earlier) and no precursor was present. The implosions in (a) and (b) were produced by similar current pulses, which allowed the streaks to be synchronized, and thus share the same time scale relative to the start of current.

data presented in the previous sections, and the various mechanisms observed, are relevant to experiments at much higher current and wire number.

An interesting feature in the XUV and streak images of the W array in Figures 5.21 and 5.23, respectively, is the absence of a precursor column. It appears that we have found a configuration for W on COBRA such that the wire cores burn through, implode, and stagnate before the mechanism which causes a well-formed precursor initiates. As mentioned in Ref. [64], this mechanism could be collisionality, which may abruptly turn on when the density increases above the appropriate threshold for the material being used. To illustrate this further, we can give the precursor more time to turn on by delaying stagnation,

which can be achieved most easily by simply doubling the number of wires. This was done by using a 16-wire W array on a 16-mm array diameter. The results are shown in Fig. 5.26(a). Note that the precursor is now present just after the implosion phase begins on the streak, as well as in the XUV image prior to stagnation. In Fig. 5.26(b), we include results from an 8-wire case (i.e., no precursor) for quick comparison.

CHAPTER 6

SPECTROSCOPIC MEASUREMENTS OF ABLATED PLASMA IN ALUMINUM ARRAYS

In the previous chapters, visible streak images of radial implosions were shown. In this chapter we discuss an alternative setup that was used to streak visible-light spectra from aluminum arrays (see Fig 6.1). In this case, light from the experiment was first sent through a Czerny-Turner spectrometer (see Fig. 6.2). The dispersed light at the output of the spectrometer was then sent to the streak camera, which enabled us to record the visible spectra as a continuous function of time.

This experimental setup was expected to produce distinct spectral lines that could later be analyzed to determine plasma parameters such as temperature, density, and magnetic field, and all as a function of time. It was also thought that if these lines were going to be seen, then we would have to look early in time, before the plasma temperature rose above a few eV. However, upon conducting an initial run of experiments to seek out useful lines, we found only continuum (see Fig. 6.3). Moreover, it was found that the continuum turned on almost instantly at the time of wire breakdown (i.e., the resistive voltage collapse in Fig. 6.3—at least for the larger-diameter (>100 μm) wires tested during this run).

Reevaluating the experiment led to some new thoughts on which way to proceed. First, only 5-wire arrays with >100-μm wires were tested. The thick wires affected the experiment by delaying the resistive voltage collapse to around 50 ns. By 50 ns, however, the total load current is increased to about 400 kA. Since there were only five wires being used, this is about 80 kA per wire, which is thought to produce plasma temperatures well above where lines in the visible

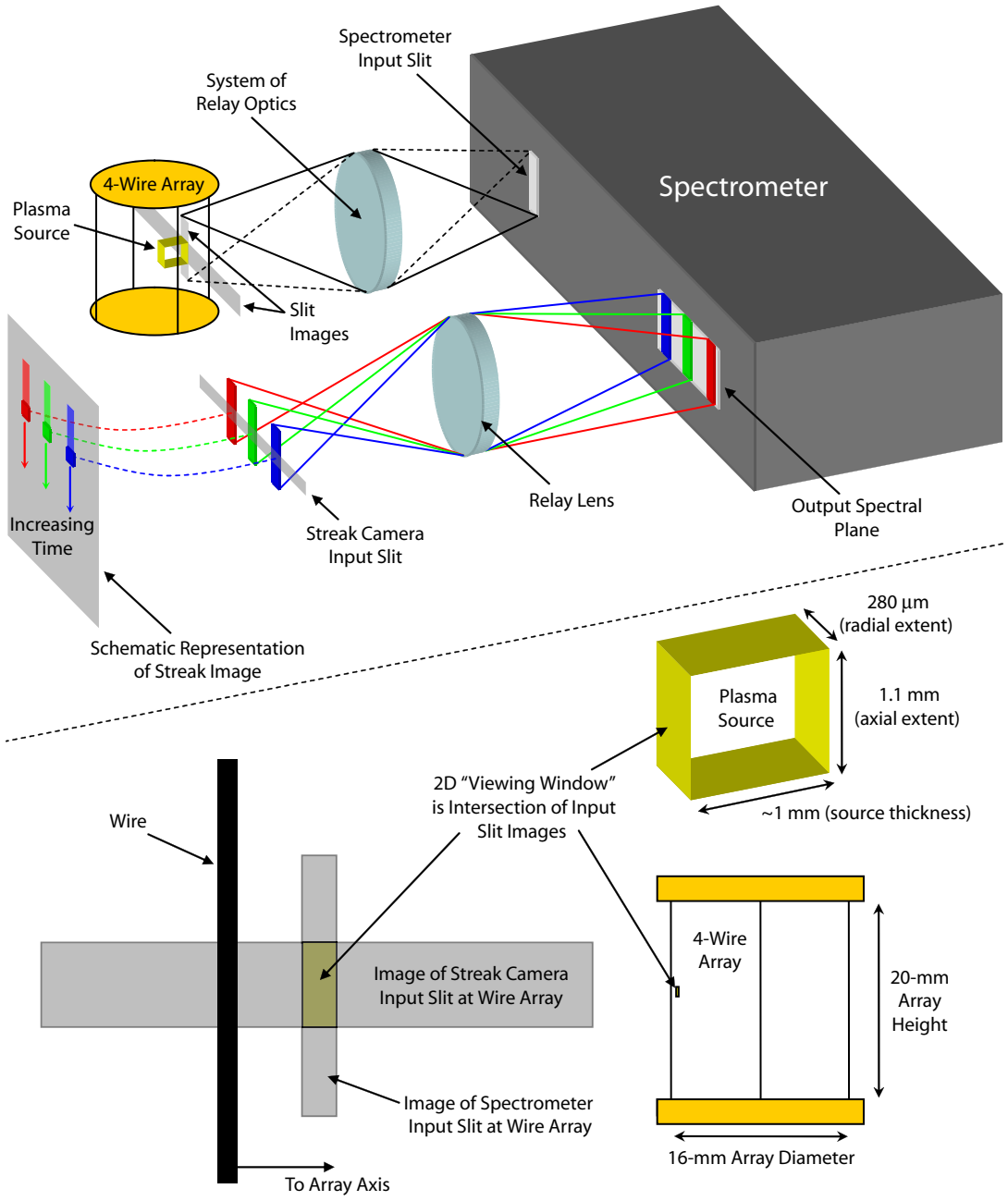

Figure 6.1: (Color) Illustration of setup for streaking visible-light spectra.

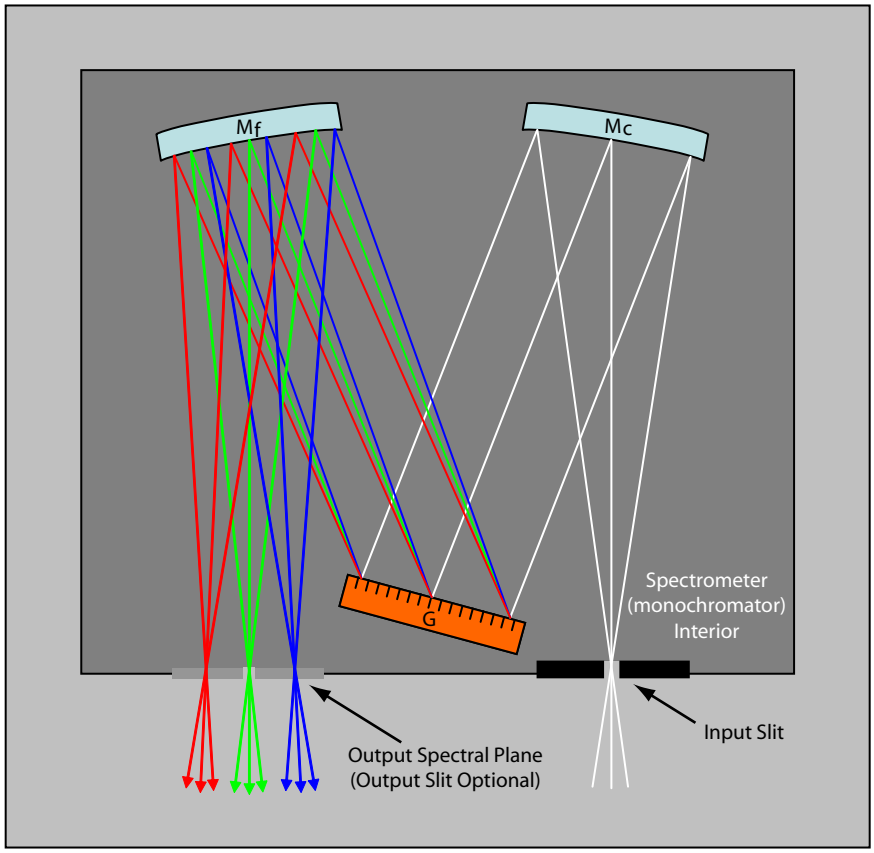

Figure 6.2: (Color) Graphic of the Czerny-Turner spectrometer configuration illustrating the working principles.

spectrum would appear. Thus, two ways around this are to (1) use more wires, thereby reducing the current per wire, and (2) use thinner wires so that wire breakdown occurs earlier ($\lesssim$20 ns), where the total load current is still $\lesssim$100 kA. This was later attempted, the results of which are shown in Fig. 6.4, where a 16-wire array was tested and 12 μm wire-diameters were used.

In Fig. 6.4, we see that the wire breakdown indeed occurs earlier in time (around 10-15 ns) and at much lower current per wire (<10 kA per wire). However, we still don't observe much light until around 40–50 ns. And this light seems to turn on more gradually, as opposed to an abrupt turn-on when the

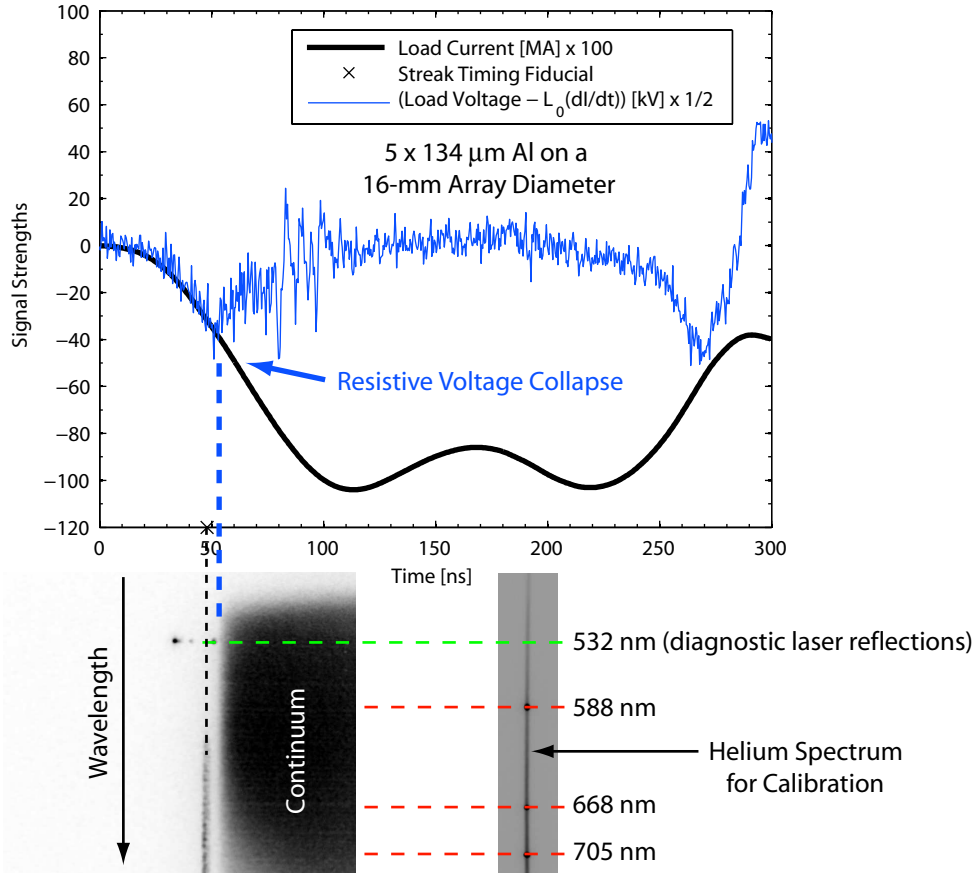

Figure 6.3: (Color) Spectral streak revealing only continuum emission.

wire breakdown occurs around 50 ns. So the reasonable assumption that there is light being produced just after breakdown, leads us to the conclusion that the relay optics from the experiment to the spectrometer/streak camera (to be discussed in the next section) are not efficient enough to observe any faint emission that may be present at this time. Thus it is impossible to say from this result whether this load produces useful visible lines in the time range from breakdown (about 15 ns) to the first observance of light (near 40 ns)—or even before breakdown as the aluminum metal is being heated through several phase transitions. It is certainly possible to reconfigure the experimental setup to increase the light-gathering efficiency. However certain precautions must be taken. For

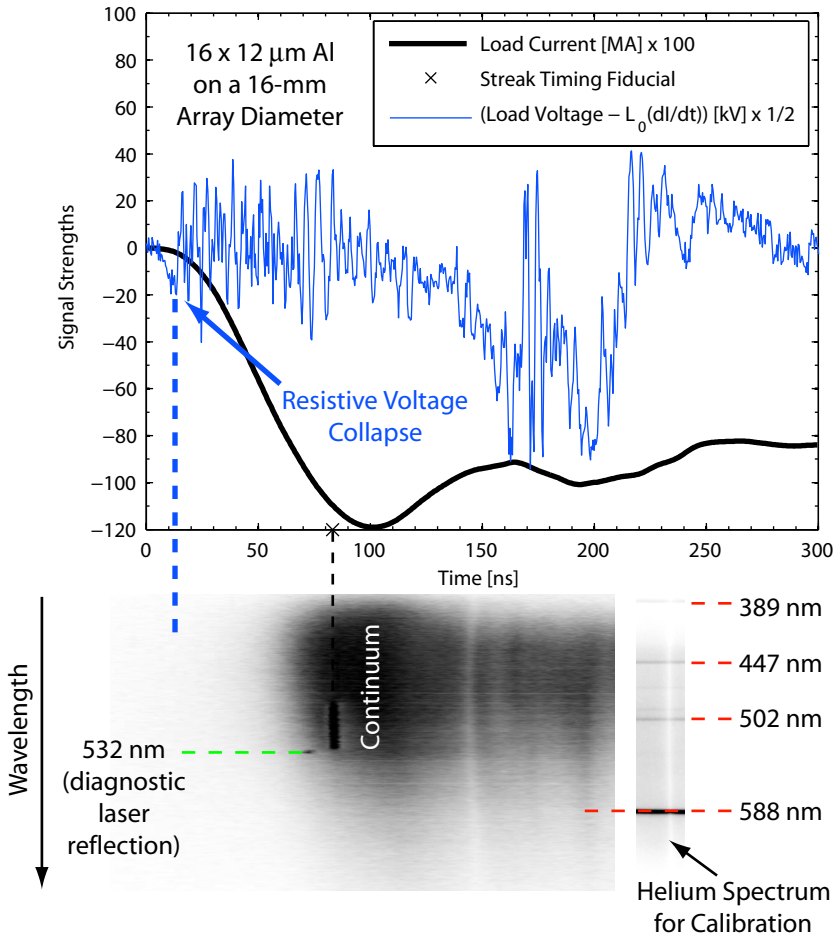

Figure 6.4: (Color) Streak of 16-wire array with 12-μm wire diameters. Resistive voltage collapse occurs earlier in the current pulse and at less current per wire than the experiment shown in Fig. 6.3, but still only continuum emission is observed.

example, if the gain is increased to a level sufficient to observe faint emission from 0 to 40 ns, then care must be taken to stop recording light on the streak camera before the intensity increases near 40 ns, as the intensity after 40 ns will surely saturated the camera. (Note: Saturating the streak camera can burn the image intensifier and/or ruin the streak tube, which must be avoided as these components are very sensitive and very expensive to replace.)

Increasing the light gathering efficiency for earlier time measurements,

where breakdown occurs earlier and with less current per wire, would certainly be worth investigating in the future. However, the path taken instead was to collect more continuum data with the intention of analyzing this data to determine electron density as a function of time. This route however required an absolute calibration of the entire system. Thus we needed to account for absolute sensitivities and efficiencies as a function of wavelength for all elements in the system, including the relay optics, the spectrometer, and the streak camera detector. In the next section, we describe the experimental setup and system used for these continuum experiments, followed by a section describing the steps taken to calibrate the system absolutely.

6.1 Experimental Setup & System

For these experiments, an axial slice (parallel to the wires) was imaged onto the input slit of the spectrometer (see Fig. 6.1). The spectral plane at the output of the spectrometer was then imaged onto the input slit of the streak camera. The input slit to the spectrometer and the input slit to the streak camera were oriented perpendicular to one another. This was done so that the spectral dimension ran parallel to the streak camera input slit, and so that the axial slice being imaged (at any given wavelength) was also oriented perpendicular to the streak camera input slit. In effect then, the streak camera input slit acts to crop the imaged slice down to a much smaller rectangle. This small rectangle is dispersed over the selected range of wavelengths along the streak input slit and swept as a continuous function of time.

The small rectangle that is imaged is of course our light source. Since the final streak image contains no spatial information (i.e., the streak image is wave-

length vs. time), we must assume the light emission across our source to be constant, and take the size of the rectangle as our spatial resolution (we therefore want this rectangular "viewing window" to be small). The spatial resolution in the radial dimension of the array is thus controlled by (1) the magnification of our image at the spectrometer input slit and (2) the size of the spectrometer input slit. Similarly, the spatial resolution in the axial direction of the array is determined by (1) the magnification of our image at the streak camera input slit (constant for all wavelengths), and (2) the size of the streak camera input slit. For the experiments reported here, the spectrometer input slit was set to 10 μm, and the image magnification at the spectrometer input slit was $\approx$0.0357, giving our viewing window a radial extent of

$$\text{radial resolution} = \frac{\text{spectrometer slit width}}{\text{magnification to spectrometer}} \approx \frac{10\ \mu\text{m}}{0.0357} \approx 280\ \mu\text{m}.$$

Likewise, the streak input slit was set to 50 μm, and the image magnification at the streak input slit was 0.0460, giving our viewing window an axial extent of

$$\text{axial resolution} = \frac{\text{streak slit width}}{\text{magnification to streak}} \approx \frac{50\ \mu\text{m}}{0.0460} \approx 1.1\ \text{mm}.$$

For analysis of the spectra, the depth of the viewing window must also be known. In our case these depths change with time, but were roughly determined by the size of the coronal plasma surrounding the wires in laser shadowgraph and XUV framing camera images (usually on the order of 1 mm for the times of interest—however this will be discussed more later). Also, the choice of a 50-μm streak camera input slit results in $\lesssim$2-ns temporal resolution for our 200-ns sweep speed and $\lesssim$5-ns temporal resolution for our 500-ns sweep speed (the only two speeds used during these experiments).

The magnifications that are largely responsible for our spatial resolution are the result of the relay optics from the source to the spectrometer, and then from

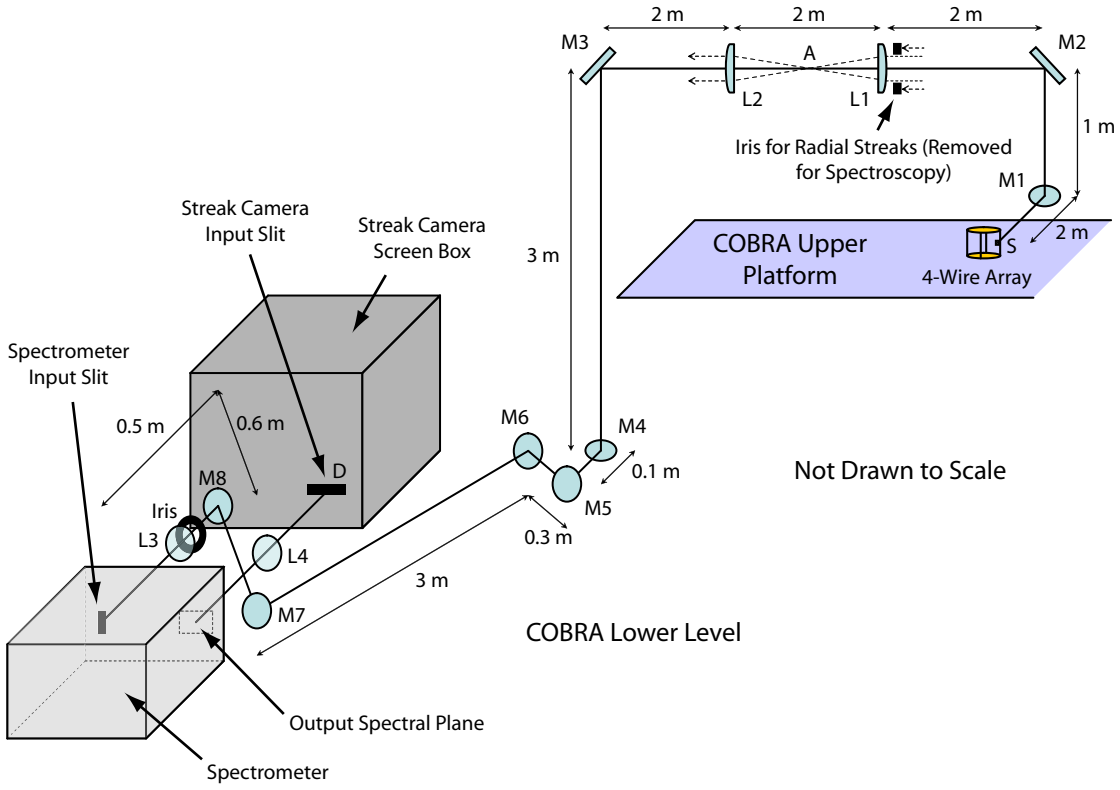

Figure 6.5: (Color) Illustration of relay optics from source to spectrometer, and from spectrometer to streak camera.

the spectrometer to the streak camera. In our case, the design of the segment from the source to the spectrometer was largely constrained by the physical location of the streak camera (and thus the spectrometer) relative to the experiment chamber. Figure 6.5 illustrates this segment, where the path from the source S through to mirror M6 is unchanged from the standard radial streak setup. This allowed easy back-and-forth conversion from one setup to the other. Mirror M7 was slightly repositioned off the input axis into the streak camera to allow light from the spectrometer to pass directly on into the streak camera. M8 was then added, and centered on the input axis of the spectrometer. The lens L3 was then chosen to match certain requirements to be discussed below. These re-

quirements are in part, however, related to matching the input light cone to the acceptance angle of the spectrometer. This technique is commonly referred to as f-number matching, where the f-number (or $f/\#$) is defined as the focal length of an element f divided by the numerical aperture NA of the element [75]. For example, if a light source fills a 50-mm-diameter lens that has a usable diameter of 45 mm, the numerical aperture will then be about 45 mm. If the lens has a focal length of 150 mm, and the light source that fills the lens is collimated (i.e., parallel rays), then the light will be focused 150 mm from the lens. Thus the $f/\#$ of this system is

$$f/\# \equiv \frac{f}{NA} = \frac{150}{45} = 3.3. \tag{6.1}$$

The odd thing about dealing with $f/\#$'s, however, is that this $f/\#$ of 3.3 would be written as $f/3.3$. In other words, care must be taken to not confuse the dimensionless number 3.3 below the slash symbol ('/') with the numerical aperture of the system (which in our example here is 45 mm).

For the Czerny-Turner spectrometer (see Fig. 6.2), the element that determines the input $f/\#$ is the spherical collimating mirror M_c, where the NA is effectively the width or diameter of this mirror, and the focal length is the distance from the input slit to the mirror. This mirror is responsible for collecting the diverging light that entered through the spectrometer input slit, and collimating it so that the collimated beam can uniformly illuminate the grating G. Thus, if the effective $f/\#$ of the light entering the spectrometer is less than the $f/\#$ of the spectrometer, then the light will overfill the collimating mirror in the spectrometer, and light will be lost. If the effective $f/\#$ of the light entering the spectrometer is greater than the $f/\#$ of the spectrometer, then the collimating mirror will be underfilled, therefore underfilling the grating, and hence decrease the spectral resolution of the system (the fundamental resolving power of a grating

is determined by and defined as the number of grooves illuminated). Ideally, one would like perfect $f/\#$ matching, however, we will see in a moment that underfilling the collimating mirror, and hence underfilling the grating, serves an important practical purpose in our case, which is fine since we did not need the maximum spectral resolution of the rather large grating used.

Typically, the Czerny-Turner configuration is symmetric, in that the output half, or the segment from the grating to the output spectral plane is basically a mirror image of the input half, or the segment from the input slit to the grating. The grating is the dispersive element responsible for separating the collimated beam into its various spectral components. The light dispersed by the flat reflection grating is thus a series of collimated light beams, one for each spectral component, and with each beam coming off the grating at a slightly different angle. This angle, β (measured with respect to the grating normal), for a given wavelength, λ, depends on the linear groove density of the grating n (i.e., the number of grooves per unit length), and can be determined from [75]

$$\sin\alpha + \sin\beta = 10^{-6} kn\lambda, \tag{6.2}$$

where α is the angle of the incident light (again measured relative to the grating normal), k is the reflection order number (we will always be using first order reflection so that $k = 1$), and where n is in [grooves/mm], and λ is in [nm]. The deviation angle, D_v, is defined as the difference between the angles of reflection and incidence (i.e., $\beta - \alpha$), and is a constant for the center wavelength in a Czerny-Turner spectrometer [75]. [Note: It is important to keep the sign of the angles consistent. That is to say, the grating normal is defined as zero degrees (or radians), with one side of this normal defined as positive angle values and the other side negative. For example, if the incident light is on one side of the normal, and the outgoing light is on the other, then one of the two angles will be

positive and the other will be negative, and thus the deviation angle, D_v, will be the sum of the magnitudes of the two angles. Alternatively, if they are both on the same side of the normal, then they will both be positive or both be negative, and D_v will be the magnitude of the difference of the two angles. Unlike with a simple mirror, this scenario of both being on the same side of the normal can actually happen with a reflection grating, and hence the importance of being consistent with your sign convention.]

The dispersed light columns are then collected by the focusing mirror M_f, and focused onto the spectral plane at the output of the spectrometer. The focused light produces images of the input slit in its various spectral components—or colors since we are talking about visible wavelengths (see Figs. 6.1 and 6.2). The focal length of the spectrometer is defined as the focal length of the output focusing mirror (which, for the Czerny-Turner configuration, typically has the same focal length as the input collimating mirror—as was the case for our spectrometer). In addition to establishing the output $f/\#$ of the device, the output focal length also determines the absolute dispersion of the instrument (along with the grating groove density). This is because the dispersed light comes off the grating at various angles. Consider for example two spectral components coming off the grating at two different angles. The longer the physical distance from the grating to the spectral plane (which is about twice the focal length of the focusing mirror in a Czerny-Turner spectrometer—see Fig. 6.2), the greater the physical separation of the two spectral lines at the spectral plane (where again these two lines are the focused images of the spectrometer input slit in the two different colors). The bottom line is: the longer the spectrometer focal length, the greater the instrument dispersion.

For these experiments we used a Lambda Minuteman 305-M half-meter monochromator with the output slit removed, thus converting the instrument to a spectrometer (or polychromator). The "half-meter" indicates that the instrument focal length is 500 mm (in our case this goes for the focal length of the input collimating mirror as well). Both spherical mirrors were 60-mm wide by 60-mm tall. Thus the instrument's input and output $f/\#$'s were $\approx$8.3. Also, we used this spectrometer with a 60-mm wide by 60-mm tall grating. Thus it seems we should be able to select our input optic (i.e., lens L3 in Fig. 6.5) simply by matching the $f/\#$'s and available lenses. However, there is a subtlety in using a monochromator as a spectrometer, and that is the output focusing mirror is the same size as the grating and input collimating mirror. This works fine for a monochromator as a fully-filled grating will fully fill the focusing mirror for the one wavelength of interest. (A monochromator incorporates an exit slit at the spectral plane to select only the light from the center wavelength.) However, all wavelengths other than this center wavelength will partially miss the focusing mirror, and increasingly so the greater the difference between a given wavelength and the center wavelength. By partially missing the focusing mirror, we will be loosing light as a function of wavelength. The analysis of our spectra (to be discussed later) requires an absolute accounting of all photons. Loosing them is okay, as long as we can account for them. But accounting for lost photons due to partially missing the focusing mirror as a function of wavelength is somewhat cumbersome and, as it turns out, completely unnecessary. By simply underfilling the collimating mirror and grating, we gain more clearance on the focusing mirror. To explain the design choice actually made for lens L3 in Fig. 6.5 (i.e., the amount of fill/underfill chosen), we first need to explain some more subtleties about the entire system (we will come back to this issue

later when the design choices are presented).

After the focusing mirror, the light of a given color converges and is focused onto the output spectral plane, producing an image of the spectrometer input slit in that color. After the focal plane the light begins diverging. To map the spectral image at the output plane of the spectrometer onto the input slit of the streak camera, we must use a relay optic to collect the diverging light, and refocus it onto the streak input slit. Considering the angle of the diverging light cone at the output of the spectrometer, one might once again be tempted to only consider the $f/\#$ for selecting the appropriate relay optic. However, once again the subtleties of using a spectrometer as opposed to a monochromator must be considered carefully (especially when requiring an absolute accounting of all photons).

The technicality arises from the fact that the spectral image at the output plane of the spectrometer is not an isotropically radiating source. Rather it is a anisotropic source with an angular dependence on wavelength (i.e., the axis of each diverging light cone is coming out of the spectrometer at a different angle, and from a different position on the spectral plane—see Fig. 6.2).

All of this would be okay if we were using an output slit (i.e., monochromator mode). Then we would only be concerned with the one center wavelength (i.e., a single light cone and its axis), and therefore simple $f/\#$-matching would suffice. However, in our spectrometer case, if we simply $f/\#$-match the spectrometer input optics (i.e., fill the grating) and $f/\#$-match the output optics to the device's $f/8.3$, then we are guaranteed to loose light not only because of missing the focusing mirror inside the spectrometer, but also because of missing the relay optic L4 (see Fig. 6.5). Another way of looking at this is that the

dispersion of the device effectively decreases the required output $f/\#$. If we choose the spectrometer input optic L3 such that we underfill the grating, then matching L4 to $f/8.3$ might be okay (hence another good reason for underfilling in our case), but it is certainly not okay to match L4 to an effective $f/\#$ defined as the spectrometer focal length divided by the spot-size of the underfilling light on the focusing mirror (although this would again be okay if using an output slit). Regardless, the bottom line is that more careful analysis is required.

With all of the issues above taken into consideration, an experimental system was designed. This design also had to take into account numerous unavoidable constraints such as the diameters and focal lengths of available optics, the relative physical placements of the spectrometer and streak camera, light paths, and so on. The design process was iterative, and thus not all decisions can be presented here in a linear, sequential fashion (i.e., one choice led to the next choice, which led to the next, etc.). Many choices were fed back to alter earlier choices and this process continued repeatedly for many cycles until an acceptable system was obtained. For this process it was beneficial to make use of some simple computer code for quick calculations and recalculations. Examples of such calculations are included as Appendix C.1. Here the Mathematica notebook actually used to select the grating and relay optic L4 is shown. The output displaying the calculated results is also shown.

In an attempt to describe the design process as clearly as possible, we begin with our choice of lens L3, the input optic to the spectrometer. Due to the space constraints between the spectrometer and the streak camera screen box (about 600 mm between the two—see Fig. 6.5), choosing and placing an available optic that accomplishes certain necessary tasks becomes tricky. The first

and most important requirement for an optic is that it actually focuses at the desired location. Thus for lens L3, we need the light to be focused on the input slit of the spectrometer, and we need to place the optic on the input axis of the spectrometer. Since we also need a mirror prior to L3 (in order to align the light onto the input axis), and since some room for focal adjustment is desirable, we would like to place the lens no more than about 300–350 mm from the input slit. (Note: We could use a mirror to redirect the light coming out of L3 onto the input axis and thus free up more room for placing L3, but this is undesirable for practical alignment and focusing reasons. Plus it does not actually free up much more room as the optical path going from the spectrometer output to the streak camera input must be avoided—see Fig. 6.5.)

Due to the magnification caused by optics L1 and L2 in Fig. 6.5 (relaying the light from the experiment chamber to L3), the light just prior to L3 is essentially composed of parallel rays that fill the preceding 50-mm-diameter mirror (M8). With the need to focus the light in about 325 mm or less, the use of the entire 50-mm diameter will result in $f/6$, thus overfilling the spectrometer's collimating mirror and grating. Moving the lens closer to the spectrometer will only make matters worse, therefore it was desirable to place L3 near our constrained maximum of about 325 mm. As just stated, however, using the full 50-mm from this distance will still overfill the collimating mirror. To avoid this we simply use an iris to aperture-down the lens and achieve the desired level of underfill. This loss of photons is okay, since it is a geometric loss that we can easily determine at one wavelength and apply to all the rest (i.e., the fraction of photons lost is constant for all wavelengths, unlike the aforementioned losses due to dispersion).

Now since the rays approaching L3 are nearly parallel, we can choose a lens with a focal length approximately equal to the distance we want to place L3 from the spectrometer input slit. Doing this, we chose a 50-mm-diameter lens with a 300-mm focal length for L3, and placed it approximately 320 mm from the spectrometer input slit. After some consideration on how much of a spectral bandwidth we wanted to view (to be discussed shortly), an iris diameter of 25.5 mm was chosen. This resulted in a conservative underfilling, where about 65% of the collimating mirror and grating surfaces were illuminated.

The next element along the light path that needed to be selected was the grating (see Fig. 6.2). Again, bandwidth considerations dominated our decision (i.e., spectral resolution for continuum measurements is not of the utmost importance). We desired more bandwidth, therefore less dispersion, and hence a lower groove density. Our choice was a grating with 100 grooves/mm. And with our chosen level of underfill, nearly 4000 grooves were illuminated (thus our resolving power was nearly 4000).

The linear dispersion of a spectrometer is the change in wavelength per change in linear position at the output spectral plane, and is given by [75]

$$d\lambda/dx = \frac{10^6 \cos\beta}{knL_B} \quad [\text{nm/mm}], \tag{6.3}$$

where L_B is the exit focal length of the spectrometer in [mm]. We don't actually need to determine β in this case; instead we can simply make use of the instrument manual. The manufacturer specification for our 305-M is 1.67 nm/mm, but this was determined using $n = 1200$ grooves/mm. Therefore $d\lambda/dx = C/n$ where C is a constant that lumps together the device-dependent parameters above, and for the 305-M, $C = 1.67 \times 1200 = 2004$ nm$\cdot$ grooves/mm^2. Thus, for our 100-grooves/mm grating, $d\lambda/dx = C/n = 2004/100 = 20.04$ nm/mm. For our

design purposes, the reciprocal linear dispersion is more useful, and

$$dx/d\lambda = 1/20.04 = 0.05 \quad \text{mm/nm}. \tag{6.4}$$

With all design requirements considered, we decided that a spectral bandwidth of approximately 250 nm was a reasonable goal, which would almost cover the entire visible spectrum from 400 to 700 nm. Using the reciprocal linear dispersion (Eqn. 6.4), we have $250 \times 0.05 = 12.5$ mm. Thus our spectrum will be 12.5 mm wide at the output plane of the spectrometer.

We next need to map this spectral image onto the input slit of the streak camera. The streak camera slit length is 25 mm. However, if the image of the photocathode at the streak camera input slit does not fully span the slit length, then it is the extent of this image that actually matters. The manual states that the photocathode is 17 mm, and that the streak camera's internal relay optics have a magnification ratio of 1:1. Thus our usable slit length is 17 mm. Since we do not want to run the risk of losing any photons off one of the sides of the photocathode, we will design our system assuming that our photocathode is at most only 15 mm. Therefore or first selection criteria for our relay optic L4 is that we map a 12.5-mm image at the spectral plane of the spectrometer to a 15-mm image at the input slit of the streak camera (i.e., a desired magnification of 1.2).

Given the discrete selection of available lens focal lengths, this mapping is effectively a 1:1 magnification. Therefore since the magnification is $s_2/s_1 = 1$, where s_1 is the distance from the spectrometer output plane to the lens, and s_2 is distance from the lens to the streak camera, clearly $s_1 = s_2$. The thin-lens equation, $1/f = 1/s_1 + 1/s_2$, where f is the lens focal length, states that with $s_1 = s_2 \equiv s$, $1/f = 2/s \rightarrow f = s/2$. Now, the quasi-fixed distance between

the output plane of the spectrometer and the input slit of the streak camera is approximately 608 mm, thus $2s = 608 \rightarrow s = 608/2$, and therefore $f = s/2 = 608/4 \approx 150$ mm. A focal length of 150 mm is nice because it is readily available from retailers.

Things are even better than they seem. The calculated focal length of 150 mm was only rounded to the nearest available focal length. If we plug $f = 150$ mm back into the thin lens equation holding $s_1 + s_2 = 608$ mm, we get two solutions: $s_{1(2)} = 267$ mm and $s_{2(1)} = 341$ mm, thus there are two positions that will focus the image, one with a magnification of $267/341 = 0.78$ and one with a magnification of $341/267 = 1.28$. Since we were originally seeking a magnification of 1.2, we're in luck. Thus we choose a lens with a 150-mm focal length and position it about 267 mm from the spectrometer output plane (i.e., 341 mm from the streak input slit).

Another benefit of the 150-mm focal length is that most major retailers stock this focal length with the option of a larger 50-mm diameter (i.e., for common focal lengths, the 50-mm diameter is typically the largest available from a retailer without having to make a custom/expensive order). We want the largest available diameter to avoid loosing dispersed light off the sides of the lens (we will check to make sure our system clears this criterion shortly). Now, with the choice of a 50-mm diameter (with about a 45 mm usable) and a 150-mm focal length for L4, our minimum possible $f/\#$ is $150/45 = 3.3$. Checking the streak camera manual assures us that we won't loose any photons once they enter the streak camera as the input optics have a wide acceptance angle of $f/1$.

Now that we have selected our components, we must make sure this design does not loose any photons as a function of wavelength at the focusing mirror

in the spectrometer and at the relay lens L4 (this was of course done prior to purchasing any components). To do this, we will refer to Fig. 6.6, where we have labeled all of the design values chosen above. For our desired range of wavelengths (i.e., about 250 nm), the lower bound is represented by the blue rays, the upper bound by the red rays, and the center wavelength is represented by the green rays.

For this discussion, it is useful to calculate the transverse separation between the optical axes of two colors Δx per unit longitudinal length from the grating Δy. We will take these two colors to be the center wavelength and one of the end wavelengths (i.e., a difference of 125 nm). Since the system is symmetric about the center wavelength, it doesn't matter which end wavelength we choose, and we only need to do the calculation once. From our discussion of linear dispersion, we know that a spectral width of 250 nm is equivalent to a spatial width of 12.5 mm at the output spectral plane. Therefore we know that a wavelength difference of 125 nm will be a spatial width of 6.25 mm at the output spectral plane. We also know that the distance from the grating to the output spectral plane is about 1000 mm (see Figs. 6.2 or 6.6). Thus,

$$\xi_{125nm} \equiv \frac{\Delta x}{\Delta y} = \frac{6.25 \text{ mm}_{\text{trans}}}{1000 \text{ mm}_{\text{long}}} = 0.00625 \text{ [mm}_{\text{trans}}/\text{mm}_{\text{long}}] \tag{6.5}$$

Now let's make sure that no light from our desired bandwidth of 250 nm misses the focusing mirror in the spectrometer. We first align the center wavelength to be in the middle of the focusing mirror, and define this central position as $x = 0$. Therefore we want to find the distance from $x = 0$ to the optical axis of one of the end wavelengths. The distance from the grating to the focusing mirror is about 500 mm (see Fig. 6.2), thus the spatial separation between the two optical axes at the focusing mirror is $\xi_{125nm} \cdot 500 = 3.125$ mm. Hence, if our center wavelength is 525 nm (positioned at $x = 0$), then the optical axes of 400 nm and 650 nm are

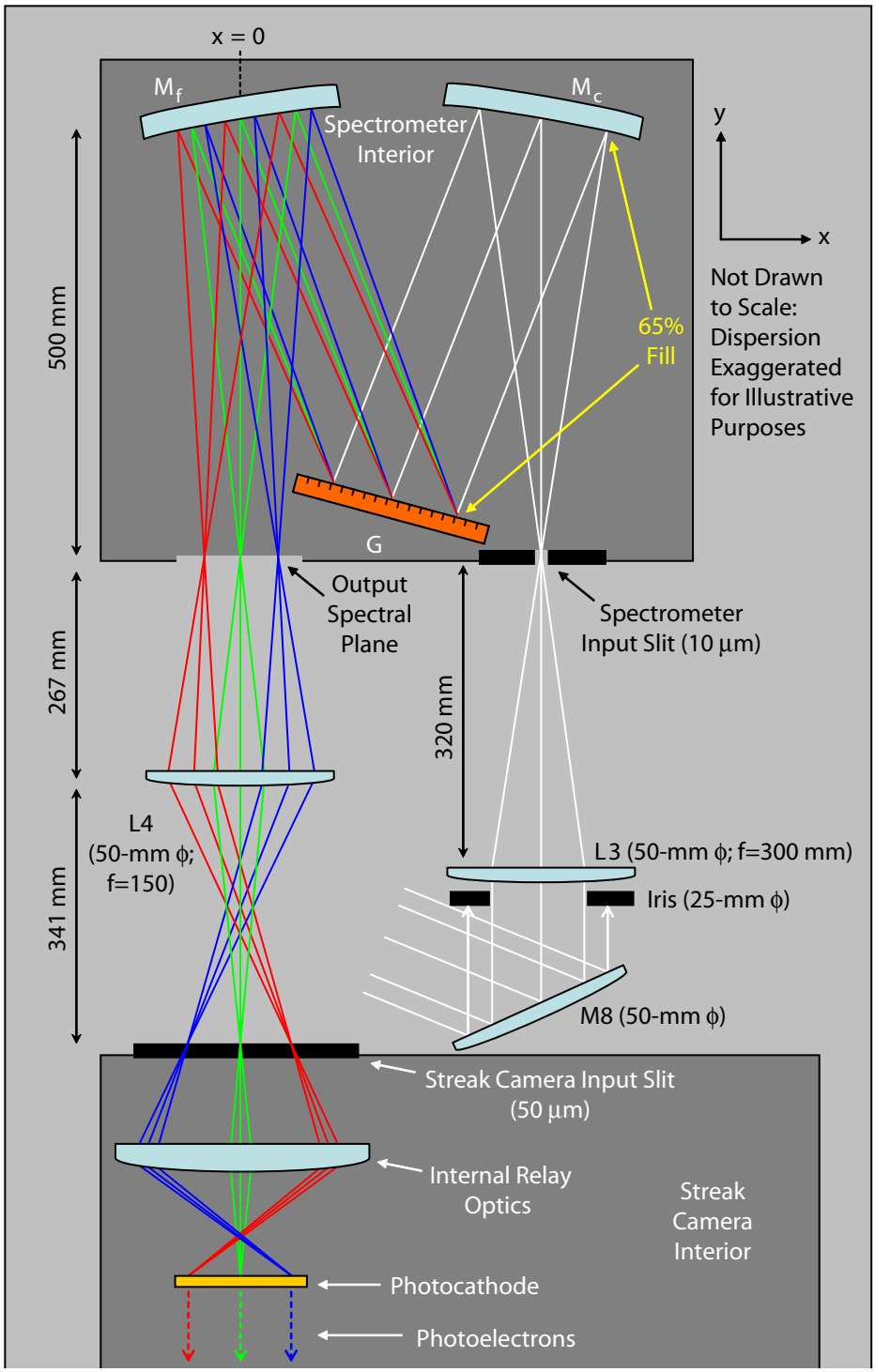

Figure 6.6: (Color) Geometrical illustration of the light paths through lens L3 of Fig. 6.5, through the spectrometer to lens L4 of Fig. 6.5, and on into the streak camera (top-down view).

positioned at $x = \pm 3.125$, respectively.

At this point we have only calculated the positions of the *axes* of the collimated beams. The spot size of these collimated beams is, due to our iris setting and associated underfill, about 40 mm. Thus, due to the dispersion, we will actually be using about 46 mm of the focusing mirror's 60-mm width. Clearly we are in no danger of loosing any photons due to missing the focusing mirror. However, we still need to make sure that photons do not miss the relay lens L4.

From Fig. 6.6, we see that the distance from the grating to the relay lens L4 is about 500 + 500 + 267 = 1267 mm, and therefore the optical axis separation between the center wavelength and either of the end wavelengths is $\xi_{125nm} \cdot 1267 = 7.9$ mm. Again, this is only the separation between the optical axes; the spot size must still be considered. In this case though, the spot size is not constant (as it is for the collimated beams going from the grating to the focusing mirror). Instead, the spot size of a given color is focused down to a 1:1 image of the spectrometer input slit at the spectral output plane. After the output plane, the spot size begins expanding as the now divergent rays defocus. This expansion occurs until the rays are (hopefully) intercepted by the relay lens L4.

To calculate the spot size at L4, we note the simple geometrical relationship of the converging and diverging light cones. Essentially, the focal point acts as the pinhole in a pinhole camera (with a different pinhole for each color). Thus the spot of a given color on the focusing mirror is imaged to a corresponding spot on L4 with a magnification of $y_2/y_1 = 267/500 = 0.534$. Since the spot size of any color on the focusing mirror is about 40 mm wide (due to our iris/underfill), the corresponding spot size on L4 is $40 \times 0.534 = 21.4$ mm.

With spot sizes and axes displacements known, we can now answer whether all of the light from the end wavelengths will be intercepted by L4. The radius of the spots in any color is 21.4/2 = 10.7 mm. Since the center wavelength shares an optical axis with the lens L4, we know that the axis of an end wavelength must be 7.9 mm from the L4 axis. Thus the spot edges of the end wavelengths will be 10.7+7.9 = 18.6 mm from the L4 axis. Therefore we need our lens to have a usable diameter of at least 18.6×2 = 37.2 mm. Since our 50-mm-diameter lens has an usable diameter of 45 mm, we are safe, and no photons will be lost.

[Note: What we have essentially done is $f/\#$-matched the relay lens to the spectrometer output while accounting for the diverging optical axes of the different colors. If we were using our 305M as a monochromator, then there would only be a single optical axis, and therefore simple $f/\#$ matching could be used to determine our lens diameter. In our case however, where we are using the 305M as a spectrometer, had we used just simple $f/\#$ matching, we would have gotten an answer that says a lens with a usable diameter of ≥21.4 mm is sufficient, and therefore we might have bought one of the readily available 25-mm-diameter lenses. However, as our desired spectral band requires a usable diameter of 37.2 mm, we clearly would have lost light—and probably without ever knowing it!]

6.2 Absolute System Calibration

The absolute calibration of the system can be considered in two parts. The first was calibrating the segment from the source (i.e., the wire array z-pinch load) to the streak camera input slit (including wavelength dependencies), and the second was calibrating the streak camera detector (again including wavelength

dependencies, but also correcting for streak tube irregularities). In what follows, we will refer to optical components and various focal points by their labels in Fig. 6.5.

6.2.1 Calibration from Source to Detector

The calibration from the wire-array z-pinch load to the streak camera input slit made use of a single-wavelength source [i.e., a 633-nm helium-neon (HeNe) continuous-wave (CW) laser]. Using a convex lens, the laser was focused to a point within the viewing window of our experiment (i.e., the viewing window formed by the intersection of the overlaid images of the streak camera input slit and spectrometer input slit mapped back to the wire-array load region). After the focal spot, the diverging laser light expanded such that mirror M1 was more than fully illuminated, hence assuring that lens L1 was more than fully illuminated. The portion of the diverging laser light that illuminated L1 was selected such that the intensity was approximately uniform across the entire surface of the lens.

With this setup, power measurements were made at focal point A just after lens L1. Due to the 1-m focal length of L1, and to the distance from the source to L1, point A was approximately 1 m after L1. Therefore demagnification led to a very small spot size at A. This spot size was smaller than the sensor area on the power meter, thus allowing the intensity/power of the light collected by L1 to be measured in its entirety.

Power measurements of the 633-nm light were then made at point D, the input slit to the streak camera. Since we were using a single-wavelength source,

no dispersion occurred within the spectrometer, and thus a single spot appeared at D. The spot size at D was again smaller than the sensor area on the power meter, again allowing us to measure the 633-nm intensity in its entirety.

With the previous measurements, we can determine the 633-nm efficiency from A to D. (This assumes that the efficiency remains constant as the position of the laser focal point at the source is varied within our experimental viewing window, which is a fair assumption given the small dimensions of our viewing window relative to the large distances between optical elements). This efficiency was determined to be $\eta_{633,AD} = 0.0335$.

So far, however, we have only resolved the efficiency at 633 nm. To get the efficiency as a function of wavelength, we acquired wavelength-dependent data from the manufactures of each component in the system. For the components after lens L1 to the input of the streak camera (i.e., just after lens L4), we used manufacturer data for aluminum mirror reflectivities as a function of wavelength and incident/reflected angle, first-order grating reflectivity as a function of wavelength and deviation angle, and lens transmissions as a function of wavelength. Specifically, this segment from just after L1 to just after L4 consisted of four aluminum mirrors with 45° angles, two aluminum mirrors with about 8° angles, two MgF_2-coated aluminum mirrors with about 8° angles (in the spectrometer), one 100-groove/mm grating with a 21-degree deviation angle, and three lenses. (For clarity, a 45° angle of incidence and/or reflection results in a 90° redirection of the optical path. Likewise, an 8° angle of incidence/reflection results in a 164° redirection of the optical path.)

For each of the individual components, the manufacturer-supplied wavelength-dependent data was in terms of absolute efficiency. Therefore we

normalized these efficiency data to their respective values at 633-nm. Thus, our system's total wavelength-dependent efficiency from the focal point just after L1 to the detector input was

$$\eta_{AD} = \eta_{633,AD} \cdot \eta^{4}_{633,45^\circ-Al} \cdot \eta^{2}_{633,8^\circ-Al} \cdot \eta^{2}_{633,45^\circ-MgF_2-Al} \cdot \eta_{633,G_{21^\circ-D_v}} \cdot \eta^{3}_{633,L}. \tag{6.6}$$

To get the efficiency from the source to L1, we first need to make some assumptions about the source. For our purposes, we assume that the source is an isotropic radiator, and thus the radiation expands uniformly into 4π steradians. Since the lens is 5.13 m from the source, S, and since the lens has a usable diameter of 45 mm, the geometric efficiency of the isotropic radiator into the optical system is

$$\eta_{4\pi R,SA} = \frac{\pi(45/2)^2}{4\pi(5130)^2} = 4.8 \times 10^{-6}. \tag{6.7}$$

Again, we need to account for wavelength-dependence, and for this segment, we have two 45-degree-aluminum mirrors, one lens, and the experiment chamber window (1/4" plate glass). However, in this case, since we are using a geometrical argument as opposed to a measured power at 633 nm, we must use the absolute efficiencies for each component as opposed to efficiencies normalized to their respective values at 633 nm. Thus,

$$\eta_{SA} = \eta_{4\pi R,SA} \cdot \eta^{2}_{45^\circ-Al} \cdot \eta_{L} \cdot \eta_{plate-glass}. \tag{6.8}$$

Finally, the total wavelength-dependent efficiency from the source to the detector is:

$$\eta_{SD} = \eta_{SA} \cdot \eta_{AD}. \tag{6.9}$$

The MATLAB code for implementing these calculations is included as Appendix C.2.1.

6.2.2 Calibration of Streak-Camera Detector

The streak camera stores images in tagged image file format (i.e., *.tif files). These images have a resolution defined by 1024 pixel rows in the vertical/time direction, and 1280 pixel columns in the horizontal/wavelength direction. Therefore, our streak images can be thought of as 1024×1280 matrices (thus the appropriateness of MATLAB), and we will denote the pixel row by the index i and the pixel column by index j. Depending on the light intensity, each pixel can take a value between approximately 500 and 16,384 (see Note 2 below). Also, the streak camera's system response to various intensity levels at a single wavelength is stated to be linear by the camera's manufacturer, Hamamatsu. Thus a linear intensity response has been assumed for the calibration procedures below.

To calibrate the intensities on the streak images, we needed to determine the number of photons responsible for a given pixel value, and we needed to do this for each wavelength. Additionally, to calibrate our wavelength and time scales, we needed to correct for streak aberrations that lead to wavelength drift as a function of time (i.e., a slight curvature to lines that represent constant position/wavelength, and that are ideally vertical in the streak images) and to the curvature of lines representing constant moments in time (i.e., lines that are ideally horizontal in the streak images). For simplicity, we will look at each task separately, and put them together in the end.

[Note 1: All calibration procedures to be described below were repeated at least three times—once for each of the three different streak camera setups used. The various setups were denoted by Roman numerals in the calibration data files and MATLAB codes—Roman numeral I represents a 200-ns streak with an im-

age intensifier gain of 213 (control software setting of 35); Roman numeral II represents a 200-ns streak with an image intensifier gain of 700 (control software setting of 45); and Roman numeral III represents a 500-ns streak with an image intensifier gain of 361 (control software setting of 40). Moreover, the procedures solely related to wavelength calibrations were repeated additional times to account for the three different grating positions used in the continuum experiments. These repetitions were denoted by uppercase A, B, or C in the calibration data files and MATLAB codes, and represent wavelength selector settings of 37.45 nm, 33.45 nm, and 35.00 nm, respectively, on the 305-M spectrometer used in these experiments.]

[Note 2: Although these streaks are saved as unsigned 16-bit images, only 14 of the 16 bits are accessible (i.e., the maximum pixel value is $2^{14} = 16,384$, not $2^{16} = 65,536$). Also, one might assume that zero input photons leads to a pixel value of zero. However, the lower limit of approximately 500 means that zero input photons is actually represented by a pixel value of about 500. This was verified by null tests, where streaks were taken with the shutter on the input slit closed. With these null tests, an individual pixel could have a value slightly less than 500 (perhaps 490 or so), but on average the values were either 503 or 504 (depending on the image intensifier gain and streak speed used). This lower limit is an offset that must be subtracted from *all* images before *any* calibration processing is done. If this offset is not subtracted first, then raw, uncalibrated pixel values will not scale properly to calibrated pixel values. In fact, this lower offset was only discovered after having difficulties getting various calibrations to scale properly (i.e., to the author's knowledge, this lower limit is not mentioned anywhere in the streak camera manuals). The MATLAB code for computing and writing the zeroing to be used for each setup is included as

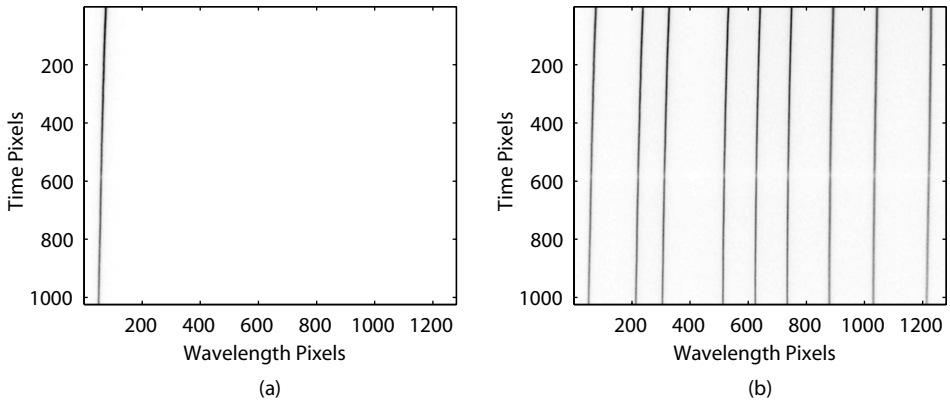

Figure 6.7: (a) Single streak image of CW HeNe laser source focused onto streak input slit. (b) Sum of all calibration streak images showing all calibration locations.

Appendix C.2.2.]

6.2.3 Pixel-Value Calibration

The basic idea of the pixel-value calibration is to streak a known flux of photons. To do this, we used a CW HeNe laser source, and focused its beam onto the input slit of the streak camera. Since the spot size is less than 1-mm in diameter, and since the streak cathode size is about 17 mm in diameter, the resulting streak image is a bright vertical line, where the line-width is a small fraction of total image width (see Fig. 6.7(a)).

For this procedure, the streak input slit was opened wide to assure that the entire beam was streaked. Thus by monitoring the laser intensity with a calibrated power meter, we were able to determine the number of photons streaked.

The fact that the beam-width has a finite spatial distribution also needs to be accounted for. Typically, laser beam intensity profiles will have a 2D Gaussian

distribution, that is

$$g(x,y) = g_0 e^{-\left[\frac{(x-x_0)^2}{2\sigma_x^2} + \frac{(y-y_0)^2}{2\sigma_y^2}\right]}, \tag{6.10}$$

where $g(x,y)$ is a density in units of photons per second per unit-length-squared. Upon analyzing a 1D line-out across the vertical/streaked laser line, we observe a 1D Gaussian distribution. This can result from a 2D Gaussian having one of its spatial dependencies integrated out, either directly or indirectly. In the case of a streaked image, where we can regard x and y as pixel locations on the image, the y-dependence is integrated out indirectly via the streak's temporal dependence. That is to say, we actually have $g(x,y) \rightarrow g(x,y,t)$ because $y_0 \rightarrow y_0(t) = y_0^i + vt$, where $y_0^i = y_0(t=0)$, and v is the streak speed in pixels per second. In mathematical terms, we have

$$g(x,y,t) = g_0 e^{-\left\{\frac{[x-x_0]^2}{2\sigma_x^2} + \frac{[y-(y_0^i+vt)]^2}{2\sigma_y^2}\right\}}, \tag{6.11}$$

and upon integrating over all time we have

$$g(x) = \int_{-\infty}^{\infty} g(x,y,t)dt \tag{6.12}$$

$$g(x) = \frac{g_0\sigma_y\sqrt{2\pi}}{v} e^{-\frac{(x-x_0)^2}{2\sigma_x^2}} \tag{6.13}$$

where our distribution is now a density measured in photons per pixel-squared (i.e., it is still a density in two spatial dimensions, as only time has been integrated out; it's just that it no longer varies in the y-direction). This makes sense intuitively since the inverse proportionality to v states that, for a faster sweep speed, there will be less photons distributed per pixel. The function $g(x)$ is what we are actually observing when we take a 1D line-out across the vertical laser line in the streak image. For these reasons, the beam profile can be regarded as a 2D Gaussian with reasonable confidence. We will also assume for simplicity that $\sigma_x \approx \sigma_y \equiv \sigma$. We still need a way, however, to relate $g(x)$ above to what we

are measuring with our power meter; we will now show how this can be done, and in so doing, point out an interesting subtlety.

Above we integrated out the y-dependence via the temporal nature of the streak, and the resulting $g(x)$ is measured in photons per pixel-squared (or equivalently, per-unit-length-squared). However, we can also integrate out the y-dependence from the same initial 2D-Gaussian directly, giving

$$\begin{aligned} g^*(x) &= \int_{-\infty}^{\infty} g(x,y)dy && (6.14)\\ &= g_0\sigma\sqrt{2\pi}e^{-\frac{(x-x_0)^2}{2\sigma^2}} && (6.15)\\ &= g_0^* e^{-\frac{(x-x_0)^2}{2\sigma^2}}, && (6.16) \end{aligned}$$

where $g_0^* \equiv g_0\sigma\sqrt{2\pi}$. The difference is that now the resulting $g^*(x)$ is measured in photons per second per unit-length [i.e., the time-dependence remains as it has not been integrated out, but it is no longer a density in two spatial dimensions (only one)]. Noting the subtle difference between $g^*(x)$ here and the $g(x)$ above, we can go further with $g^*(x)$ by integrating out the x-dependence, giving

$$\begin{aligned} I &= \int_{-\infty}^{\infty} g(x)dx && (6.17)\\ I &= g_0^*\sigma\sqrt{2\pi} && (6.18)\\ I &= 2g_0\pi\sigma^2, && (6.19) \end{aligned}$$

where I is the total intensity of the beam measured in photons per second, and thus is the quantity that we are actually measuring with our power meter. So we can re-write the amplitude of the Gaussian in terms of the measured intensity as

$$g_0 = \frac{I}{2\pi\sigma^2}. \quad (6.20)$$

[Note: We actually measured the intensity in watts (i.e., joules per second) with the power meter. However, since we used a single wavelength source (i.e., 633

nm), we determined the equivalent number of photons per second using the fact that there are $h\nu$ joules of energy per photon, where h is Planck's constant, and ν is the frequency equal to c/λ, where c is the speed of light, and λ is the 633-nm wavelength. For these calibration streaks, the laser intensity into the streak camera was about 4.5×10^{-8} W (or 1.4×10^{11} 633-nm photons per second).]

At this point we are confronted by how to calculate σ from our streaked data. There turns out to be a simple solution to this when one realizes the simple Gaussian relationship

$$\sigma = \frac{FWHM}{2\sqrt{2\ln 2}}, \tag{6.21}$$

where $FWHM$ is the full-width-half-maximum of the distribution. This makes for a simple algorithm in our data processing code. First find the peak in the 1D Gaussian by searching across a row of pixels. Then find the pixel locations on both sides of this peak where the pixel value drops to half of the peak pixel value (interpolating as needed). Next count the number of pixels between the two pixel locations, and this is the $FWHM$. Finally, plug the $FWHM$ into Eqn. 6.21 to determine the standard deviation σ. The MATLAB functions for implementing this are included as Appendices C.2.3, C.2.4, and C.2.5. Typically, the data resulted in $FWHM$s of about 10 pixels.

Now, plugging Eqn. 6.20 into Eqn. 6.13 (again, assuming $\sigma_x \approx \sigma_y \equiv \sigma$) we get

$$g(x) = \frac{I}{\sigma v\sqrt{2\pi}} e^{-\frac{(x-x_0)^2}{2\sigma^2}}. \tag{6.22}$$

To use this in a simple data-processing algorithm, we only use the peak value. Thus $x = x_0$, and

$$g(x) \to g_{ij} = \frac{I}{\sigma v\sqrt{2\pi}}, \tag{6.23}$$

where g_{ij} is the total number of photons deposited in the single pixel where the peak occurs. Then we have

$$g'_{ij} \cdot C_{633,ij} = g_{ij} = \frac{I}{\sigma v \sqrt{2\pi}}, \tag{6.24}$$

where g'_{ij} is the un-calibrated numerical value of the pixel, and $C_{633,ij}$ is the calibration factor measured in the number of photons deposited in the pixel per number value of the pixel. Rearranging, we have

$$C_{633,ij} = \frac{I}{g'_{ij} \sigma v \sqrt{2\pi}}, \tag{6.25}$$

or, alternatively,

$$C_{633,ij} = \frac{2I\sqrt{\ln 2}}{g'_{ij} v \cdot FWHM \cdot \sqrt{\pi}}. \tag{6.26}$$

For a calibration streak such as that shown in Fig. 6.7(a), the algorithm just described finds one $C_{633,ij}$ for each row of pixels (i.e., for one pixel in each row). In other words, the vertical line in Fig. 6.7(a) yields a vertical calibration line one pixel wide. To improve matters, vertical calibration lines were produced at nine different horizontal locations. The actual locations calibrated are shown in Fig. 6.7(b), where the images that resulted from individual streaks have been summed for illustrative purposes. Also, at each location, five calibration streaks were taken, and the algorithm was run for each of the five repeats. The results of the five repeats are then averaged to improve the statistics (i.e., to average out any slight power fluctuations in the CW laser source).

[Note: The nine calibration positions (or vertical lines) shown in Fig. 6.7(b) are, from left to right, denoted in alphabetical order as a,b,c,...,i in the calibration data files and MATLAB codes.]

The $C_{633,ij}$ values are of course only good for 633-nm photons. To determine the calibration as a function of wavelength $C(\lambda)_{ij}$, we make use of the

photo-cathode sensitivity data and input optics transmission data provided in the streak camera manuals. We again normalize these data to their respective values at 633 nm, and then apply the resulting relative wavelength-dependence to our determined $C_{633,ij}$ values.

With the processes described above, there remains the question on how to handle the pixels between the calibration lines. One method is to use some sort of interpolation algorithm. This method will remain an option, and we will discuss it again in a moment. For now, however, we discuss a "white-wash" method as an intermediate step. With this method, a constant white-light source (a tungsten lamp in our case) illuminates the entire streak input slit more-or-less uniformly. This illumination is then streaked. To average out any non-uniformities in the illumination, this process was repeated several times, and with the lamp slightly moved each time. The resulting streak images were first zeroed (by subtracting the offset value of 503 or 504), and then averaged to reduce any non-uniformities in the illumination. We will represent the resulting zeroed and averaged white-wash image by the matrix $\mathbf{I}$, with elements I_{ij}.

Assuming the illumination to be uniform, any non-uniformities appearing in $\mathbf{I}$ are due to nonuniform sensitivities. To balance the sensitivities, we first choose an arbitrary pixel value to normalize the white wash image to. In our case we chose the average of all pixel values in the image, $I_{avg} \equiv \sum_{ij} I_{ij}/(1024 \times 1280)$. Next we create a new 1024×1280 matrix, $\mathbf{W}$, and make the following assignment to each element: $W_{ij} = I_{avg}/I_{ij}$. Thus, if we multiply each element in $\mathbf{I}$ by its corresponding element in $\mathbf{W}$, we get a perfectly uniform image with the constant pixel value of I_{avg} (i.e., $I'_{ij} = W_{ij} \cdot I_{ij} = I_{avg}$). The matrix $\mathbf{W}$ is our white-wash calibration matrix, and the MATLAB code used to determine it for

each streak setup is included as Appendix C.2.6.

With **W** determined, we first zero (i.e., subtract 503 or 504) and then multiply (element-wise) *all* images by **W** prior to any processing. Taking the calibration images discussed above for example, we first subtract 503(4) from all pixels, then multiply the resulting pixel values by the corresponding elements of **W**, and only then find the calibration values $C_{633,ij}$. In this way, all pixels should be equally sensitive prior to determining the calibration values, and thus, since the calibration laser is constant, all derived calibration values $C_{633,ij}$ should be the same, even in between the vertical calibration lines. This is why an interpolation method is not theoretically necessary. However, in practice, even after applying the white-wash matrix, the calibration values from the vertical laser lines do not come out precisely equal, and thus one may want to interpolate between the lines or simply use the average value of all the lines.

Whether to interpolate or average depends on what one believes the source of error to be. If the error is due to nonuniform illumination by the white-light source, then it is probably best to trust the laser calibration and interpolate between the vertical calibration lines. However, if one believes the error is more likely due to the Gaussian and $FWHM$ approximations used to calibrate the vertical laser lines, then it is perhaps more appropriate to average. Since the laser was focused, the Gaussian was very sharply peaked (i.e., a $FWHM$ of about 10 pixels). As the laser was repositioned to streak vertical calibration lines at different horizontal locations, any resulting change to the focal spot size will yield different $FWHM$ values. Therefore, any errors associated with relating the $FWHM$ to the calibration value will become more apparent, and one will obtain non-constant calibration values from one vertical line to the next. However, this error

will remain constant along a given vertical line (due to the constant focal spot size and $FWHM$ along the given line), and thus the calibration value along a given vertical line will remain approximately constant. This is what we actually observe (i.e., non-constant calibration values from vertical line to vertical line, and constant calibration values along a given vertical line). Also, this error is likely greater for more sharply-peaked distributions, such as our 10-pixel-wide distributions. For these reasons, it is believed that using the average calibration value is more appropriate than using an interpolation scheme. (Additionally, we analyzed the experimental continuum data using both interpolation as well as averaging, and the averaging led to more reasonable results—we'll discuss this more later however.)

Since we zeroed and then applied the white-wash matrix to the calibration streaks, we must also zero and apply the white-wash matrix to the streak images acquired from our actual experiments. This is so that all pixel sensitivities will be on the same relative scale. Only then can we apply the determined calibration values $C_{ij}(\lambda)$ to our continuum data to determine the number of photons deposited per pixel at each wavelength. The MATLAB code for applying our calibration values to our continuum data is shown in Appendix C.2.8. However, to fully understand this code, we need to understand what it is doing to calibrate wavelength and timing.

6.2.4 Wavelength Calibration

The first step in our wavelength calibration was to send light with distinctive and known spectral features through our spectrometer, thereby producing an

image of a known spectrum on the input slit of the streak camera. This static image was then recorded simply by setting the streak camera to focus mode and pausing the live update (for a description of live/focus mode, see Sec. 5.1.1). In our case we used the light from a helium discharge lamp, which produced six distinctive and well-known spectral lines within our viewing bandwidth. A static picture of the helium spectrum was taken just prior to each continuum experiment, thereby accounting for any spectral shifts that may have occurred due to optical adjustments made between experiments. Examples of how these first-order wavelength calibrations were initially used can be seen in Figs. 6.3 and 6.4 (where the calibration spectra and streak images have been rotated 90° counter-clockwise to align the time-axes with that of the electrical signals). However, any aberration during the streaking process will make the use of a solely static spectral image somewhat inaccurate for calibration.

Looking at Fig. 6.7(b), we see that the lines are not perfectly vertical, despite the fixed laser position. As these lines represent the trajectory of a particular wavelength, we must quantify these deviations in order to determine the (necessarily time-dependent) wavelength calibration for the continuum streaks. To do this, we again streak a CW HeNe laser source, just as we did for the pixel calibrations. However in this case, we position the laser focal spot to precisely where a particular helium line was when the static helium picture was taken. To do this, we first open the image file of the helium spectrum (thus displaying this image on the monitor of the streak camera PC). Second, we set the streak camera to live mode thereby opening and displaying another image window on the PC screen, this one being the continually-updated image of the laser spot. Next, we align the two image windows, and by using the image of the helium spectrum as our reference, we position the laser spot directly on the helium line

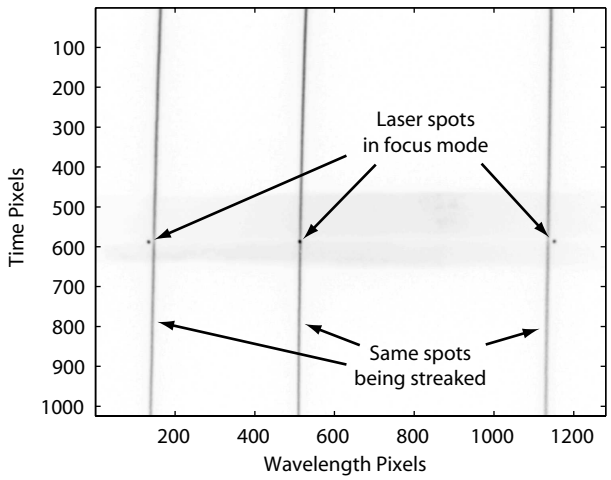

Figure 6.8: Images of laser spots taken in focus mode superimposed on images of same laser spots being streaked. This illustrates how streak trajectories can significantly miss their corresponding focus-mode positions.

that is to be calibrated. With the alignment set, we take the streak camera out of focus mode, streak an image, save the image for later, and then repeat for the next helium line of interest.

[Note 1: Upon carrying out this procedure, we noticed the important fact that positions in the focus mode do not precisely match positions in streak mode. That is, if the focused laser spot has the weighted-average pixel position (i,j) in focus mode, then in streak mode, and at the same row i, it is likely to have the position (i,j'), where j' is significantly different from j. This is shown in Fig. 6.8.]

[Note 2: In the calibration data files and MATLAB codes, the helium lines calibrated (i.e., the six brightest lines within our viewable bandwidth) are, from left to right, denoted numerically by 1,2,3,...,6. Also, the direction of left to right in the images corresponds to the direction of decreasing wavelength. The wave-

length of the helium line that corresponds to each number depends on the grating rotation of a particular experiment's setup. The wavelengths of the lines used were: 667.8, 587.6, 501.6, 492.2, 471.3, 447.1, and 388.9 nm, but the line denoted by the number 1 corresponded to either 667.8 or 587.6 nm, depending on the grating rotation and resulting viewable bandwidth of the particular shot. These assignments have been recorded for each experiment and are viewable in the MATLAB code included as Appendix C.2.9.]

With the six helium calibration lines streaked for each of the three grating rotations used, we then find the trajectory coordinates of each of the streaked lines. To do this, we record the column index of the highest-valued pixel found in each pixel-row of the image. These records are then saved in output files for later use. This is essentially the procedure followed in the MATLAB code of Appendices C.2.9, C.2.10, C.2.11, and C.2.12. However, the way they work together in detail (e.g., passing data to one another, etc.) is far too complicated to explain here. Thus, the code has been appropriately commented should one want to follow it exactly. Also, whenever a MATLAB M-file has something like "AI" in its filename (such as the M-file "vert_curves_AI.m" in Appendix C.2.11), the indication is that this particular file is only for the experiments where grating rotation "A" and streak camera setup "I" were used. There also exists M-files for the other various combinations of "B" or "C" and "II" or "III" used in the different experiments. However they are not included in this thesis because of their redundancy.

With the trajectories of the helium lines recorded, we can specify the time at which we want to produce a spectrum from a continuum streak, follow the helium line trajectories to the desired time, perform a linear interpolation be-

tween the six helium lines, and thus establish our wavelength scale. However, as previously mentioned, other streak aberrations lead to lines of constant time that are not straight, but curved. Thus, we must first find the coordinates of the constant-time curve of interest, and then find the intersections of this curve with the six helium line curves. Then we can establish the precise wavelength scale for the desired time.

6.2.5 Timing Calibration

To find the coordinates of the constant-time curves, the diagnostic laser on COBRA was re-configured such that its timing was synchronized to the streak camera via a delay generator. The delay generator allowed for adjusting the relative timing between the laser pulse emission and the streak camera triggering. A portion of the beam was sent through a fiber over to the streak camera. The output of the fiber was aligned to send the laser light into the streak camera. Optics were used so that the light coming out of the fiber illuminated the entire streak input slit. The short 150-ps laser pulse provides an effectively instantaneous flash relative to the 2- or 5-ns time-resolution of the streak camera setups used. Thus the laser flash produces an image of the input slit at one moment in time. An example of this is shown in Fig. 6.9(a). The curvature of a constant-time curve is not constant over the duration of the streak, however. Thus we needed to produce laser flashes at various times within the streak window. To this end, several streaks were taken. Starting with a laser flash near the beginning of the streak window (i.e., near the top of the streak image), we worked our way down simply by increasing the delay to the laser in increments of about 1/20th of the overall streak duration. This way we collected about 20 constant-time curves,

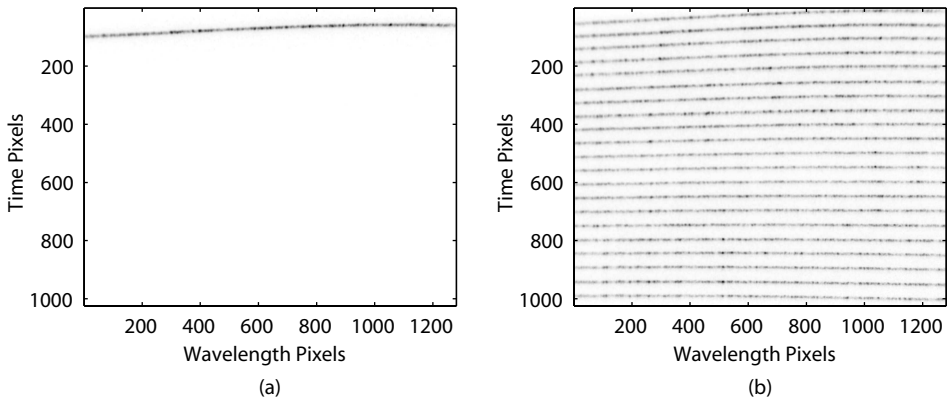

Figure 6.9: Diagnostic laser configured to illuminate entire streak input slit. The short 150-ps pulse provides an effectively instantaneous flash, producing an image of the input slit at one moment in time. The result of this for one laser pulse is shown in (a). In (b), several of these images have been superimposed to illustrate the different times at which constant-time-curve calibration data has been taken.

nearly evenly spaced from the beginning of the streak window to the end. For illustrative purposes, Fig. 6.9(b) shows all of the constant time curves collected in a single superimposed image. This gives one an idea of the time-curve calibration data available. For times in between these calibration lines, we simply do a linear interpolation.

With the series of constant-time curves collected, MATLAB codes similar to the ones described in Sec. 6.2.4 were used to scan this data, and record the curve coordinates in output files. The MATLAB code for streak camera setup I is included as Appendix C.2.13.

Now, just as was done with the radial implosion streaks discussed in Chapter 5, we again flash a portion of the diagnostic laser into the streak camera during an actual experiment to produce a timing fiducial. (We simultaneously monitor the laser flash with a photodiode, and record the photodiode's signal

on an oscilloscope along with a signal from the main load current of the experiment. Thus, accounting for all propagation delays, we know the experiment load current relative to the photodiode, the photodiode relative to the timing fiducial on the streak image, and hence the timing of the streak image relative to the experiment load current.) As is standard, we define $t = 0$ to be the time when the load current begins. We also know the duration of the streak window, and the number of pixels in the time-direction of the streak window, thus we know the streak speed in pixels per nanosecond. Therefore, when one desires a spectrum at a certain time t, we move to the center pixel column of the image, find the intersection of the center pixel column with the timing fiducial, determine the number of pixel rows to move up or down on the image to move from the timing fiducial to the time of interest t, and then move to that pixel row (while staying in the center pixel column). (Note: We define the center pixel column to be the universal time basis, and the constant-time curvature to be about the center column.)

Once we have moved to the pixel row corresponding to the time of interest t (and still in the center pixel column), we now look up the closest two constant-time curves (or the closest single time curve if at the very beginning or end of the streak window), and interpolate between these two curves to define our time curve of interest.

6.2.6 Putting the Pieces Together

With the coordinates of our time curve of interest in hand, we then need to find where this curve intersects with the curves of the six helium calibration

lines, which is done by looking up their coordinates (see Sec. 6.2.4). We next interpolate between the six helium lines to establish our wavelength scale. We now have our time of interest calibrated as a function of wavelength.

At this point we are ready to look up the pixel intensity calibration factors $C_{ij}(\lambda)$ using the coordinates of our newly determined time curve of interest. Again, for the reasons previously mentioned, we chose to trust that the white wash adequately balanced the sensitivities of all the pixels, and thus we averaged the $C_{ij}(\lambda)$ values across the nine calibration lines *a*–*i*, and thus $C_{ij}(\lambda) \rightarrow C(\lambda)$.

Applying $C(\lambda)$ to the pixels of our time curve of interest gives us the number of photons deposited per pixel. However, since we would like to know the rate at which our plasma source produces photons, we must divide by the integration time of the photon deposition (assuming that this time is short relative to the time scale of the experiment, and thus assuming that the photon production rate is approximately constant over this integration time). The integration time for a streak is the time difference between the leading and trailing edges of the slit image being positioned over a given pixel. For these experiments, our streak slit width was always set to 50 μm physically. This results in an image slit width of about 9-10 pixels. Thus, since all streaks have 1024 pixel rows in the time direction, a 200-ns streak window will have a streak speed of 1024/200 pixels/ns, and therefore it will take about 1.9 ns to clear 9-10 pixels (i.e., our integration time and hence our time resolution are about 1.9 ns). For a 500-ns streak window, this time is multiplied by 5/2 giving about 4.75 ns. Thus dividing our calibrated number of photons deposited per pixel by the appropriate integration time leads to our calibrated number of photons deposited per sec-

ond.

Since our time resolution can be thought of as 9-10 pixels wide, and since our time curve of interest is only 1-pixel wide, we can improve our statistics without sacrificing any information or time resolution simply by averaging the spectra produced by the four, one-pixel-wide time curves just prior to and the four just after our time curve of interest with the one produced at our time-curve of interest (i.e., nine one-pixel-wide spectra averaged in total).

We now have a calibrated spectral measurement of continuum intensity (with improved statistics) at a desired time at the input to the streak camera. To get the continuum power at the plasma source, we must divide the intensity at the streak camera input slit by the wavelength-dependent efficiency of our system up to the streak camera input slit, as was found in Sec. 6.2.1.

Finally, we have an absolutely calibrated measurement (with improved statistics) of the continuum intensity radiated isotropically by our plasma source within our viewable bandwidth at a desired time relative to the experiment current pulse. Again, as mentioned in Sec. 6.1, our plasma source is the small rectangular box of plasma viewed by our system of optics and slits, where the radial extent of this source is about 280 μm, the axial extent is about 1.1 mm, and the thickness is to be determined by the laser and XUV images. The MATLAB code that assembles all of the calibration pieces discussed, and finally delivers this calibrated spectrum at a specified time (and for a 0.280×1.1-mm viewing window), is included as Appendix C.2.8. This code was mentioned earlier, but now we have all of the pieces necessary for understanding how it functions. (Note: The code in Appendix C.2.8 uses the function included as Appendix C.2.7 to determine the root directory. This is also true of the code discussed in the next

section.)

6.3 Continuum Results

Since our time resolution was finite, a short MATLAB script was written (see Appendix C.2.14) to step through all the times of all the experiments in time steps equal to the time resolution of the given experiment and record the output spectra as simple text files for quick loading and viewing. Now with so many spectra to look at, and with so many variables, we needed a way to visualize the data easier. Thus a MATLAB script was written (see Appendix C.2.15) to cycle through and plot all the output spectra of a given experiment, and while doing so, record the plots as the frames of a movie. These movie frames also included plots of the current pulse with a marker indicating what part of the current pulse the presently displayed spectrum corresponds to. Figure 6.10 shows examples of these movie frames at four different times. After viewing these movies, it was apparent that the spectra remained reasonably flat over the course of a shot, but the overall intensity was somewhat proportional to the current level. By the time of peak current, the intensity levels were consistently in the range of about 1–6 x 10^{16} photons/sec/sterad/cm^2/Å.

To determine useful plasma state parameters such as electron density and temperature, theoretical plasma spectroscopy models must be used to simulate our experimental conditions, and then tuned to synthesize continuum levels that match the levels we have recorded. A model appropriate for analyzing absolute continuum levels from a partially ionized aluminum plasma should include radiation mechanisms such as free-bound (radiative recombination), and

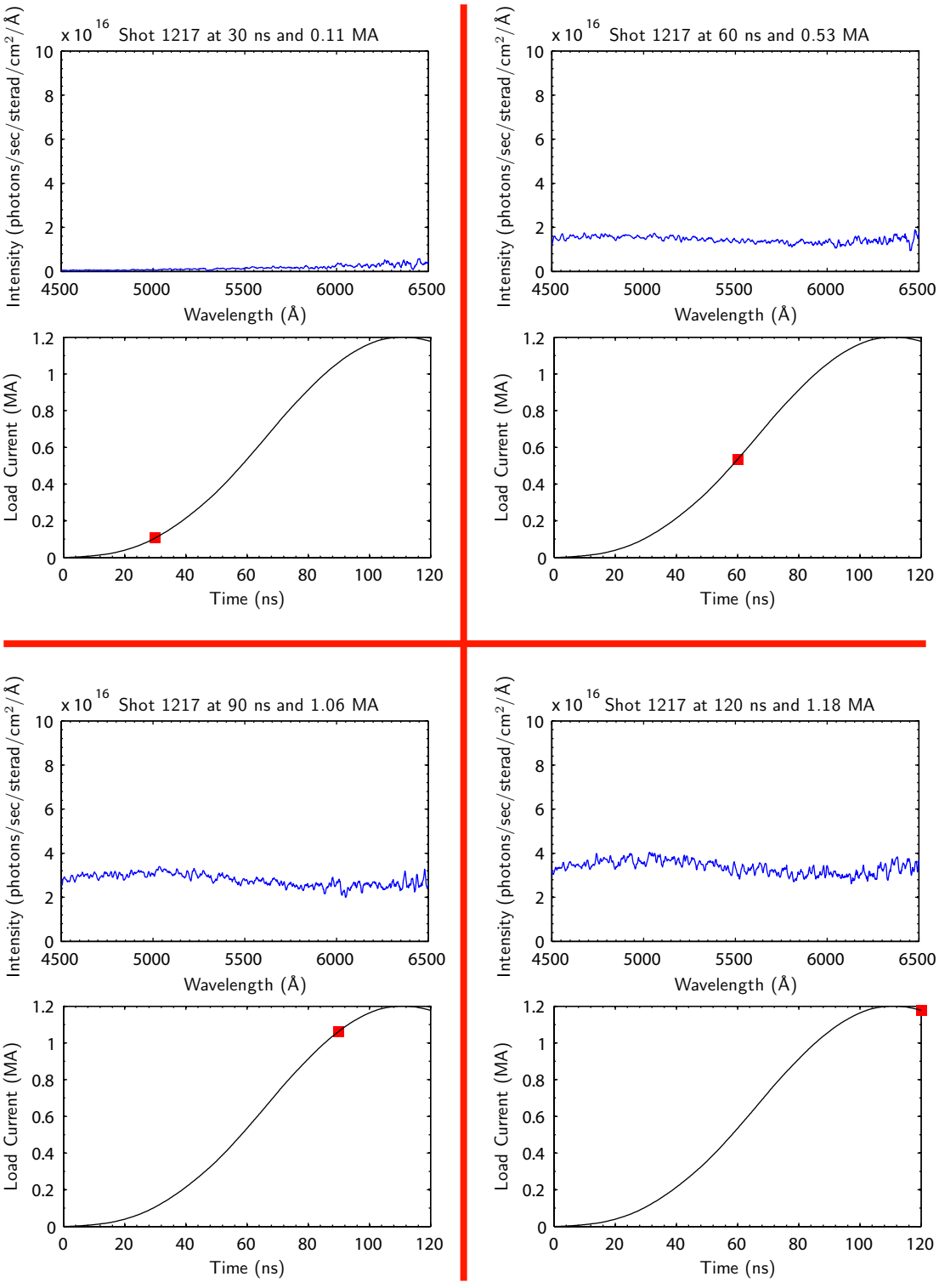

Figure 6.10: (Color) Four spectral movie frames taken from the same shot at different times. The time of the spectrum in a given frame relative to the current pulse is also indicated.

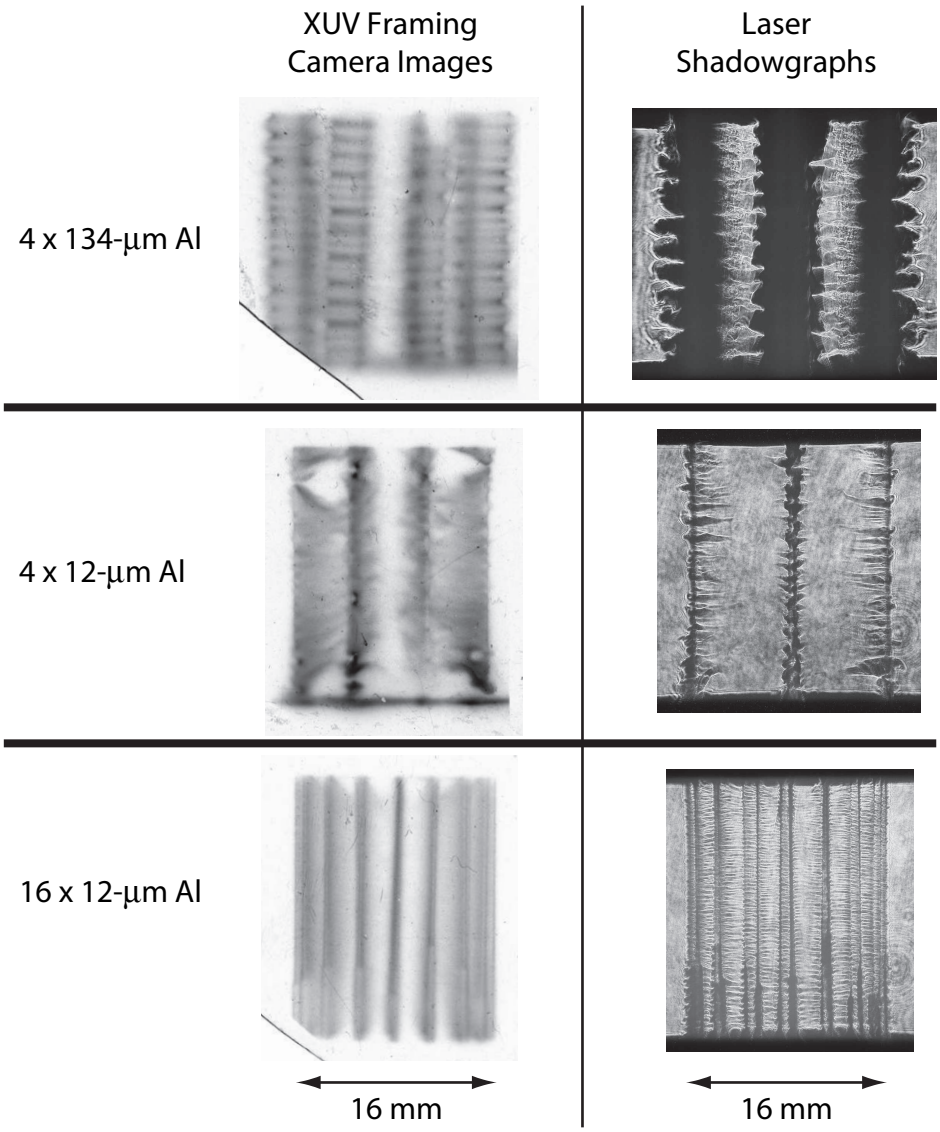

Figure 6.11: Examples of the XUV framing camera images and laser shadowgraphs used to determine plasma thicknesses in the continuum/spectroscopy experiments.

free-free (thermal bremsstrahlung and cyclotron radiation), and bound-bound (line radiation). To create a model such as this from scratch is beyond the scope of this thesis. Thus a collaboration has been established with specialists at the Weizmann Institute in Israel (i.e., with Professor Yitzhak Maron and his students).

Professor Maron has requested that, for each spectrum, we provide the data as a plot in units of [photons/sec/sterad/cm^2/Å] as well as in units of [photons/sec/sterad/cm^3/Å]. To deliver the latter requires us to determine the source size. However, to deliver the former, we simply zipped up our movie files and sent them. This way, Professor Maron and his group could watch the entire evolution of the spectra, as well as pause the movie on a given frame to be analyzed.

To determine the source size, we used our laser shadowgraph and XUV framing camera images such as those shown in Fig. 6.11. Of course these imaging frames only provide us with a snapshot in time, and the wire cores and the coronal plasma surrounding the wire cores are known to expand with time. However, due to the complexity of simulating the plasma and its radiated spectra, only a limited number of spectra (~10) can be analyzed (at least initially). Thus only a handful of times were selected for spectral analysis, and these times were chosen such that laser shadowgraph and XUV imaging data are available, thereby allowing us to determine the thickness of the radiating source. For these selected times, the plasma thickness was estimated (usually on the order of 1 mm), and the final data set has been delivered to Professor Maron.

CHAPTER 7

CONCLUSIONS

7.1 Summary & Discussion

Throughout this thesis, results were presented from two experimental studies conducted on the COBRA pulsed-power generator. The first study presented results characterizing the implosion dynamics and radiation output of wire-array z-pinch loads on COBRA. In the second study, a new diagnostic setup was developed to record the visible-light spectra emitted from aluminum wire-array plasmas as a continuous function of time. The setup for the spectroscopy study was described in Sec. 6.1, and results from these experiments showed that the emitted spectra consisted solely of continuum radiation (see Sec. 6.3). To determine electron density from the continuum data, an absolute calibration of the detection system was performed, and the procedure for this calibration was discussed in Sec. 6.2. The resulting absolutely calibrated data has been delivered to specialists at the Weizmann Institute in Israel for further analysis and determination of the electron density.

For the study of implosion dynamics and radiation characteristics, we made use of COBRA's extensive diagnostics suite to record a variety of data for 20 different cylindrical wire-array load configurations (see Table 5.1). The diagnostics used were described in detail in Sec. 2.2, while their particular setup for this study was described in Sec. 5.1.1. Taken as a whole, the data produced by the various diagnostics has allowed us to develop a more complete understanding of wire-array z-pinch phenomena. Several key observations and possibilities, as well as an overall picture derived from these observations, are discussed now.

Bolometer and PCD measurements indicated that the highest x-ray powers (300–500 GW) and total x-ray energy yields (6–10 kJ) were achieved by scaling the wire-array loads to stagnate before peak current, where $d|I|/dt$ is still positive. Perhaps the high powers and yields are related to the fact that energy is still being driven into the system prior to peak current, as the driving voltage, which is in phase with dI/dt, is of the appropriate sign for the Poynting flux to be directed radially inward. After peak current, where $d|I|/dt$ is negative, the sign of the driving voltage is such that the Poynting flux is directed radially outward. For a sine-squared current pulse, the Poynting flux into the pinch is maximized at 2/3 of the time to peak current with a full width at half maximum of about 1/4 of the zero-to-peak rise time, and goes to zero at peak current. Thus the time of the Poynting flux peak is comparable to our higher-yield stagnation times.

The Poynting flux is a measure of electromagnetic power flow in the system, and in Sec. 5.2.4, we saw that the waveform representing the electrical power into the load closely resembles the waveform of the total radiated power out of the load, both in shape and magnitude (see Fig. 5.15). These plots suggest that the electrical power into the load (i.e., ohmic and/or compressional) contribute significantly and directly to the radiated power on COBRA. Therefore, if a large portion of the radiation at stagnation is being driven directly by electromagnetic power input, then it is reasonable to expect higher powers and total yields when the machine power input is maximum (i.e., when the Poynting flux is maximum and directed into the load). Also, if radiation power and yield are truly maximized when $d|I|/dt$ is positive, then this would suggest that the pdV mechanism is responsible, since the I^2R mechanism only depends on the current magnitude.

Radiation during stagnation being driven directly by electromagnetic power input could have important consequences for wire-array z-pinch research on larger current generators as well. For instance, on Z, the total conversion efficiency from stored electrical energy to total radiated output energy is about 15%, and for the W load shown in Fig. 5.15, the conversion efficiency was about 10%. Thus, if such high conversion efficiencies are indeed being obtained by non-kinetic mechanisms on COBRA, then it certainly seems plausible that large direct contributions from I^2R or pdV mechanisms could explain the excess power radiated by wire-array z-pinches on Z, where the kinetic energy of the implosion alone cannot account for the total radiated power (usually differing by a factor of about 2 to 4 [3]).

The increased energy conversion of the arrays that stagnated before peak current might also be explained by impedance-matching arguments. For these loads, the current was reduced by up to 20%, which suggests that their dynamic impedances were better matched to the driver. Related to this were the observations of particularly large $\dot{L}I$ voltages for the loads imploding before peak current (i.e., nearly 1 MV for W and over 500 kV for Al). It should also be noted that increased energy conversion and total radiated power were obtained by using arrays with closer wire spacings (e.g., the 785-μm wire spacing), a trend that is consistent with power observations made on Z [27, 76].

In order to scale an array to implode early, we used a 4-mm array diameter. This forces us to consider whether the smaller diameter could have been responsible for the higher power and yield, similar to the results reported in Ref. [42]. To this end, we compare the 16-wire W arrays of Sec. 5.2.1, which are identical except for their 4 and 8 mm diameters. The streak trajectories for

these two tests appear to approach similar constant implosion velocities, about 300 km/s. If we assume the masses involved with these two implosions were approximately equal, then the final kinetic energies for these two implosions should have been approximately equal. Therefore the higher yields from the smaller array diameters might instead be due to greater current transfer to the pinch axis, leading to more magnetic compression and heating. This argument is reasonable since a load with a smaller initial array diameter requires less of a net change in load inductance to achieve the same final state at stagnation as a load with a larger initial array diameter. In other words, there is less of an inductive "hill to climb" for a smaller-diameter array when it comes to transferring current to the array axis. For example, assuming a constant $\dot{I}$, in order to transfer current to a stagnated column that is about 1 mm in diameter, an array with an 8-mm diameter requires about a 70% greater change in energy than an array with a 4-mm diameter. Thus, as long as the smaller-diameter array does not result in a significant increase in trailing mass (making current paths at larger radii more favorable due to higher plasma densities at larger radii), current should transfer to axis more easily for the case of a smaller-diameter array. In other words, if the amount of trailing mass left at the initial array radius is the same for two different array diameters, then a larger fraction of the total current would likely flow through the trailing mass of the larger-diameter array since current flow at larger diameters is less inductive. The result would be less efficient transfer of current to the array axis for larger-diameter arrays, leading to less dense pinch columns, and therefore less intense radiation from the pinch columns. Also, smaller array diameters have been observed to produce smaller-diameter pinch columns with higher densities and stronger radiation as far back as 1986, though they were specifically interested in radiation sources

above 1 keV [77].

The higher peak x-ray powers found with low-mass, small-diameter arrays could also be explained by the short duration of the implosion phase, in that a very fast run-in could be better for mitigating the negative effects of Rayleigh-Taylor (R-T) growth. As the R-T process evolves, some bubbles are seen to outrun others, leading to a spread in the arrival time of the bubbles/mass on axis. This spread will grow in time. However the time for this spread to develop is reduced if the duration of the implosion phase is reduced. In our examples using 4-mm diameters with $\Pi \gtrsim 40$, the implosion phase observed on the streaks lasted only about 6 ns, and resulted in significantly faster rising x-ray pulses. Also, the large $\dot{L}I$ voltages for the low-mass, 4-mm-diameter arrays suggest rapid current transfer to axis (again, these were nearly 1 MV for W and over 500 kV for Al). Perhaps there is some optimal array diameter that might be found with more experiments.

Observations of the precursor column made in these experiments included a notable reduction in soft x-ray radiation as the initial wire-spacing was changed from 1.6 mm to 785 μm. This could be a result of less soft radiation escaping the array perimeter due to the optical depth of the more closely spaced wire cores and coronal plasmas, or this could be the result of less current advected into the interior of the array and compressing the precursor column to higher densities and temperatures. Current transport into the precursor column is supported by observations of more unstable precursor columns as the wire spacing becomes $\geq$1.6 mm, as well as by recent work at Cornell with micro-$\dot{B}$ probes placed inside the array interior during experiments [65]. Likely related to these observations are the phenomena reported in Ref. [46], where the precursor radiation from an

Al array with 785-μm wire spacing is seen to decay prior to stagnation.

We compared optical streak trajectories to trajectories produced by the thin-shell model, the rocket ablation-snowplow model, and an inductance unfold model. We saw that in order to get a fit to the streak trajectory data, the rocket ablation-snowplow model requires the tuning of several parameters, including the ablation velocity, for which values chosen were typically in the range of 110–170 km/s. We also saw from the inductance unfold model that the trajectory of the effective current sheath seemed to correspond to the trailing implosion trajectory in the corresponding streak image. The arrival on axis of the trailing streak trajectory and of the effective current sheath were correlated in time to the onset of harder x-ray signals and electron beam generation. Particularly for W, this resulted in a distinctive time separation (~10 ns) between the rapid rise in sub-keV x-ray radiation at stagnation, and the onset of subsequent intense >1-keV radiation. For Al, the separation was less distinct, as the initial x-ray pulse at stagnation consisted of more $\gtrsim$1-keV radiation than W (perhaps due to Al K-shell emission), while subsequent higher-energy radiation and electron beam generation were substantially less intense than that for W.

Localized hot spots were observed in time-integrated pinhole camera images. These hot spots correspond to regions of intense continuum and line radiation in spectral images produced by the WB-FSSR. The discrete temporal and spatial nature of the hot spots occurring on axis were observed in a time-dependent x-ray streak image, suggesting a micro-pinch-effect origin similar to the hot spots observed in X pinches [78, 79, 33]. As described in Ref. [33], for the case of a wire-array z-pinch, if the imploding bubbles clear out mass sufficiently around the azimuth, leaving the stagnated column as the only available current

path, then this region of the column should be further compressed/pinched, resulting in bright thermal (and line) emission. This effect is illustrated in Fig. 7.1.

Putting together the various timing correlations described above with the presence of hot spots, a possible overall picture could be as follows. From the visible streak images, we see that the arrival on axis of the main implosion trajectory is well-correlated with a rapid rise in soft x-ray power. Lagging the main implosion is a less intense trailing trajectory that seems to be the remaining material moving toward the axis. This trailing trajectory appears correlated with the trajectory of the effective current sheath derived from an inductance unfold of load voltage measurements, which is also correlated with the onset of energetic electrons and higher-energy x-rays. Thus it seems possible that the final arrival of current on axis compresses the plasma and drives micro-pinches at discrete locations, leading to emission of intense bursts of continuum and line radiation. As micro-pinches rapidly neck down, small gaps develop causing local current disruptions (see Fig. 7.1). As large voltages can occur across these gaps, energetic electrons can be generated, leading to hard x-ray emission on the anode side of the micro-pinch. X-pinch observations suggest that the time difference between hot spot formation and energetic electron production is $\lesssim$1 ns [79].

7.2 Looking Forward

Based on the discussion above, there are several possibilities for future research on COBRA. To determine whether the high radiation powers and total energy yields were more due to stagnation times prior to peak current or to arrays with

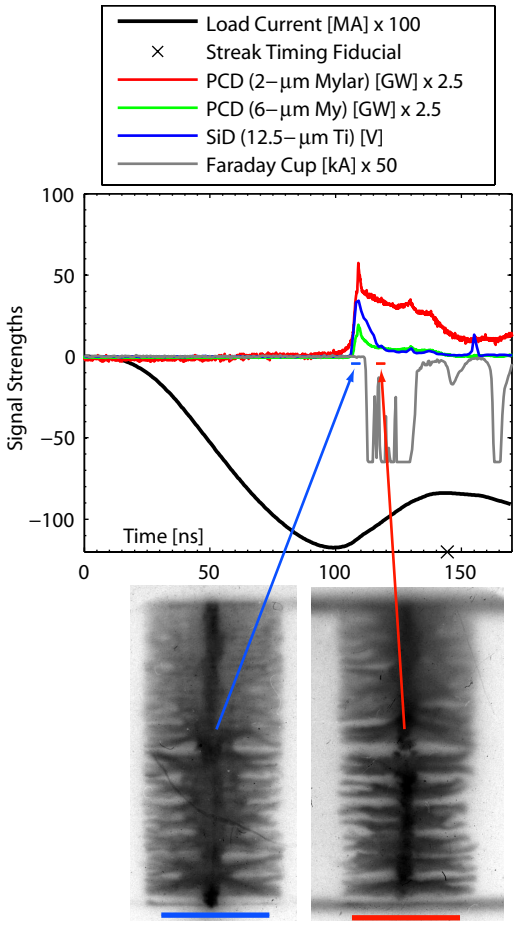

Figure 7.1: (Color) Two time-gated XUV frames and their timings relative to various signals for an Al implosion. The very fast spike-like burst at the beginning of this particular x-ray pulse (which occurs rarely) is similar to the fast pulses produced by X pinches. The XUV frames show two dominant micro-pinch regions—one half way up the array and one at the bottom/cathode end of the array. The later XUV frame shows that these two neck-down regions have opened up after the fast initial x-ray burst, forming mini-diode-like gaps. The onset of electron-beam detection by the Faraday cup occurs at a time between these two frames (likely at the time when the neck-down regions first begin to open), suggesting that the energetic electrons detected are the result of electron acceleration across these mini-diode-like gaps. The vertical positions of these micro-pinch regions correspond to the vertical positions of continuum on the WB-FSSR images and to the vertical positions of bright spots on time-integrated pin-hole camera images.

small (e.g. 4-mm) diameters (or both), the 4-mm-diameter arrays discussed in Chapter 5 should be re-tested using thicker wires. The thickness of these wire should be varied such that stagnation time moves later, perhaps with some experiments stagnating at peak current, and others stagnating after peak current. The results of these experiments could then be compared to the results presented in Chapter 5. It would be particularly interesting to see how stagnation after peak current compares with stagnation before peak current when the current levels at stagnation are the same.

Along these lines, it would be interesting to see how impedance-matching of the load effects total energy conversion from the generator to the x-ray yield. Relative to a short circuit load, our highest-yielding wire-array load reduced the peak of the current pulse by about 20%. A matched load, which maximizes energy transfer into the load, would reduce the peak of the current pulse by 50%. It would be interesting to see if we could increase the total radiated energy yield by finding a load that reduces the current beyond 20%. To this end, lighter loads could be tested in an attempt to increase the $\dot{L}I$ voltage, thereby raising the dynamic impedance, and decreasing the current. To prevent the lighter array from imploding too early, a larger array diameter could be used.

Other future endeavors could include more experiments with various materials in order to better isolate general wire-array implosion processes from material-dependent artifacts. Also, further investigations into the nature of hot-spots/micro-pinches and their effects on overall x-ray production are needed. For instance, we observe a greater number of hot spots in higher-yield implosions, such as with the 4-mm-diameter arrays that stagnated before peak current.

As trajectories tuned to fit streak data were not unique (due to the number of free parameters), it is desirable to remove at least one degree of freedom by making a reliable direct measurement of the average ablation velocity. For sparse, non-radiating arrays, recent work at Cornell has resulted in just such a measurement using point-projection radiography [18]. At the moment, it is unclear whether the ablation velocities from sparse arrays are applicable to wire-arrays with close wire spacings. Additional techniques that could be used, however, include end-on laser-probing/interferometry and side-on spectral measurements of the injected coronal plasma. Both methods are currently being investigated on COBRA.

Finally, the effect of machine rise time on implosion performance is an important issue as the community looks to scale to higher-current machines, since driver costs can be reduced if a slower current rise is acceptable. It is possible to utilize COBRA's variable pulse-shape capabilities to drive implosions using 175–200-ns rise times. The results of these experiments could then be compared with the results discussed throughout this article, as well as with 240-ns rise-time results produced on MAGPIE.

In closing, wire-array z-pinch research is an exciting field of study to be involved with today. The applications of these plasma radiating sources are numerous, and they are enabling us to explore new realms of pure and applied science such as high-energy-density physics, astrophysics, materials science, extreme equations of state, and so on. Perhaps most exciting, are the new developments in pulsed-power technology which will inevitably lead to higher energies and densities than are currently available. There is presently optimism within the community that advanced accelerator concepts based on new LTD (linear

transformer driver) technology could ultimately result in current pulses sufficient for driving high-yield thermonuclear fusion—but only time will tell. Until then, the plasma dynamics and mysterious radiation mechanisms of wire-array z-pinches are more than sufficient to keep at least one author content.

APPENDIX A

EXPERIMENTAL DATA FROM IMPLOSION DYNAMICS AND RADIATION CHARACTERISTICS STUDY

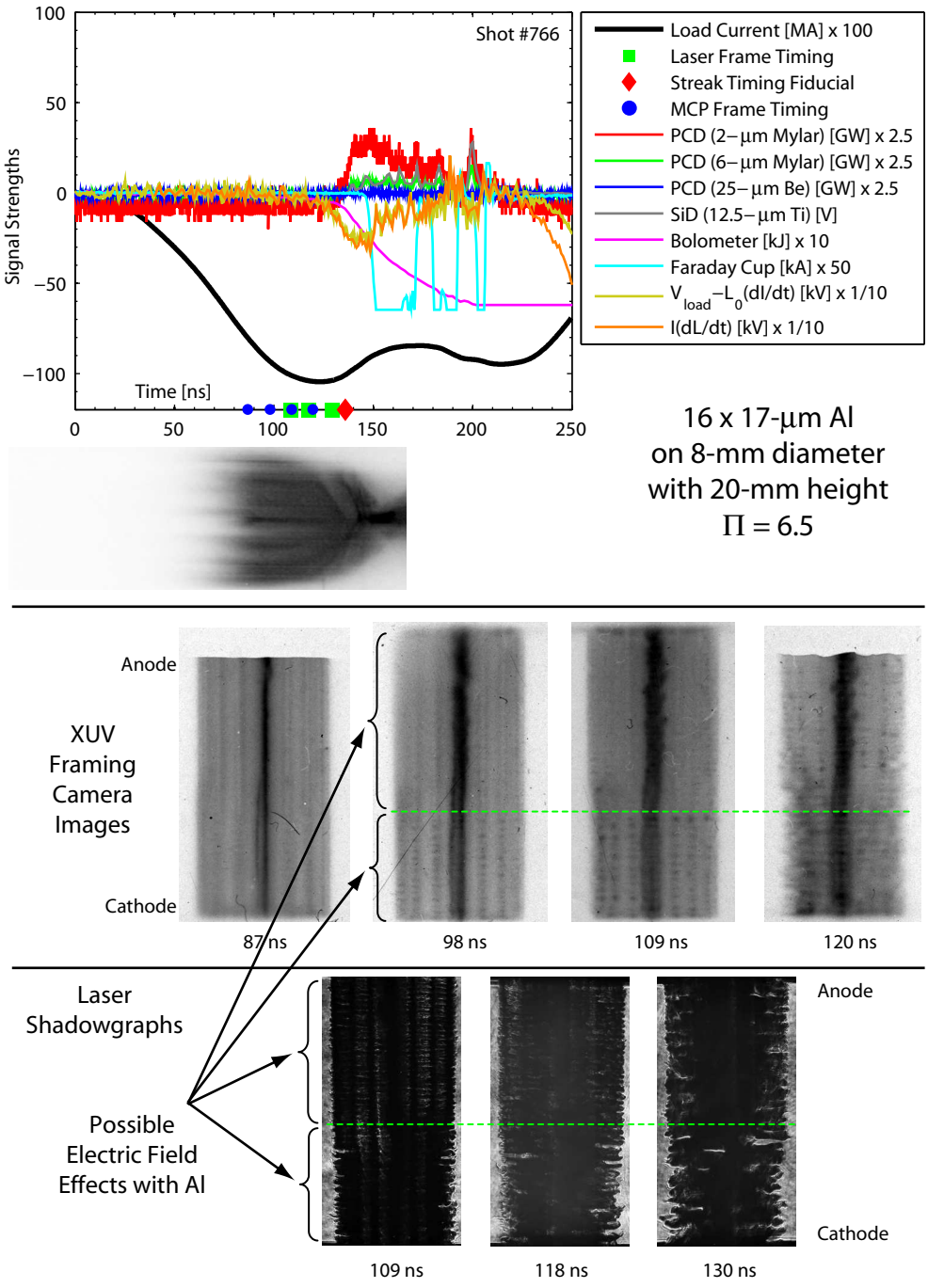

Figure A.1: (Color) Visible streak, XUV framing camera, laser shadowgraph, and various signal data for shot 766.

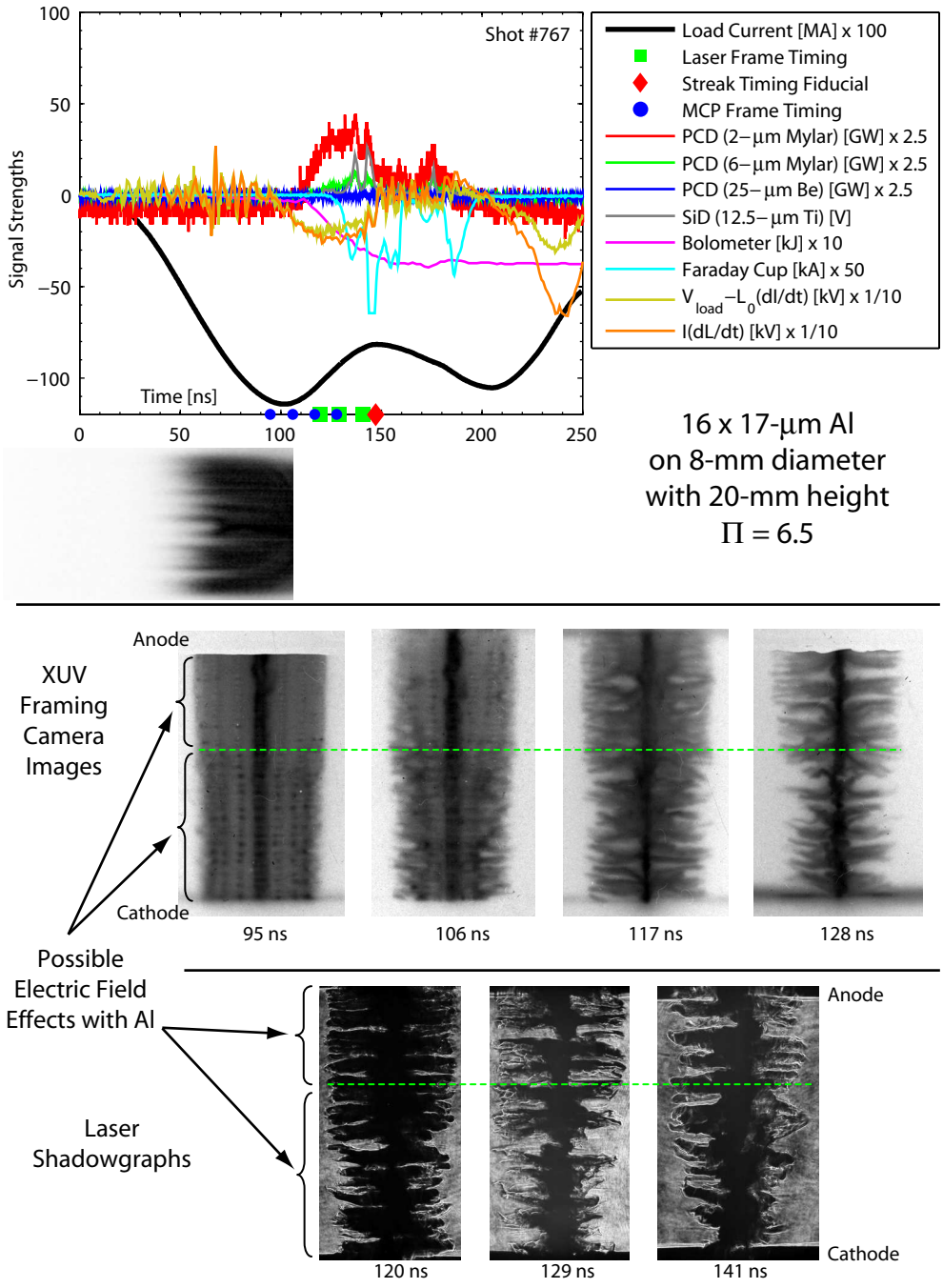

Figure A.2: (Color) Visible streak, XUV framing camera, laser shadowgraph, and various signal data for shot 767.

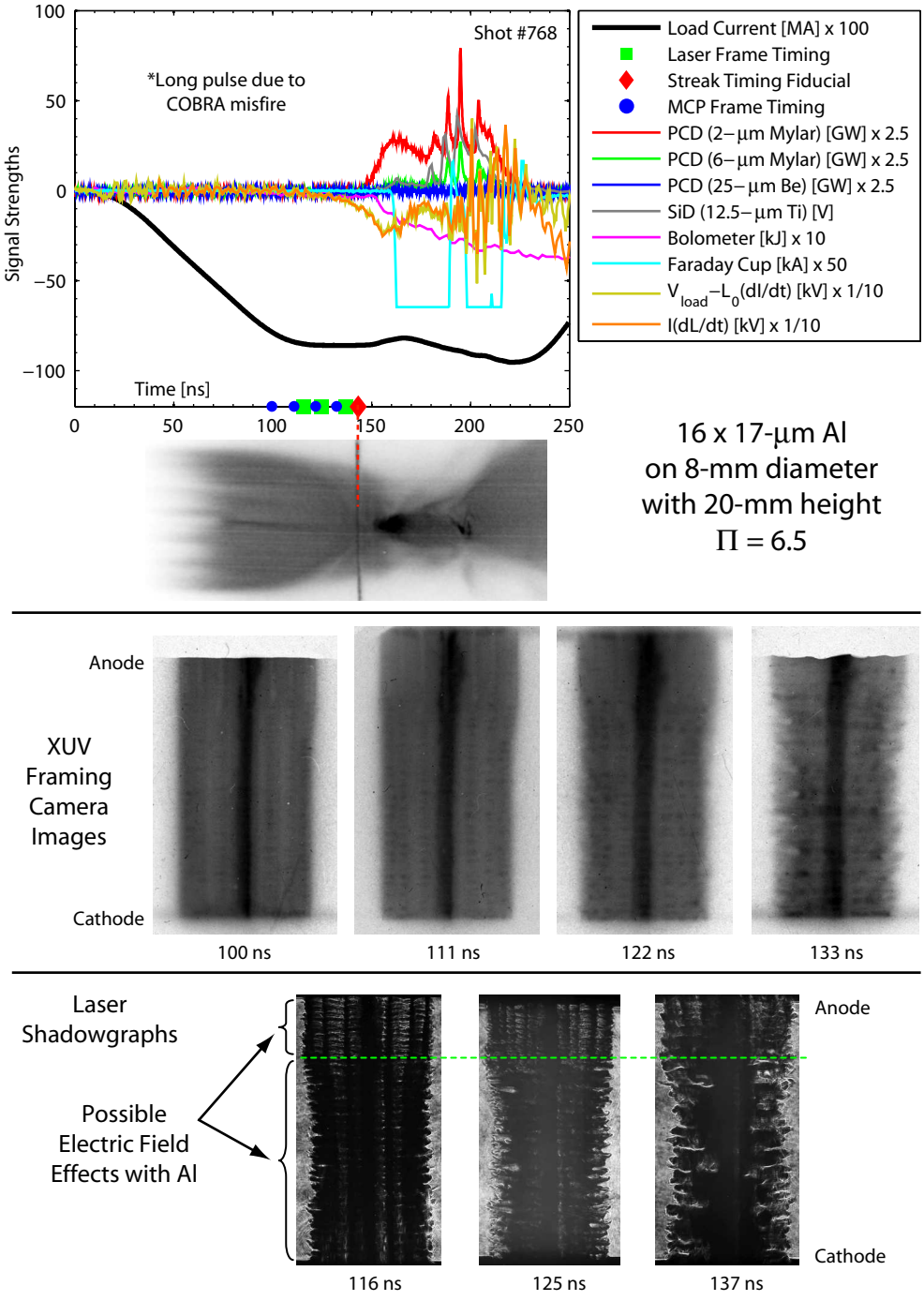

Figure A.3: (Color) Visible streak, XUV framing camera, laser shadowgraph, and various signal data for shot 768.

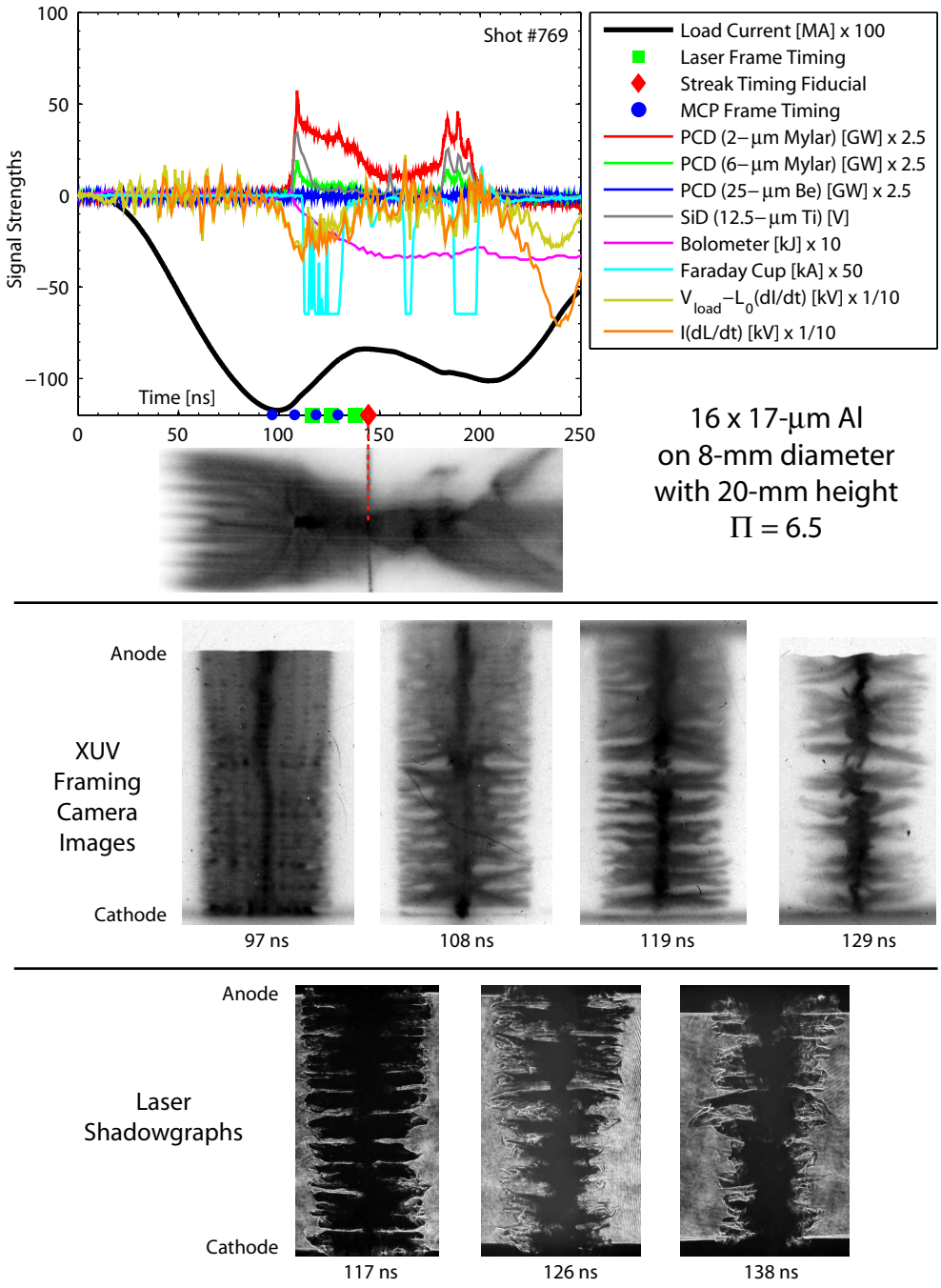

Figure A.4: (Color) Visible streak, XUV framing camera, laser shadowgraph, and various signal data for shot 769.

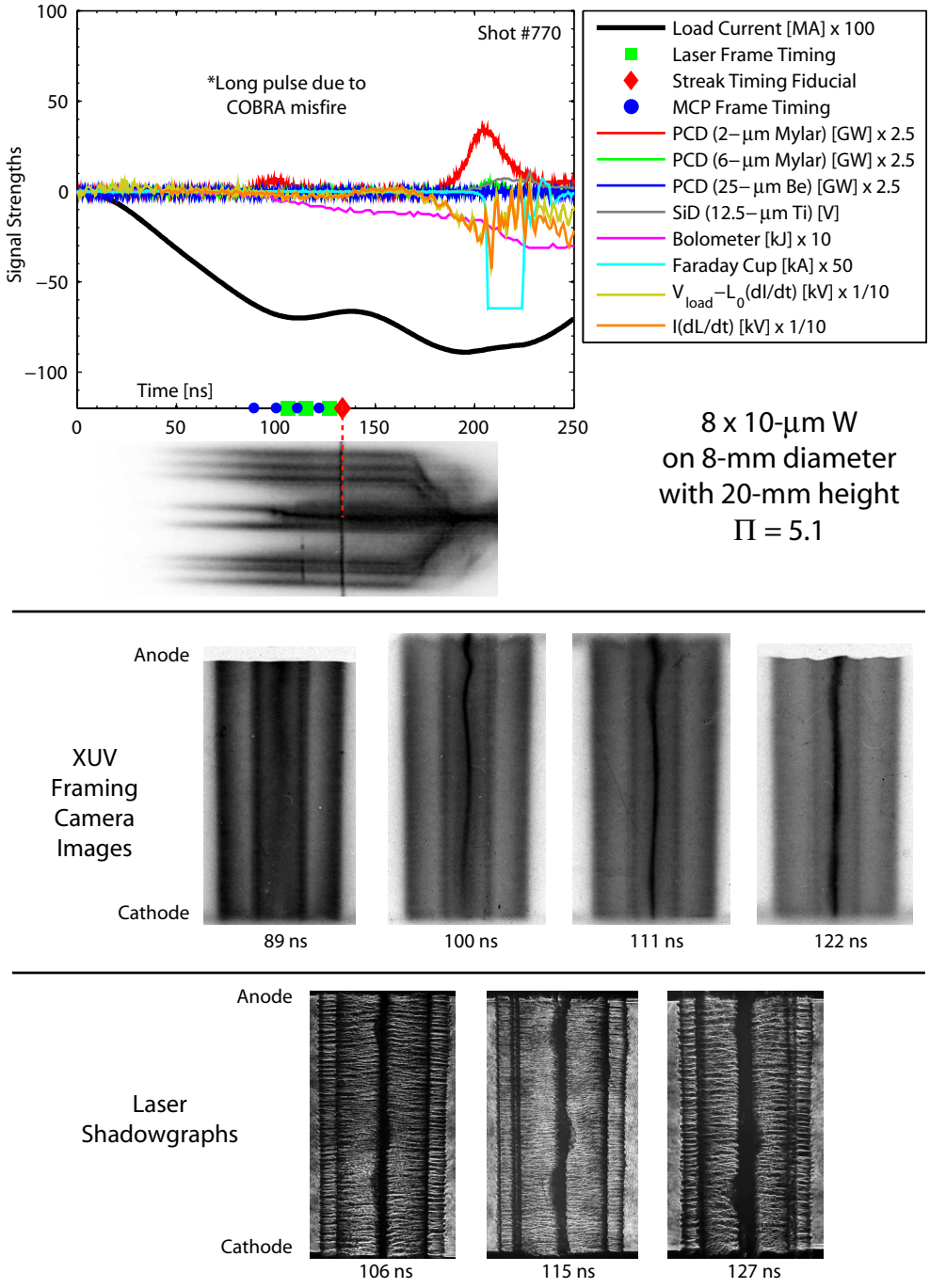

Figure A.5: (Color) Visible streak, XUV framing camera, laser shadowgraph, and various signal data for shot 770.

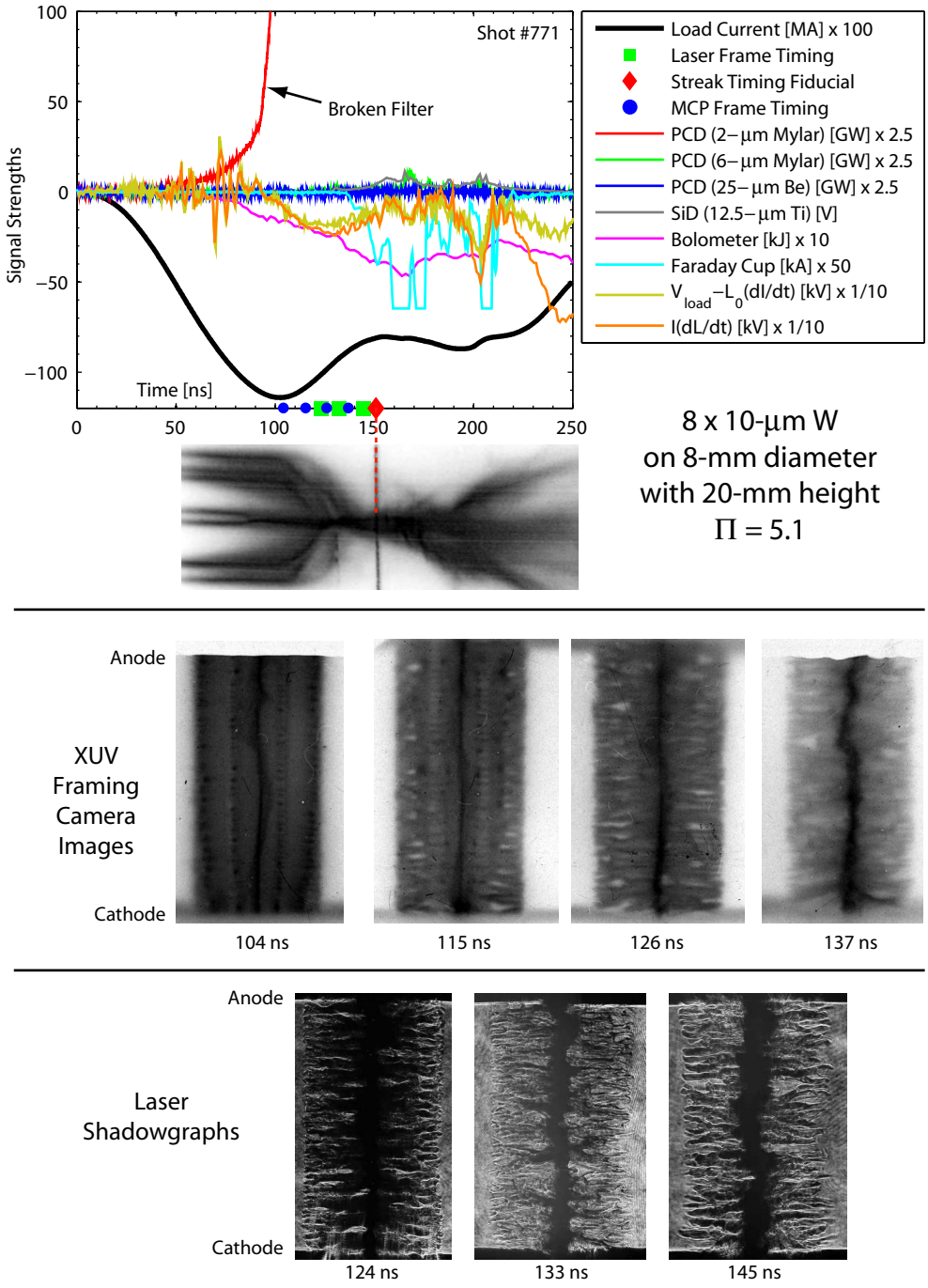

Figure A.6: (Color) Visible streak, XUV framing camera, laser shadowgraph, and various signal data for shot 771.

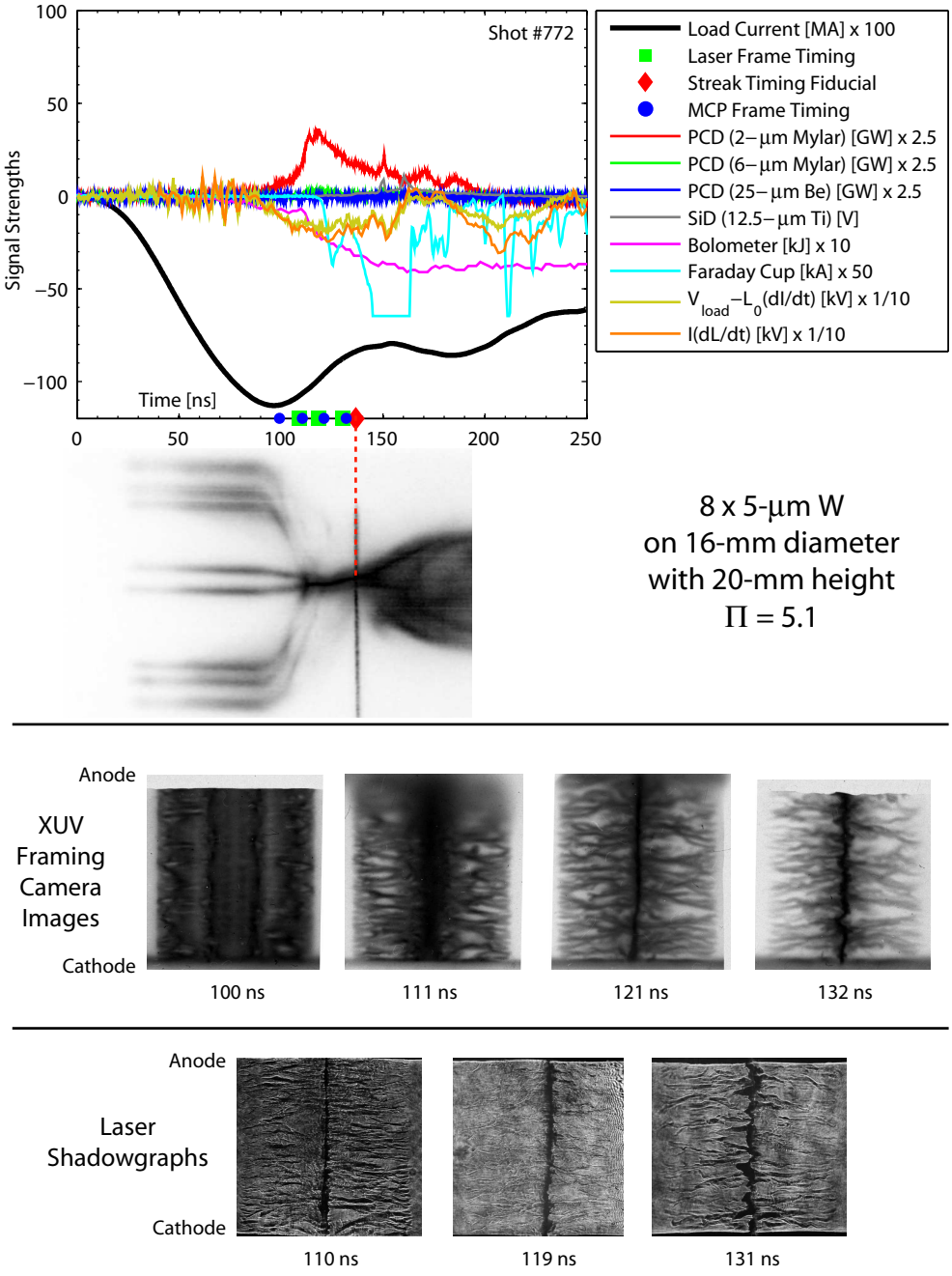

Figure A.7: (Color) Visible streak, XUV framing camera, laser shadowgraph, and various signal data for shot 772.

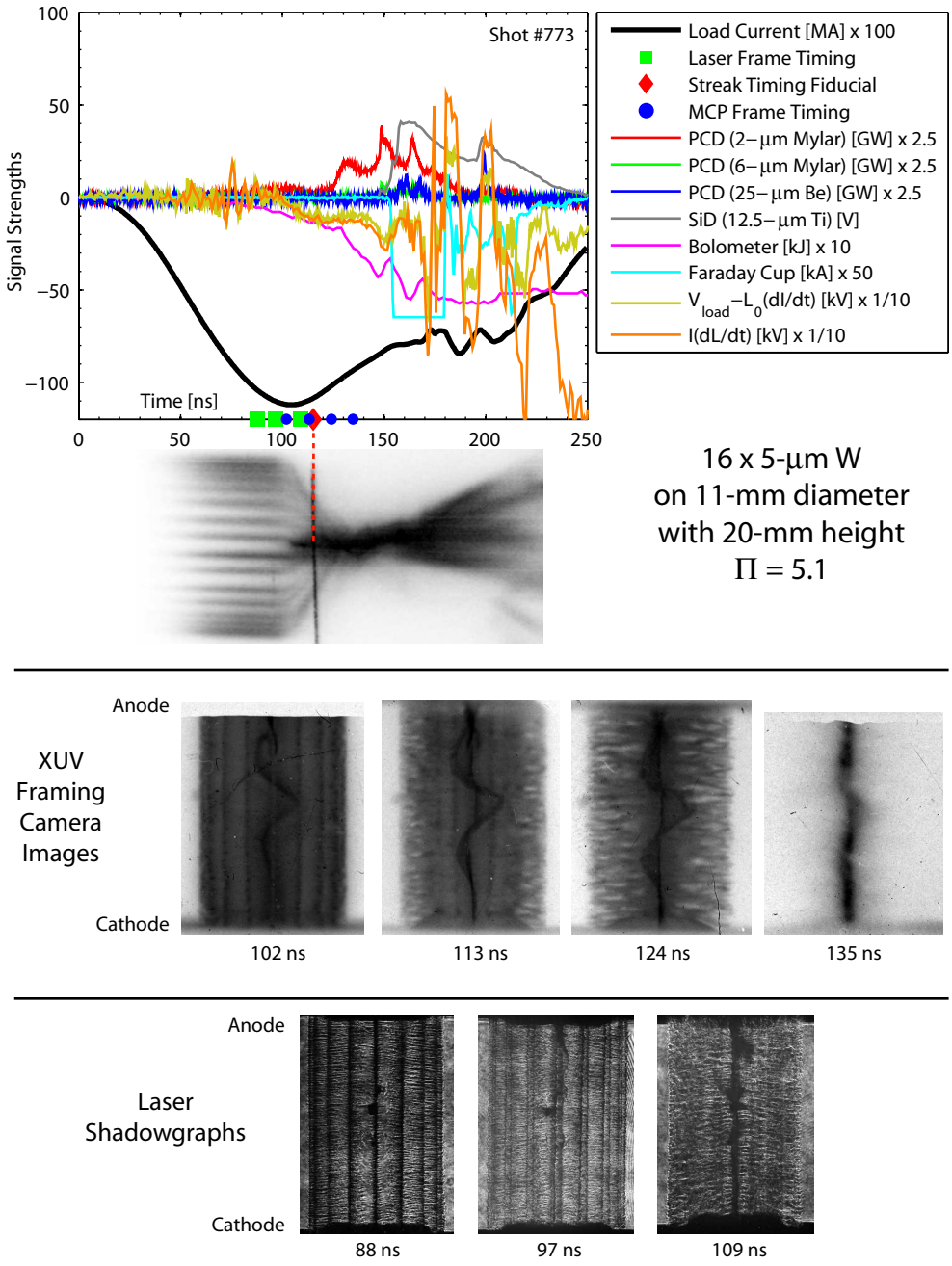

Figure A.8: (Color) Visible streak, XUV framing camera, laser shadowgraph, and various signal data for shot 773.

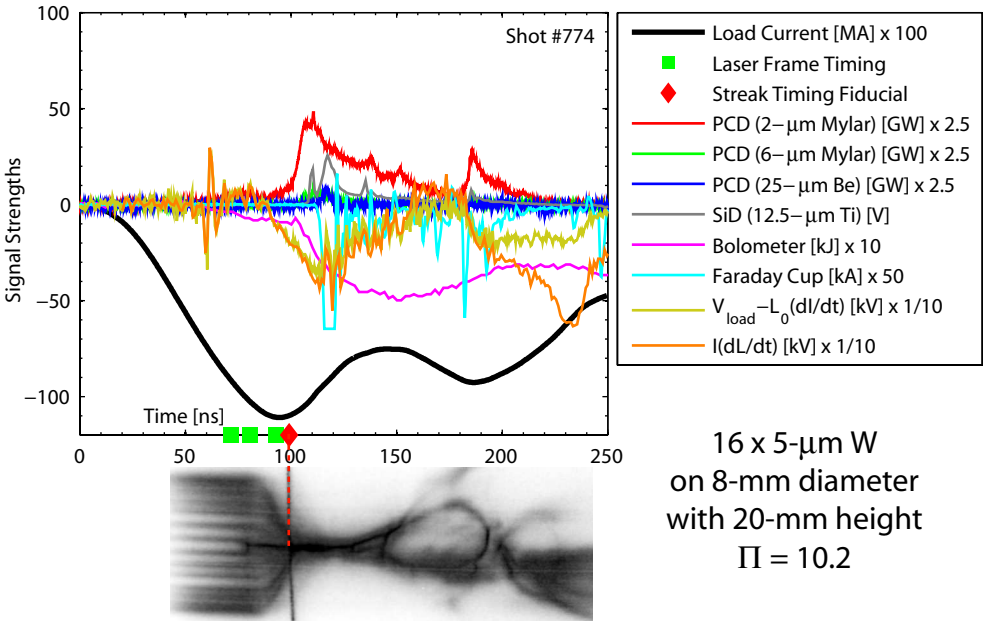

*No XUV Framing Camera on this Shot

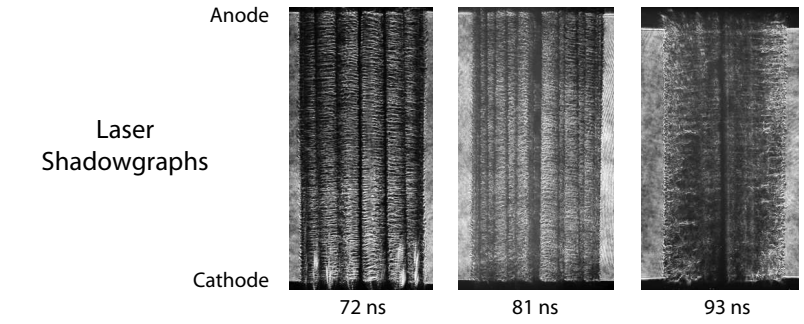

Figure A.9: (Color) Visible streak, XUV framing camera, laser shadowgraph, and various signal data for shot 774.

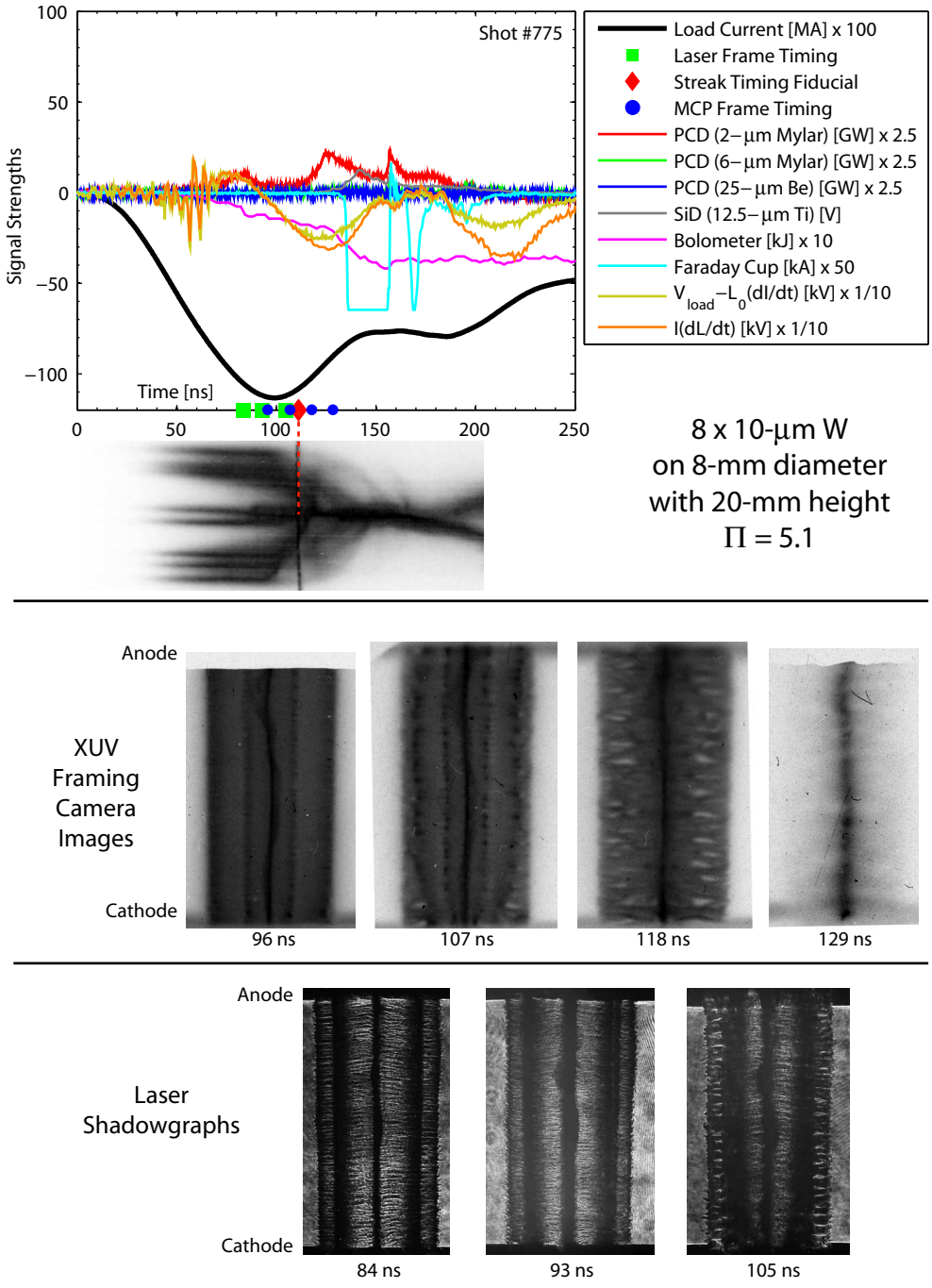

Figure A.10: (Color) Visible streak, XUV framing camera, laser shadowgraph, and various signal data for shot 775.

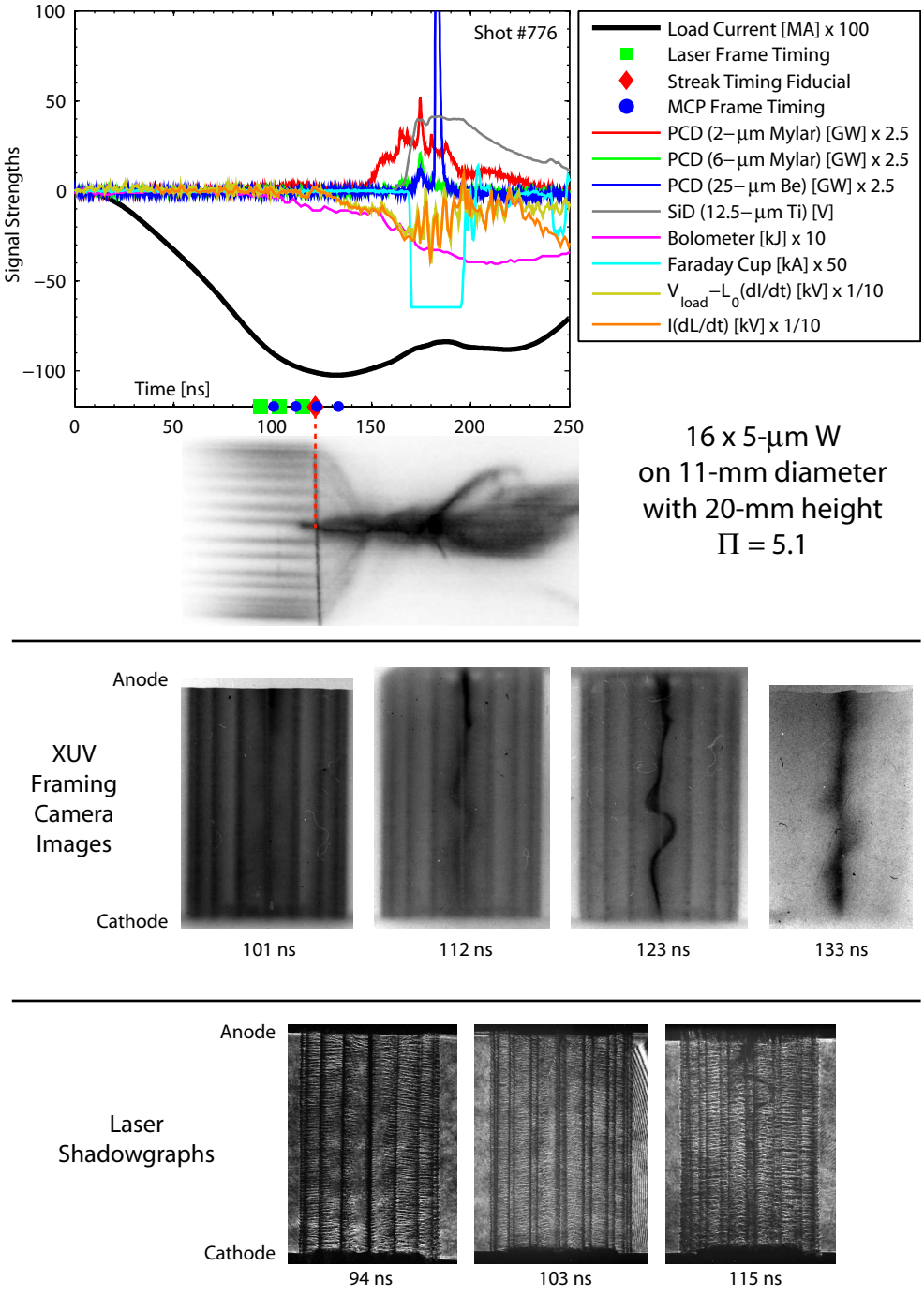

Figure A.11: (Color) Visible streak, XUV framing camera, laser shadowgraph, and various signal data for shot 776.

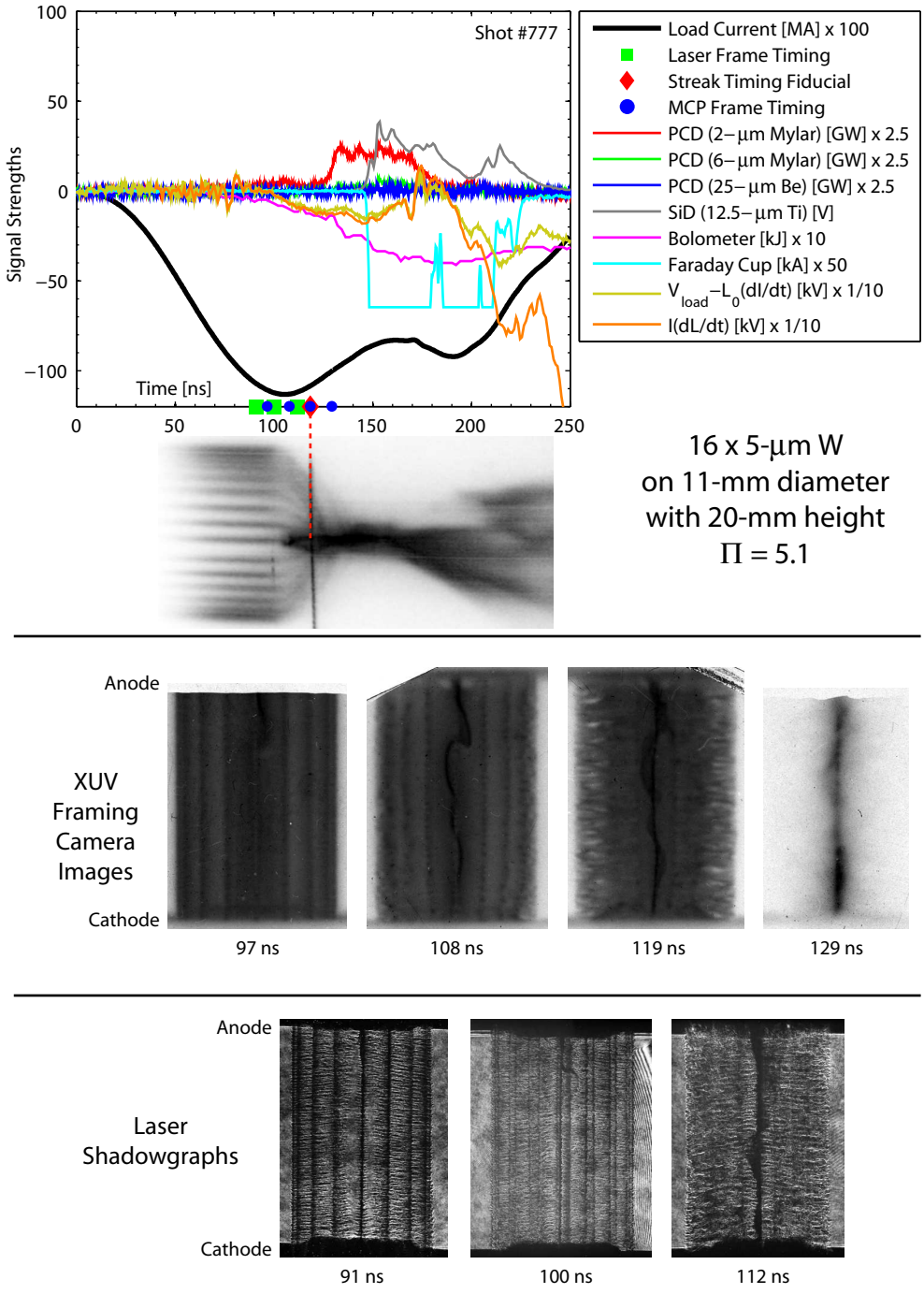

Figure A.12: (Color) Visible streak, XUV framing camera, laser shadowgraph, and various signal data for shot 777.

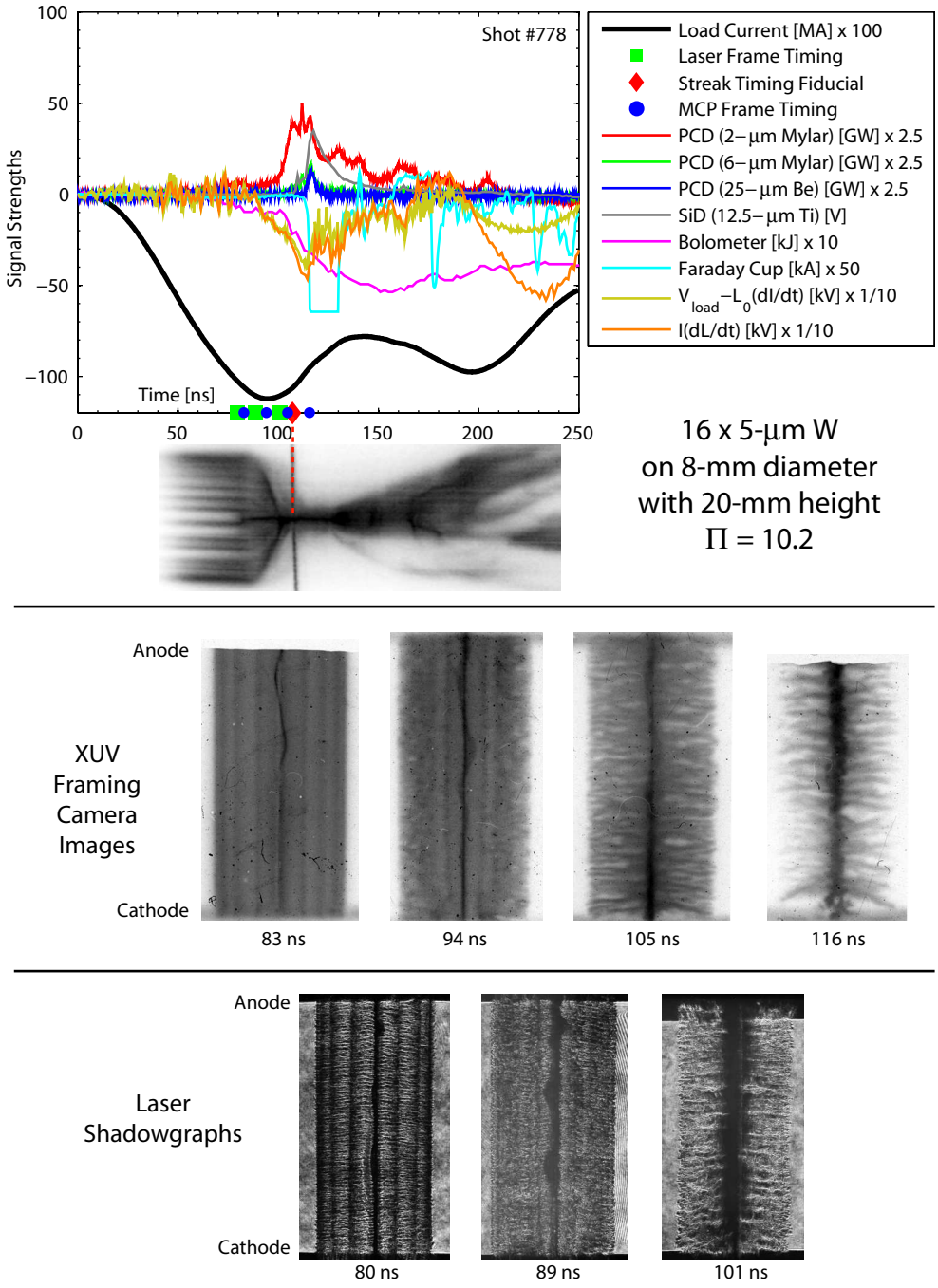

Figure A.13: (Color) Visible streak, XUV framing camera, laser shadowgraph, and various signal data for shot 778.

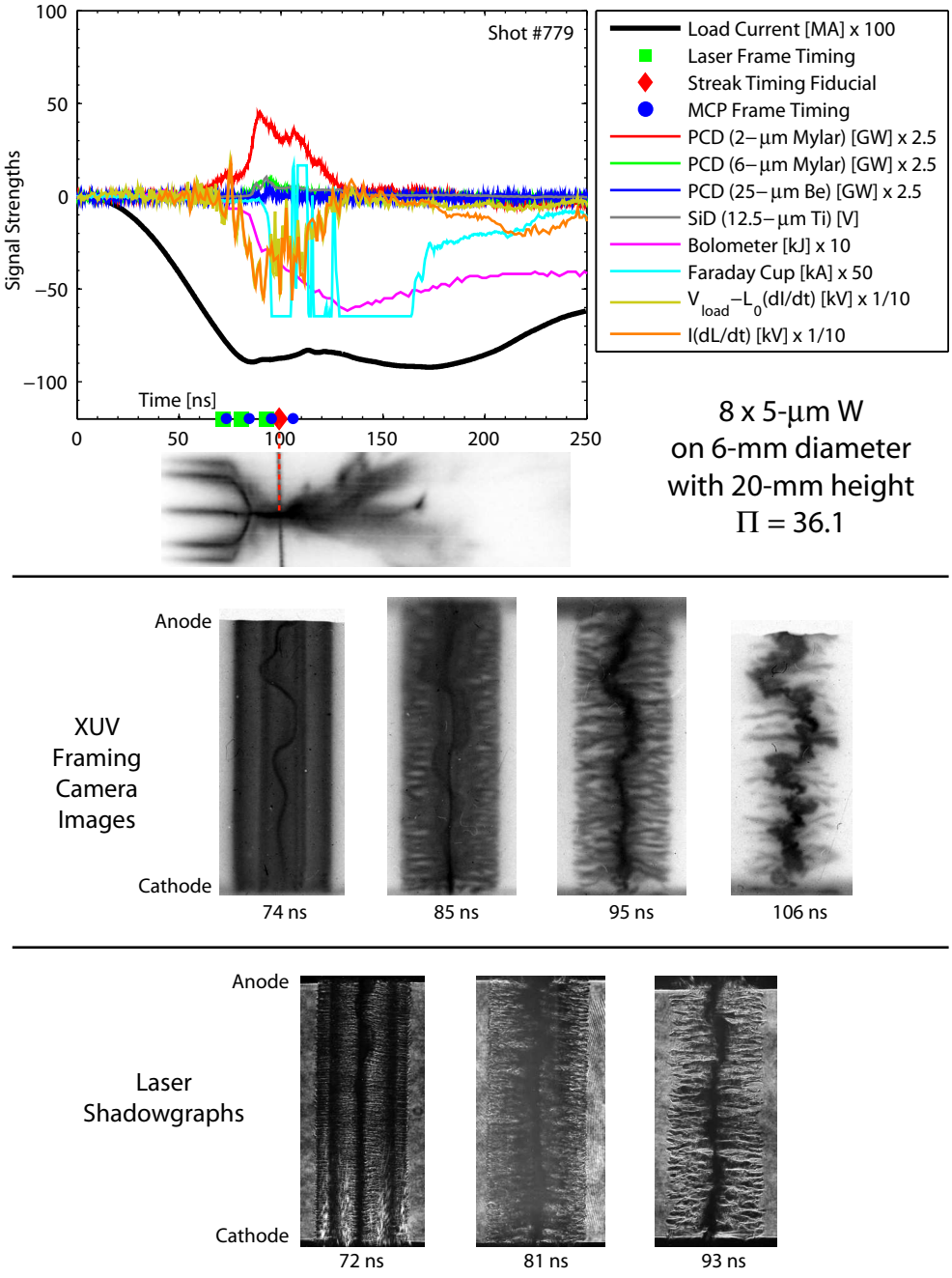

Figure A.14: (Color) Visible streak, XUV framing camera, laser shadowgraph, and various signal data for shot 779.

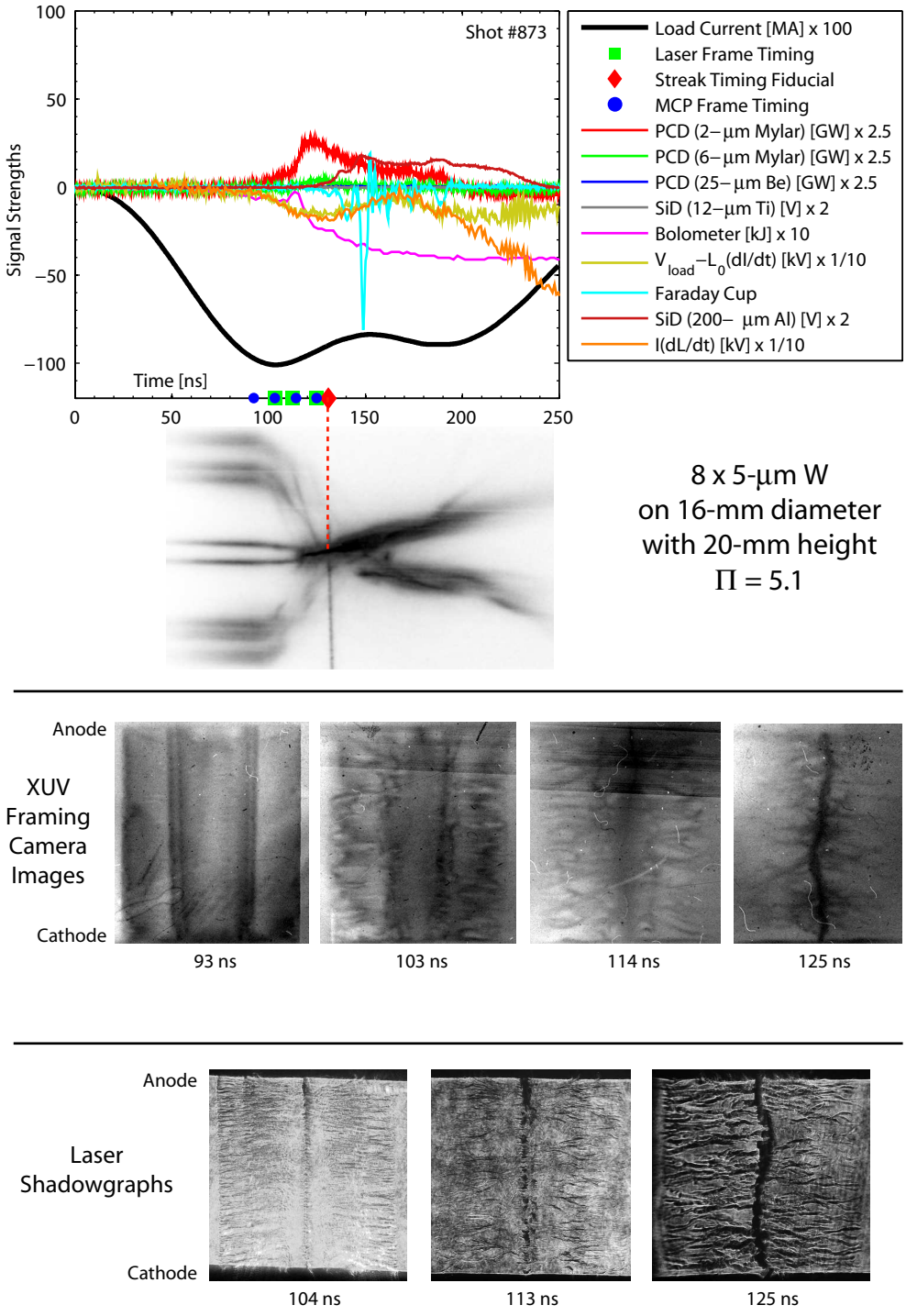

Figure A.15: (Color) Visible streak, XUV framing camera, laser shadowgraph, and various signal data for shot 873.

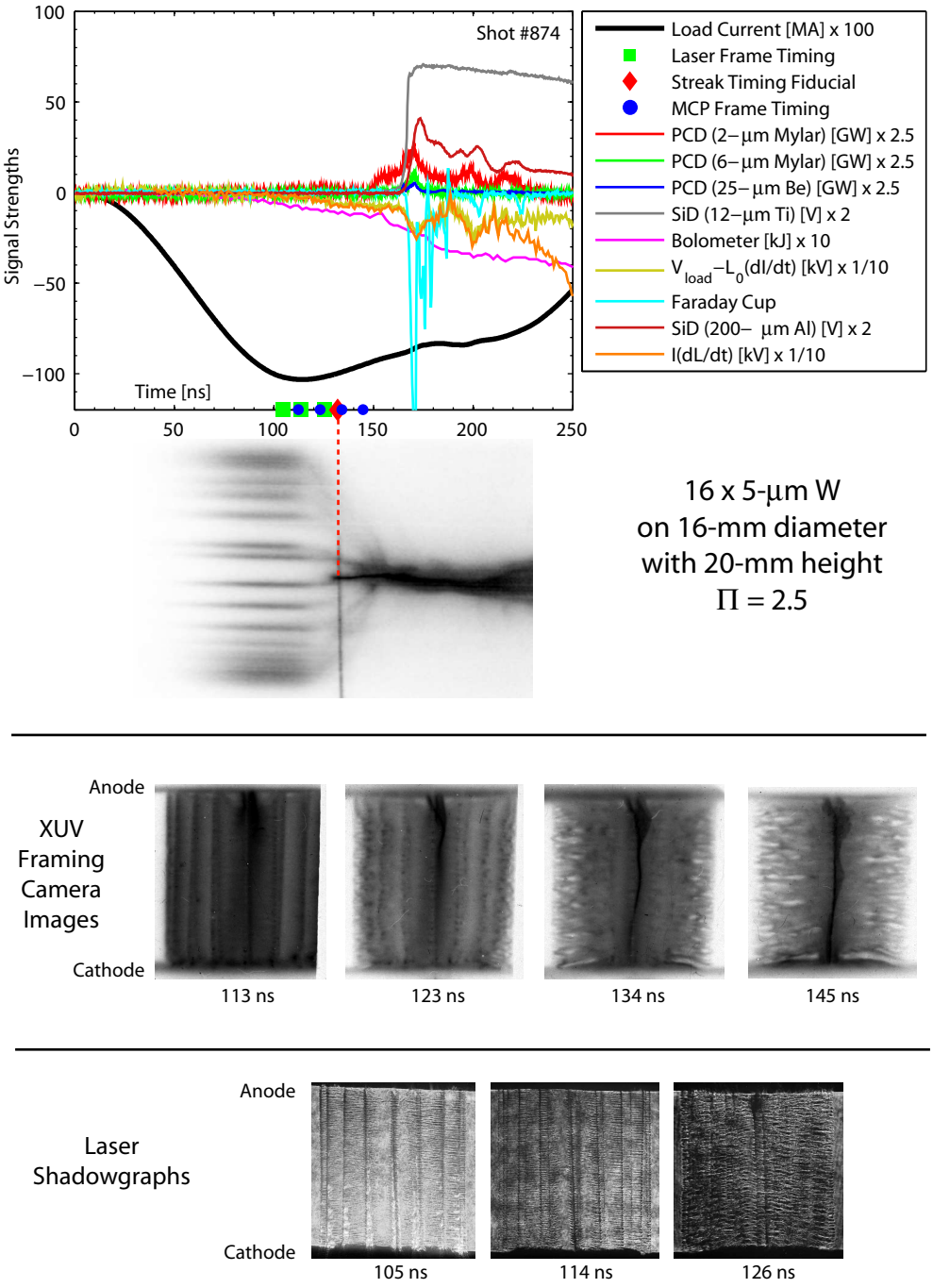

Figure A.16: (Color) Visible streak, XUV framing camera, laser shadowgraph, and various signal data for shot 874.

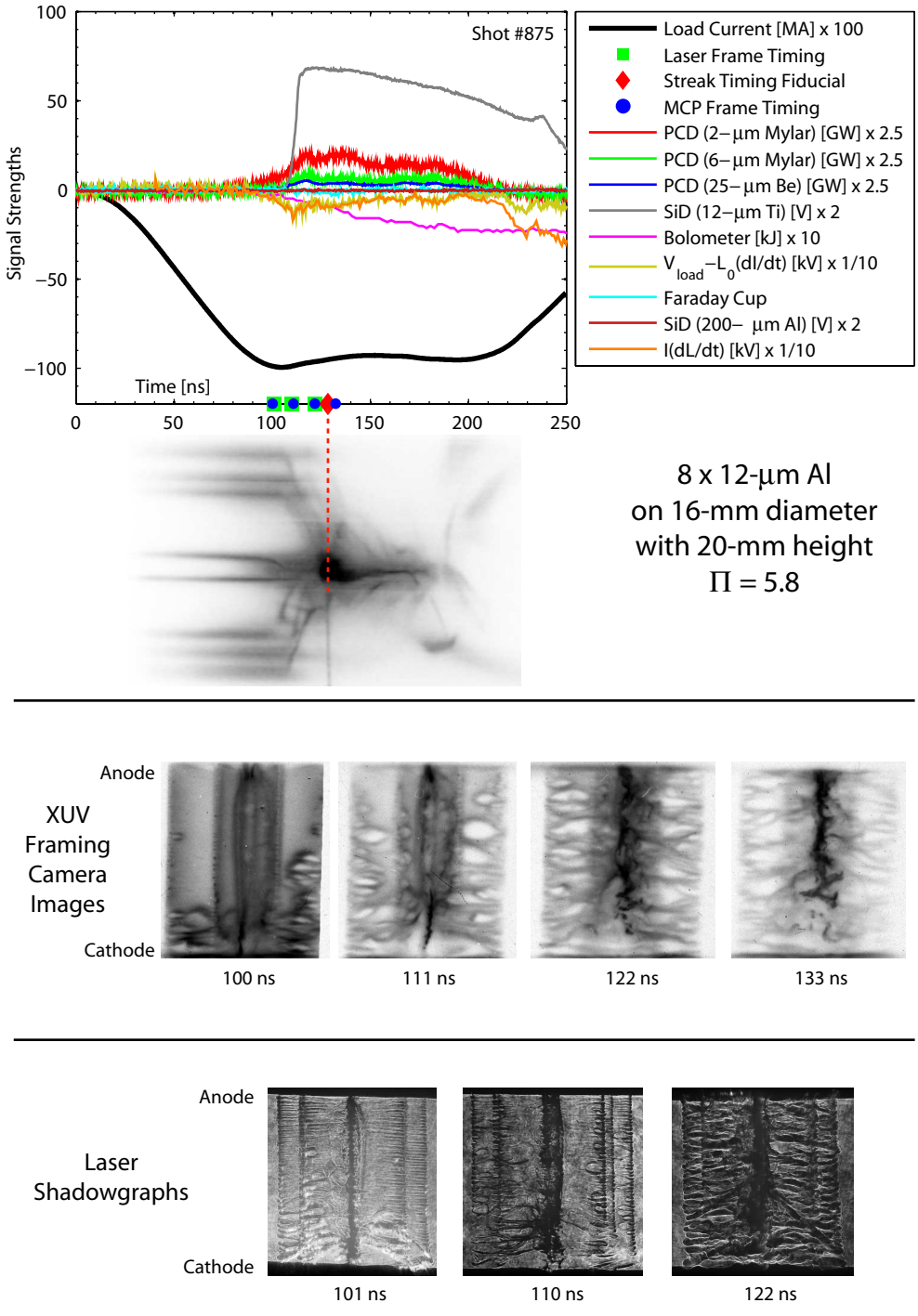

Figure A.17: (Color) Visible streak, XUV framing camera, laser shadowgraph, and various signal data for shot 875.

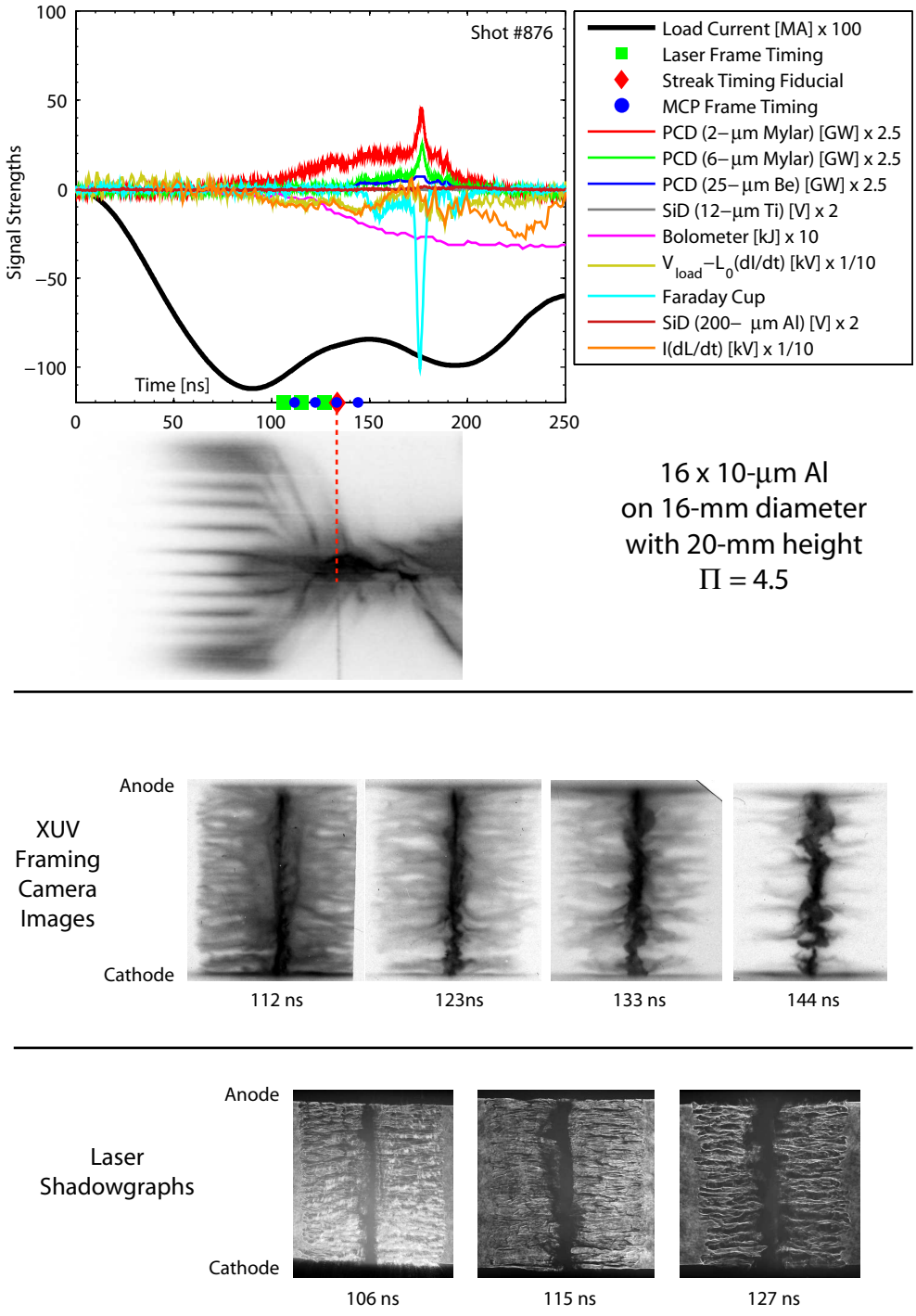

Figure A.18: (Color) Visible streak, XUV framing camera, laser shadowgraph, and various signal data for shot 876.

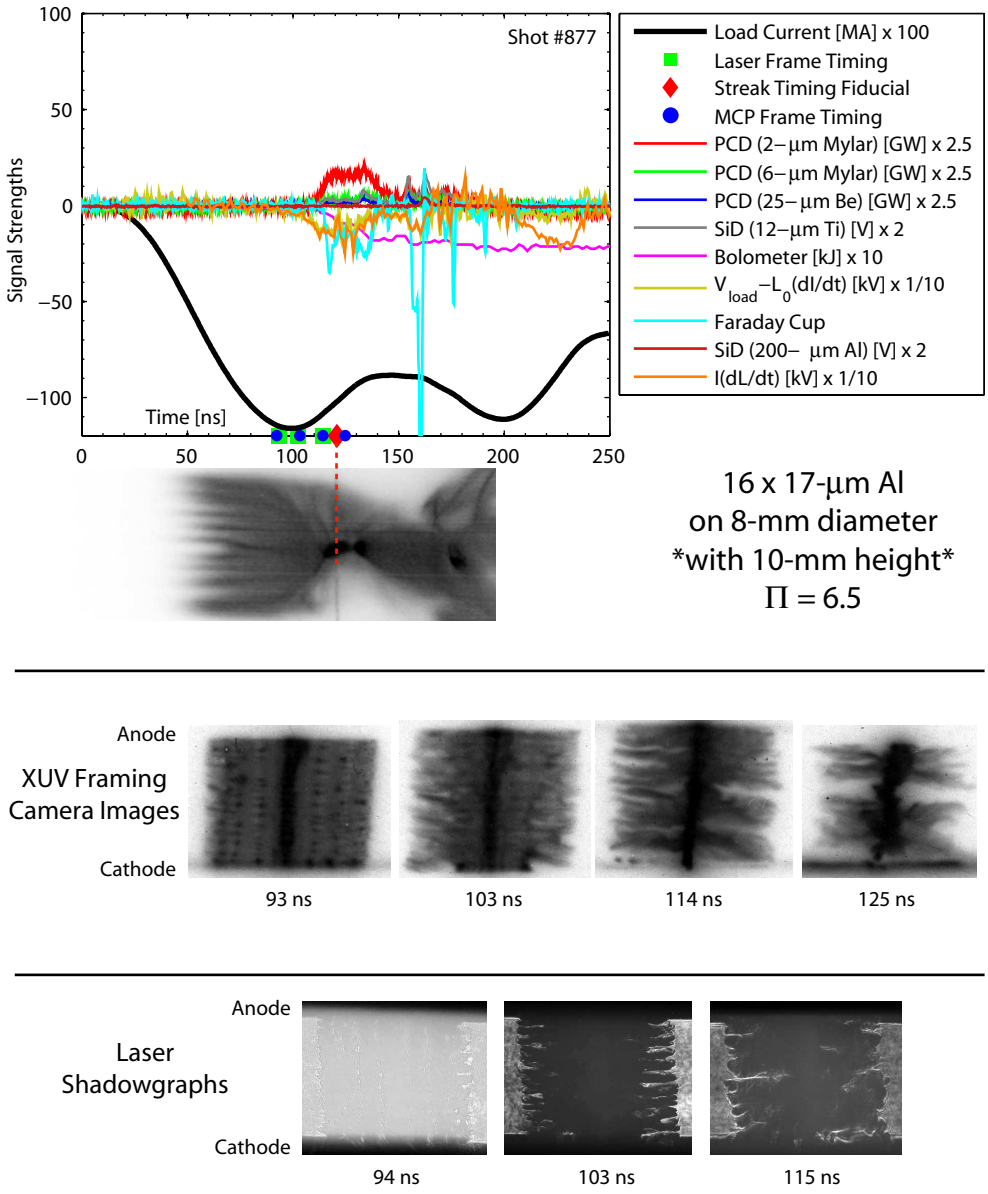

Figure A.19: (Color) Visible streak, XUV framing camera, laser shadowgraph, and various signal data for shot 877.

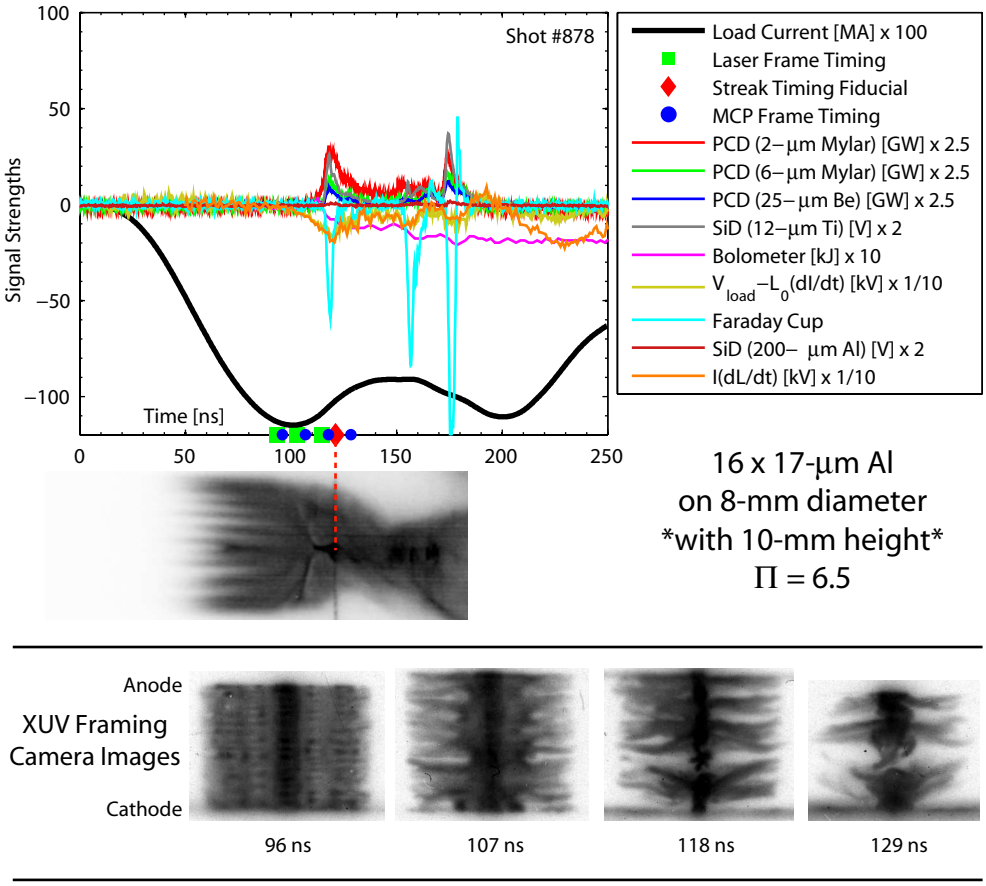

Figure A.20: (Color) Visible streak, XUV framing camera, laser shadowgraph, and various signal data for shot 878.

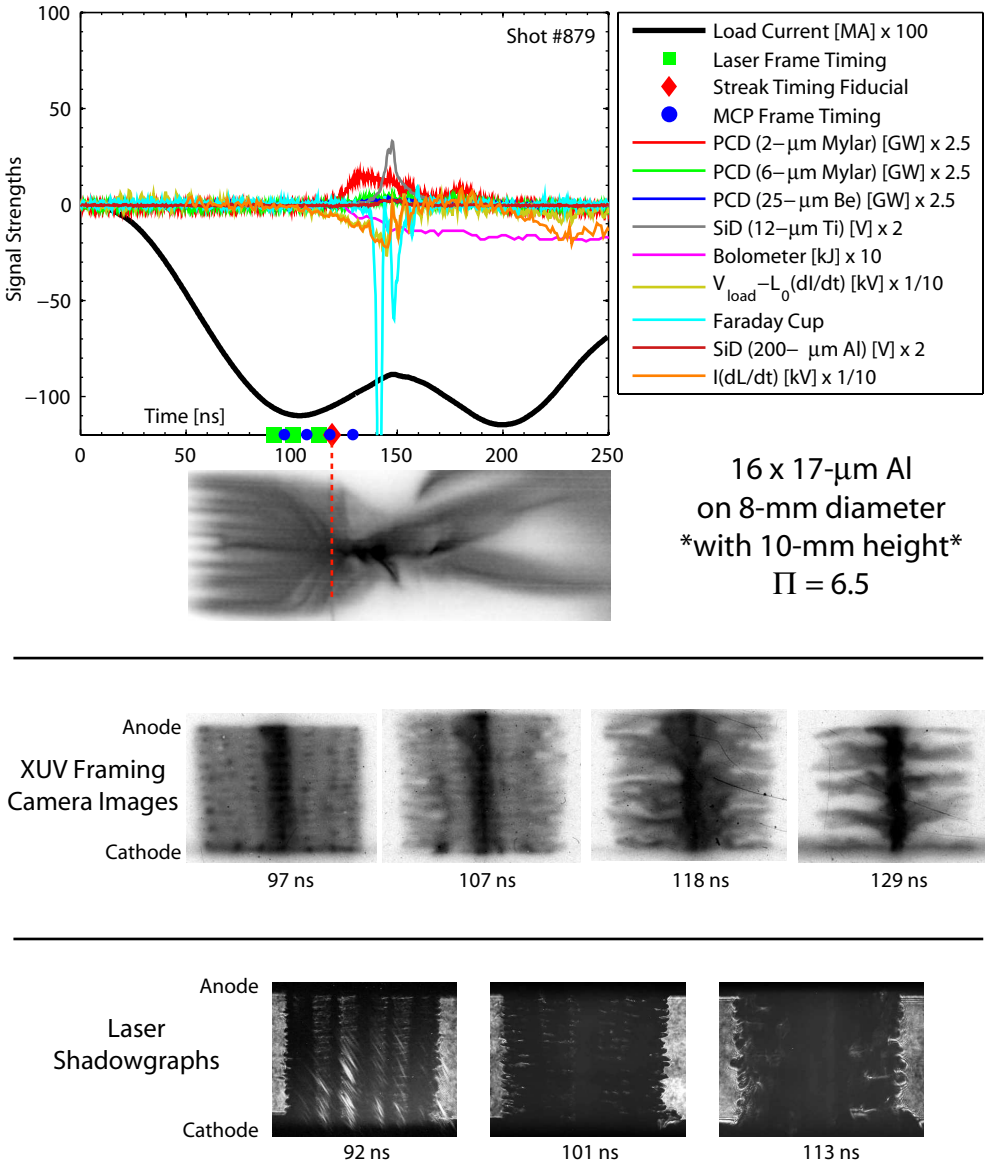

Figure A.21: (Color) Visible streak, XUV framing camera, laser shadowgraph, and various signal data for shot 879.

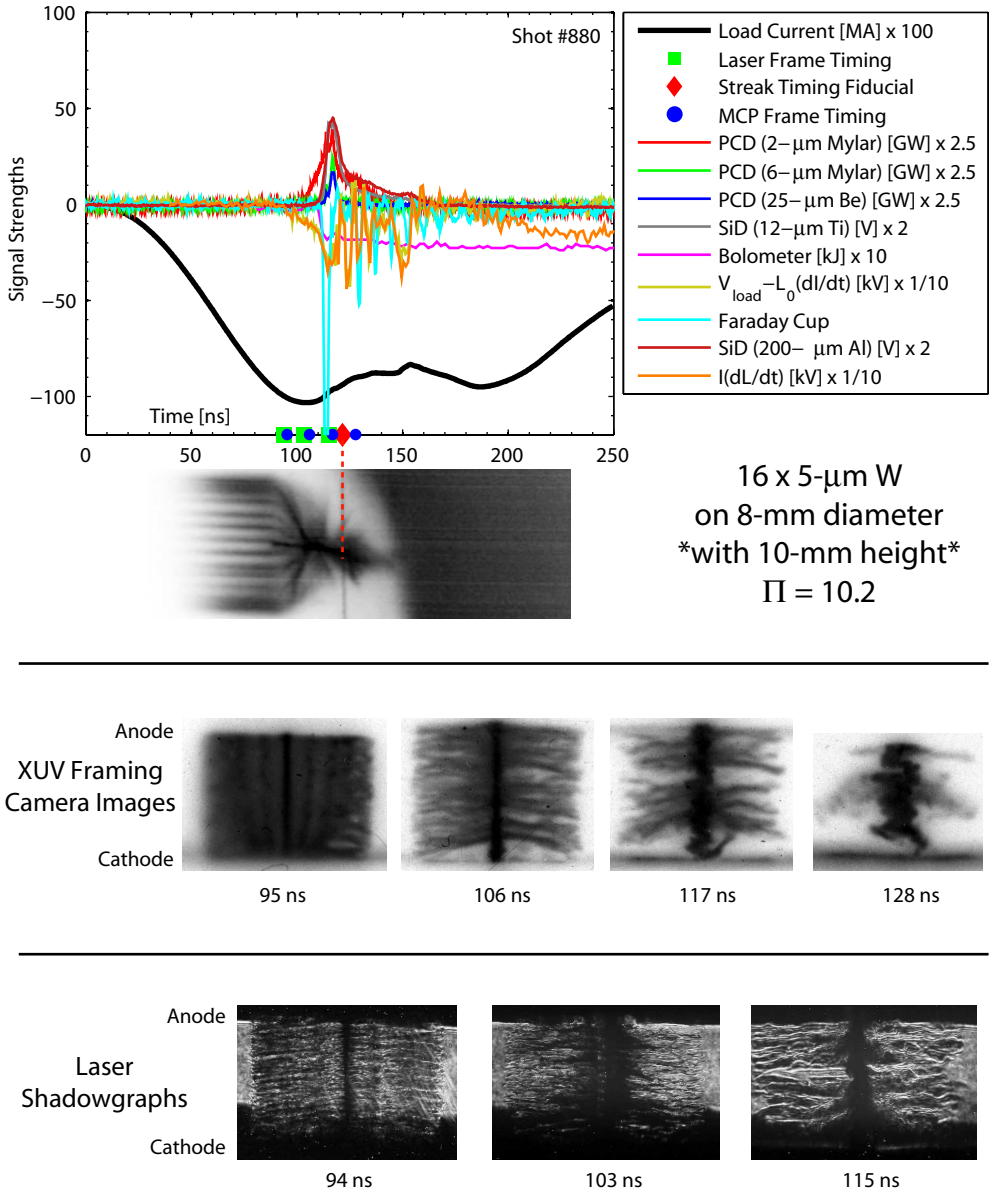

Figure A.22: (Color) Visible streak, XUV framing camera, laser shadowgraph, and various signal data for shot 880.

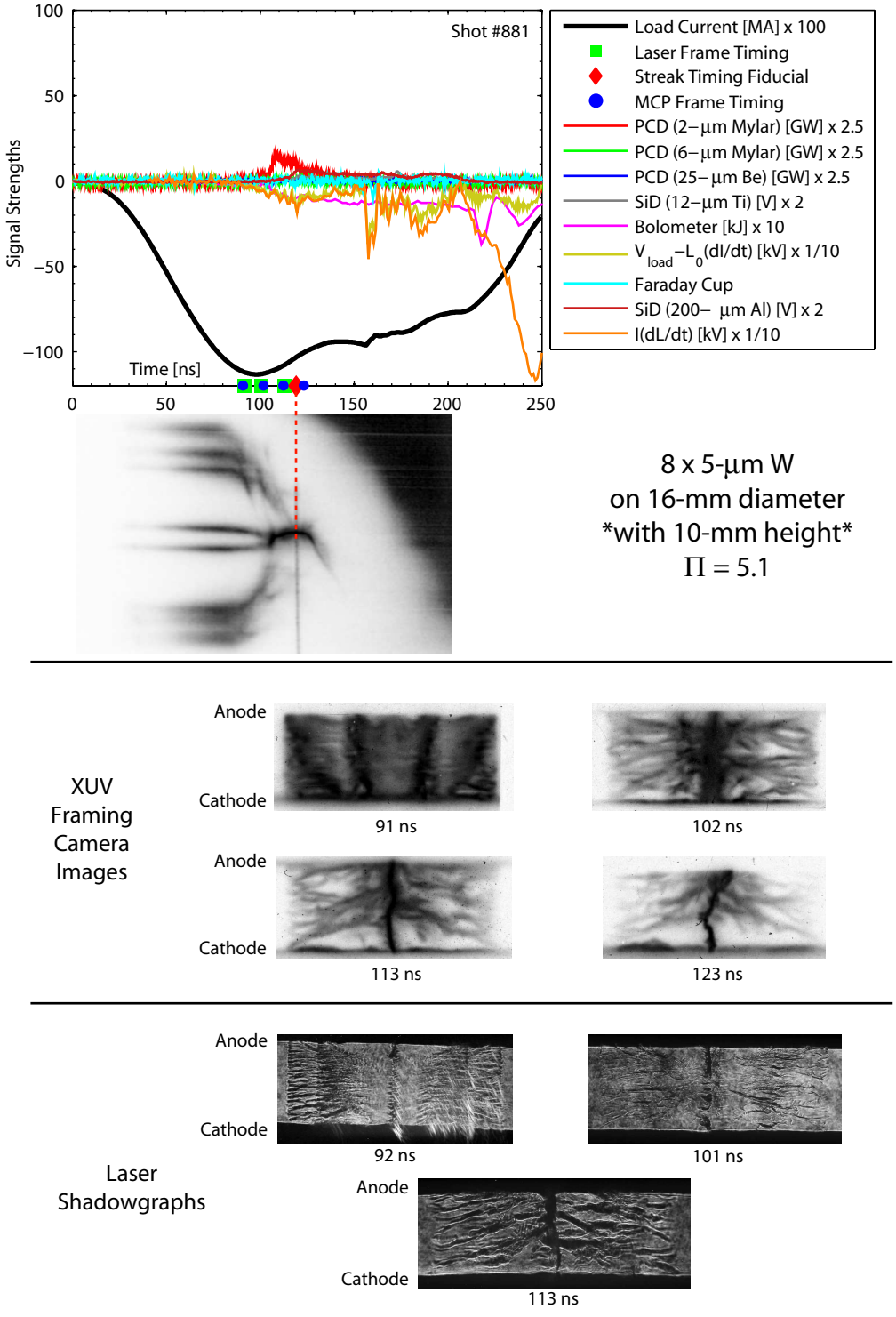

Figure A.23: (Color) Visible streak, XUV framing camera, laser shadowgraph, and various signal data for shot 881.

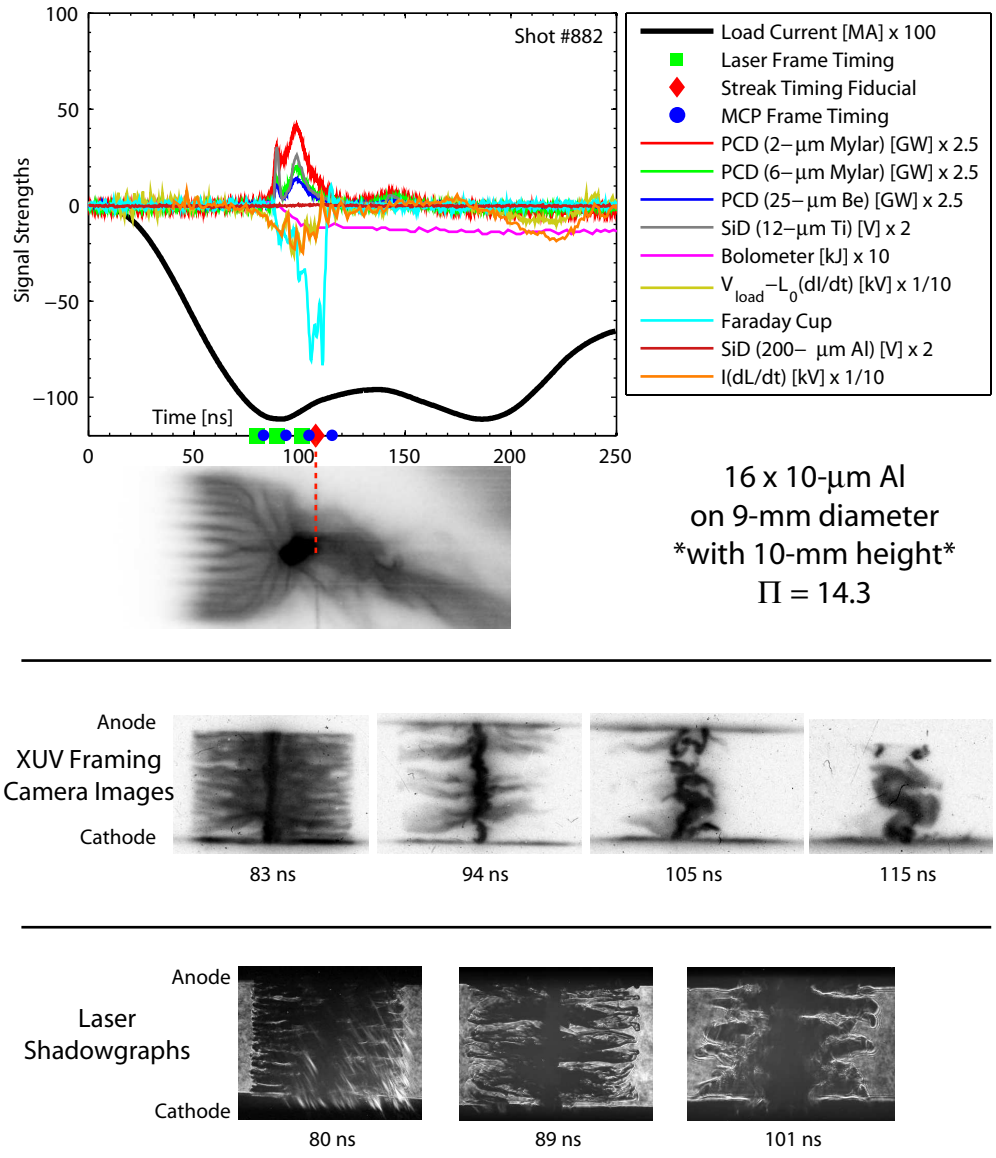

Figure A.24: (Color) Visible streak, XUV framing camera, laser shadowgraph, and various signal data for shot 882.

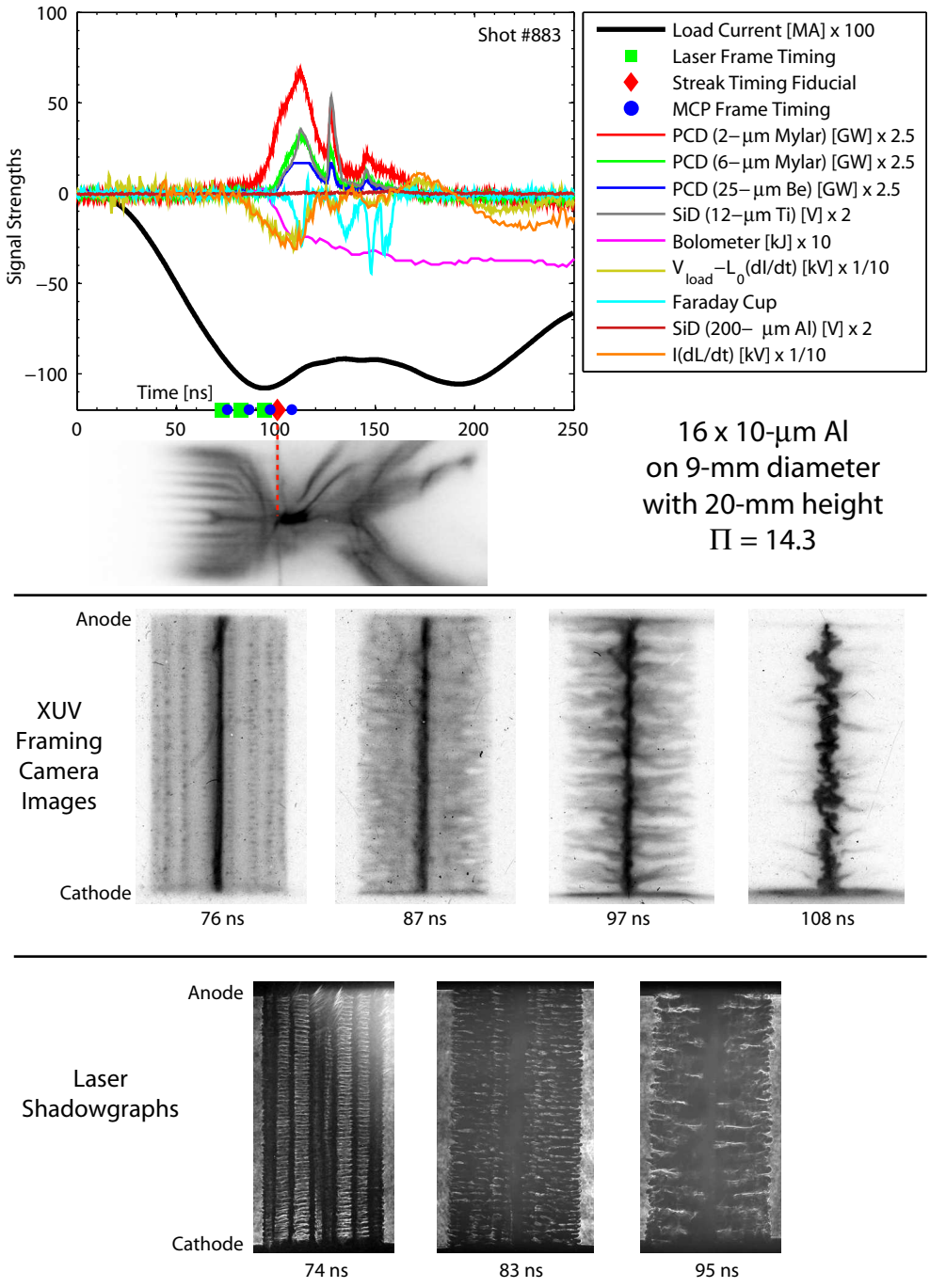

Figure A.25: (Color) Visible streak, XUV framing camera, laser shadowgraph, and various signal data for shot 883.

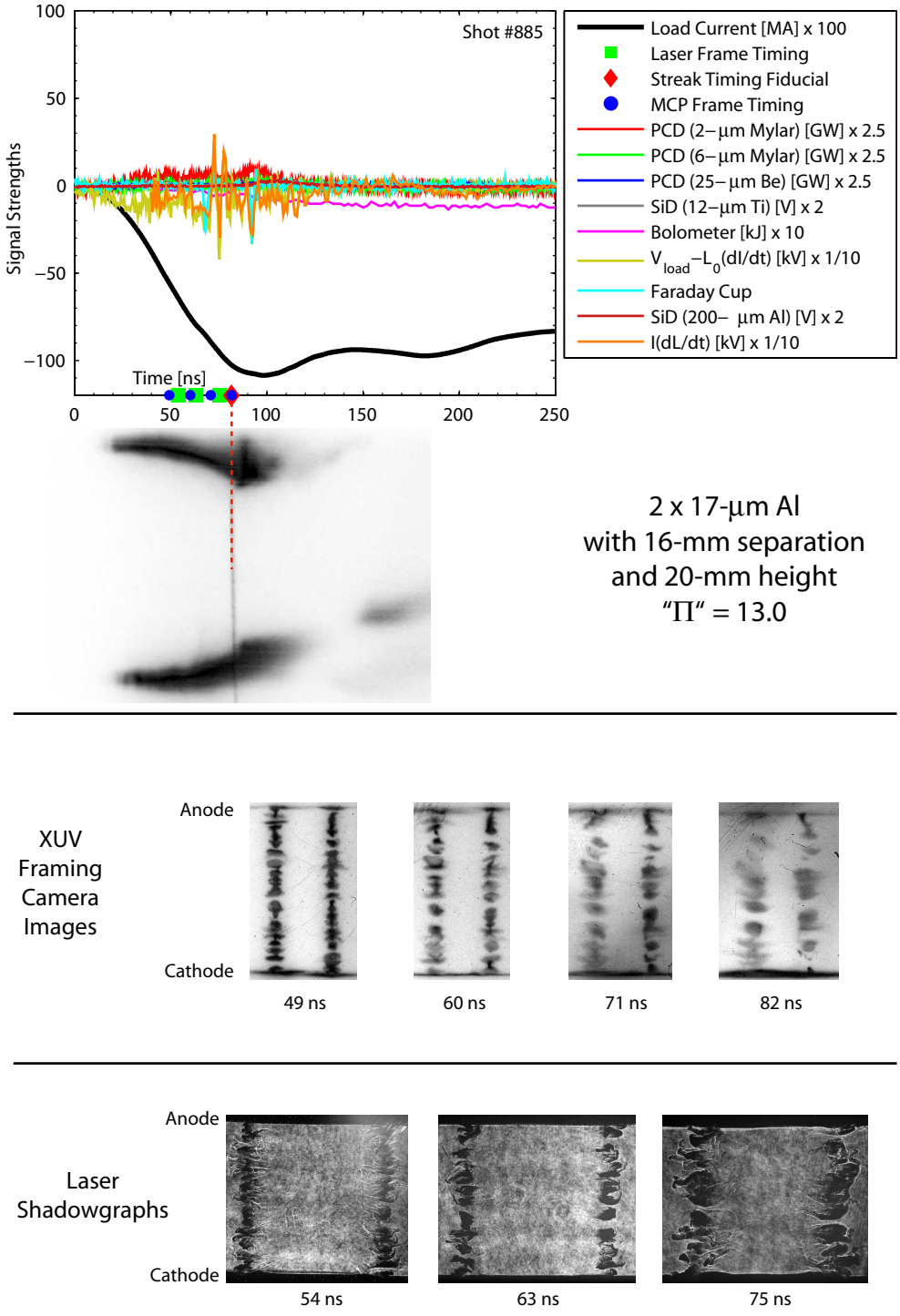

Figure A.26: (Color) Visible streak, XUV framing camera, laser shadowgraph, and various signal data for shot 885.

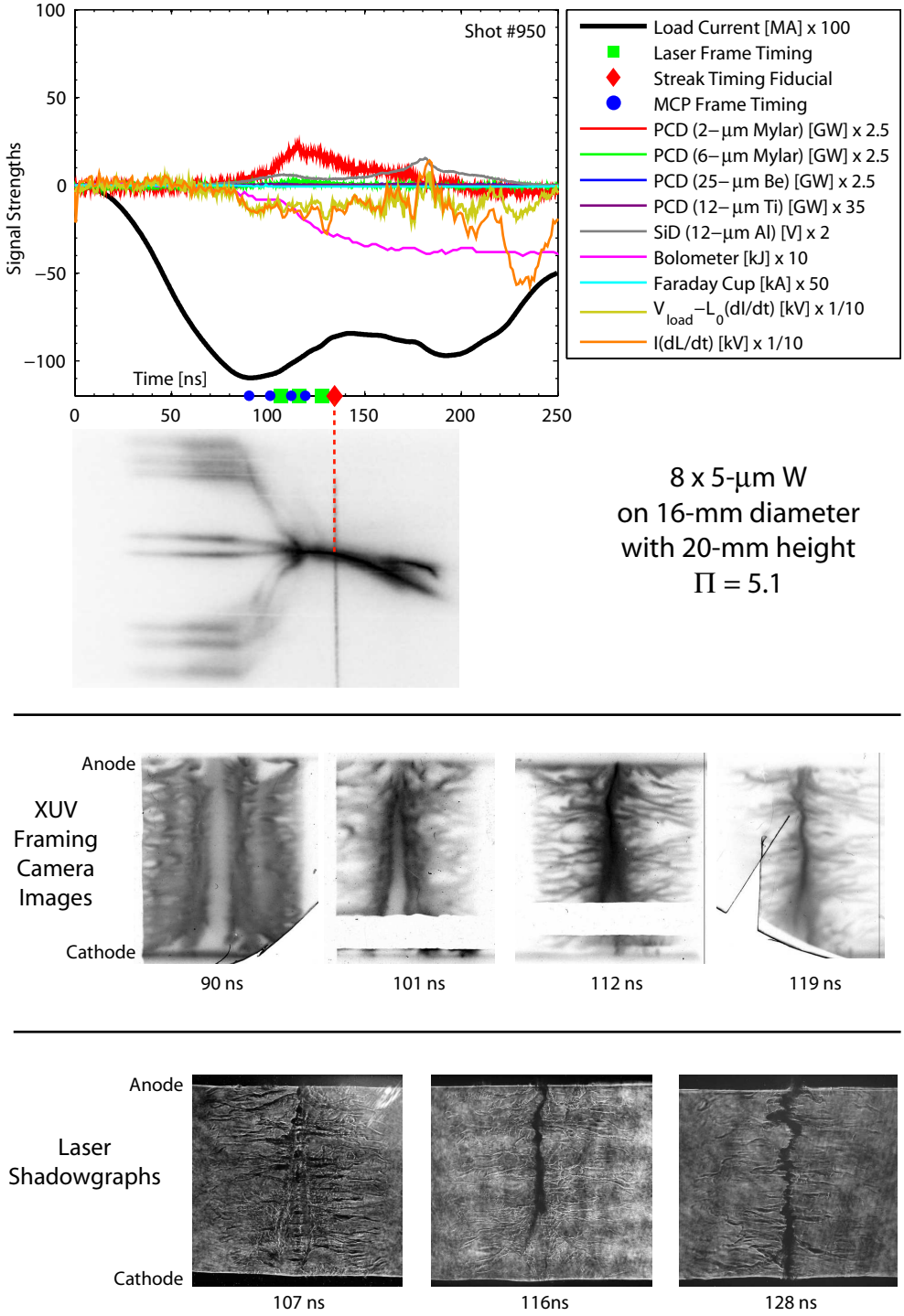

Figure A.27: (Color) Visible streak, XUV framing camera, laser shadowgraph, and various signal data for shot 950.

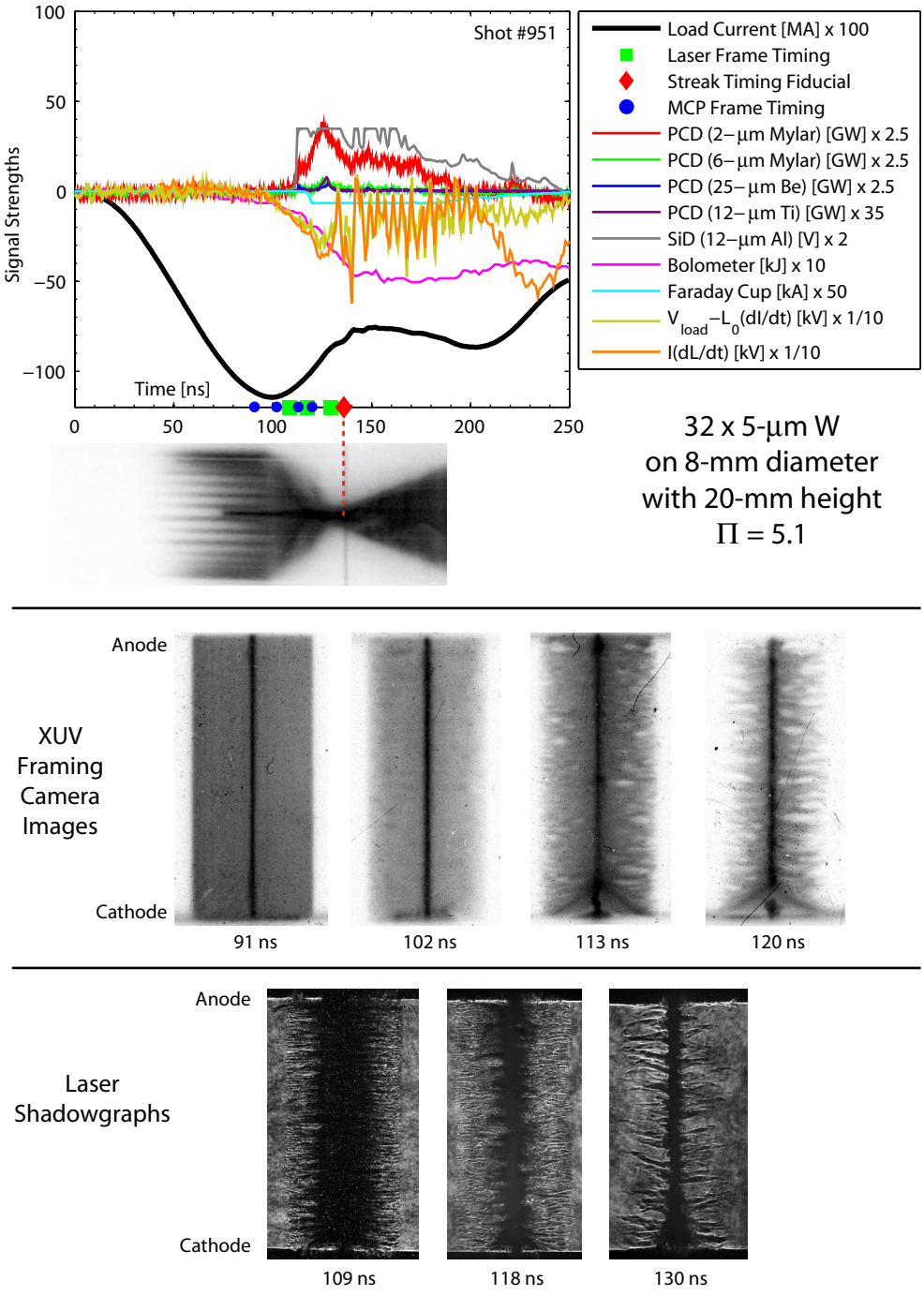

Figure A.28: (Color) Visible streak, XUV framing camera, laser shadowgraph, and various signal data for shot 951.

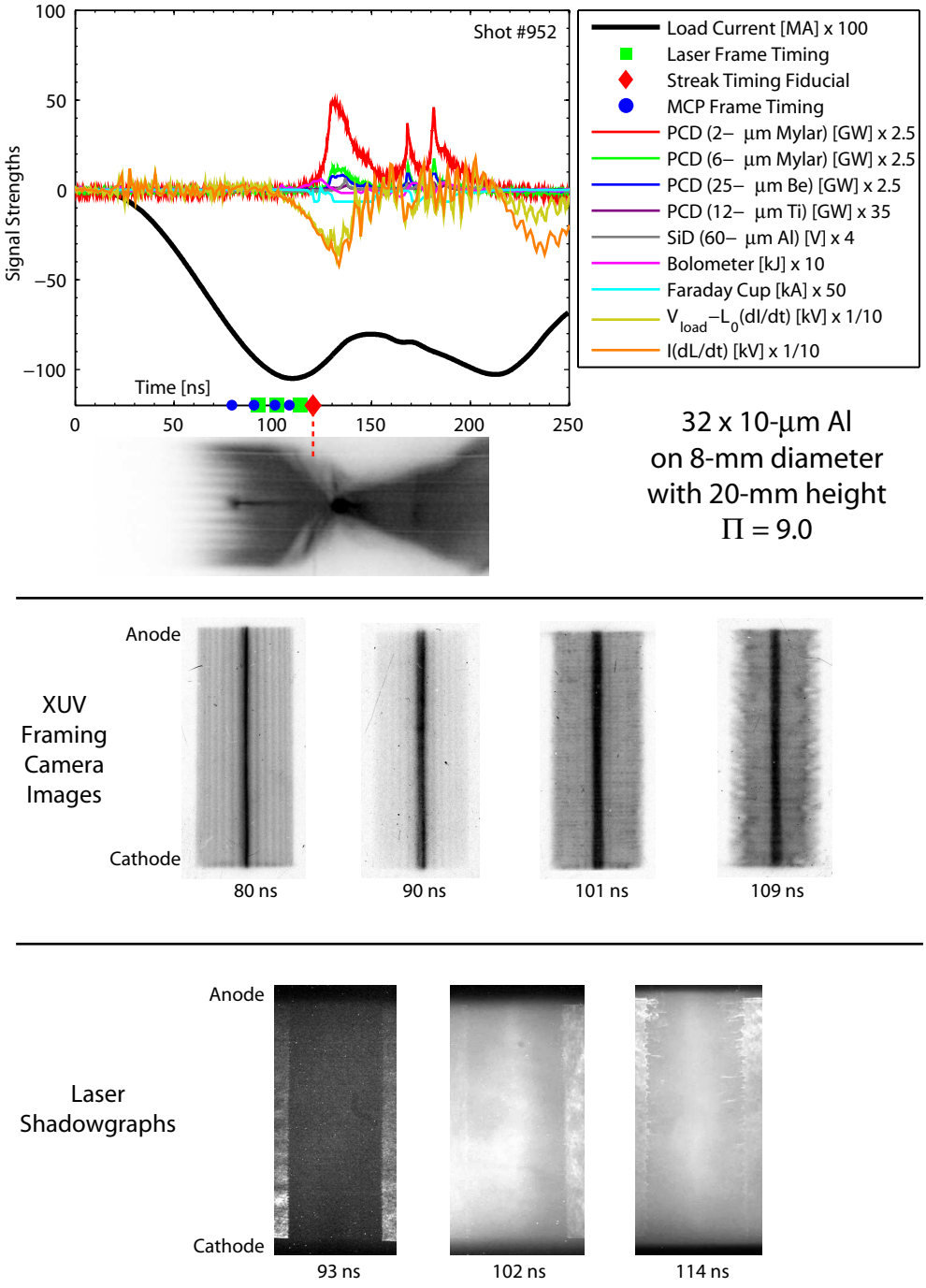

Figure A.29: (Color) Visible streak, XUV framing camera, laser shadowgraph, and various signal data for shot 952.

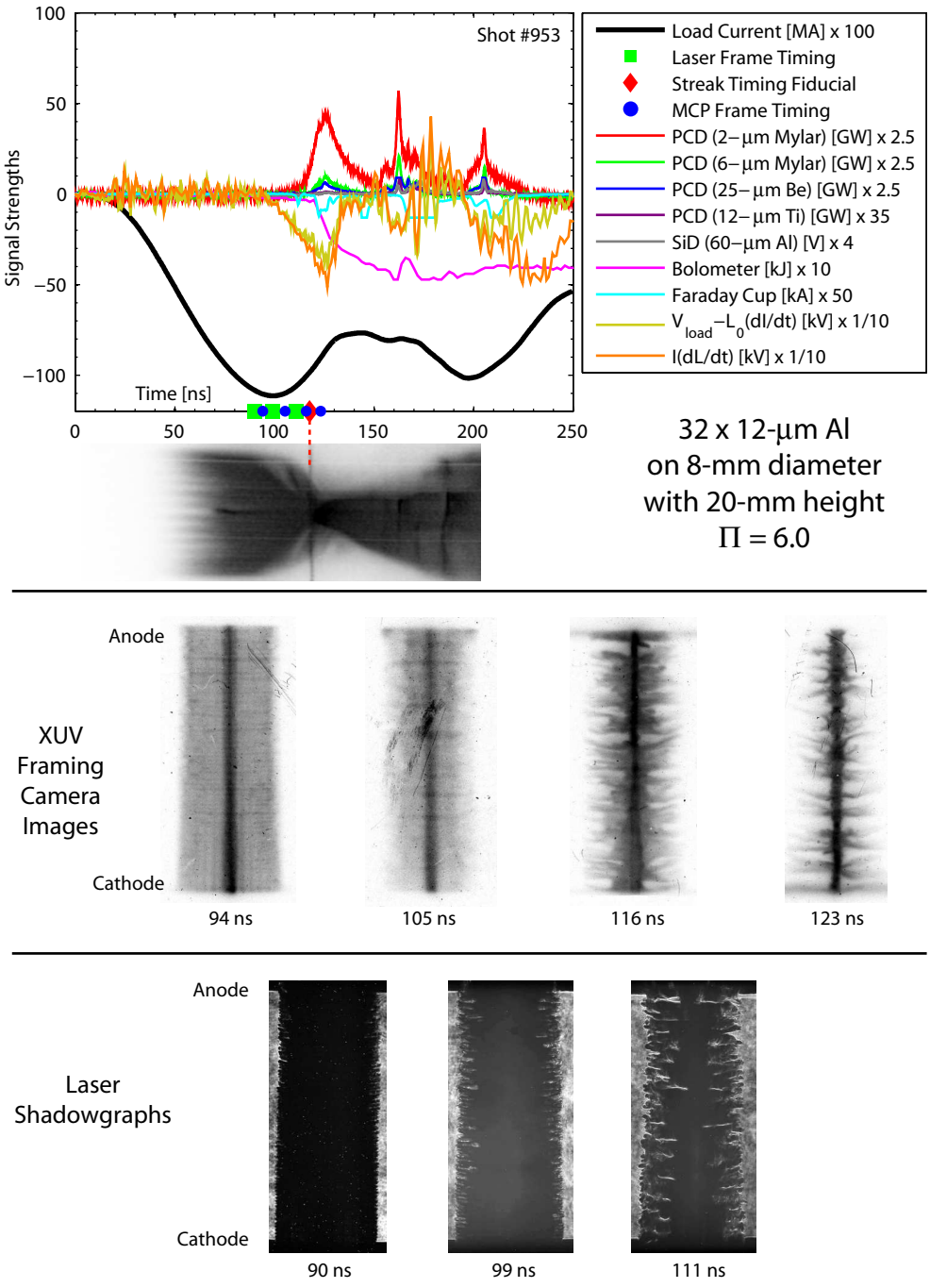

Figure A.30: (Color) Visible streak, XUV framing camera, laser shadowgraph, and various signal data for shot 953.

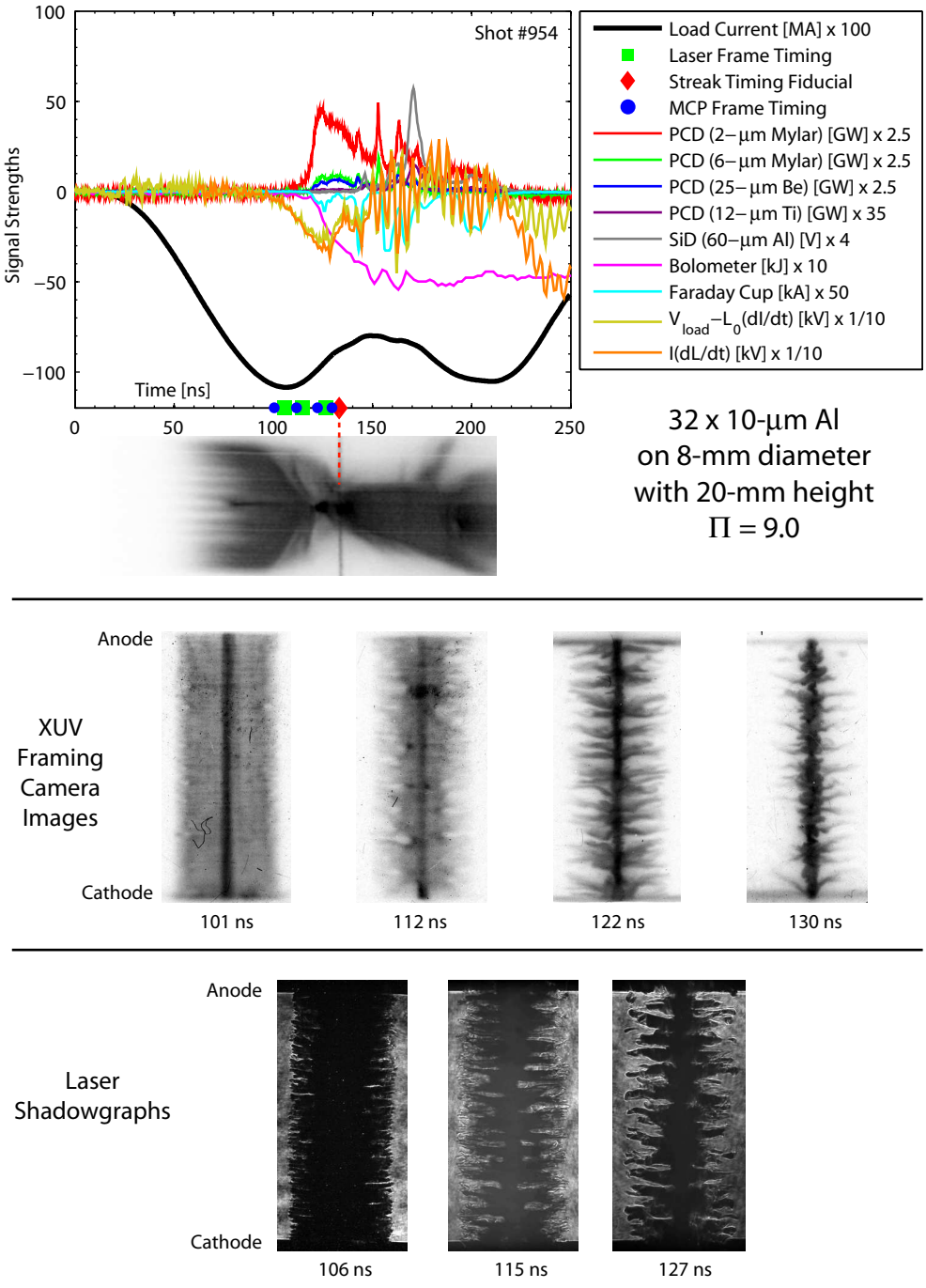

Figure A.31: (Color) Visible streak, XUV framing camera, laser shadowgraph, and various signal data for shot 954.

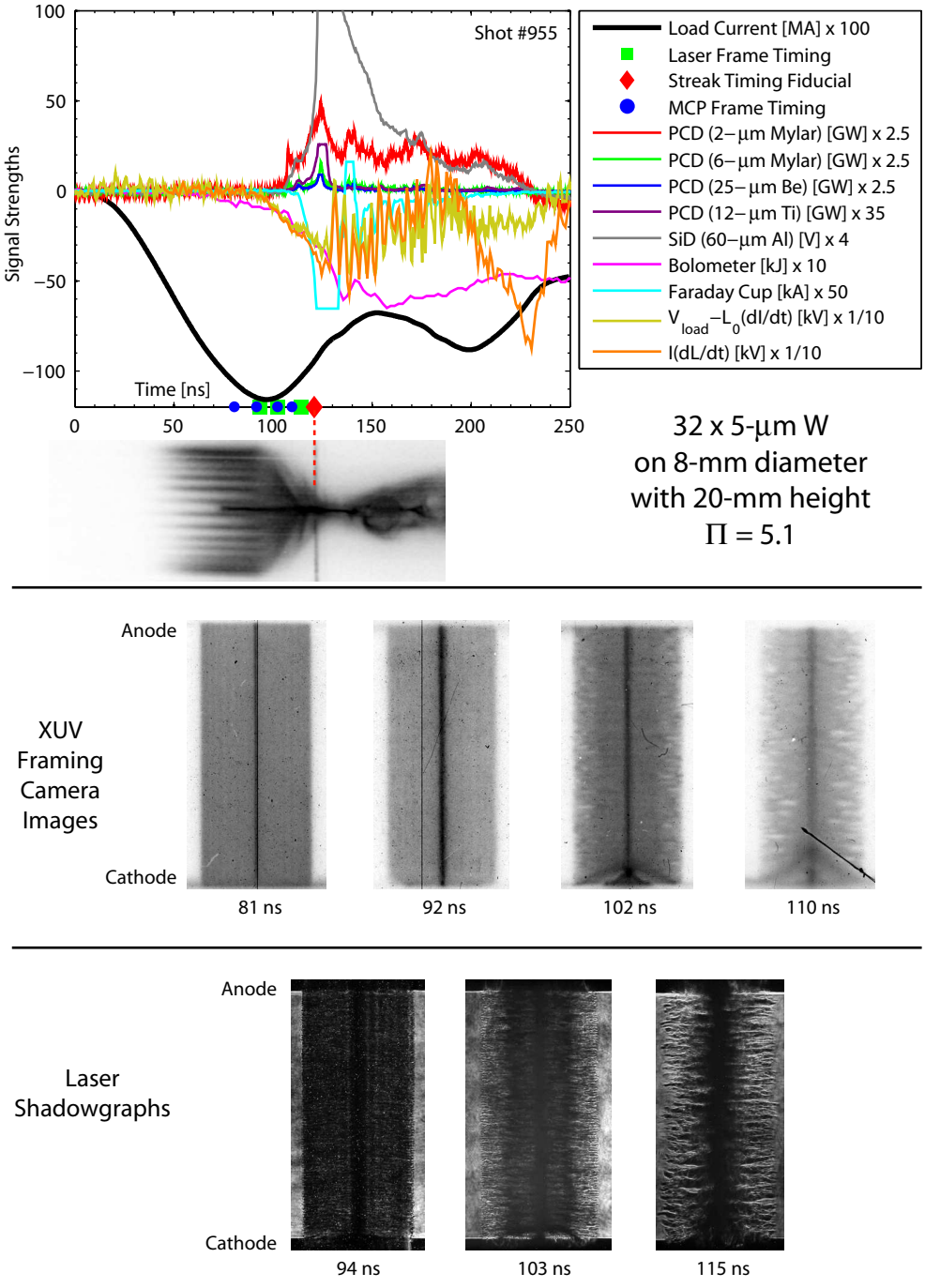

Figure A.32: (Color) Visible streak, XUV framing camera, laser shadowgraph, and various signal data for shot 955.

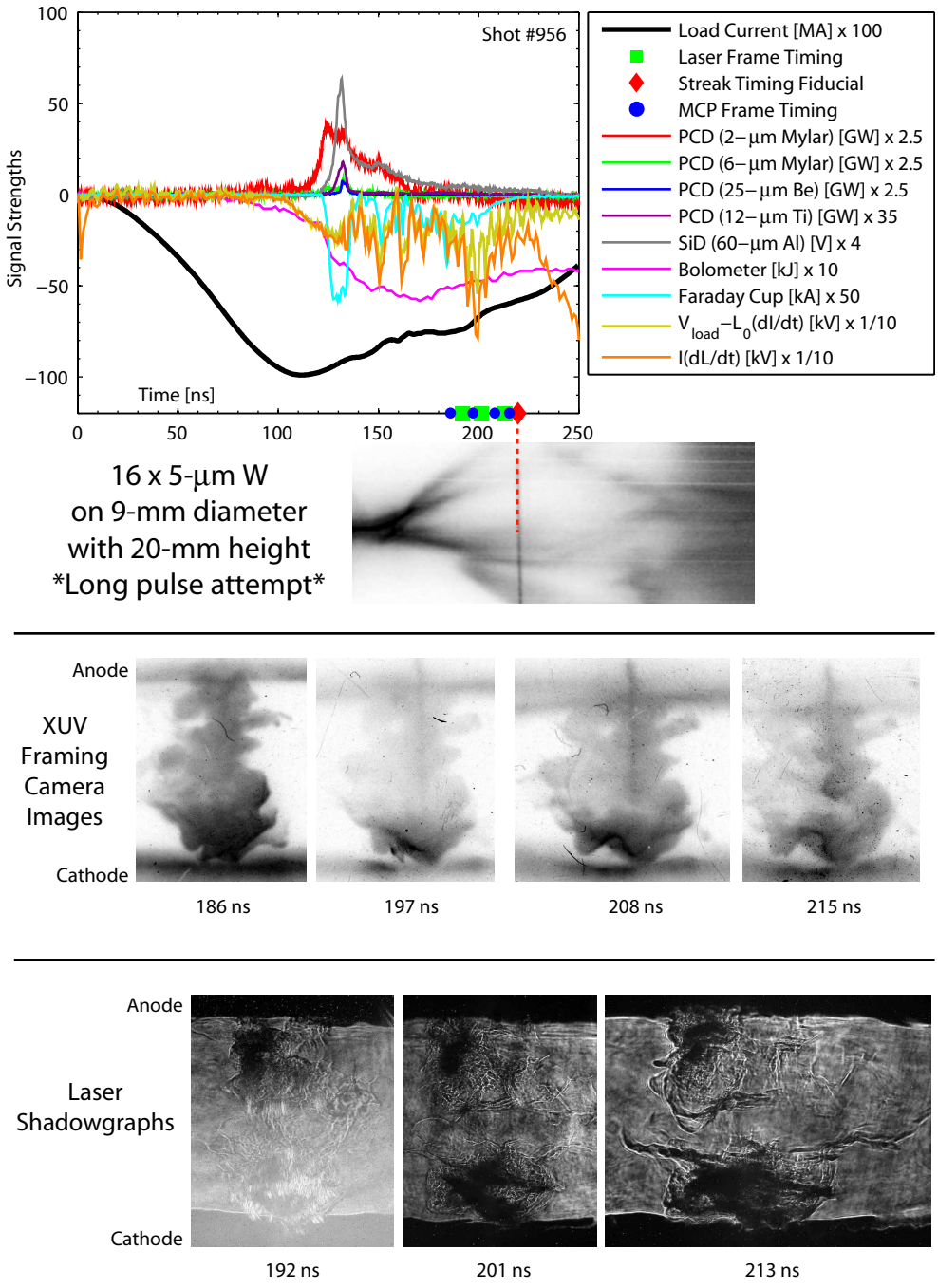

Figure A.33: (Color) Visible streak, XUV framing camera, laser shadowgraph, and various signal data for shot 956.

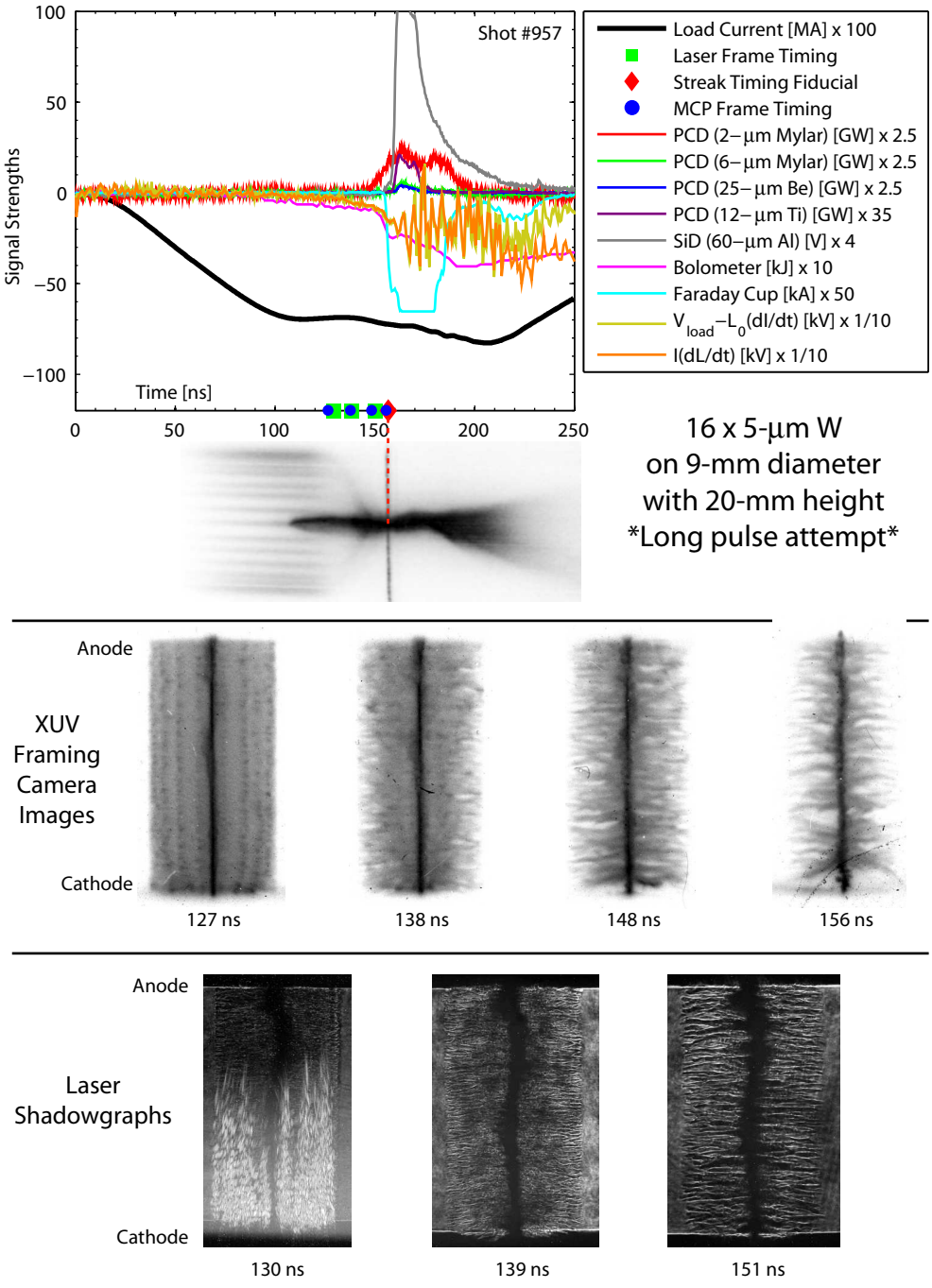

Figure A.34: (Color) Visible streak, XUV framing camera, laser shadowgraph, and various signal data for shot 957.

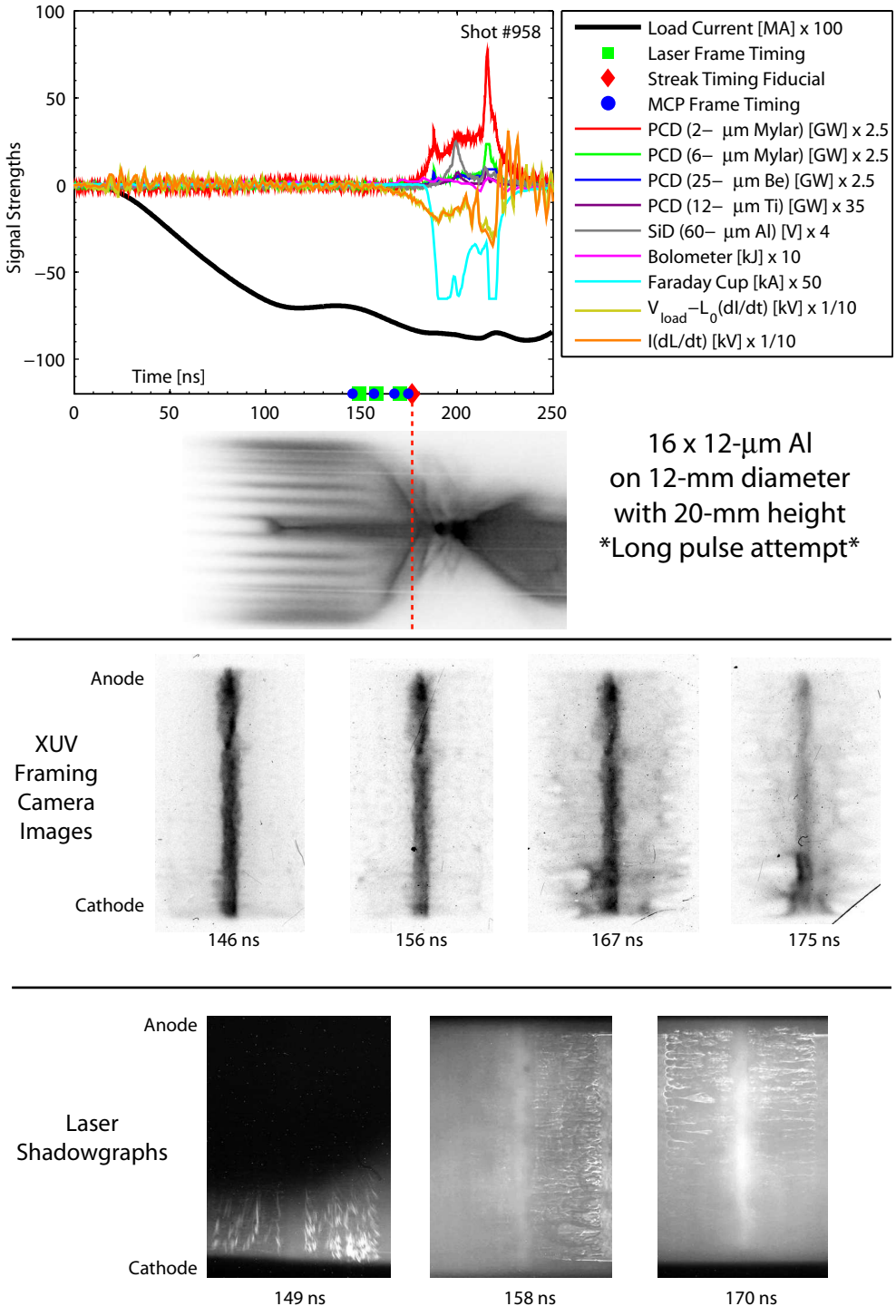

Figure A.35: (Color) Visible streak, XUV framing camera, laser shadowgraph, and various signal data for shot 958.

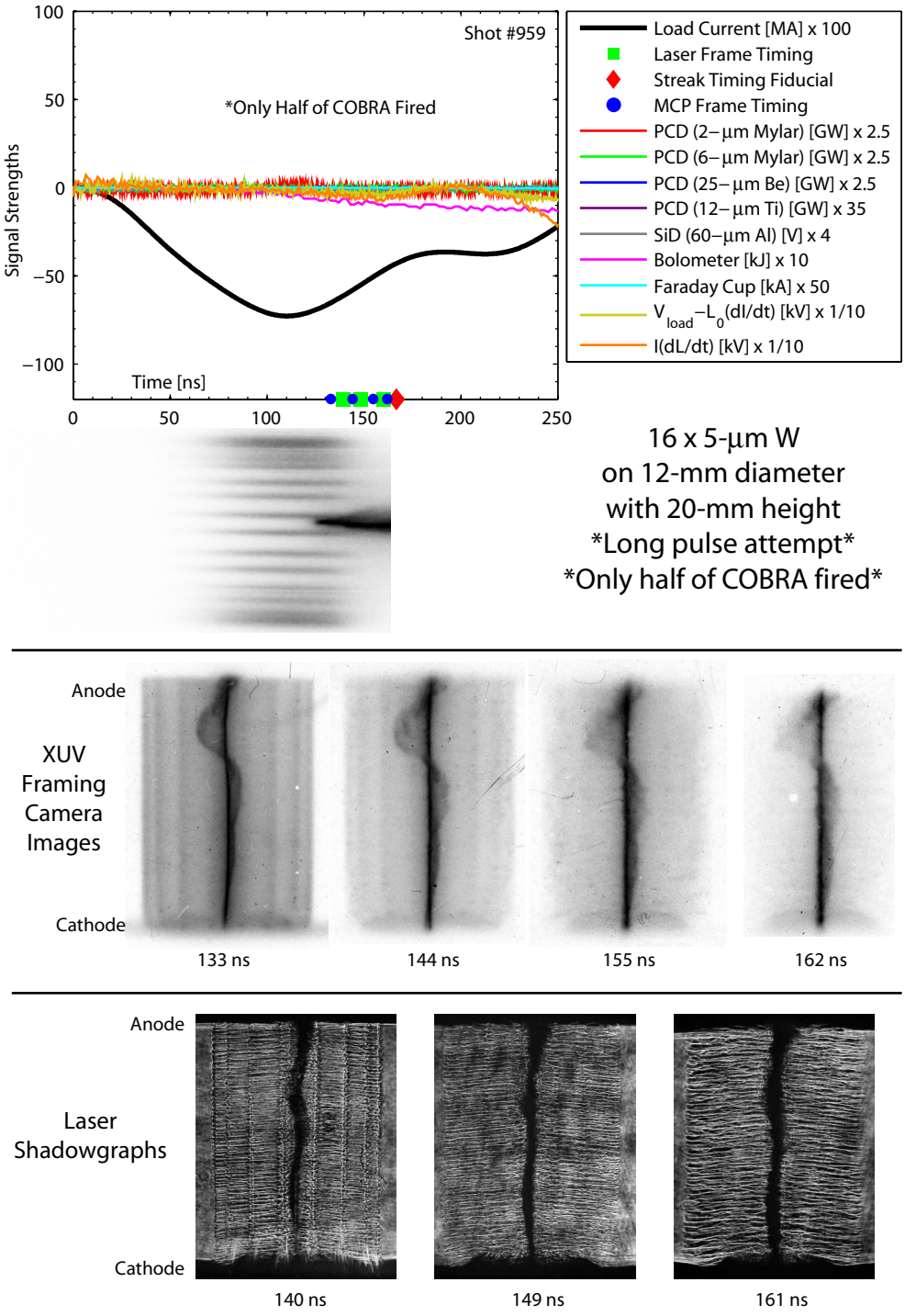

Figure A.36: (Color) Visible streak, XUV framing camera, laser shadowgraph, and various signal data for shot 959.

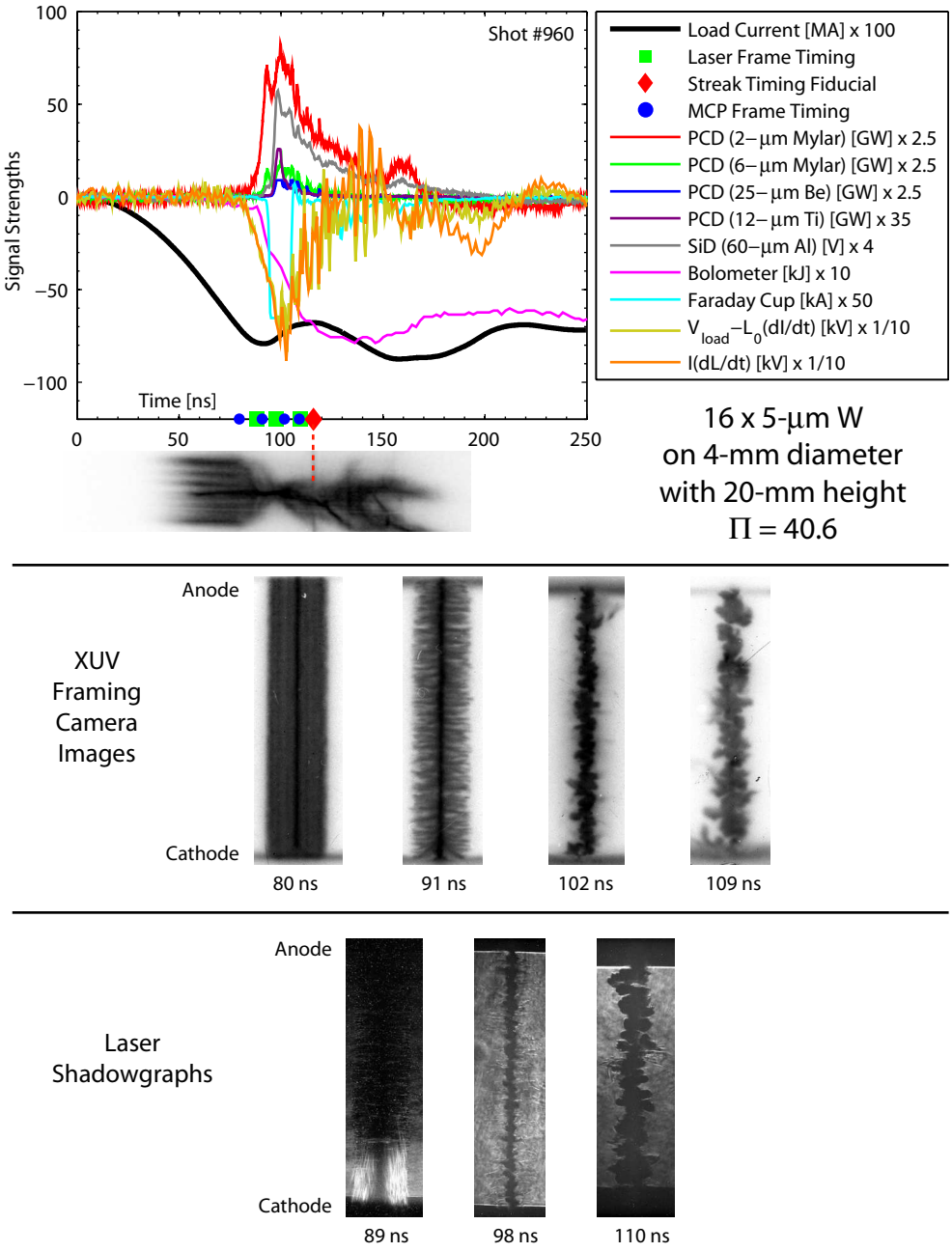

Figure A.37: (Color) Visible streak, XUV framing camera, laser shadowgraph, and various signal data for shot 960.

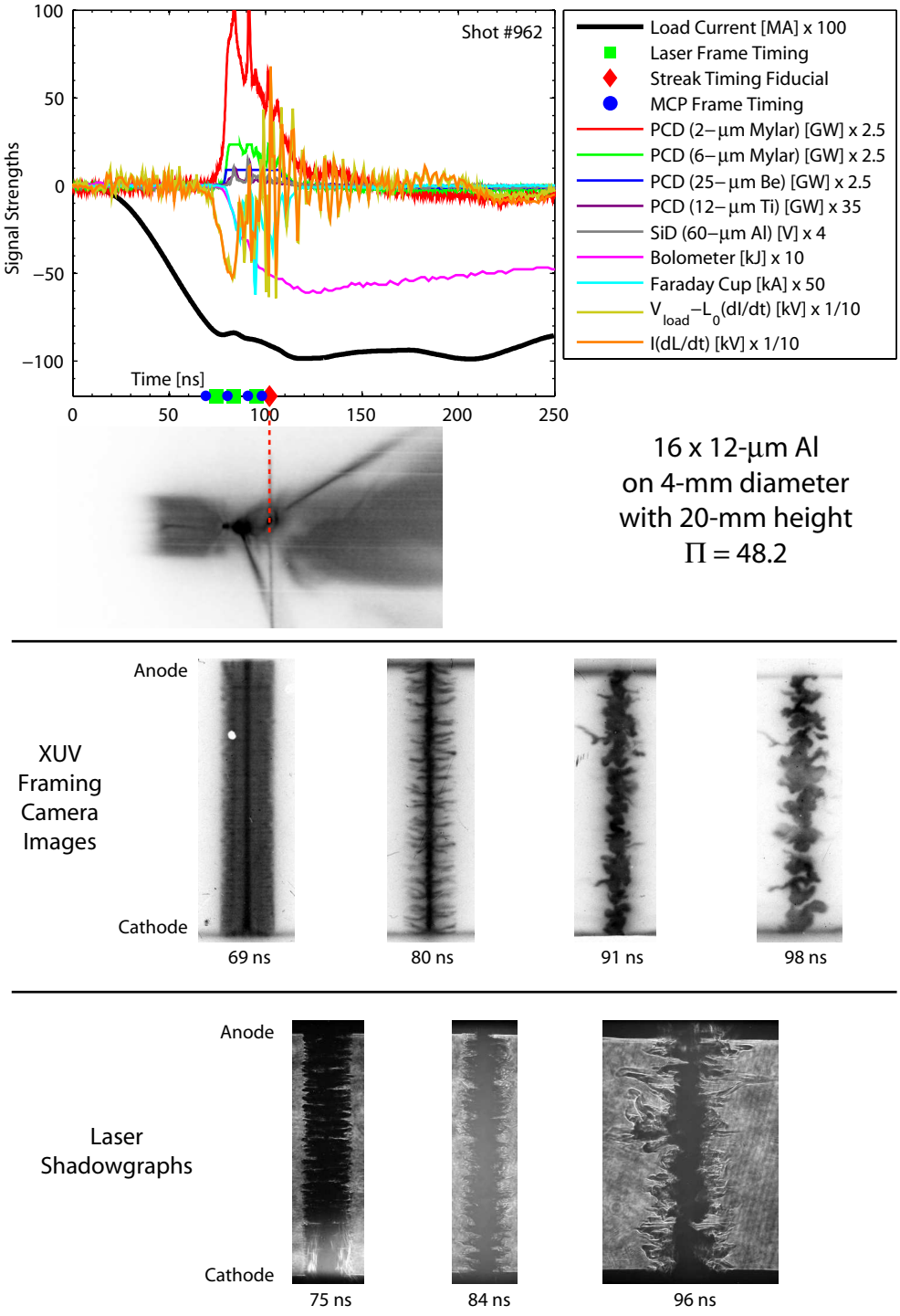

Figure A.38: (Color) Visible streak, XUV framing camera, laser shadowgraph, and various signal data for shot 962.

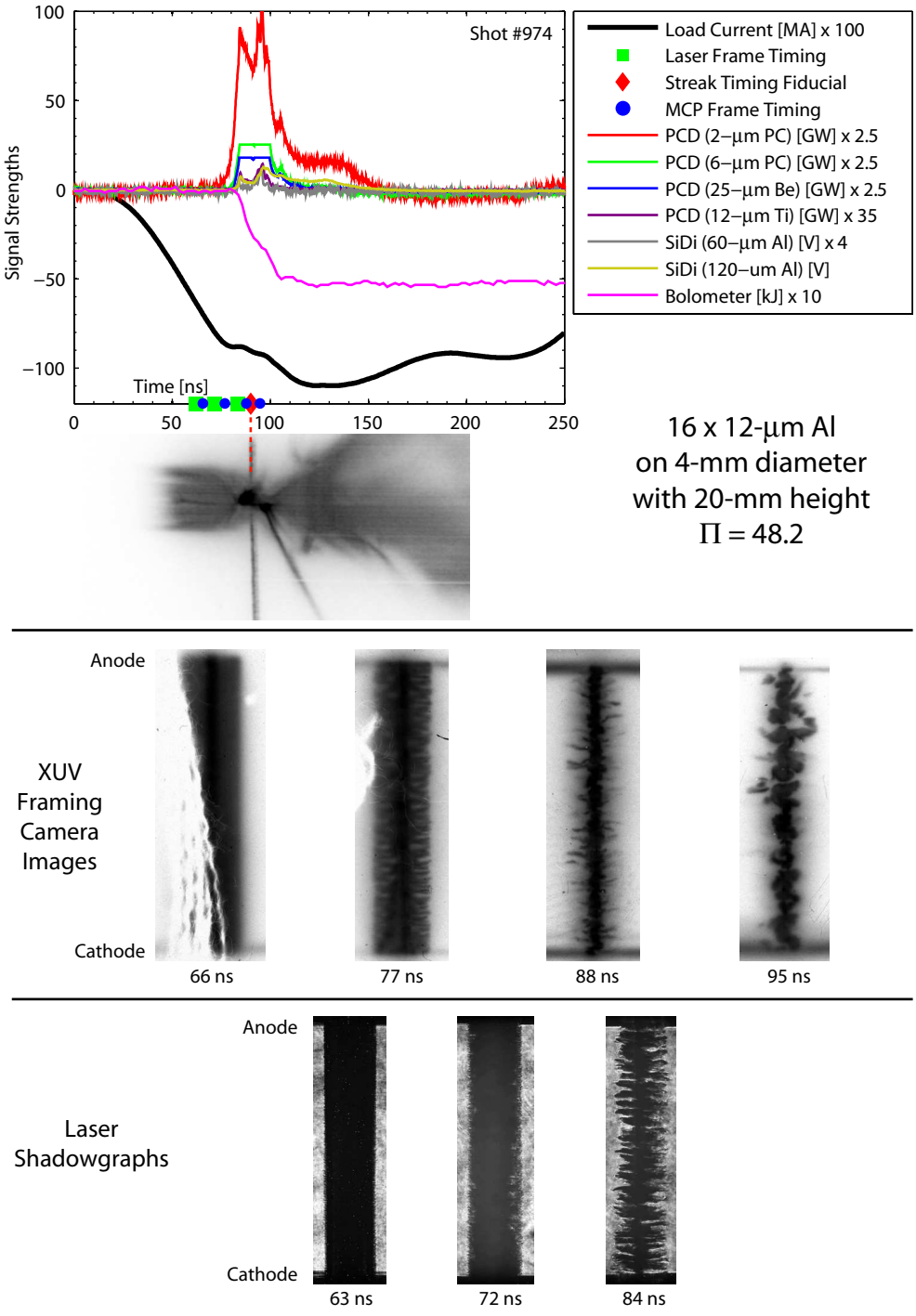

Figure A.39: (Color) Visible streak, XUV framing camera, laser shadowgraph, and various signal data for shot 974.

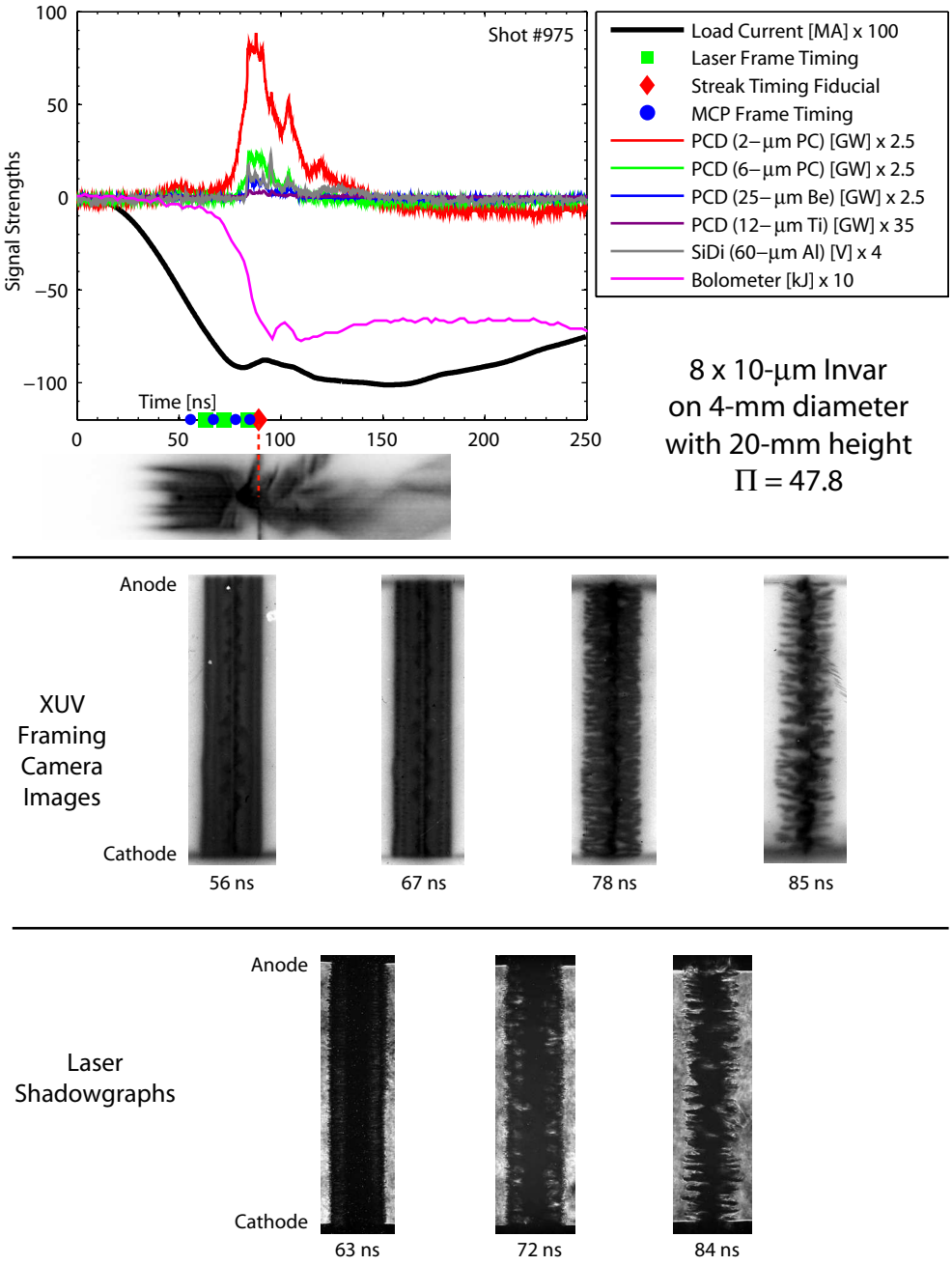

Figure A.40: (Color) Visible streak, XUV framing camera, laser shadowgraph, and various signal data for shot 975.

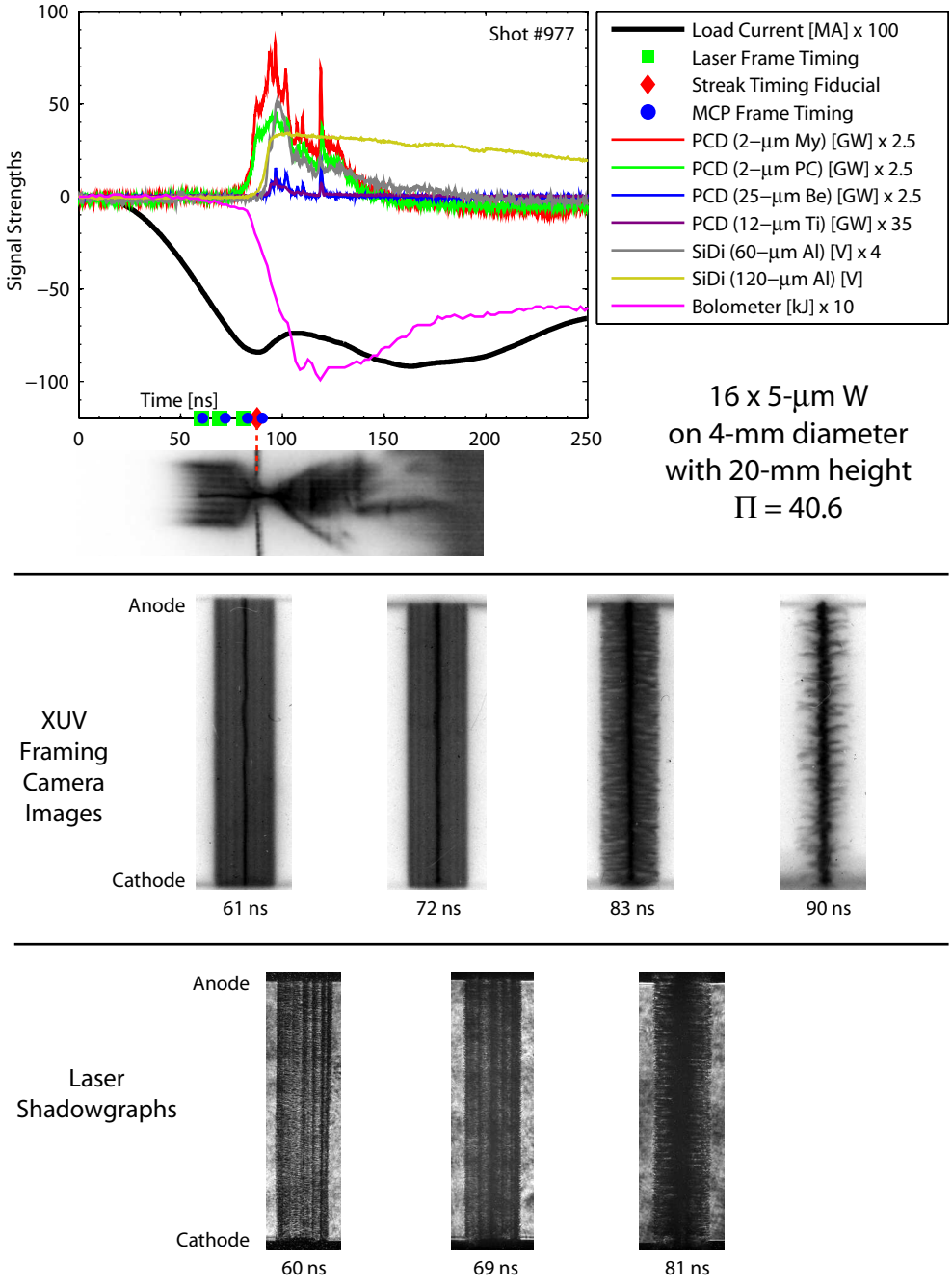

Figure A.41: (Color) Visible streak, XUV framing camera, laser shadowgraph, and various signal data for shot 977.

APPENDIX B

CODE FOR IMPLOSION DYNAMICS STUDY

B.1 shot_info.m

```
function shot_info_array = shot_info()

%This function is an array containing shot information needed by
%RMAnalyze.m and ablation_snow_plow.m. and it is one of the input
%arguments for RMAnalyze.m and ablation_snow_plow.m. The columns from
%left to right are: shot number, number of wires, wire diameter, wire
%material (either 'W', 'Al', 'Ni', or 'Mo'), array diameter, ablation
%velocity, fraction of load current applied to models, fraction of
%initial mass operated on at start of snow-plow, fraction of initial
%mass ablated at start of snow-plow, V_load time shift, V_load
%calibration, V_load DC offset (now obsolete and handled in the main
%code RMAnalyze.m), array height in mm, return current radius in mm,
%load inductance adjustment factor, inductance trajectory integration
%start time;

shot_info_array = {

766 16 17.0 'Al'    8 170 0.9  .3  .4  17.0 2.0 0 20 45 1.05 40;
767 16 17.0 'Al'    8 170 0.9  .3  .4  17.0 2.0 0 20 45 1.05 40;
768 16 17.0 'Al'    8 100 0.9  .3  .4  17.0 2.0 0 20 45 1.02 40;
769 16 17.0 'Al'    8 130 0.92 .3  .4  17.0 2.1 0 20 45 1.05 40;
770  8 10.2  'W'    8 125 0.90 .02 .65 17.0 2.0 0 20 45 1.30 40;
771  8 10.2  'W'    8 140 0.9  .10 .62 17.0 2.0 0 20 45 1.15 40;
772  8  5.1  'W'   16 220 0.9  .15 .5  17.0 2.0 0 20 45 1.20 40;
773 16  5.1  'W' 11.3 90  1.0  .05 .4  17.0 2.0 0 20 45 1.15 40;
774 16  5.1  'W'    8 160 0.9  .25 .5  17.0 2.0 0 20 45 1.10 20;
775  8 10.2  'W'    8 130 0.90 .10 .5  17.0 2.0 0 20 45 1.00 20;
776 16  5.1  'W' 11.3 125 0.95 .1  .6  17.0 2.0 0 20 45 1.15 40;
777 16  5.1  'W' 11.3 100 0.95 .14 .5  17.0 2.0 0 20 45 1.10 40;
778 16  5.1  'W'    8 180 0.90 .20 .5  17.0 1.7 0 20 45 1.18 40;
779  8  5.1  'W'    6 180 0.90 .2  .5  17.0 1.7 0 20 45 1.15 40;
873  8  5.1  'W'   16 125 0.95 .1  .6  18.0 3.3 0 20 45 1.45 40;
874 16  5.1  'W'   16 120 0.90 .1  .6  18.0 3.3 0 20 45 1.45 40;
875  8 12.7 'Al'   16 210 0.90 .02 .6  18.0 3.3 0 20 45 1.45 40;
876 16 10.2 'Al'   16 180 0.90 .1  .65 18.0 3.3 0 20 45 1.40 40;
```

```
877 16 17.0 'Al'    8 140 0.90 .2  .55 18.0 3.3 0 10 45 1.20 50;
878 16 17.0 'Al'    8 180 0.90 .15 .41 18.0 3.3 0 10 45 1.18 50;
879 16 17.0 'Al'    8 140 0.92 .25 .40 18.0 3.3 0 10 45 1.20 50;
880 16  5.1  'W'    8 150 0.95 .1  .4  18.0 3.3 0 10 45 1.40 40;
881  8  5.1  'W'   16 150 0.95 .1  .4  18.0 3.3 0 10 45 1.20 40;
882 16 10.2 'Al'    9 140 0.90 .3  .4  18.0 3.3 0 10 45 1.10 40;
883 16 10.2 'Al'    9 175 0.90 .3  .45 18.0 3.3 0 20 45 1.14 40;
885  2 17.0 'Al'   16  10 0.5  .99 .01 18.0 3.3 0 20 45 1.20 40;
950  8  5.1  'W'   16 125 0.9  .1  .7  18.0 3.4 0 20 45 1.02 20;
951 32  5.1  'W'    8 125 0.95 .1  .6  18.0 3.4 0 20 45 0.96 20;
952 32 10.2 'Al'    8 120 0.90 .15 .65 18.0 3.4 0 20 45 1.08 40;
953 32 12.7 'Al'    8 90  0.91 .10 .68 18.0 3.4 0 20 45 1.06 35;
954 32 10.2 'Al'    8 115 0.90 .15 .67 18.0 3.4 0 20 45 0.97 60;
955 32  5.1  'W'    8 120 0.93 .1  .6  18.0 3.4 0 20 45 1.01 45;
956 16  5.1  'W'    9 150 0.9  .12 .55 18.0 3.4 0 20 45 1.04 45;
957 16  5.1  'W'    9 122 0.93 .1  .65 18.0 3.4 0 20 45 1.10 60;
958 16 12.5 'Al'   12 125 0.85 .10 .70 18.0 3.4 0 20 45 1.02 90;
959 16  5.1  'W'   12 170 0.9  .1  .5  18.0 3.4 0 20 45 1.10 50;
960 16  5.1  'W'    4 140 0.95 .1  .5  18.0 3.4 0 20 45 1.04 40;
962 16 12.5 'Al'    4 120 0.90 .1  .55 18.0 3.4 0 20 45 1.00 50;
974 16 12.5 'Al'    4 110 0.87 .1  .68 18.0 3.4 0 20 45 1.10 40;
975  8 10.2 'In'    4 170 0.92 .02 .7  18.0 3.4 0 20 45 0.00 40;
977 16  5.1  'W'    4 140 0.95 .1  .5  18.0 3.4 0 20 45 1.10 20;

};
```

B.2 didt_zero.m

```
function didt_zero(shot_number)
%This function allows one to manually check where t=0 is being
%established in the RMAnalyze.m function.

%%%%%%%%%%%%%%%%%%%%%%%%%%%%%%%%%%%%%%%%%%%%%%%%%%%%%%%%%%%%%%%%%%%%%%%%%%%
%Adjust the dI/dt threshold value for detecting current start:
didt_thresh = -3*10^11;
if (shot_number == 954)
    didt_thresh = -4*10^11;
end
if (shot_number == 955)
    didt_thresh = -6*10^11;
end
```

```
%%%%%%%%%%%%%%%%%%%%%%%%%%%%%%%%%%%%%%%%%%%%%%%%%%%%%%%%%%%%%%%%%%%%%%%%

clf; %clear figures
fig1 = gcf; %define fig1 as current figure

%set directories to where "ILoad.txt" files are (i.e., where dI/dt
%data files are):
didt_path(1)={'C:\research\shot_processing\950\cobra-scope\'};
didt_signal(1)={'-dev1ILoad.txt'};

number_of_didts=length(didt_signal); %number of dI/dt data sets

%organize dI/dt info:
for n=1:number_of_didts
    didts(n,:)={didt_path{n}, didt_signal{n}};
end

%path to signal data---note that this here, as well as anything to do
%with "signal", "signals", or "signals_data_array" is irrelevant in
%this function didt_zero.m; this is because didt_zero.m was adapted
%from RMAnalyze.m, so just use more dI/dt data here:
path(1)={'C:\research\shot_processing\950\cobra-scope\'};
signal(1)={'-dev1ILoad.txt'};
didt_scope(1)=1;
plotq(1)='n';
color(1)={'r'};
legend_label(1)={''};

number_of_signals=length(didt_scope);%number of signal data sets

%organize info for signals data:
for m=1:number_of_signals
    signals(m,:)={path{m},signal{m},didt_scope(m),plotq(m),...
        color{m},legend_label{m}};
end

%create shot number text string:
shot_number_string=int2str(shot_number);

%load dI/dt data and scale time values to be in nanoseconds:
for n=1:number_of_didts
    didts_data_array{n}=load(strcat(didts{n,1},'00',...
        shot_number_string,didts{n,2}));
    didts_data_array{n}(:,1)=didts_data_array{n}(:,1)*10^9;
```

```
end

%load signal data and scale time values to be in nanoseconds:
for m=1:number_of_signals
    signals_data_array{m}=load(strcat(signals{m,1},'00',...
        shot_number_string,signals{m,2}));
    signals_data_array{m}(:,1)=signals_data_array{m}(:,1)*10^9;
end
%end of data loading section of code

%find rough DC offsets and dI/dt record lengths:
for n=1:number_of_didts
    dc_offs(n) = mean(didts_data_array{n}(1:100,2));
    didt_record_lengths(n) = size(didts_data_array{n},1);
end

%find dI/dt start, first zero crossing and precise DC offsets:
for n=1:number_of_didts
    averaged_didts_data_array{n}(:,:) = didts_data_array{n}(:,:);
    for i=110:didt_record_lengths(n)-110
        averaged_didts_data_array{n}(i,2) = ...
            mean(didts_data_array{n}(i-50:i+50,2));
    end
end
for n=1:number_of_didts
    [minval,minpos] = min(...
        averaged_didts_data_array{n}(1:didt_record_lengths(n),2));
    m=minpos;
    flag=1;
    while((m>10) && (flag))
        if(mean(didts_data_array{n}(m-5:m+5,2)) > ...
                (didt_thresh+dc_offs(n)))
            zp_time(n)=didts_data_array{n}(m,1);
            zp_pos(n)=m;
            flag=0;
        end
        m=m-1;
    end
    dc_offs(n) = mean(didts_data_array{n}(1:m+1,2));
    m=minpos;
    flag=1;
    while((flag) && (m < (didt_record_lengths(n) - 10)))
        if(mean(didts_data_array{n}(m-5:m+5,2)) > dc_offs(n))
            peak_time(n)=didts_data_array{n}(m,1);
```

```
            flag=0;
        end
        m=m+1;
    end
end
master_rise_time = peak_time(1) - zp_time(1);

%shift all dI/dt data sets to time base with current start at t=0:
for n=1:number_of_didts
    time_step(n) = didts_data_array{n}(2,1) - ...
        didts_data_array{n}(1,1);
    zp_time(n) = peak_time(n) - master_rise_time;
    zp_time_index(n) = round((zp_time(n) - ...
        didts_data_array{n}(1,1))/time_step(n));
    didts_data_array{n}(:,1) = didts_data_array{n}(:,1) - zp_time(n);
    didts_data_array{n}(:,2) = didts_data_array{n}(:,2) - dc_offs(n);
end

%shift signal data to time base with current start at t=0:
for m=1:number_of_signals
    signals_data_array{m}(:,1) = signals_data_array{m}(:,1) - ...
        zp_time(signals{m,3});
    signal_record_lengths(m) = size(signals_data_array{m},1);
end

% Calculate total load current, i.e., the integral of dI/dt (this
% here is also irrelevant for this function didt_zero.m, and is again
% due to didt_zero.m being adapted from RMAnalyze.m):
load_current = zeros(didt_record_lengths(1),2);
load_current(:,1) = didts_data_array{1}(:,1);
for i=2:didt_record_lengths(1)
    load_current(i,2) = load_current(i-1,2) + ...
        didts_data_array{1}(i,2)*time_step(1)*10^-9;
end
load_current(:,2)=load_current(:,2)/10^6; %scale to mega-amperes

%optional global time shifting for debugging purposes:
global_time_shift = 0;
for n=1:number_of_didts
    didts_data_array{n}(:,1)=didts_data_array{n}(:,1)+...
        global_time_shift;
    averaged_didts_data_array{n}(:,1)=...
        averaged_didts_data_array{n}(:,1)+global_time_shift;
end
```

```
for m=1:number_of_signals
    signals_data_array{m}(:,1)=signals_data_array{m}(:,1)+...
        global_time_shift;
end
load_current(:,1)=load_current(:,1)+global_time_shift;

%plot configuration:
plot_start_time = -50; %in nanoseconds
plot_end_time = 50; %in nanoseconds
xlims_time = [plot_start_time,plot_end_time];
ylims = [-150,100]; %plot scale
ax1 = gca; %set axes ax1 to current axes
%set axes ax1 to various properties:
set(ax1,'XColor','k','YColor','k','XLim',xlims_time,'Parent',fig1)

ti=1; %initial index for data plotting
tf=zp_time_index(1)+round(plot_end_time/time_step(1)); %final index
%make line of dI/dt data on axes with various properties:
hl20 = line(didts_data_array{1}(ti:tf,1),...
    didts_data_array{1}(ti:tf,2),'Color','r',...
    'LineWidth',2,'Parent',ax1);

end %end of function didt_zero.m
```

B.3 RMAnalyze.m

```
function RMAnalyze(shot_number,shot_info)
%This function processes and plots all signal data. It requires a
%shot number and the shot information stored in shot_info.m. This
%code synchronizes the different time bases of the various data that
%were recorded on different oscilloscopes. This code also uses the
%voltage monitor data to determine the load inductance and the mean
%radial position of the current distribution. The mean radial
%position of the current distribution is then recorded in the output
%file xxxx-inductance_trajectory.txt (where xxxx is the shot number).
%This inductance file is used by the code in ablation_snow_plow.m to
%plot the trajectory of the mean radial position of the current
%distribution alongside the trajectories generated by the thin-shell
%and rocket ablation-snowplow models. This RMAnalyze.m code can also
%be used to plot total electrical powers and bolometer normalized
%powers.
```

```
%%%%%%%%%%%%%%%%%%%%%%%%%%%%%%%%%%%%%%%%%%%%%%%%%%%%%%%%%%%%%%%%%%%%%%%%%%%

%set thresholds for detecting current start here (can test them using
%didt_zero.m):
didt_thresh = -3*10^11;
if (shot_number == 945)
    didt_thresh = -6*10^11;
end
if (shot_number == 947)
    didt_thresh = -4*10^11;
end

%generating inductance trajectory? 'y' or 'n':
generate_inductance = 'y';

%plot absolute powers or signal data? 'p' or 's':
power_or_signals = 's';

%directory for saving signal plots in:
output_plot_path='C:\research\shot_processing\950\signal_plots\';

%%%%%%%%%%%%%%%%%%%%%%%%%%%%%%%%%%%%%%%%%%%%%%%%%%%%%%%%%%%%%%%%%%%%%%%%%%%

%specify directories for load current data (i.e., dI/dt data) of the
%various scopes:

didt_path(1)={'C:\research\shot_processing\950\cobra-scope\'};
didt_signal(1)={'-dev1ILoad.txt'};

didt_path(2)={'C:\research\shot_processing\950\command3\'};
didt_signal(2)={'-dev2ILoad.txt'};

didt_path(3)={'C:\research\shot_processing\950\tds210\'};
didt_signal(3)={'-dev3ILoad.txt'};

didt_path(4)={'C:\research\shot_processing\950\cobra-scope\'};
didt_signal(4)={'-dev4ILoad.txt'};

didt_path(5)={'C:\research\shot_processing\950\cobra-scope\'};
didt_signal(5)={'-dev2ILoad.txt'};

didt_path(6)={'C:\research\shot_processing\950\tds210\'};
didt_signal(6)={'-dev2ILoad.txt'};
```

```
didt_path(7)={'C:\research\shot_processing\950\tds210\'};
didt_signal(7)={'-dev4ILoad.txt'};

%%%%%%%%%%%%%%%%%%%%%%%%%%%%%%%%%%%%%%%%%%%%%%%%%%%%%%%%%%%%%%%%%%%%%%%%%%%%

%specify paths to various signal data, as well as plotting options
%and corresponding dI/dt scope number:

path(1)={'C:\research\shot_processing\950\cobra-scope\'};
signal(1)={'-dev4PCD1_2um_My.txt'};
didt_scope(1)=4; %dI/dt scope number specified above
plotq(1)='y'; %plot this signal? 'y' or 'n'
color(1)={'r'}; %plot this signal with the specified color
legend_label(1)={'PCD (2-\mum Mylar) [GW] x 2.5'}; %plot legend label

path(2)={'C:\research\shot_processing\950\cobra-scope\'};
signal(2)={'-dev4PCD61_6um_My.txt'};
didt_scope(2)=4;
plotq(2)='y';
color(2)={'g'};
legend_label(2)={'PCD (6-\mum Mylar) [GW] x 2.5'};

path(3)={'C:\research\shot_processing\950\cobra-scope\'};
signal(3)={'-dev4PCD2_25um_Be.txt'};
didt_scope(3)=4;
plotq(3)='y';
color(3)={'b'};
legend_label(3)={'PCD (25-\mum Be) [GW] x 2.5'};

path(4)={'C:\research\shot_processing\950\command3\'};
signal(4)={'-dev2PCD59_12um_Ti.txt'};
didt_scope(4)=2;
plotq(4)='y';
color(4)={[.5 .0 .5]};
legend_label(4)={'PCD (12-\mum Ti) [GW] x 35'};

path(5)={'C:\research\shot_processing\950\tds210\'};
signal(5)={'-dev3DiagDiode.txt'};
didt_scope(5)=3;
plotq(5)='n';
color(5)={'r'};
legend_label(5)={'Diag. Laser'};

path(6)={'C:\research\shot_processing\950\cobra-scope\'};
```

```
signal(6)={'-dev2quad cam mon.txt'};
didt_scope(6)=5;
plotq(6)='n';
color(6)={'r'};
legend_label(6)={'MCP Frames'};

if (shot_number==950 || shot_number==951)

    path(7)={'C:\research\shot_processing\950\command3\'};
    signal(7)={'-dev2SiDi_12um_Al.txt'};
    didt_scope(7)=2;
    plotq(7)='y';
    color(7)={[.5 .5 .5]};
    legend_label(7)={'SiD (12-\mum Al) [V] x 2'};

    x=8;

else

    path(7)={'C:\research\shot_processing\950\command3\'};
    signal(7)={'-dev2SiDi_60um_Al.txt'};
    didt_scope(7)=2;
    plotq(7)='y';
    color(7)={[.5 .5 .5]};
    legend_label(7)={'SiD (60-\mum Al) [V] x 4'};

    x=8;

end

path(x)={'C:\research\shot_processing\950\tds210\'};
signal(x)={'-dev4Bolo V.txt'};
didt_scope(x)=7;
plotq(x)='y';
color(x)={'m'};
legend_label(x)={'Bolometer [kJ] x 10'};

path(x+1)={'C:\research\shot_processing\950\tds210\'};
signal(x+1)={'-dev2Faraday.txt'};
didt_scope(x+1)=6;
plotq(x+1)='y';
color(x+1)={'c'};
legend_label(x+1)={'Faraday Cup [kA] x 50'};
```

```
path(x+2)={'C:\research\shot_processing\950\cobra-scope\'};
signal(x+2)={'-dev1VLoad.txt'};
didt_scope(x+2)=1;
plotq(x+2)='y';
color(x+2)={[.8 .8 .1]};
legend_label(x+2)={'V_{load}-L_0(dI/dt) [kV] x 1/10'};

%%%%%%%%%%%%%%%%%%%%%%%%%%%%%%%%%%%%%%%%%%%%%%%%%%%%%%%%%%%%%%%%%%%%%%%%%%%%

number_of_didts=length(didt_signal);%number of dI/dt data sets

%orgainize dI/dt info:
for n=1:number_of_didts
    didts(n,:)={didt_path{n}, didt_signal{n}};
end

number_of_signals=length(didt_scope);%number of signal data sets

%organize signal info:
for m=1:number_of_signals
    signals(m,:)={path{m},signal{m},didt_scope(m),plotq(m),...
        color{m},legend_label{m}};
end

%determine number of signals to plot:
if(generate_inductance=='y')
    num_to_plot=3;
else
    num_to_plot=2;
end
for m=1:number_of_signals
    signals(m,:)={path{m},signal{m},didt_scope(m),plotq(m),...
        color{m},legend_label{m}};
    if(plotq(m)=='y')
        num_to_plot=num_to_plot+1;
    end
end

clf; %clear figure
fig1 = gcf; %set fig1 to current figure

%specify plot parameters:
awidth = 4; %axes width
aheight = 3; %axes height
```

```
lwidth = 2.5;  %legend width
if power_or_signals == 'p'
    nsignals = 3; %number of labels in legend
else
    nsignals = num_to_plot+2; %number of labels in legend
end
lspacing = 0.15; %spacing between labels in legend
ltb_margin = 1.25*lspacing/2; %legend top and bottom margins
lheight = lspacing*(nsignals-1)+2*ltb_margin; %legend height
alspace = 0.05; %spacing between axes and legend
lmargin = 1.0; %margin between figure left edge and axes left edge
rmargin = 1.0;%margin between figure right edge and axes right edge
bmargin = 1.0;%margin between fig. bottom edge and axes bottom edge
tmargin = 1.0; %margin between figure top edge and axes top edge
fleft = 1; %position of left edge of figure on screen
fbottom = 1; %position of bottom edge of figure on screen
fwidth = awidth+lmargin+rmargin+alspace+lwidth; %figure width
fheight = aheight+tmargin+bmargin; %figure height
aleft = lmargin; %position of left edge of axes in figure
abottom = bmargin; %position of bottom edge of axes in figure
lleft = lmargin+alspace+awidth; %pos. of left edge of legend in fig.
lbottom = abottom+aheight-lheight; %pos. of bot. edge of leg. in fig.
set(fig1, 'Units', 'inches'); %set figure units
set(fig1, 'Position', [fleft fbottom fwidth fheight]); %set fig. pos.
%figure settings:
set(gcf, 'PaperPositionMode', 'manual');
set(gcf, 'PaperUnits', 'inches');
set(gcf, 'PaperSize', [fwidth fheight]);
set(gcf, 'PaperPosition', [fleft fbottom fwidth fheight]);

%create shot number text string:
shot_number_string=int2str(shot_number);

%load dI/dt data and scale time values to be in nanoseconds:
for n=1:number_of_didts
    didts_data_array{n}=load(strcat(didts{n,1},'00',...
        shot_number_string,didts{n,2}));
    didts_data_array{n}(:,1)=didts_data_array{n}(:,1)*10^9;
end

%load signal data and scale time values to be in nanoseconds:
for m=1:number_of_signals
    signals_data_array{m}=load(strcat(signals{m,1},'00',...
        shot_number_string,signals{m,2}));
```

```
    signals_data_array{m}(:,1)=signals_data_array{m}(:,1)*10^9;
end
%end of data loading section of code

%find rough DC offsets and dI/dt record lengths:
for n=1:number_of_didts
    dc_offs(n) = mean(didts_data_array{n}(1:100,2));
    didt_record_lengths(n) = size(didts_data_array{n},1);
end

%find dI/dt start, first zero crossing and precise DC offsets:
for n=1:number_of_didts
    averaged_didts_data_array{n}(:,:) = didts_data_array{n}(:,:);
    for i=110:didt_record_lengths(n)-110
        averaged_didts_data_array{n}(i,2) = ...
            mean(didts_data_array{n}(i-50:i+50,2));
    end
end
for n=1:number_of_didts
    [minval,minpos] = min(averaged_didts_data_array{n}(1:...
        didt_record_lengths(n),2));
    m=minpos;
    flag=1;
    while((m>10) && (flag))
        if(mean(didts_data_array{n}(m-5:m+5,2)) > ...
                (didt_thresh+dc_offs(n)))
            zp_time(n)=didts_data_array{n}(m,1);
            zp_pos(n)=m;
            flag=0;
        end
        m=m-1;
    end
    dc_offs(n) = mean(didts_data_array{n}(1:m+1,2));
    m=minpos;
    flag=1;
    while((flag) && (m < (didt_record_lengths(n) - 10)))
        if(mean(didts_data_array{n}(m-5:m+5,2)) > dc_offs(n))
            peak_time(n)=didts_data_array{n}(m,1);
            flag=0;
        end
        m=m+1;
    end
end
master_rise_time = peak_time(1) - zp_time(1);
```

```
%shift all dI/dt data sets to time base with current start at t=0:
for n=1:number_of_didts
    time_step(n) = didts_data_array{n}(2,1) - ...
        didts_data_array{n}(1,1);
    zp_time(n) = peak_time(n) - master_rise_time;
    zp_time_index(n) = round((zp_time(n) - ...
        didts_data_array{n}(1,1))/time_step(n));
    didts_data_array{n}(:,1) = didts_data_array{n}(:,1) - ...
        zp_time(n);
    didts_data_array{n}(:,2) = didts_data_array{n}(:,2) - ...
        dc_offs(n);
end

%shift all signal data to time base with current start at t=0:
for m=1:number_of_signals
    signals_data_array{m}(:,1) = signals_data_array{m}(:,1) - ...
        zp_time(signals{m,3});
    signal_record_lengths(m) = size(signals_data_array{m},1);
end

%calculate total load current, i.e., the integral of dI/dt:
load_current = zeros(didt_record_lengths(1),2);
load_current(:,1) = didts_data_array{1}(:,1);
for i=2:didt_record_lengths(1)
    load_current(i,2) = load_current(i-1,2) + ...
        didts_data_array{1}(i,2)*time_step(1)*10^-9;
end
load_current(:,2)=load_current(:,2)/10^6; %scale to mega-amperes

%optional global time shifting for debugging purposes:
global_time_shift = 0;
for n=1:number_of_didts
    didts_data_array{n}(:,1)=didts_data_array{n}(:,1)+...
        global_time_shift;
    averaged_didts_data_array{n}(:,1)=...
        averaged_didts_data_array{n}(:,1)+global_time_shift;
end
for m=1:number_of_signals
    signals_data_array{m}(:,1)=signals_data_array{m}(:,1)+...
        global_time_shift;
end
load_current(:,1)=load_current(:,1)+global_time_shift;
```

```
%process special signals:
vload_rescale = 1/10000;
L_machine = 10e-9; %COBRA baseline inductance
mu0 = 4*pi*10^-7; %permeability of free space
mu = mu0;
%load shot information from shot_info array:
for p=1:size(shot_info,1)
    if (shot_info{p,1}==shot_number)
        vload_time_shift = shot_info{p,10};
        vload_cal = shot_info{p,11};
        vload_dc_off = shot_info{p,12};
        r0 = shot_info{p,5}/2/1000;
        array_height = shot_info{p,13}/1000;
        return_current_radius = shot_info{p,14}/1000;
        f_load_inductance_adjustment = shot_info{p,15};
        induct_traj_int_start_time = shot_info{p,16};
    end
end
%inductance formula for co-axial cylindrical configuration:
L_load_0_coax = mu/2/pi*log(return_current_radius/r0)*array_height;
L_load_0 = L_load_0_coax * f_load_inductance_adjustment;
L0 = L_machine + L_load_0; %total inductance measured by voltage mon.
faraday_cup_rescale = 1/10;
bolo_rescale = 5.5;
%PCD calibration values in watts/volt:
PCD1_cal = 102;
PCD2_cal = 26;
PCD3_cal = 27;
PCD61_cal = 36.9;
PCD59_cal = 39.4;
PCD_rescale = 1.0;
SiD_rescale = 2.0;
%time shifts for various positions around COBRA experiment chamber:
A_time_shift = -3.24;
B_time_shift = -1.65;
C_time_shift = -1.99;
DiagDiode_time_shift = 22.4; %time shift for diagnostic laser diode
DiagDiode_rescale = 10;
%channel delays for diagnostic laser beams in nanoseconds:
t1_to_t2 = 9;
t1_to_t3 = 21;
%streak fiducial timing:
t1_to_streak_fiducial = 49.8 - DiagDiode_time_shift;
quad_cam_rescale = 10;
```

```
%cable timing delays for MCP channels:
quad_cam_t1_cable_length = 11;
quad_cam_t2_cable_length = 21.9;
quad_cam_t3_cable_length = 32.7;
quad_cam_t4_cable_length = 40;
for m=1:number_of_signals
    if (size(signals{m,2})==size('-dev1VLoad.txt'))
        if (signals{m,2}=='-dev1VLoad.txt')
            signals_data_array{m}(:,1)=signals_data_array{m}(:,1)+...
                vload_time_shift;
            vload_index = m;
            vload_time=signals_data_array{m}(:,1);
            vload=signals_data_array{m}(:,2)*vload_cal;
            didt_on_vload_time=...
                interp1(didts_data_array{signals{m,3}}(:,1),...
                didts_data_array{signals{m,3}}(:,2),...
                signals_data_array{m}(:,1));
            vload_time_step = signals_data_array{m}(2,1) - ...
                signals_data_array{m}(1,1);
            vload_zp_index_array = ...
                find((signals_data_array{m}(:,1) < ...
                vload_time_step+0.01) & ...
                (signals_data_array{m}(:,1) > ...
                -vload_time_step-0.01));
            vload_dc_off = mean(...
                signals_data_array{m}(vload_zp_index_array(1)-200:...
                vload_zp_index_array(1),2));
            signals_data_array{m}(:,2)=...
                ((signals_data_array{m}(:,2)-vload_dc_off)*...
                vload_cal - 1*L0*didt_on_vload_time) * vload_rescale;
            electrical_power = signals_data_array{m};
            electrical_power(:,2) = signals_data_array{m}(:,2).*...
                10000.*load_current(:,2).*10^6;
            vload_didt_scope_index = signals{m,3};
        end
    end
    if (size(signals{m,2})==size('-dev2Faraday.txt'))
        if (signals{m,2}=='-dev2Faraday.txt')
            signals_data_array{m}(:,2)=...
                signals_data_array{m}(:,2) * faraday_cup_rescale;
            signals_data_array{m}(:,2)=...
                signals_data_array{m}(:,2) - ...
                mean(signals_data_array{m}(1:100,2));
            signals_data_array{m}(:,1)=...
```

```
            signals_data_array{m}(:,1) + 2.6;...
            % +2.6 is for ILoad cable delay correction
    end
end
if (size(signals{m,2})==size('-dev4Bolo V.txt'))
    if (signals{m,2}=='-dev4Bolo V.txt')
        bolo_index=m;
        bolo_time_step = signals_data_array{m}(2,1) - ...
            signals_data_array{m}(1,1);
        bolo_zp_index_array = ...
            find((signals_data_array{m}(:,1) < ...
            bolo_time_step+0.01) & ...
            (signals_data_array{m}(:,1) > -bolo_time_step-0.01));
        bolo_zp_dc_off = mean(...
            signals_data_array{m}(bolo_zp_index_array(1)-10:...
            bolo_zp_index_array(1)+10,2));
        signals_data_array{m}(:,2)=signals_data_array{m}(:,2)-...
            bolo_zp_dc_off;
        signals_data_array{m}(:,2)=signals_data_array{m}(:,2)*...
            bolo_rescale;
        signals_data_array{m}(:,1)=signals_data_array{m}(:,1)+...
            A_time_shift + 0.9;...
            %0.9 for ILoad cable delay correction
        bolo_time_scan=250;
        power_start_index = find((signals_data_array{m}(:,1) <...
            0+bolo_time_step+0.01) &...
            (signals_data_array{m}(:,1) > -bolo_time_step-0.01));
        power_stop_index = find((signals_data_array{m}(:,1) <...
            bolo_time_scan+bolo_time_step+0.01) &...
            (signals_data_array{m}(:,1) > ...
            bolo_time_scan-bolo_time_step-0.01));
        fit_start = time_index(-150,signals_data_array{m}(:,1));
        fit_end = time_index(750,signals_data_array{m}(:,1));
        bolo_fit = signals_data_array{m}(:,2);
        bolo_fit_time = signals_data_array{m}(:,1);
        pstop=98;
        mstop=98;
        for i=110:length(signals_data_array{m}(:,1))-110
            bolo_fit(i) = mean(signals_data_array{m}(i-1:i+1,2));
        end
        bolo_fit_length = length(signals_data_array{m}(:,1));
        bolo_power = zeros(bolo_fit_length-1,2);
        bolo_diffs = zeros(bolo_fit_length-1,1);
        bolo_diffs(:,1) = diff(bolo_fit);
```

```
        bolo_power(:,2) = -1*bolo_diffs(:,1)*10^-9*1000/10/...
            (bolo_time_step*10^-9);
        bolo_power(:,1) = bolo_fit_time(2:bolo_fit_length,1);
        ti_index=time_index(0,bolo_power(:,1));
        tf_index=time_index(180,bolo_power(:,1));
        max_bolo_power_diffs = ...
            max(bolo_power(ti_index:tf_index,2))
        t1_index=time_index(0,bolo_fit_time);
        t2_index=time_index(bolo_time_scan,bolo_fit_time);
        bolo_max = min(bolo_fit(t1_index:t2_index));
        bolo_max_index = find(bolo_fit(:)==bolo_max);
        bolo_max_in_kJ = -1 * bolo_max / 10
        bolo_max_time = bolo_fit_time(bolo_max_index(1))
    end
end
if (size(signals{m,2})==size('-dev4PCD1_2um_My.txt'))
    if (signals{m,2}=='-dev4PCD1_2um_My.txt')
        PCD_index=m;
        PCD1_time_step=signals_data_array{m}(2,1)-...
            signals_data_array{m}(1,1);
        signals_data_array{m}(:,1)=signals_data_array{m}(:,1)+...
            A_time_shift;
        signals_data_array{m}(:,2)=signals_data_array{m}(:,2)*...
            PCD_rescale*PCD1_cal/PCD1_cal;
    end
end
if (size(signals{m,2})==size('-dev2PCD59_12um_Ti.txt'))
    if (signals{m,2}=='-dev2PCD59_12um_Ti.txt')
        signals_data_array{m}(:,1)=...
            signals_data_array{m}(:,1) + B_time_shift;
        signals_data_array{m}(:,2)=...
            signals_data_array{m}(:,2)*PCD_rescale*PCD59_cal/...
            PCD1_cal*14*(B_time_shift/A_time_shift)^2;
        signals_data_array{m}(:,2)=...
            signals_data_array{m}(:,2)-...
            mean(signals_data_array{m}(1:100,2));
    end
end
if (size(signals{m,2})==size('-dev4PCD2_25um_Be.txt'))
    if (signals{m,2}=='-dev4PCD2_25um_Be.txt')
        signals_data_array{m}(:,1)=...
            signals_data_array{m}(:,1) + A_time_shift;
        signals_data_array{m}(:,2)=signals_data_array{m}(:,2)*...
            PCD_rescale*PCD2_cal/PCD1_cal;
```

```
    end
end
if (size(signals{m,2})==size('-dev4PCD61_6um_My.txt'))
    if (signals{m,2}=='-dev4PCD61_6um_My.txt')
        signals_data_array{m}(:,1)=...
            signals_data_array{m}(:,1) + A_time_shift;
        signals_data_array{m}(:,2)=signals_data_array{m}(:,2)*...
            PCD_rescale*PCD61_cal/PCD1_cal;
    end
end
if (size(signals{m,2})==size('-dev2SiDi_12um_Al.txt'))
    if (signals{m,2}=='-dev2SiDi_12um_Al.txt')
        signals_data_array{m}(:,1)=...
            signals_data_array{m}(:,1) + B_time_shift;
        signals_data_array{m}(:,2)=...
            signals_data_array{m}(:,2)*SiD_rescale;
    end
end
if (size(signals{m,2})==size('-dev2SiDi_60um_Al.txt'))
    if (signals{m,2}=='-dev2SiDi_60um_Al.txt')
        signals_data_array{m}(:,1)=...
            signals_data_array{m}(:,1) + B_time_shift;
        signals_data_array{m}(:,2)=...
            signals_data_array{m}(:,2)*SiD_rescale*2;
    end
end
if (size(signals{m,2})==size('-dev3DiagDiode.txt'))
    if (signals{m,2}=='-dev3DiagDiode.txt')
        laser_signal_index = m;
        signals_data_array{m}(:,1)=signals_data_array{m}(:,1)+...
            DiagDiode_time_shift + 1.6;...
            %1.6 for ILoad cable delay correction
        signals_data_array{m}(:,2)=...
            signals_data_array{m}(:,2) * DiagDiode_rescale;
        [maxval,maxpos] = max(signals_data_array{m}(1:...
            signal_record_lengths(m),2));
        laser_flag = 0;
        if (maxval > 5)
            laser_flag = 1;
        end
        laser_thresh = 1/10 * maxval;
        pos = maxpos;
        flag=1;
        while((pos>10) && (flag))
```

```
            if(mean(signals_data_array{m}(pos-5:pos+5,2)) < ...
                    (laser_thresh))
                laser_t1_pos=pos;
                flag=0;
            end
        pos=pos-1;
        end
        laser_t1 = signals_data_array{m}(laser_t1_pos,1);
        laser_t2 = laser_t1 + t1_to_t2;
        laser_t3 = laser_t1 + t1_to_t3;
        streak_fiducial = laser_t1 + t1_to_streak_fiducial;
    end
end
if (size(signals{m,2})==size('-dev2quad cam mon.txt'))
    if (signals{m,2}=='-dev2quad cam mon.txt')
        signals_data_array{m}(:,2)=...
            signals_data_array{m}(:,2) * quad_cam_rescale;
        [maxval,maxpos] = max(signals_data_array{m}(1:...
            signal_record_lengths(m),2));
        quad_cam_flag = 0;
        if (maxval > 5 && signals_data_array{m}(maxpos,1) > ...
                0 && signals_data_array{m}(maxpos,1) < 300)
            quad_cam_flag = 1;
        end
        quad_cam_thresh = 1/10 * maxval;
        pos = maxpos;
        flag=1;
        while((pos>10) && (flag))
            if(mean(signals_data_array{m}(pos-5:pos+5,2)) < ...
                    (quad_cam_thresh))
                quad_cam_pos=pos;
                flag=0;
            end
        pos=pos-1;
        end
        quad_cam_t1 = signals_data_array{m}(quad_cam_pos,1) + ...
            quad_cam_t1_cable_length;
        quad_cam_t2 = signals_data_array{m}(quad_cam_pos,1) + ...
            quad_cam_t2_cable_length;
        quad_cam_t3 = signals_data_array{m}(quad_cam_pos,1) + ...
            quad_cam_t3_cable_length;
        quad_cam_t4 = signals_data_array{m}(quad_cam_pos,1) + ...
            quad_cam_t4_cable_length;
    end
```

```
    end
end

if power_or_signals == 's'
    plot_end_time = 250;
    xlims_time = [0,plot_end_time];
    ylims_ILoad = [-1.2,0];
    ylims_signals = [-120,100];
    box on;
    ax1 = gca;
    set(ax1,'Units','inches');
    set(ax1,'Position',[aleft abottom awidth aheight]);
    set(ax1,'XColor','k','YColor','k','XLim',xlims_time,'YLim',...
        ylims_signals,'XMinorTick','on','YMinorTick','on',...
        'FontSize', 8,'FontName','Helvetica','Parent',fig1)
    xlabel('Time [ns]')
    ylabel('Signal Strengths')
    laser_flag = 1;
    quad_cam_flag = 1;

    hold on;

    if (laser_flag)

        load_current_laser_t1_index_array = ...
            find((load_current(:,1) < laser_t1+time_step(1)+.01) &...
            (load_current(:,1) > laser_t1-time_step(1)-0.01));
        hl4 = scatter(load_current(...
            load_current_laser_t1_index_array(1),1),...
            ylims_signals(1),55,'g','filled','s','Parent',ax1);

        load_current_laser_t2_index_array = ...
            find((load_current(:,1) < laser_t2+time_step(1)+.01) &...
            (load_current(:,1) > laser_t2-time_step(1)-0.01));
        hl5 = scatter(load_current(...
            load_current_laser_t2_index_array(1),1),...
            ylims_signals(1),55,'g','filled','s','Parent',ax1);

        load_current_laser_t3_index_array = ...
            find((load_current(:,1) < laser_t3+time_step(1)+.01) &...
            (load_current(:,1) > laser_t3-time_step(1)-0.01));
        hl6 = scatter(load_current(...
            load_current_laser_t3_index_array(1),1),...
            ylims_signals(1),55,'g','filled','s','Parent',ax1);
```

```
    load_current_streak_fiducial_index_array = ...
        find((load_current(:,1) < ...
        streak_fiducial+time_step(1)+0.01) & ...
        (load_current(:,1) > streak_fiducial-time_step(1)-0.01));
    hl7 = scatter(load_current(...
        load_current_streak_fiducial_index_array(1),1),...
        ylims_signals(1),50,'r','filled','d','Parent',ax1);

end

if (quad_cam_flag)

    load_current_quad_cam_t1_index_array = ...
        find((load_current(:,1) < ...
        quad_cam_t1+time_step(1)+0.01) & ...
        (load_current(:,1) > quad_cam_t1-time_step(1)-0.01));
    hl8 = scatter(load_current(...
        load_current_quad_cam_t1_index_array(1),1),...
        ylims_signals(1),20,'b','filled','o','Parent',ax1);

    load_current_quad_cam_t2_index_array = ...
        find((load_current(:,1) < ...
        quad_cam_t2+time_step(1)+0.01) & ...
        (load_current(:,1) > quad_cam_t2-time_step(1)-0.01));
    hl9 = scatter(load_current(...
        load_current_quad_cam_t2_index_array(1),1),...
        ylims_signals(1),20,'b','filled','o','Parent',ax1);

    load_current_quad_cam_t3_index_array = ...
        find((load_current(:,1) < ...
        quad_cam_t3+time_step(1)+0.01) & ...
        (load_current(:,1) > quad_cam_t3-time_step(1)-0.01));
    hl10 = scatter(load_current(...
        load_current_quad_cam_t3_index_array(1),1),...
        ylims_signals(1),20,'b','filled','o','Parent',ax1);

    load_current_quad_cam_t4_index_array = ...
        find((load_current(:,1) < ...
        quad_cam_t4+time_step(1)+0.01) & ...
        (load_current(:,1) > quad_cam_t4-time_step(1)-0.01));
    hl11 = scatter(load_current(...
        load_current_quad_cam_t4_index_array(1),1),...
        ylims_signals(1),20,'b','filled','o','Parent',ax1);
```

```
end

ti=zp_time_index(1);
tf=zp_time_index(1)+round(plot_end_time/time_step(1));
hl3 = line(load_current(ti:tf,1),load_current(ti:tf,2)*100,...
    'Color','k','LineWidth',2.0,'Parent',ax1);

if (laser_flag && quad_cam_flag)
    hlvec1 = [hl3,hl4,hl7,hl8];
    labelmat1 = {'Load Current [MA] x 100';...
        'Laser Frame Timing';'Streak Timing Fiducial';...
        'MCP Frame Timing'};
end

if (laser_flag && not(quad_cam_flag))
    hlvec1 = [hl3,hl4,hl7];
    labelmat1 = {'Load Current [MA] x 100';...
        'Laser Frame Timing';'Streak Timing Fiducial'};
end

if (not(laser_flag) && quad_cam_flag)
    hlvec1 = [hl3,hl8];
    labelmat1 = {'Load Current [MA] x 100';'MCP Frame Timing'};
end

if (not(laser_flag) && not(quad_cam_flag))
    hlvec1 = [hl3];
    labelmat1 = {'Load Current [MA] x 100'};
end

hlvec2(1)=0;
labelmat2(1)={''};
label_count=1;
for m=1:number_of_signals
    if (signals{m,4}=='y')
        ti=1;
        tf=size(signals_data_array{m},1);
        hl2 = line(signals_data_array{m}(ti:tf,1),...
            signals_data_array{m}(ti:tf,2),'LineWidth',1.0,...
            'Color',signals{m,5},'Parent',ax1);
        hlvec2(label_count)=hl2;
        labelmat2(label_count,1)={signals{m,6}};
        label_count = label_count + 1;
```

```
    end
end
if generate_inductance == 'y'
    options = odeset('Events',@events,'InitialStep',.1e-9,...
        'MaxStep',1e-9);
    time_span = [induct_traj_int_start_time*10^-9, 250*10^-9];
    ic = L_load_0;
    didt_time = ...
        didts_data_array{vload_didt_scope_index}(:,1)*10^-9;
    didt = didts_data_array{vload_didt_scope_index}(:,2);
    current = zeros(length(didt),2);
    current(:,1) = didt_time(:);
    for i=2:length(didt)
        current(i,2) = current(i-1,2) + didt(i)*(didt_time(i)-...
            didt_time(i-1));
    end
    i=1;
    while ((vload_time(i) < -30) && (i < length(vload_time)))
        vload_dc_off_index = i;
        i=i+1;
    end
    vload_dc_off = mean(vload(1:vload_dc_off_index));
    vload = vload - vload_dc_off;
    [L_load_time, L_load_vals,TE,RE,IE] = ...
        ode23(@(t,L_load) inductance(t,L_load,didt_time,didt,...
        current(:,1),current(:,2),vload_time*10^-9,vload,...
        L_machine),time_span,ic,options);
    mu = 4*pi*10^-7;
    mean_current_radius = ...
        return_current_radius*...
        exp(-2*pi/mu*(L_load_vals/array_height/...
        f_load_inductance_adjustment));
    inductance_trajectory_array(:,1) = L_load_time*10^9;
    inductance_trajectory_array(:,2) = mean_current_radius*1000;
    didt_on_L_load_time = interp1(didt_time,didt,L_load_time);
    vload_on_L_load_time = ...
        interp1(vload_time*10^-9,vload,L_load_time);
    ILdot = vload_on_L_load_time - ...
        (L_load_vals + L_machine) .* didt_on_L_load_time;
    ILdot_time = L_load_time;
    dlmwrite(strcat(output_plot_path,int2str(shot_number),...
        '-inductance_trajectory.txt'), ...
        inductance_trajectory_array, 'delimiter', '\t',...
        'precision', 6)
```

```
        ti=1;
        tf=length(ILdot);
        ILdoth = line(ILdot_time(ti:tf)*10^9,ILdot(ti:tf)* ...
            vload_rescale,'LineWidth',1.0,'Color',[1.0 .5 0.0],...
            'Parent',ax1);
        hlvec2(label_count)=ILdoth;
        labelmat2(label_count,1)={'I(dL/dt) [kV] x 1/10'};
        label_count = label_count + 1;
    end
    hlvec = cat(2,hlvec1,hlvec2);
    if (num_to_plot==0)
        labelmat = cat(1,labelmat1);
    else
        labelmat = cat(1,labelmat1,labelmat2);
    end
    legend1 = legend(hlvec,labelmat,'FontSize',8,...
        'FontName','Helvetica');
    set(legend1,'Units','inches');
    set(legend1,'Position', [lleft lbottom lwidth lheight]);
    title(strcat('Shot #',int2str(shot_number)),'Color','k',...
        'FontSize',8)
    print('-depsc2','-r600',...
        strcat(output_plot_path,int2str(shot_number),'.eps'))
end
if power_or_signals == 'p'
    pstart=0;
    mstart=0;
    astart=250;
    astop=300;
    mstart_index = find((signals_data_array{PCD_index}(:,1) < ...
        mstart+PCD1_time_step+0.01) & ...
        (signals_data_array{PCD_index}(:,1) > ...
        mstart-PCD1_time_step-0.01));
    mstop_index = find((signals_data_array{PCD_index}(:,1) < ...
        mstop+PCD1_time_step+0.01) & ...
        (signals_data_array{PCD_index}(:,1) > ...
        mstop-PCD1_time_step-0.01));
    power2_start_index = ...
        find((signals_data_array{PCD_index}(:,1) < ...
        pstart+PCD1_time_step+0.01) & ...
        (signals_data_array{PCD_index}(:,1) > ...
        pstart-PCD1_time_step-0.01));
    power2_stop_index = find((signals_data_array{PCD_index}(:,1) <...
        pstop+PCD1_time_step+0.01) & ...
```

```
    (signals_data_array{PCD_index}(:,1) > ...
    pstop-PCD1_time_step-0.01));
bolo_stop_index=find((bolo_fit_time(:) < ...
    pstop+bolo_time_step+0.01) & (bolo_fit_time(:) > ...
    pstop-bolo_time_step-0.01));
bolo_val_at_stop=bolo_fit(bolo_stop_index(1));
bolo_val_in_kJ = -1 * bolo_val_at_stop / 10
raw_integral=cumtrapz(...
    signals_data_array{PCD_index}(power2_start_index(1):...
    power2_stop_index(1),1),...
    signals_data_array{PCD_index}(power2_start_index(1):...
    power2_stop_index(1),2))/2.5/1000;
integrated_pcd_energy_in_kJ=max(raw_integral);
raw_peak_power = max(...
    signals_data_array{PCD_index}(mstart_index(1):...
    mstop_index(1),2))/2.5;
peak_radiated_power_in_GW = raw_peak_power * bolo_val_in_kJ /...
    integrated_pcd_energy_in_kJ
signals_data_array{PCD_index}(:,2) = ...
    signals_data_array{PCD_index}(:,2) / 2.5 * ...
    bolo_val_in_kJ / integrated_pcd_energy_in_kJ;

plot_start_time = 60;
plot_end_time = 180;
xlims_time = [plot_start_time,plot_end_time];
ylims_signals = [-100,500];
ax1 = gca;
set(ax1,'Units','inches');
set(ax1,'Position',[aleft abottom awidth aheight]);
set(ax1,'XColor','k','YColor','k','XLim',xlims_time,'YLim',...
    ylims_signals,'YMinorTick','on','XMinorTick','on',...
    'Parent',fig1);
ylabel('Power [GW]')
xlabel('Time [ns]')
ti=zp_time_index(1);
tf=zp_time_index(1)+round(plot_end_time/time_step(1));
h101 = line(electrical_power(:,1),...
    electrical_power(:,2)*10^-9,'Parent',ax1);
h102 = line(bolo_power(10:bolo_fit_length-30,1),...
    bolo_power(10:bolo_fit_length-30,2),...
    'Color','g','Parent',ax1);

hlvec2(1)=0;
labelmat2(1)={''};
```

```
    label_count=1;
    for m=1:number_of_signals
        if m==PCD_index
            ti=1;
            tf=size(signals_data_array{m},1);
            hl2 = line(signals_data_array{m}(ti:tf,1),...
                signals_data_array{m}(ti:tf,2),...
                'Color',signals{m,5},'Parent',ax1);
            hlvec2(label_count)=hl2;
            labelmat2(label_count,1)={signals{m,6}};
            label_count = label_count + 1;
        end
    end
    box on;
    legend1 = legend('Elecrical power into load',...
        'Radiated power out (bolo-diff)',...
        'Radiated power out (bolo-norm)');
    set(legend1,'Units','inches');
    set(legend1,'Position', [lleft lbottom lwidth lheight]);
    title(strcat('Shot #',int2str(shot_number)),'Color','k')
    %saveas(fig1,strcat(output_plot_path,int2str(shot_number),'_power
    %.bmp'));
    print('-depsc2','-r600',...
        strcat(output_plot_path,int2str(shot_number),'_power.eps'))
end

% commented out section just below can be used to plot all di/dt's to
% make sure they are lined up properly:
% for n=1:number_of_didts
%     hl1 = line(didts_data_array{n}(zp_time_index(n)-100:...
%         zp_time_index(n)+round(plot_end_time/time_step(n)),1),...
%         didts_data_array{n}(zp_time_index(n)-100:...
%         zp_time_index(n)+round(plot_end_time/time_step(n)),2),...
%         'Color','k');
%     ax1 = gca;
%     set(ax1,'XColor','k','YColor','k','XLim',[-100,300])
%     ylim('auto')
%     grid on
% end


% commented out code for looking at time differences between scopes i
% and j:
% for i=1:number_of_didts
```

```
%     for j=1:number_of_didts
%         didt_time_deltas(i,j) = zp_time(i) - zp_time(j);
%     end
% end
% didt_time_deltas

end %end of function RMAnalyze()

%function specifying dL/dt for differential equation solver:
function dLdt = ...
    inductance(t,L_load,didt_time,didt,I_time,I,V_time,V,L_machine)
    didt = interp1(didt_time,didt,t);
    I = interp1(I_time,I,t);
    V = interp1(V_time,V,t);
    dLdt = -(L_load+L_machine)*didt/I + V/I;
end

%function for determining when to terminate dL/dt diff.eq. solve:
function [value,isterminal,direction] = events(t,L)
    value = L;
    isterminal = 0;
    direction = -1;
end

%function for determining the index of a given time 't' in a vector
%of time points 'time_data':
function index = time_index(t,time_data)
    time_step = time_data(2)-time_data(1);
    index_array = find((time_data(:) < t+time_step+0.01) & ...
        (time_data(:) > t-time_step-0.01));
    index = index_array(1);
end
```

B.4 ablation_snow_plow.m

```
function ablation_snow_plow(shot_number,shot_info)
%This function calculates and plots trajectories generated from the
%thin-shell and rocket ablation-snowplow models, as well as the
%trajectory of the mean radial position of the current distribution
%as determined by load voltage measurements. This function requires
%the shot number and the shot information array stored in shot_info.m
```

```
%as input arguments. The trajectory of the mean radial position of
%the current distribution is loaded into the variable
%"inductance_trajectory_array" from an external file as specified
%below (this file is generated by RMAnalyze.m by setting the variable
%"generate_inductance" in RMAnalyze.m to 'y').

hold on;
clf;

output_plot_path='C:\research\shot_processing\950\signal_plots\';

didt_path='C:\research\shot_processing\950\cobra-scope\';
didt_signal='-dev1ILoad.txt';

inductance_trajectory_array = dlmread(strcat(output_plot_path,...
    int2str(shot_number),'-inductance_trajectory.txt'),'\t');

for (p=1:size(shot_info,1))
    if (shot_number == shot_info{p,1})
        N = shot_info{p,2};%N is the number of wires in the array
        d = shot_info{p,3};%d is the diameter of the wires in microns
        D = shot_info{p,5};%D is the initial array diamter in mm
        material = shot_info{p,4};%choose 'W','Al','Ni',or 'Mo'
        f_current = shot_info{p,7};%fraction of current applied
        f_mass = shot_info{p,8};...
            %fraction of initial mass in snowplow at snowplow start
        v_abl_tuned = shot_info{p,6};...
            %ablation velocity (km/s)
        f_turn_pt = shot_info{p,9};...
            %fraction initial mass ablated at snowplow start
    end
end
%%%%%%%%%%%%%%%%%%%%%%%%%%%%%%%%%%%%%%%%%%%%%%%%%%%%%%%%%%%%%%%%%%%%%%%
switch (material)
    case 'W';
        mass_in_kg_per_m_cubed = 18820;
    case 'Al'
        mass_in_kg_per_m_cubed = 2643;
    case 'Ni'
        mass_in_kg_per_m_cubed = 8908;
    case 'Mo'
        mass_in_kg_per_m_cubed = 10280;
end
r0 = D/2/1000;
```

```
d = d * 10^-6;
mass_in_kg_per_m = mass_in_kg_per_m_cubed * (pi * (d/2)^2);
mhat = N * mass_in_kg_per_m;
mu0 = 4 * pi * 10^-7;
mu = mu0;
trailing_mass_percentage = (1.0 - f_turn_pt - f_mass) * 100

plot_time_duration = 250;
xlims_time = [-5,plot_time_duration];
ylims_implosion = [0, 5]
ylims_ablation = [0,100];
ax1 = gca;
set(ax1,'XColor','k','YColor','k','XLim',xlims_time,'YLim',...
    ylims_implosion,'YAxisLocation','Left','XMinorTick','on',...
    'YMinorTick','on');
xlabel(ax1,'Time (ns)')
ylabel(ax1,'Radial Position (mm)')
ax3 = axes('Position',get(ax1,'Position'),'XAxisLocation','top',...
    'YAxisLocation','left','Color','none','XColor','k','YColor',...
    'k','XLim',xlims_time,'YLim',ylims_implosion,'XMinorTick',...
    'on','XTickLabel',[]);

%%%%%%%%%%%%%%%%%%%%%%%%%%%%%%%%%%%%%%%%%%%%%%%%%%%%%%%%%%%%%%%%%%%%%%%%%%%%%%%
shot_number_string=int2str(shot_number);
didt_data=load(strcat(didt_path,'00',shot_number_string,...
    didt_signal));
didt_data(:,1)=didt_data(:,1)*10^9;
%end of data loading section of code

%find rough dc offsets and didt record lengths
dc_off = mean(didt_data(1:100,2));
didt_record_length = size(didt_data,1);

%find didt start, first zero crossing and precise dc offsets
didt_thresh = -3*10^11;

averaged_didt_data(:,:) = didt_data(:,:);
for i=110:didt_record_length-110
    averaged_didt_data(i,2) = mean(didt_data(i-100:i+100,2));
end

[minval,minpos] = min(averaged_didt_data(1:didt_record_length,2));
m=minpos;
flag=1;
```

```
while((m>10) && (flag))
    if(mean(didt_data(m-5:m+5,2)) > (didt_thresh+dc_off))
        zp_time=didt_data(m,1);
        zp_pos=m;
        flag=0;
    end
    m=m-1;
end
dc_off = mean(didt_data(1:m+1,2));
m=minpos;
flag=1;
while((flag) && (m < (didt_record_length - 10)))
    if(mean(didt_data(m-5:m+5,2)) > dc_off)
        peak_time=didt_data(m,1);
        peak_pos=m;
        flag=0;
    end
    m=m+1;
end

didt_data(:,1) = didt_data(:,1) - zp_time;
didt_data(:,2) = didt_data(:,2) - dc_off;
rise_time_to_first_hump = peak_time - zp_time;
time_step = didt_data(2,1) - didt_data(1,1);

% Calculate integral of dI/dt
load_current = zeros(didt_record_length,2);
load_current(:,1) = didt_data(:,1);
for i=2:didt_record_length
    load_current(i,2) = load_current(i-1,2) + didt_data(i,2)*...
        time_step*10^-9;
end

%commented out code just below is for using a sine-squared pulse:
% for i=1:didt_record_length
%     if (load_current(i,1) > 0 && load_current(i,1) < 500)
%         load_current(i,2) = -1.0e6*(sin(load_current(i,1)/250 ...
%             * pi/2))^2;
%     else
%         load_current(i,2)=0;
%     end
% end
```

```
[minval,minpos] = min(load_current(1:didt_record_length,2));
peak_current = minval/10^6;
peak_current_pos = minpos;
integrated_rise_time = load_current(peak_current_pos,1);

number_of_runs = 1
for run=0:number_of_runs;

switch (run)
    case 0;
        v_abl = 30;
        implosion_line_style = '-';
        ablation_line_style = 'none';
        implosion_line_color = 'k';
        ablation_line_color = 'k';
        implosion_label = '0D Thin-Shell Trajectory (no ablation)';
        ablation_label = ' ';
    case 1;
        v_abl = v_abl_tuned;
        implosion_line_style = '-';
        ablation_line_style = '-';
        implosion_line_color = 'r';
        ablation_line_color = 'g';
        implosion_label = ...
            ['Ablation/Snowplow Trajectory (V_{ablation} = ',...
            num2str(v_abl),' km/s)'];
        ablation_label = [ 'Percent Ablation (V_{ablation} = ',...
            num2str(v_abl),' km/s)'];
end
v_abl = v_abl * 1000;

mhat_dot(:,1) = load_current(:,1);
mhat_dot(:,2) = mu .* (f_current.*load_current(:,2)).^2 ./ ...
    (4 * pi * r0 * v_abl);
mhat_dot_record_length = size(mhat_dot,1);

mhat_ablated = zeros(mhat_dot_record_length,2);
mhat_ablated(:,1) = mhat_dot(:,1);
for i=2:mhat_dot_record_length
    if (mhat_ablated(i,1) > 0)
        if (mhat_ablated(i-1,2) < mhat)
            mhat_ablated(i,2) = mhat_ablated(i-1,2) + ...
                mhat_dot(i,2)*time_step*10^-9;
        else
```

```
            mhat_ablated(i,2) = mhat_ablated(i-1,2);
        end
    else
        mhat_ablated(i,2) = 0;
    end
end

percent_ablated = mhat_ablated;
percent_ablated(:,2) = mhat_ablated(:,2)/ mhat * 100;
flag = 1;
for i=2:mhat_dot_record_length-1
    if (percent_ablated(i-1,2)<f_turn_pt*100 && ...
            percent_ablated(i+1,2)>f_turn_pt*100 && flag)
        turning_point = percent_ablated(i,1)
        flag = 0;
    end
end

load_current(:,1) = load_current(:,1)*10^-9;

if (run==0)
    t0 = 0;
else
    t0 = turning_point*10^-9;
end

rho_r = linspace(1e-6,r0,100);
t_to_r = t0 - (r0 - rho_r)/v_abl;
load_current_r = interp1(load_current(:,1),load_current(:,2),t_to_r);
rho_t0 = mu./(8.*pi^2*r0.*rho_r.*v_abl^2).*(load_current_r).^2;

if (t0 < (r0/v_abl))
    rho_is_0_somewhere = 'yes'
    for i=1:length(rho_r)
        if (rho_r(i)<(r0-t0*v_abl))
            rho_t0(i) = 0.0;
            last_r = rho_r(i);
        end
    end
    rho_is_0_up_to_here = last_r
else
    rho_is_0_somewhere = 'no'
end
```

```
if (run==0)
    rho_t0(:) = 0;
end

options = odeset('Events',@events,'InitialStep',1e-9,...
    'MaxStep',2e-9,'RelTol',.001);
if (run==0)
    m0 = mhat;
else
    m0 = f_mass*mhat;
end
time_span = [t0, 250*10^-9];
ic = [r0, 0, m0];
[r_time, r_vals,TE,RE,IE] = ode23(@(t,r) ...
    snow_plow(t,r,load_current(:,1),f_current.*load_current(:,2),...
    rho_r,rho_t0,v_abl,t0,r0,mu),time_span,ic,options);
r_time(1)=0;
r_vals(1)=r0;
h1 = line(r_time(1:size(r_vals,1))*10^9, ...
    r_vals(1:size(r_vals,1),1)*10^3,'Color',implosion_line_color,...
    'Parent',ax1,'LineStyle',implosion_line_style);
h2 = 0;
% h2 = line(percent_ablated(:,1), percent_ablated(:,2),'Color',...
%     ablation_line_color,'Parent',ax2,'LineStyle',...
%     ablation_line_style);

if (run==0)
    hvec(1) = h1;
    labelmat(1,1) = {implosion_label};
else
    hvec(run+1) = h1;
    labelmat(run+1,1) = {implosion_label};
    %hvec(2*run) = h1;
    %labelmat(2*run,1) = {implosion_label};
    %hvec(2*run+1) = h2;
    %labelmat(2*run+1,1) = {ablation_label};
end

title(strcat('Shot #',int2str(shot_number),...
    ': Inductance Trajectory and Thin-Shell, Ablation, and Snow',...
    '-Plow Models'),'Color','k')

load_current(:,1) = load_current(:,1)*10^9;
```

```
end %end of run loop

h3 = line(inductance_trajectory_array(:,1),...
    inductance_trajectory_array(:,2),'Color','b','Parent',ax1,...
    'LineStyle','-');
hvec(number_of_runs+2) = h3;
labelmat(number_of_runs+2,1) = {'Inductance Trajectory'};
%hvec(2*number_of_runs+2) = h3;
%labelmat(2*number_of_runs+2,1) = {'Inductance Trajectory'};

%set(ax1,'XGrid','on');

legend(hvec,labelmat);
fig1=gcf;
saveas(fig1,strcat(output_plot_path,int2str(shot_number),...
    '-implosion_trajectories_and_ablation.bmp'));


% clf;
% m_r=zeros(length(rho_r),1);
% m_r0 = 0.9 * pi * (1e-3)^2;
% for k=2:length(rho_r)
%     if (rho_r(k) >= 0)
%         if (rho_r(k) >= 1e-3)
%             m_r(k) = 2*pi*rho_r(k)*rho_t0(k)*(rho_r(k)-...
%                 rho_r(k-1)) + m_r(k-1);
%         else
%             m_r(k) = 0.9 * pi * rho_r(k)^2;
%         end
%     else
%         m_r(k)=0.0;
%     end
% end
% plot(rho_r*10^3,rho_t0*1000/1e6)
% axis([1 8 .5e-5 1e-3])
% set(gca,'YScale','log')
% xlabel('radius (mm)')
% ylabel('density (g/cm^3)')
% title('Density Distribution')
% %plot(rho_r*10^3,m_r/mhat)
% %axis([1 8 0 1])
% %xlabel('radius (mm)')
% %ylabel('mass fraction')
% %title('Mass Fraction')
```

```
end %end of function ablation_snow_plow()

function drdt = snow_plow(t,r,load_current_time,load_current,...
    rho_r,rho_t0,v_abl,t0,r0,mu)
    load_current = interp1(load_current_time,load_current,t);
    rp = r(1)+v_abl*(t-t0);
    if (rp>r0)
        rho = 0*r0/r(1)*interp1(rho_r,rho_t0,r0);
        r(1)
    else
        rho = rp/r(1)*interp1(rho_r,rho_t0,rp);
    end
%     if (abs(r(2))<v_abl)
%         rho = 0;
%     end
    drdt = [r(2); (2*pi*r(1)*rho./r(3)).*(r(2)+v_abl)^2 - ...
        mu*(load_current.^2)/(4*pi*r(1).*r(3)); ...
        -2*pi*r(1)*rho.*(r(2)+v_abl)^2];
end

function [value,isterminal,direction] = events(t,r)
    value = r(1);
    isterminal = 1;
    direction = -1;
end
```

APPENDIX C

CODE FOR CONTINUUM/SPECTROSCOPY STUDY

C.1 Mathematica Notebook for Optics/Grating Selection

```
(* See pages 111-117 in lab notebook *)

(* n is grooves/mm *)
n = 100;
(* ω is the blaze angle in degrees *)
ω = 1.29;
(* λB is the blaze wavelength satisfying the Littrow condition in nm *)
2 * Sin[ω * π / 180] / n / 10^-6
```

```
450.257
```

```
(* For the 305 M: *)
(* γ is the rotation angle of the grating in
   the 305 M in degrees and measured from the zero-order normal *)
γ = -(ω);
α = -10.5 - γ;
β = 10.5 - γ;
(* Dv is the constant deviation angle for the 305 M *)
Dv = β - α;
(* λ305M is the center wavelength (effective blaze wavelength) for the 305 M *)
λ305M = (Sin[α * π / 180] + Sin[β * π / 180]) / 10^-6 / n
```

```
442.717
```

```
(* Method 1 resolving power R1 (ideal): *)

n = 100;
Wg = 40.0;
R1 = n * Wg;
λmax = 710;
dλ1 = λmax / R1 (* result in nm *)
```

```
0.1775
```

```
(* Method 2 resolving power R2 (with 305-M geometry restrictions): *)

n = 100;
Wg = 40.0;
γmax = -2.05;
α = -10.5 - γmax;
β = 10.5 - γmax;
λmax = (Sin[α * π / 180] + Sin[β * π / 180]) / 10^-6 / n
```

```
703.452
```

```
R2 = Wg * (Sin[α * π / 180] + Sin[β * π / 180]) / 10^-6 / λmax;
dλ2 = λmax / R2 (* result in nm *)
```

```
0.175863
```

```
(* System resolution *)
```

```
n = 100;
Const = 2004;
dλdx = Const / n;
Wslit = 0.010; (* in mm *)
dλslit = Wslit * dλdx (* result in nm *)
```

```
0.2004
```

```
dλres = dλ1;
FWHM = Sqrt[dλres^2 + dλslit^2] (* result in nm *)
```

```
0.267706
```

```
(* Calculations that consider dispersion, fraction of grating surface used,
 desired bandwidth, magnification, size of photocathode image on streak camera input slit,
 size of relay optic L4, position of relay optic L4,
 distance between spectrometer output plane and streak camera input slit,
 and color spot-sizes and spot-positions on optic L4: *)
n = 100;
λhigh = 675;
λlow = 425;
Const = 2004;
dλdx = Const / n;
dxdλ = 1 / dλdx;
λrange = λhigh - λlow;
Δλ = λrange / 2;
λcenter = (λhigh + λlow) / 2;
phigh = dxdλ * Δλ;
plow = -dxdλ * Δλ;
Δx = λrange * dxdλ;
mmCathodeSize = 15;
s1 = 267;
s2 = 341;
mmLength = s1 + s2;
Magnification = s2 / s1 * 1.0 ;
fL4 = 1. / (1 / s1 + 1 / s2 ); (* lens focal length *)
D1 = 500; (* spectrometer focal length *)
d = 45; (* effective lens aperture *)
Wg = 39; (* light spot-size / grating width used *)
Δx * Magnification;
rlightCone = Wg / D1 * s1 / 2; (* light cone radius *)
ξhigh = phigh / 2 / D1 * (D1 + s1) + phigh / 2;
ξlow = -ξhigh;
ParametricPlot[{d / 2 * {Cos[ϕ], Sin[ϕ]},
   {rlightCone * Cos[ϕ] + ξhigh, rlightCone * Sin[ϕ]}, {rlightCone * Cos[ϕ], rlightCone * Sin[ϕ]},
   {rlightCone * Cos[ϕ] + ξlow, rlightCone * Sin[ϕ]}}, {ϕ, 0, 2 * π}, AspectRatio → Automatic,
  PlotLabel → "Light spots for λlow, λcenter, and λhigh on 45-mm-diameter optic", PlotStyle →
   {{RGBColor[0, 0, 0]}, {RGBColor[1, 0, 0]}, {RGBColor[0, 1, 0]}, {RGBColor[0, 0, 1]}}];
```

Light spots for λlow, λcenter, and λhigh on 45-mm-diameter optic

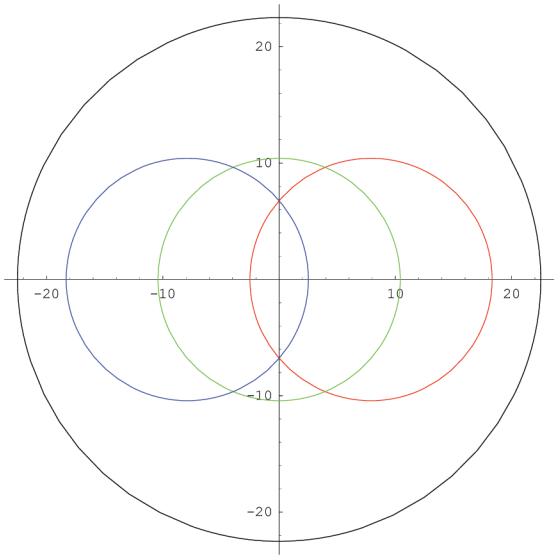

λhigh - λlow

250

fL4

149.748

s1

267

s2

341

s1 + s2

608

Magnification

1.27715

Δx * 1.

12.475

Magnification * Δx

15.9326

C.2 MATLAB M-Files for Streak Camera Calibration and Data Processing

C.2.1 efficiency.m

```
function efficiency
%This function calculates the efficiency from the wire-array source
%to the input slit of the streak camera as well as from the
%wire-array source through the input optics of the streak camera,
%and all as a function of wavelength. The wavelength-dependent
%efficiency data is saved in output files as specified below. This
%function also outputs the cathode sensitivity data that was provided
%by the manufacturer in the user manual test report (again as a
%function of wavelength) in a format for use by other functions such
%as spectra.m

wavelength = (350:10:750)';
clf;

% Vmcp = [400 600 700 800 900 1000];
% measured_gain = [1 27 110 420 1400 3900];
% II_setting = (0:1:63)';
% voltage_step = (1000-400)/63;
% II_voltage = (400:voltage_step:1000)';
% II_gain = interp1(Vmcp,measured_gain,II_voltage);

wavelength_from_manual = (200:10:960)';

%Photocathode Radiant Sensitivity [mA/W]:
cat_sens_from_manual = [...
    11.377 16.649 22.812 28.836 35.605 39.436 43.880 44.905 43.478...
    43.119 43.110 43.994 45.946 47.606 49.243 52.575 55.361 57.336...
    59.008 59.194 59.479 59.536 59.023 57.423 56.126 54.270 52.627...
    50.546 48.994 46.887 45.303 43.547 42.001 40.263 38.565 37.054...
    35.619 33.962 32.688 31.100 29.737 28.491 27.172 26.061 24.809...
    23.870 22.664 21.656 20.507 19.331 18.377 17.154 16.283 15.130...
    14.003 12.947 11.722 10.673  9.645  8.455 7.325  6.271  5.099...
    3.888  2.783  1.805  1.112  0.680  0.419  0.256  0.156  0.094...
    0.056  0.034  0.020  0.013  0.008...
    ]';
```

```
%Quantum Efficiency [%]:
quant_eff_from_manual = [...
     7.051  9.827 12.852 15.540 18.389 19.552 20.919 20.615 19.247...
    18.430 17.812 17.591 17.797 17.881 17.952 18.619 19.061 19.208...
    19.248 18.813 18.431 17.999 17.419 16.553 15.811 14.948 14.181...
    13.330 12.652 11.860 11.231 10.584 10.012  9.416  8.852  8.351...
     7.884  7.385  6.986  6.534  6.143  5.789  5.432  5.127  4.805...
     4.552  4.256  4.006  3.738  3.473  3.254  2.995  2.803  2.569...
     2.345  2.140  1.912  1.718  1.533  1.327  1.135  0.960  0.771...
     0.581  0.411  0.263  0.160  0.097  0.059  0.036  0.021  0.013...
     0.008  0.005  0.003  0.002  0.001...
     ]';

streak_input_optics_efficiency = ...
    load('streak_input_optics_efficiency.txt');
strk_in_opt_eff = interp1(streak_input_optics_efficiency(:,1),...
    streak_input_optics_efficiency(:,2),wavelength,...
    'linear','extrap');

cat_sens = interp1(wavelength_from_manual,cat_sens_from_manual,...
    wavelength,'linear','extrap');
quant_eff = interp1(wavelength_from_manual,quant_eff_from_manual,...
    wavelength,'linear','extrap');

cat_sens_norm_factor = interp1(wavelength,cat_sens,632.8);
cat_sens_norm = cat_sens/cat_sens_norm_factor;

quant_eff_norm_factor = interp1(wavelength,quant_eff,632.8);
quant_eff_norm = quant_eff/quant_eff_norm_factor;

mirror45deg_from_file = load('mirror45deg.txt');
mirror45deg = interp1(mirror45deg_from_file(:,1),...
    mirror45deg_from_file(:,2),wavelength,'linear','extrap');
mirror45deg = mirror45deg/100;
mirror45deg_633nm = interp1(wavelength,mirror45deg,632.8);

mirror8deg_from_file = load('mirror8deg.txt');
mirror8deg = interp1(mirror8deg_from_file(:,1),...
    mirror8deg_from_file(:,2),wavelength,'linear','extrap');
mirror8deg = mirror8deg/100;
mirror8deg_633nm = interp1(wavelength,mirror8deg,632.8);

mirror8deg_mgf2_from_file = load('mirror8deg_mgf2.txt');
mirror8deg_mgf2 = interp1(mirror8deg_mgf2_from_file(:,1),...
```

```
    mirror8deg_mgf2_from_file(:,2),wavelength,'linear','extrap');
mirror8deg_mgf2 = mirror8deg_mgf2/100;
mirror8deg_mgf2_633nm = interp1(wavelength,mirror8deg_mgf2,632.8);

grating21deg_from_file = load('grating21deg.txt');
grating21deg = interp1(grating21deg_from_file(:,1),...
    grating21deg_from_file(:,2),wavelength,'linear','extrap');
grating21deg_633nm = interp1(wavelength,grating21deg,632.8);

lens_reflect_input = [
    400  .25
    450  .21
    500  .20
    550  .21
    600  .35
    650 1.0
    700 2.0
    750 3.3
    ];
lens_reflect = interp1(lens_reflect_input(:,1),...
    lens_reflect_input(:,2),wavelength,'linear','extrap');
lens_eff = (100 - lens_reflect)/100;
lens_eff_633nm = interp1(wavelength,lens_eff,632.8);

laser_port_efficiency_from_file = load('laser_port_efficiency.txt');
laser_port_efficiency = ...
    interp1(laser_port_efficiency_from_file(:,1),...
    laser_port_efficiency_from_file(:,2),wavelength,...
    'linear','extrap');

r = (84+38+80)*.0254; %distance to first lense

A_to_B_eff = (pi*.045^2)/(4*pi*r^2) .* ...
    laser_port_efficiency .* mirror45deg.^2 .* lens_eff;

B_to_E_eff_633nm = 0.0335;
B_to_E_geo_eff = B_to_E_eff_633nm / (mirror45deg_633nm^4 * ...
    mirror8deg_633nm^2 * mirror8deg_mgf2_633nm^2 * ...
    grating21deg_633nm * lens_eff_633nm^3);
B_to_E_eff = B_to_E_geo_eff .* mirror45deg.^4 .* mirror8deg.^2 .* ...
    mirror8deg_mgf2.^2 .* grating21deg .* lens_eff.^3;

A_to_E_eff = A_to_B_eff .* B_to_E_eff;
```

```
A_thru_streak_input_optics_eff = A_to_E_eff .* strk_in_opt_eff;

hold on;

% plot(wavelength,A_to_E_eff,'r')
% plot(wavelength,A_to_E_eff .* cat_sens_norm,'g')
% plot(wavelength,A_to_E_eff .* quant_eff_norm,'b')

c = 3.0e8; % in meters/second
nu = c./(wavelength * 1e-9); % in 1/seconds
h = 6.626e-34; % in m^2*kg/s
joules_per_photon = h*nu;

% plot(wavelength,cat_sens_norm,'g')
% plot(wavelength,quant_eff_norm ./ joules_per_photon /...
% 10000000000000000000 * 3.15,'b')

plot(wavelength,A_to_E_eff,'r')
plot(wavelength,A_thru_streak_input_optics_eff,'g')

dlmwrite('A_to_E_efficiency.txt',[wavelength A_to_E_eff],...
    'delimiter','\t','precision',6);
dlmwrite('A_thru_streak_input_optics_efficiency.txt',...
    [wavelength A_thru_streak_input_optics_eff],...
    'delimiter','\t','precision',6);
dlmwrite('cathode_sensitivity_normalized_to_633nm.txt',...
    [wavelength cat_sens_norm],'delimiter','\t','precision',6);
dlmwrite('quantum_efficiency_normalized_to_633nm.txt',...
    [wavelength quant_eff_norm],'delimiter','\t','precision',6);

end
```

C.2.2 zero.m

```
function zero
%This function reads the streak images from the null tests conducted
%with the streak input slit shutter closed for the various sweep
%speeds and image intensifier gains, then calculates the average
%image value which is the zero value (i.e., the average offset stored
%in the images despite zero photons entering the system). The offset
%values are stored in output files as specified below. These output
%files are then used by other functions such as spectra.m.
```

```
clf;
hold on;

path1 = 'C:\research\shot_processing\1217\continuum\zero\';

for i=1:5
    switch i
        case 1
            setup = 'a';
        case 2
            setup = 'b';
        case 3
            setup = 'I';
        case 4
            setup = 'II';
        case 5
            setup = 'III';
    end
    I_sum = zeros(size(double(imread(strcat(path1,'a1.tif')))));
    for j=1:3
        file = strcat(path1,setup,int2str(j),'.tif');
        I = double(imread(file));
        I_sum = I_sum + I;
        if i == 5
            switch j
                case 1
                    color = 'r';
                case 2
                    color = 'g';
                case 3
                    color = 'b';
            end
            plot(I(500:600,600),color)
        end
    end
    I_avg = I_sum ./ 3;
    I_avg_mean = mean(mean(I_avg));
    if i==3
        I_zero = I_avg_mean;
    end
    if i==4
        II_zero = I_avg_mean;
    end
```

```
    if i==5
        III_zero = I_avg_mean;
    end
end

% plot(I(:,600))
% plot(I_avg(:,600),'r')

% imagesc(test2,[mI-1000 mI+1000]); colormap(gray);

dlmwrite(strcat(path1,'I_zero.txt'),I_zero,'delimiter','\t',...
    'precision',6);
dlmwrite(strcat(path1,'II_zero.txt'),II_zero,'delimiter','\t',...
    'precision',6);
dlmwrite(strcat(path1,'III_zero.txt'),III_zero,'delimiter','\t',...
    'precision',6);

status = fclose('all')

end
```

C.2.3 cal_I.m

```
function cal_I
%This function reads in the nearly vertical-line images of the
%streaked HeNe CW laser spots for photon per pixel value calibration.
%These calibration values and their coordinates are stored in output
%files as specified below. These output files are then used by other
%functions such as spectra.m. Here zeroing is applied along with the
%white wash matrix for proper scaling and smoothing of various pixel
%sensitivities, respectively.

cal_path = strcat('C:\research\shot_processing\1217\continuum\',...
    'streak_cam_calibration\');
white_path = strcat('C:\research\shot_processing\1217\continuum\',...
    'streak_cam_calibration\all_positions_white\');
zero_path = 'C:\research\shot_processing\1217\continuum\zero\';

white = load(strcat(white_path,'white_cal_I.txt'));
offset = load(strcat(zero_path,'I_zero.txt'));
streak_input_optics_efficiency = ...
    load('streak_input_optics_efficiency.txt');
```

```
streak_input_optics_efficiency_at_633nm = ...
    interp1(streak_input_optics_efficiency(:,1),...
    streak_input_optics_efficiency(:,2),632.8);

file = strcat(cal_path,'aI1.tif');
size_I = size(double(imread(file)));
I_sum = zeros(size_I);
num_of_rows = size_I(1);
num_of_columns = size_I(2);

fwhm_to_sigma_coef = 1/(2*sqrt(2*log(2)));
measured_Intensity = 4.5e-8; % in joules/second (Watts)
Intensity_in = ...
    measured_Intensity * streak_input_optics_efficiency_at_633nm;
lambda = 6.328e-7; % in meters
c = 3.0e8; % in meters/second
nu = c/lambda; % in 1/seconds
h = 6.626e-34; % in m^2*kg/s
joules_per_photon = h*nu;
photons_per_second = Intensity_in / joules_per_photon;
v = num_of_rows / 2.0e-7; % in pixels per second

num_of_curves_1 = 9;
for c1 = 1:num_of_curves_1

    c1

    switch c1
        case 1
            let = 'a';
        case 2
            let = 'b';
        case 3
            let = 'c';
        case 4
            let = 'd';
        case 5
            let = 'e';
        case 6
            let = 'f';
        case 7
            let = 'g';
        case 8
            let = 'h';
```

```
    case 9
        let = 'i';
end
for take=1:5

    file = strcat(cal_path,let,'I',int2str(take),'.tif');

    I = double(imread(file));
    I_white = (I-offset) .* white;
    for i = 1:size_I(1)
        [max_vals(i),max_pos(i)] = max(I_white(i,:));
    end
    mean_pos = mean(max_pos);
    if mean_pos < (num_of_columns / 3)
        start = round(num_of_columns / 3 * 2);
        stop = num_of_columns;
        background = mean(mean(I_white(:,start:stop)));
    end
    if mean_pos >= (num_of_columns/3) && ...
            mean_pos <= (num_of_columns/3*2)
        start1 = 1;
        stop1 = round(num_of_columns/6);
        start2 = num_of_columns - round(num_of_columns/6);
        stop2 = num_of_columns;
        temp_I_white = cat(2,I_white(:,start1:stop1),...
            I_white(:,start2:stop2));
        background = mean(mean(temp_I_white));
    end
    if mean_pos > (num_of_columns / 3 * 2)
        start = 1;
        stop = round(num_of_columns / 3);
        background = mean(mean(I_white(:,start:stop)));
    end
    I_final = I_white - background;
    max_vals = max_vals - background;
    for i=1:num_of_rows
        j = max_pos(i);
        while I_final(i,j) > max_vals(i)/2
            j = j - 1;
        end
        j_left = j;
        j = max_pos(i);
        while I_final(i,j) > max_vals(i)/2
            j = j + 1;
```

```
            end
            j_right = j;
            j_interp_left = interp1(I_final(i,j_left:j_left+1),...
                [j_left j_left+1],max_vals(i)/2);
            j_interp_right = interp1(I_final(i,j_right-1:j_right),...
                [j_right-1 j_right],max_vals(i)/2);
            fwhm(i) = j_interp_right - j_interp_left;
            sigma(i) = fwhm(i) .* fwhm_to_sigma_coef;
            A(i) = photons_per_second ./ (2.*pi.*sigma(i).^2);
            c633(i) = photons_per_second ./ ...
                (max_vals(i) .* sigma(i) .* v .* sqrt(2*pi));...
                % number of 633-nm photons per image value
        end
        cal_data_out = cat(2,max_pos',c633');
        out_file = ...
            strcat(cal_path,'cal_',let,'I',int2str(take),'.txt');
        dlmwrite(out_file,cal_data_out,...
            'delimiter','\t','precision',6);
        cal_curve_coords(:,c1,take) = max_pos(:);
    end
end
for take=1:5
    dlmwrite(strcat(cal_path,'cal_curve_coords_I',...
        int2str(take),'.txt'),cal_curve_coords(:,:,take),...
        'delimiter','\t','precision',6);
end

% imagesc(I_white); colormap(gray);
% hold on;

% plot(c633)
% ylim([0 12e-4])

status = fclose('all')

end
```

C.2.4 cal_I_avg.m

```
function cal_I_avg
%This code simply averages the calibration results produced by
%cal_I.m for the several repeat streaks that were taken to improve
```

```
%statistics. The output is used in the same way as that specified by
%cal_I.m (this just produces an average result instead of a result
%from a single streak).

cal_path = strcat('C:\research\shot_processing\1217\continuum\',...
    'streak_cam_calibration\');

num_of_curves_1 = 9;
for c1 = 1:num_of_curves_1

    c1

    switch c1
        case 1
            let = 'a';
        case 2
            let = 'b';
        case 3
            let = 'c';
        case 4
            let = 'd';
        case 5
            let = 'e';
        case 6
            let = 'f';
        case 7
            let = 'g';
        case 8
            let = 'h';
        case 9
            let = 'i';
    end
    cal1 = load(strcat(cal_path,'cal_',let,'I1.txt'));
    cal2 = load(strcat(cal_path,'cal_',let,'I2.txt'));
    cal3 = load(strcat(cal_path,'cal_',let,'I3.txt'));
    cal4 = load(strcat(cal_path,'cal_',let,'I4.txt'));
    cal5 = load(strcat(cal_path,'cal_',let,'I5.txt'));
    cal_avg = (cal1+cal2+cal3+cal4+cal5)/5;
    cal_avg(:,1) = round(cal_avg(:,1));
    dlmwrite(strcat(cal_path,'cal_',let,'I_avg.txt'),cal_avg,...
        'delimiter','\t','precision',6);
end

status = fclose('all')
```

```
end
```

C.2.5 cal_curve_coords_avg.m

```
function cal_curve_coords_avg
%This code simply averages the calibration curve coordinates produced
%by cal_I.m for the several repeat streaks that were taken to improve
%statistics. The output is used in the same way as that specified by
%cal_I.m (this just produces an average result instead of a result
%from a single streak).

cal_path = strcat('C:\research\shot_processing\1217\continuum\',...
    'streak_cam_calibration\');

cal_curve_coords_1 =load(strcat(cal_path,'cal_curve_coords_I1.txt'));
cal_curve_coords_2 =load(strcat(cal_path,'cal_curve_coords_I2.txt'));
cal_curve_coords_3 =load(strcat(cal_path,'cal_curve_coords_I3.txt'));
cal_curve_coords_4 =load(strcat(cal_path,'cal_curve_coords_I4.txt'));
cal_curve_coords_5 =load(strcat(cal_path,'cal_curve_coords_I5.txt'));
cal_curve_coords_avg = (cal_curve_coords_1+cal_curve_coords_2+...
    cal_curve_coords_3+cal_curve_coords_4+cal_curve_coords_5)/5;
cal_curve_coords_avg = round(cal_curve_coords_avg);
dlmwrite(strcat(cal_path,'cal_curve_coords_I_avg.txt'),...
    cal_curve_coords_avg,'delimiter','\t','precision',6);

cal_curve_coords_1=load(strcat(cal_path,'cal_curve_coords_II1.txt'));
cal_curve_coords_2=load(strcat(cal_path,'cal_curve_coords_II2.txt'));
cal_curve_coords_3=load(strcat(cal_path,'cal_curve_coords_II3.txt'));
cal_curve_coords_4=load(strcat(cal_path,'cal_curve_coords_II4.txt'));
cal_curve_coords_5=load(strcat(cal_path,'cal_curve_coords_II5.txt'));
cal_curve_coords_avg = (cal_curve_coords_1+cal_curve_coords_2+...
    cal_curve_coords_3+cal_curve_coords_4+cal_curve_coords_5)/5;
cal_curve_coords_avg = round(cal_curve_coords_avg);
dlmwrite(strcat(cal_path,'cal_curve_coords_II_avg.txt'),...
    cal_curve_coords_avg,'delimiter','\t','precision',6);

cal_curve_coords_1 = load(strcat(cal_path,...
    'cal_curve_coords_III1.txt'));
cal_curve_coords_2 = load(strcat(cal_path,...
    'cal_curve_coords_III2.txt'));
cal_curve_coords_3 = load(strcat(cal_path,...
```

```
    'cal_curve_coords_III3.txt'));
cal_curve_coords_4 = load(strcat(cal_path,...
    'cal_curve_coords_III4.txt'));
cal_curve_coords_5 = load(strcat(cal_path,...
    'cal_curve_coords_III5.txt'));
cal_curve_coords_avg = (cal_curve_coords_1+cal_curve_coords_2+...
    cal_curve_coords_3+cal_curve_coords_4+cal_curve_coords_5)/5;
cal_curve_coords_avg = round(cal_curve_coords_avg);
dlmwrite(strcat(cal_path,'cal_curve_coords_III_avg.txt'),...
    cal_curve_coords_avg,'delimiter','\t','precision',6);

status = fclose('all')

end
```

C.2.6 white.m

```
function white
%This function reads in the image data from the streaks of the
%uniform constant white-light source (i.e., the streaks of uniform
%illumination by our tungsten lamp). This function then uses this
%data to calculate the white-wash matrix for each of the streak
%setups used. These matrices are then stored in output files as
%specified below. These output files are then used by other functions
%such as spectra.m when applying the white-wash matrix.

% clf;
% hold on;

path = strcat('C:\research\shot_processing\1217\continuum\',...
    'streak_cam_calibration\all_positions_white\');
path2 = 'C:\research\shot_processing\1217\continuum\zero\';

fileI = strcat(path,'I1.tif');
fileII = strcat(path,'II1.tif');
fileIII = strcat(path,'III1.tif');

offsetI = load(strcat(path2,'I_zero.txt'));
offsetII = load(strcat(path2,'II_zero.txt'));
offsetIII = load(strcat(path2,'III_zero.txt'));

I = double(imread(fileI)) - offsetI;
```

```
II = double(imread(fileII)) - offsetII;
III = double(imread(fileIII)) - offsetIII;

for i=2:8
    fileI = strcat(path,'I',int2str(i),'.tif');
    fileII = strcat(path,'II',int2str(i),'.tif');
    fileIII = strcat(path,'III',int2str(i),'.tif');

    I = I + (double(imread(fileI)) - offsetI);
    II = II + double(imread(fileII) - offsetII);
    III = III + double(imread(fileIII) - offsetIII);
end

I = I / 8;
II = II / 8;
III = III / 8;

for i=1:length(I(:,1))
    pmI(i) = mean(I(i,:));
    pmII(i) = mean(II(i,:));
    pmIII(i) = mean(III(i,:));
end

mI = mean(pmI);
mII = mean(pmII);
mIII = mean(pmIII);

Ical = mI ./ I;
IIcal = mII ./ II;
IIIcal = mIII ./ III;

% test_file = strcat(path,'I1.tif');
% test_image = double(imread(test_file));
% test1 = I .* Ical;
% test2 = test_image .* Ical;
% imagesc(test2,[mI-1000 mI+1000]); colormap(gray);

dlmwrite(strcat(path,'white_cal_I.txt'),Ical,'delimiter','\t',...
    'precision',6);
dlmwrite(strcat(path,'white_cal_II.txt'),IIcal,'delimiter','\t',...
    'precision',6);
dlmwrite(strcat(path,'white_cal_III.txt'),IIIcal,'delimiter','\t',...
    'precision',6);
```

```
% cal_path = strcat('C:\research\shot_processing\1217\continuum\',...
%     'streak_cam_calibration\');
% coords = load(strcat(cal_path,'cal_I.txt'));
% for i=1:length(I(:,1))
%     I_traj(i) = I(i,coords(i));
% end
% plot(I_traj)
% hold on;
% plot((I_traj.*(I_traj.^.06))*4.0,'r')
% plot(I_traj,'k')

% plot(test_image(:,30))
% hold on
% plot(test2(:,30))

status = fclose('all')

end
```

C.2.7 root.m

```
function [p] = root
%This function is used to establish the root directory. In this case
%it is the root above the '\streak_image_processing\' sub-directory.
%It is used so that the collection of spectroscopy data files and
%MATLAB M-files can be moved to other locations/computers and still
%function properly as long as the relative directory structure is
%preserved between the various M-files and data files.
pf = mfilename('fullpath');

for i=1:length(pf)-length('streak_image_processing\root')
    p(i) = pf(i);
end

end
```

C.2.8 spectra.m

```
function spectra(shot_number,time)
%This function requires a shot number and a time that falls within
```

```
%the streak window for the shot number as input arguments. It then
%returns a fully calibrated spectrum for the specified shot number
%and time. This calibrated data is returned in a formatted plot and
%text file data columns, as specified below. The calibration makes
%use of several calibration files produced by other functions to
%correct for streak tube aberrations in the time and spatial
%dimensions, as well as absolute pixel value calibrations as a
%function of wavelength. The calibration files used are read in as
%specified below.

quick_mode = 'n';

if shot_number == 1222
    message_to_user = strcat('Streak camera slit left open o',...
        'n this shot, thus data is unusable')
    error(strcat('Streak camera slit left open on this shot',...
        ', thus data is unusable'))
end
if shot_number == 1226
    message_to_user = strcat('No laser/streak timing fid',...
        'ucial on this shot, thus poor timing info')
    error(strcat('No laser/streak timing fid',...
        'ucial on this shot, thus poor timing info'))
end

use_cat_sens_c_or_quant_eff_q = 'q';

clf;

switch shot_number
    case 1217
        fiducial_time = 13.7;
    case 1218
        fiducial_time = 64.5;
    case 1219
        fiducial_time = 94.1;
    case 1220
        fiducial_time = 146.5;
    case 1221
        fiducial_time = 199.7;
    case 1222
        fiducial_time = 49.3;
    case 1223
        fiducial_time = 80.5;
```

```
    case 1224
        fiducial_time = 158.1;
    case 1225
        fiducial_time = 78.9;
    case 1226
        fiducial_time = 80;98;
    case 1227
        fiducial_time = 8.1;
    case 1228
        fiducial_time = 34.1;
    case 1229
        fiducial_time = 83.3;
end

root_path = root;
output_path = strcat(root_path,'1217\output_spectra_files\');
data_path = strcat(root_path,'1217\streaks\');
drift_path = strcat(root_path,'1217\continuum\drift_correction\');
spectral_cal_path = strcat(root_path,'1217\continuum\spectral_cal\');
time_tilt_path = ...
    strcat(root_path,'1217\continuum\time_tilt_correction\');
white_path = strcat(root_path,...
    '1217\continuum\streak_cam_calibration\all_positions_white\');
zero_path = strcat(root_path,'1217\continuum\zero\');
cal_path = ...
    strcat(root_path,'1217\continuum\streak_cam_calibration\');
efficiency_path = 'streak_image_processing\';

shot_setup_info = load(strcat(root,...
    'streak_image_processing\shot_setup_info_nums.txt'));
for s=1:1229-1217+1
    if shot_setup_info(s,1) == shot_number
        dial_num = shot_setup_info(s,2);
        setup_num = shot_setup_info(s,3);
    end
end
switch dial_num
    case 1
        dial = 'A';
    case 2
        dial = 'B';
    case 3
        dial = 'c';
end
```

```
switch setup_num
    case 1
        setup = 'I';
        sweep = '200ns';
    case 2
        setup = 'II';
        sweep = '200ns';
    case 3
        setup = 'III';
        sweep = '500ns';
end
data_file = strcat(data_path,int2str(shot_number),'_',sweep,'.tif');
if shot_number == 1222
    data_file = strcat(data_path,int2str(shot_number),'_',sweep,...
        '_wide_open_slit.tif');
end

I_raw = double(imread(data_file));
num_of_rows = length(I_raw(:,1));
num_of_cols = length(I_raw(1,:));
midpoint = round(num_of_cols/2);
[fid_value fid_index] = max(I_raw(:,midpoint));

if setup_num == 3
    time_scaling = 500/num_of_rows; % ns per pixel
    v = num_of_rows/500; % pixels per ns
    integration_time = 4.88; % in ns
else
    time_scaling = 200/num_of_rows;
    v = num_of_rows/200;
    integration_time = 1.95; % in ns
end
vert_pix_to_avg = round(v * integration_time);

for i=1:num_of_rows;
    time_axis(i) = fiducial_time - (fid_index-i)*time_scaling;
end
time_index = find(time_axis >= time,1,'first');

time_curves = load(strcat(time_tilt_path,'curve_coords_',setup,...
    '.txt'));

if time_curves(length(time_curves(:,1)),midpoint) < time_index
    time_curves_index = length(time_curves(:,1));
```

```
    delta = time_index - time_curves(time_curves_index,midpoint);
    for j=1:length(time_curves(1,:))
        time_curve(j) = time_curves(time_curves_index,j) + delta;
    end
else
    time_curves_index = ...
        find(time_curves(:,midpoint) >= time_index,1,'first');
    if time_curves_index == 1
        delta = time_curves(1,midpoint) - time_index;
        for j=1:length(time_curves(1,:))
            time_curve(j) = time_curves(1,j) - delta;
        end
    else
        weighting_fraction = ...
            (time_curves(time_curves_index,midpoint)-time_index)/...
            (time_curves(time_curves_index,midpoint)-...
            time_curves(time_curves_index-1,midpoint));
        for j=1:length(time_curves(1,:))
            time_curve(j) = ...
                round(time_curves(time_curves_index,j) - ...
                weighting_fraction * ...
                (time_curves(time_curves_index,j) - ...
                time_curves(time_curves_index-1,j)));
        end
    end
end

imagesc(I_raw);colormap(gray);
hold on;
plot(time_curve,'g')
ylim([1 num_of_rows]);

vert_curve_shifts = ...
    load(strcat(drift_path,'vert_curve_shifts_',dial,setup,'.txt'));
y_max_pos = load(strcat(drift_path,'y_pos_',dial,setup,'.txt'));
wavelength_cal = load(strcat(spectral_cal_path,...
    'wavelength_cal_corrected_',int2str(shot_number),'.txt'));
wavelength_pos = zeros(size(wavelength_cal));
wavelength_pos(:,2) = wavelength_cal(:,2);
for lambda_i=1:6
    for j=1:num_of_cols
        if j == wavelength_cal(lambda_i,1) + ...
                vert_curve_shifts(time_curve(j),lambda_i)
            wavelength_pos(lambda_i,1) = j;
```

```
        end
    end
end
for lambda_i=1:6
    if wavelength_pos(lambda_i,1) == 0
        for j=1:num_of_cols
            if j == wavelength_cal(lambda_i,1) + ...
                    vert_curve_shifts(time_curve(j),lambda_i) + 1
                wavelength_pos(lambda_i,1) = j;
            end
        end
    end
    if wavelength_pos(lambda_i,1) == 0
        message_to_user = strcat('error in spectra.m line 154',...
            ': wavelength_pos still 0, so need to increase to j',...
            '=="..."+2, +3, etc.')
        if dial == 'A'
            wavelength_pos(lambda_i,2) = 699;
        end
        if dial == 'B'
            wavelength_pos(lambda_i,2) = 640;
        end
        if dial == 'C'
            wavelength_pos(lambda_i,2) = 664;
        end
        wavelength_pos
    end
end

x_space = 1:num_of_cols;
wavelength_scale = interp1(wavelength_pos(:,1),...
    wavelength_pos(:,2),x_space,'linear','extrap');
% hold on;
% plot(x_space,wavelength_scale,'r')
% plot(wavelength_pos(:,1),wavelength_pos(:,2),'g')

white = load(strcat(white_path,'white_cal_',setup,'.txt'));
offset = load(strcat(zero_path,setup,'_zero.txt'));

I_plus_background = (I_raw - offset) .* white;
t0_index = find(time_axis >= 0,1,'first');
if quick_mode == 'y'
    for j=1:num_of_cols
        background(j) = mean(I_plus_background(t0_index:t0_index,j));
```

```
        vert_pix_to_avg = 1;
    end
end
if quick_mode == 'n'
    for j=1:num_of_cols
        background(j) = mean(I_plus_background(1:t0_index,j));
    end
end
for i=1:num_of_rows
    I(i,:) = I_plus_background(i,:) - background;
end
% message_to_user = 'put white, offset, and background back in'
% I=I_raw;

time_curve_archive = time_curve;
time_curve = time_curve - round(vert_pix_to_avg/2);
for strip = 1:vert_pix_to_avg
    time_curve = time_curve_archive + strip;
    for j=1:num_of_cols
        data_strip(j) = I(time_curve(j),j);
        if quick_mode == 'y'
            data_strip(j) = I(time_index,j);
        end
    end

%     cal_curve_coords = load(strcat(cal_path,...
%         'cal_curve_coords_',setup,'1.txt'));
    cal_curve_coords = load(strcat(cal_path,'cal_curve_coords_',...
        setup,'_avg.txt'));
    cal_pos = zeros(1,9);
    for pos=1:9
        switch pos
            case 1
                pos_let = 'a';
            case 2
                pos_let = 'b';
            case 3
                pos_let = 'c';
            case 4
                pos_let = 'd';
            case 5
                pos_let = 'e';
            case 6
                pos_let = 'f';
```

```
            case 7
                pos_let = 'g';
            case 8
                pos_let = 'h';
            case 9
                pos_let = 'i';
        end
%         cal_file = load(strcat(cal_path,'cal_',...
%             pos_let,setup,'1.txt'));
        cal_file = load(strcat(cal_path,'cal_',pos_let,...
            setup,'_avg.txt'));
        for j=1:num_of_cols
            if j == cal_curve_coords(time_curve(j),pos)
                cal_pos(pos) = j;
                cal_val(pos) = cal_file(time_curve(j),2);
            end
        end
    end
    for pos=1:9
        if cal_pos(pos) == 0
            for j=1:num_of_cols
                if j == cal_curve_coords(time_curve(j),pos) + 1
                    cal_pos(pos) = j;
                    cal_val(pos) = cal_file(time_curve(j),2);
                end
            end
        end
        if cal_pos(pos) == 0
            message_to_user =strcat('error in spectra.m line 236',...
                ': cal_pos still 0, so need to increase to j=',...
                '="..."+2, +3, etc.')
            message_to_user = strcat('using average time ind',...
                'ex and average calibration curve pos',...
                'ition to determine local cal',...
                'ibration value and position')
            cal_pos(pos) = round(mean(cal_curve_coords(:,pos)))
            cal_val(pos) = cal_file(round(mean(time_curve)),2)
        end
    end

    cal_val_ext_1 = interp1(cal_pos,cal_val,x_space,...
        'linear','extrap');
    cal_val_ext_1(1:cal_pos(1)) = cal_val(1);
    cal_val_ext_1(cal_pos(9):num_of_cols) = cal_val(9);
```

```
    cal_val_ext_2 = interp1(cal_pos,cal_val,x_space,...
        'spline','extrap');
    cal_val_ext_3 = interp1(cal_pos,cal_val,x_space,...
        'pchip','extrap');

    cal_val_ext = cal_val_ext_2;

%     hold on;
%     plot(cal_val_ext_1,'r')
%     plot(cal_val_ext_2,'g')
%     plot(cal_val_ext_3,'b')

%     A_to_E_eff_from_file = load(strcat(efficiency_path,...
%         'A_to_E_efficiency.txt'));
%     A_to_E_eff = interp1(A_to_E_eff_from_file(:,1),...
%         A_to_E_eff_from_file(:,2),wavelength_scale,...
%         'linear','extrap');

    A_thru_strk_in_opt_eff_from_file = ...
        load(strcat(efficiency_path,...
        'A_thru_streak_input_optics_efficiency.txt'));
    A_thru_strk_in_opt_eff = ...
        interp1(A_thru_strk_in_opt_eff_from_file(:,1),...
        A_thru_strk_in_opt_eff_from_file(:,2),wavelength_scale,...
        'linear','extrap');

    cat_sens_norm_from_file = load(strcat(efficiency_path,...
        'cathode_sensitivity_normalized_to_633nm.txt'));
    cat_sens_norm = interp1(cat_sens_norm_from_file(:,1),...
        cat_sens_norm_from_file(:,2),wavelength_scale,...
        'linear','extrap');

    quant_eff_norm_from_file = load(strcat(efficiency_path,...
        'quantum_efficiency_normalized_to_633nm.txt'));
    quant_eff_norm = interp1(quant_eff_norm_from_file(:,1),...
        quant_eff_norm_from_file(:,2),wavelength_scale,...
        'linear','extrap');

    if use_cat_sens_c_or_quant_eff_q == 'c'
        rel_sens = cat_sens_norm;
    end
    if use_cat_sens_c_or_quant_eff_q == 'q'
        rel_sens = quant_eff_norm;
    end
```

```
    %%%%%%%%%%%%%%%%%%%%%%%%%%
    cal_val_ext = mean(cal_val);
    %%%%%%%%%%%%%%%%%%%%%%%%%%

    cal_val_corrected_for_wavelength = cal_val_ext ./ rel_sens;

    photons_collected_per_pixel = data_strip .* ...
        cal_val_corrected_for_wavelength;

    photons_collected_per_pixel_per_second = ...
        photons_collected_per_pixel / (integration_time * 10^-9);

    photons_produced_at_source_per_wavelength_per_second(strip,:)=...
        photons_collected_per_pixel_per_second ./ ...
        A_thru_strk_in_opt_eff;

end
phot_sum = zeros(1,length(...
    photons_produced_at_source_per_wavelength_per_second(1,:)));
for strip=1:vert_pix_to_avg
    phot_sum = phot_sum + ...
        photons_produced_at_source_per_wavelength_per_second(...
        strip,:);
end
averaged_photons_produced_at_source_per_wavelength_per_second = ...
    phot_sum ./ vert_pix_to_avg;

avg_ph_prod_at_source_per_s_per_ster_per_cm2_per_nm = ...
    averaged_photons_produced_at_source_per_wavelength_per_second...
    ./(0.028 * 0.1087 * 4*pi);

dlmwrite(strcat(output_path,'shot_',int2str(shot_number),'_at_',...
    int2str(time),'_ns.txt'),[(wavelength_scale*...
    10)' avg_ph_prod_at_source_per_s_per_ster_per_cm2_per_nm'],...
    'delimiter','\t','precision',6)

clf;
fig1 = gcf;

awidth = 4.0;
aheight = 3.0;
xlim_vals = [4000 6500];
ylim_vals = [0 10e16];
```

```
if quick_mode == 'y'
    ylim_vals = [-1e16 8e16];
end

lmargin = .4;
rmargin = .3;
bmargin = .4;
tmargin = .3;
fleft = 1.0;
fbottom = 1.0;
fwidth = awidth+lmargin+rmargin;
fheight = aheight+tmargin+bmargin;
aleft = lmargin;
abottom = bmargin;

set(fig1, 'Units', 'inches');
set(fig1, 'Position', [fleft fbottom fwidth fheight]);

set(gcf, 'PaperPositionMode', 'manual');
set(gcf, 'PaperUnits', 'inches');
set(gcf, 'PaperSize', [fwidth fheight]);
set(gcf, 'PaperPosition', [fleft fbottom fwidth fheight]);

val_font_size = 8;
label_font_size = 10;
box on;
ax1 = gca;
set(ax1,'Units','inches');
set(ax1,'Position',[aleft abottom awidth aheight]);
set(ax1,'XColor','k','YColor','k','XLim',xlim_vals,'YLim',...
    ylim_vals,'XMinorTick','on','YMinorTick','on','FontSize',...
    val_font_size,'FontName','Helvetica','Parent',fig1);

line(wavelength_scale*10,...
    avg_ph_prod_at_source_per_s_per_ster_per_cm2_per_nm,...
    'Parent',ax1);

% xlabel('\textsf{Wavelength (\AA)}','interpreter','latex',...
%     'FontSize',label_font_size,'FontName','Helvetica');
% ylabel('\textsf{Intensity (photons/sec/sterad/cm$^2$/\AA)}',...
%     'interpreter','latex','FontSize',label_font_size,...
%     'FontName','Helvetica');
% title(['\textsf{Shot ',int2str(shot_number),' at ',...
%     int2str(time),' ns}'],'interpreter','latex',...
```

```
%     'FontSize',label_font_size,'FontName','Helvetica');
% print('-depsc2','-r600',strcat(output_path,'shot_',...
%     int2str(shot_number),'_at_',int2str(time),'_ns.eps'));

label_font_size = 6;
xlabel('\textsf{Wavelength (\AA)}','interpreter','latex',...
    'FontSize',label_font_size,'FontName','Helvetica');
ylabel('\textsf{Intensity (photons/sec/sterad/cm$^2$/\AA)}',...
    'interpreter','latex','FontSize',label_font_size,...
    'FontName','Helvetica');
title(['\textsf{Shot ',int2str(shot_number),' at ',...
    int2str(time),' ns}'],'interpreter','latex',...
    'FontSize',label_font_size,'FontName','Helvetica');
print('-dtiff','-r600',strcat(output_path,'shot_',...
    int2str(shot_number),'_at_',int2str(time),'_ns.tif'));

% clf;
% imagesc(I);colormap(gray);
% hold on;
% plot(time_curve_archive,'r')

I_write = uint16(round(I));
imwrite(I_write,strcat(output_path,int2str(shot_number),'_',...
    sweep,'-processed.tif'));

status = fclose('all')
end
```

C.2.9 spectral_cal.m

```
function spectral_cal(shot_number)
% This function contains the pixel positions for each of the helium
% lamp calibration lines recorded in focus/live mode prior to each
% experiment/shot. This function requires the shot number as an
% input argument. When this function is called, the pixel positions
% of the calibration lines are recorded in the output text file as
% specified below. The output text files for each shot are used by
% other functions to calibrate wavelength scales after correcting
% for streak tube aberrations.

s = num2str(shot_number);
```

```
clf;

path = 'C:\research\shot_processing\1217\continuum\spectral_cal\';

file = strcat(path,'he_cal_',s,'.tif');

I = double(imread(file));

for i=1:length(I(1,:))
    row(i) = mean(I(575:590,i));
end

option = 2
if option == 1
    plot(row);
else
    if option == 2
        imagesc(I); colormap(gray);
    end
end
hold on;

wavelength_cal{1217} = [
    131     667.815
    511     587.562
    902     501.567
    945     492.193
    1039    471.314
    1147    447.148
    ];

wavelength_cal{1218} = [
    130     667.815
    509     587.562
    900     501.567
    942     492.193
    1035    471.314
    1144    447.148
    ];

wavelength_cal{1219} = [
    230     587.562
    632     501.567
    675     492.193
```

```
    767     471.314
    879     447.148
    1141    388.865
    ];

wavelength_cal{1220} = [
    229     587.562
    632     501.567
    674     492.193
    768     471.314
    878     447.148
    1139    388.865
    ];

wavelength_cal{1221} = [
    231     587.562
    633     501.567
    675     492.193
    768     471.314
    879     447.148
    1140    388.865
    ];

wavelength_cal{1222} = [
    342     587.562
    738     501.567
    779     492.193
    877     471.314
    984     447.148
    1244    388.865
    ];

wavelength_cal{1223} = [
    340     587.562
    737     501.567
    780     492.193
    875     471.314
    982     447.148
    1243    388.865
    ];

wavelength_cal{1224} = [
    341     587.562
    738     501.567
```

```
    781     492.193
    875     471.314
    983     447.148
    1245    388.865
    ];

wavelength_cal{1225} = [
    340     587.562
    737     501.567
    779     492.193
    875     471.314
    982     447.148
    1243    388.865
    ];

wavelength_cal{1226} = [
    341     587.562
    738     501.567
    781     492.193
    876     471.314
    983     447.148
    1244    388.865
    ];

wavelength_cal{1227} = [
    339     587.562
    736     501.567
    778     492.193
    873     471.314
    982     447.148
    1243    388.865
    ];

wavelength_cal{1228} = [
    341     587.562
    737     501.567
    779     492.193
    876     471.314
    983     447.148
    1244    388.865
    ];

wavelength_cal{1229} = [
    341     587.562
```

```
    737     501.567
    778     492.193
    876     471.314
    983     447.148
    1244    388.865
    ];

if option == 1
    scatter(wavelength_cal{shot_number}(1,1),...
        row(wavelength_cal{shot_number}(1,1)),'filled')
    scatter(wavelength_cal{shot_number}(2,1),...
        row(wavelength_cal{shot_number}(2,1)),'filled')
    scatter(wavelength_cal{shot_number}(3,1),...
        row(wavelength_cal{shot_number}(3,1)),'filled')
    scatter(wavelength_cal{shot_number}(4,1),...
        row(wavelength_cal{shot_number}(4,1)),'filled')
    scatter(wavelength_cal{shot_number}(5,1),...
        row(wavelength_cal{shot_number}(5,1)),'filled')
    scatter(wavelength_cal{shot_number}(6,1),...
        row(wavelength_cal{shot_number}(6,1)),'filled')
else if option == 2
        scatter(wavelength_cal{shot_number}(1,1),582,'filled')
        scatter(wavelength_cal{shot_number}(2,1),582,'filled')
        scatter(wavelength_cal{shot_number}(3,1),582,'filled')
        scatter(wavelength_cal{shot_number}(4,1),582,'filled')
        scatter(wavelength_cal{shot_number}(5,1),582,'filled')
        scatter(wavelength_cal{shot_number}(6,1),582,'filled')
    end
end

for i=1217:1229
    dlmwrite(strcat(path,'wavelength_cal_',int2str(i),'.txt'),...
        wavelength_cal{i},'delimiter','\t','precision',6);
end

status = fclose('all')

end
```

C.2.10 drift_correction_AI.m

```
function drift_correction_AI
```

```
%This function finds the difference in the number of pixel columns
%between the location of the laser focal spot when in focus/live mode
%and when being streaked. This is a horizontal separation in the
%images (i.e., a separation in pixels in the spatial dimension, not
%in the time dimension). Thus this code corrects for the horizontal
%drift that occurs during the streak operation. The differences are
%found for six locations that are the approximate locations of the
%helium calibration lines that were taken in focus/live mode prior to
%each shot. The pixel rows in the vertical/time dimension where these
%horizontal differences were calculated are also recorded. Both the
%horizontal shifts and the pixel rows where the shifts were
%calculated for all six locations are saved in output text files as
%specified below. These output files are then used by other functions
%to properly determine wavelength scales.

option = 2

clf;

path ='C:\research\shot_processing\1217\continuum\drift_correction\';

file = strcat(path,'A',int2str(1),'.tif');

I = double(imread(file));
size_I = size(I);

for i=2:6
    file = strcat(path,'A',int2str(i),'.tif');
    I = I + double(imread(file));
end

for i=1:length(I(1,:))
    row(i) = mean(I(575:590,i));
end

% if option == 1
%     plot(row);
% else
%     if option == 2
%         imagesc(I); colormap(gray);
%     end
% end

A(1) = 135;
```

```
A(2) = 513;
A(3) = 903;
A(4) = 948;
A(5) = 1040;
A(6) = 1149;

for i=1:6
    [A_max(i),A_max_y(i)] = max(I(575:590,A(i)));
end

% I = zeros(size_I);
for i=1:6
    file = strcat(path,'AI',int2str(i),'.tif');
    I = I + double(imread(file));
end

for i=1:length(I(1,:))
    row(i) = mean(I(575:590,i));
end

if option == 1
    plot(row);
else
    if option == 2
        imagesc(I); colormap(gray);
    end
end

hold on;

AI(1) = 148;
AI(2) = 514;
AI(3) = 893;
AI(4) = 937;
AI(5) = 1028;
AI(6) = 1133;

marker_color = 'r';
for i=1:6
    if option == 1
        marker_size = 20;
        scatter(A(i),row(A(i)),'filled','SizeData',marker_size,...
            'MarkerFaceColor',marker_color,...
            'MarkerEdgeColor',marker_color)
```

```
        scatter(AI(i),row(AI(i)),'filled','SizeData',marker_size,...
            'MarkerFaceColor',marker_color,...
            'MarkerEdgeColor',marker_color)
    else if option == 2
            marker_size = 2;
            scatter(A(i),574+A_max_y(i),'filled',...
                'SizeData',marker_size,...
                'MarkerFaceColor',marker_color,...
                'MarkerEdgeColor',marker_color)
            scatter(AI(i),574+A_max_y(i),'filled',...
                'SizeData',marker_size,...
                'MarkerFaceColor',marker_color,...
                'MarkerEdgeColor',marker_color)
        end
    end
end
574+A_max_y
round(mean(574+A_max_y))
for i=1:6
    focus_pos_minus_streak_pos(i) = A(i)-AI(i);
end

dlmwrite(strcat(path,'focus_pos_minus_streak_pos_AI.txt'),...
    focus_pos_minus_streak_pos,'delimiter','\t','precision',6);
dlmwrite(strcat(path,'y_pos_AI.txt'),574+A_max_y,...
    'delimiter','\t','precision',6);

status = fclose('all')

end
```

C.2.11 vert_curves_AI.m

```
function vert_curves_AI
%This function reads in the image data from the streaks of the
%focused HeNe CW laser spot, where the spot was positioned in the
%approximate location of the helium calibration lines that were taken
%in focus/live mode prior to each experiment/shot. The function then
%finds the pixel coordinates of each of the six laser-spot streaks.
%These coordinates are then used by other functions such as spectra.m
%to account for the streak tube aberrations that lead to non-vertical
%streaked lines (i.e., to account for the curvature seen in the
```

```
%almost-vertical lines that result from streaking the stationary
%focused laser spot---the lines from these streaks should be
%perfectly vertical in theory).

clf;

path1=strcat('C:\research\shot_processing\1217\continuum\',...
    'streak_cam_calibration\');
path2='C:\research\shot_processing\1217\continuum\drift_correction\';

file = strcat(path1,'aI1.tif');
size_I = size(double(imread(file)));
I_sum = zeros(size_I);

y_pos_AI = load(strcat(path2,'y_pos_AI.txt'));

num_of_curves = 6;
for c1 = 1:num_of_curves

    c1

    file = strcat(path2,'AI',int2str(c1),'.tif');

    I = double(imread(file));

    I_smooth = I;
    for i = 1:size_I(1)
        for j = 3:size_I(2)-2
            I_smooth(i,j) = mean(I(i,j-2:j+2));
        end
        [max_vals(i),max_pos(i)] = max(I_smooth(i,:));
    end

    curve_coords(:,c1) = max_pos(:);

    curve_shifts(:,c1) = max_pos(:) - max_pos(y_pos_AI(c1));

    I_sum = I + I_sum;

end

imagesc(I_sum); colormap(gray);
hold on;
i_index = 1:size_I(1);
```

```
for c=1:num_of_curves
    plot(curve_coords(:,c),i_index,'r')
end

dlmwrite(strcat(path2,'vert_curve_shifts_AI.txt'),curve_shifts,...
    'delimiter','\t','precision',6);

status = fclose('all')

end
```

C.2.12 wavelength_shifter.m

```
function wavelength_shifter
%This function corrects the pixel locations of the six helium
%calibration lines taken in focus/live mode for the horizontal drift
%(i.e., drift in the spatial dimension not time dimension) that
%occurs during the streak operation. This function shifts the pixel
%locations that were originally assigned in spectral_cal.m by the
%pixel-column differences found/calculated in drift_correction_XX.m
%(where XX is A1, AIII, BIII, CII, or CIII). The corrected pixel
%locations of the six helium calibration lines are then saved to
%output text files as specified below. This function also creates the
%text file "shot_setup_info.txt". This text file contains information
%specifying the sweep speed, image intensifier gain, and spectrometer
%grating position used for each shot. This function also creates the
%text file "shot_setup_info_nums.txt" which is just a numerical
%version of "shot_setup_info.txt" (the numerical version is just
%easier to refer to in other functions such as spectra.m).

drift_path = strcat('C:\research\shot_processing\1217\',...
    'continuum\drift_correction\');
spectral_cal_path = strcat('C:\research\shot_processing\1217\',...
    'continuum\spectral_cal\');
shot_setup_info = fopen('shot_setup_info.txt','w');
shot_setup_info_nums = fopen('shot_setup_info_nums.txt','w');

for s=1217:1229
    if s == 1217
        dial = 'A';
        dial_num = 1;
        setup = 'I';
```

```
    setup_num = 1;
end
if s == 1218
    dial = 'A';
    dial_num = 1;
    setup = 'III';
    setup_num = 3;
end
if s >= 1219 && s <=1221
    dial = 'B';
    dial_num = 2;
    setup = 'III';
    setup_num = 3;
end
if s >= 1222 && s <= 1227 || s == 1229
    dial = 'C';
    dial_num = 3;
    setup = 'III';
    setup_num = 3;
end
if s == 1228
    dial = 'C';
    dial_num = 3;
    setup = 'II';
    setup_num = 2;
end

fprintf(shot_setup_info,strcat('s',int2str(s),',dial=',dial,...
    ',setup=',setup,'\n'));
fprintf(shot_setup_info_nums,strcat(int2str(s),'\t',...
    int2str(dial_num),'\t',int2str(setup_num),'\n'));

wavelength_cal = load(strcat(spectral_cal_path,...
    'wavelength_cal_',int2str(s),'.txt'));
focus_pos_minus_streak_pos = load(strcat(drift_path,...
    'focus_pos_minus_streak_pos_',dial,setup,'.txt'));

wavelength_cal_corrected = wavelength_cal;
for i=1:6
    wavelength_cal_corrected(i,1) = wavelength_cal(i,1) - ...
        focus_pos_minus_streak_pos(i);
end

dlmwrite(strcat(spectral_cal_path,'wavelength_cal_corrected_',...
```

```
        int2str(s),'.txt'),wavelength_cal_corrected,...
        'delimiter','\t','precision',6);

end

status = fclose('all')

end
```

C.2.13 time_curves_I.m

```
function time_curves_I
%This function reads in the image data from the streaks where the
%diagnostic laser was flashed/pulsed at one instant during the streak
%time window, and where the laser flash illuminated the entire streak
%entrance slit. Thus the 150-ps laser pulse-width shows up as an
%effectively instantaneous flash relative to the 200- or 500-ns
%streak windows. The flash produces an image of the streak input slit
%at one moment in time and should be perfectly horizontal. However
%the resulting lines in the streak images are slightly curved due to
%streak tube aberrations. This function thus uses this data to find
%the coordinates of these almost-horizontal lines. The coordinates
%are then saved in output text files as specified below. These output
%text files are then read by functions such as spectra.m to determine
%the constant-time coordinates for the time of interest.


clf;

path = strcat('C:\research\shot_processing\1217\continuum\',...
    'time_tilt_correction\');

file = strcat(path,'I1.tif');

size_I = size(double(imread(file)));
I_sum = zeros(size_I);

num_of_curves = 21;

for c = 1:num_of_curves

    c
```

```
    file = strcat(path,'I',int2str(c),'.tif');

    I = double(imread(file));

    I_smooth = I;
    for j = 1:size_I(2)
        for i = 3:size_I(1)-2
            I_smooth(i,j) = mean(I(i-2:i+2,j));
        end
        [max_vals(j),max_pos(j)] = max(I_smooth(:,j));
    end

    curve_coords(c,:) = max_pos(:);

    I_sum = I + I_sum;

end

imagesc(I_sum); colormap(gray);
hold on;
for c=1:num_of_curves
    plot(curve_coords(c,:),'r')
end

dlmwrite(strcat(path,'curve_coords_I.txt'),curve_coords,...
    'delimiter','\t','precision',6);

status = fclose('all')

end
```

C.2.14 scan_spectra.m

```
scan_spectra
%This function repeatedly calls spectra.m for each shot in the data
%set, stepping through the time window of a given shot's streak
%image in increments equal to the given shot's time resolution. The
%data is saved in output files and plots as specified in spectra.m.

for shot_number = 1217:1229
    if shot_number ~= 1222 && shot_number ~= 1226
```

```
shot_setup_info = load(strcat(root,...
    'streak_image_processing\shot_setup_info_nums.txt'));
for s=1:1229-1217+1
    if shot_setup_info(s,1) == shot_number
        dial_num = shot_setup_info(s,2);
        setup_num = shot_setup_info(s,3);
    end
end
switch dial_num
    case 1
        dial = 'A';
    case 2
        dial = 'B';
    case 3
        dial = 'c';
end
switch setup_num
    case 1
        setup = 'I';
        sweep = '200ns';
    case 2
        setup = 'II';
        sweep = '200ns';
    case 3
        setup = 'III';
        sweep = '500ns';
end
if sweep == '200ns'
    time_step = 2;
end
if sweep == '500ns'
    time_step = 5;
end
switch shot_number
    case 1217
        ti = 0;
        tf = 120;
    case 1218
        ti = 0;
        tf = 300;
    case 1219
        ti = 0;
        tf = 300;
    case 1220
```

```
                ti = 0;
                tf = 300;
            case 1221
                ti = 0;
                tf = 300;
            case 1223
                ti = 0;
                tf = 300;
            case 1224
                ti = 0;
                tf = 300;
            case 1225
                ti = 0;
                tf = 300;
            case 1227
                ti = 0;
                tf = 300;
            case 1228
                ti = 0;
                tf = 130;
            case 1229
                ti = 0;
                tf = 300;
        end
        for time = ti:time_step:tf
            spectra(shot_number,time)
        end
    end
end
end
```

C.2.15 spectra_movie.m

```
function spectra_movie(shot_number,inter_frame_pause)
%This function can be run after scan_spectra.m has been run. This
%function requires the shot number and inter-frame pause time as
%input arguments. This function loads the data for the desired shot
%(i.e., the data that was produced by scan_spectra.m calling
%spectra.m repeatedly), and for each time point, plots the spectrum
%as well as the load current data for the shot. This plot is then
%captured as a frame in a movie. All of the frames are assembled into
%a movie in *.avi format, as specified below. The codec compression
```

```
%can be changed as needed.


if shot_number == 1222
    message_to_user = strcat('Streak camera slit left open on th',...
        'is shot, thus data is unusable')
    error(strcat('Streak camera slit left open on this shot',...
        ', thus data is unusable'))
end
if shot_number == 1226
    message_to_user = strcat('No laser/streak timing fid',...
        'ucial on this shot, thus poor timing info')
    error(strcat('No laser/streak timing fiducial on this shot',...
        ', thus poor timing info'))
end

shot_setup_info = load(strcat(root,...
    'streak_image_processing\shot_setup_info_nums.txt'));
for s=1:1229-1217+1
    if shot_setup_info(s,1) == shot_number
        dial_num = shot_setup_info(s,2);
        setup_num = shot_setup_info(s,3);
    end
end
switch dial_num
    case 1
        dial = 'A';
    case 2
        dial = 'B';
    case 3
        dial = 'c';
end
switch setup_num
    case 1
        setup = 'I';
        sweep = '200ns';
    case 2
        setup = 'II';
        sweep = '200ns';
    case 3
        setup = 'III';
        sweep = '500ns';
end
```

```
if sweep == '200ns'
    time_step = 2;
end
if sweep == '500ns'
    time_step = 5;
end

switch shot_number
    case 1217
        ti = 0;
        tf = 120;
    case 1218
        ti = 0;
        tf = 300;
    case 1219
        ti = 0;
        tf = 300;
    case 1220
        ti = 0;
        tf = 300;
    case 1221
        ti = 0;
        tf = 300;
    case 1223
        ti = 0;
        tf = 300;
    case 1224
        ti = 0;
        tf = 300;
    case 1225
        ti = 0;
        tf = 300;
    case 1227
        ti = 0;
        tf = 300;
    case 1228
        ti = 0;
        tf = 130;
    case 1229
        ti = 0;
        tf = 300;
end
frame = 1;
for t=ti:time_step:tf
```

```
data_path = ...
    'C:\research\shot_processing\1217\output_spectra_files\';
data = load(strcat(data_path,'shot_',int2str(shot_number),...
    '_at_',int2str(t),'_ns.txt'));

load_current_path = ...
    'C:\research\shot_processing\1217\signal_plots\';
load_current_file = strcat(load_current_path,...
    int2str(shot_number),'-load_current.txt');
load_current = load(load_current_file);
I_t = -1 * interp1(load_current(:,1),load_current(:,2),t);

clf;
fig1 = gcf;

awidth = 5.0;
aheight = 2.0;
xlim_vals = [4500 6500];
ylim_vals = [0 1e17];

a2width = 5.0;
a2height = 2.0;
x2lim_vals = [ti tf];
y2lim_vals = [0 1.2];

lmargin = .45;
rmargin = .3;
bmargin = .45;
tmargin = .3;
fleft = 0.2;
fbottom = 0.4;
fwidth = awidth+lmargin+rmargin;
fheight = aheight+tmargin*2+bmargin*2+a2height;
aleft = lmargin;
abottom = bmargin*2.5 + a2height;
a2left = lmargin;
a2bottom = bmargin;

set(fig1, 'Units', 'inches');
set(fig1, 'Position', [fleft fbottom fwidth fheight]);

set(fig1, 'PaperPositionMode', 'manual');
set(fig1, 'PaperUnits', 'inches');
set(fig1, 'PaperSize', [fwidth fheight]);
```

```
    set(fig1, 'PaperPosition', [fleft fbottom fwidth fheight]);

    val_font_size = 8;
    label_font_size = 10;
    box on;
    ax1 = gca;
    set(ax1,'Units','inches');
    set(ax1,'Position',[aleft abottom awidth aheight]);
    set(ax1,'XColor','k','YColor','k','XLim',xlim_vals,...
        'YLim',ylim_vals,'XMinorTick','on','YMinorTick','on',...
        'FontSize', val_font_size,...
        'FontName','Helvetica','Parent',fig1);

    line(data(:,1),data(:,2),'Parent',ax1);
    xlabel('\textsf{Wavelength (\AA)}','interpreter','latex',...
        'FontSize',label_font_size,...
        'FontName','Helvetica','Parent',ax1);
    ylabel('\textsf{Intensity (photons/sec/sterad/cm$^2$/\AA)}',...
        'interpreter','latex','FontSize',label_font_size,...
        'FontName','Helvetica','Parent',ax1);
    title(['\textsf{Shot ',int2str(shot_number),' at  ',...
        num2str(t,'%-3.0f'),' ns and ',...
        num2str(I_t,'%3.2f'),' MA}'],'interpreter','latex',...
        'FontSize',label_font_size,'FontName','Helvetica');

    ax2 = axes;
    set(ax2,'Units','inches');
    set(ax2,'Position',[a2left a2bottom a2width a2height]);

    set(fig1,'CurrentAxes',ax2);
    scatter(t,I_t,'Parent',ax2,'r','s','f')
    line(load_current(:,1),-1*load_current(:,2),'Parent',ax2,...
        'Color','k');
    xlabel('\textsf{Time (ns)}','interpreter','latex',...
        'FontSize',label_font_size,...
        'FontName','Helvetica','Parent',ax2);
    ylabel('\textsf{Load Current (MA)}','interpreter','latex',...
        'FontSize',label_font_size,...
        'FontName','Helvetica','Parent',ax2);
%     title(['\textsf{Load Current}'],'interpreter','latex',...
%         'FontSize',label_font_size,'FontName','Helvetica');
    set(ax2,'XColor','k','YColor','k','XLim',x2lim_vals,...
        'YLim',y2lim_vals,'XMinorTick','on','YMinorTick','on',...
        'FontSize', val_font_size,'FontName','Helvetica',...
```

```
        'Parent',fig1,'YTick',[0.0,0.2,0.4,0.6,0.8,1.0,1.2]);
    box on;

%     xlabel('\textsf{Wavelength (\AA)}','interpreter','latex',...
%         'FontSize',label_font_size,'FontName','Helvetica');
%     ylabel('\textsf{Intensity (photons/sec/sterad/cm$^2$/\AA)}',...
%         'interpreter','latex','FontSize',label_font_size,...
%         'FontName','Helvetica');
%     title(['\textsf{Shot ',int2str(shot_number),' at ',...
%         int2str(time),' ns}'],'interpreter','latex',...
%         'FontSize',label_font_size,'FontName','Helvetica');
%     print('-depsc2','-r600',strcat(output_path,'shot_',...
%         int2str(shot_number),'_at_',int2str(time),'_ns.eps'));

%     pause(inter_frame_pause);

    F(frame) = getframe(fig1);
    frame = frame + 1;
end

movie(F,0,1/inter_frame_pause);

movie_path = ...
    'C:\research\shot_processing\1217\output_spectra_movies\';
movie_file = strcat(movie_path,'shot_',int2str(shot_number),'.avi');

movie2avi(F,movie_file,'fps',1/inter_frame_pause,...
    'compression','Cinepak');

end
```

BIBLIOGRAPHY

[1] C. Deeney, M. R. Douglas, R. B. Spielman, T. J. Nash, D. L. Peterson, P. L'Eplattenier, G. A. Chandler, J. F. Seamen, and K. W. Struve. Enhancement of x-ray power from a z pinch using nested-wire arrays. *Phys. Rev. Lett.*, 81:4883, 1998.

[2] R. B. Spielman, C. Deeney, G. A. Chandler, M. R. Douglas, D. L. Fehl, M. K. Matzen, D. H. McDaniel, T. J. Nash, J. L. Porter, T. W. L. Sanford, J. F. Seamen, W. A. Stygar, K. W. Struve, S. P. Breeze, J. S. McGurn, J. A. Torres, D. M. Zagar, T. L. Gilliland, D. O. Jobe, J. L. McKenney, R. C. Mock, M. Vargas, T. Wagoner, and D. L. Peterson. Tungsten wire-array z-pinch experiments at 200 TW and 2 MJ. *Phys. Plasmas*, 5:2105, 1998.

[3] M. E. Cuneo, E. M. Waisman, S. V. Lebedev, J. P. Chittenden, W. A. Stygar, G. A. Chandler, R. A. Vesey, E. P. Yu, T. J. Nash, D. E. Bliss, G. S. Sarkisov, T. C. Wagoner, G. R. Bennett, D. B. Sinars, J. L. Porter, W. W. Simpson, L. E. Ruggles, D. F. Wenger, C. J. Garasi, B. V. Oliver, R A. Aragon, W. E. Fowler, M. C. Hettrick, G. C. Idzorek, D. Johnson, K. Keller, S. E. Lazier, J. S. McGurn, T. A. Mehlhorn, T. Moore, D. S. Nielsen, J. Pyle, S. Speas, K. W. Struve, and J. A. Torres. Characteristics and scaling of tungsten-wire-array z-pinch implosion dynamics at 20 MA. *Phys. Rev. E*, 71:046406, 2005.

[4] M. E. Cuneo, R. A. Vesey, J. L. Porter, Jr., G. A. Chandler, D. L. Fehl, T. L. Gilliland, D. L. Hanson, J. S. McGurn, P. G. Reynolds, L. E. Ruggles, H. Seamen, R. B. Spielman, K. W. Struve, W. A. Stygar, W. W. Simpson, J. A. Torres, , D. F. Wenger, J. H. Hammer, P. W. Rambo, Darrell L. Peterson, and George C. Idzorek. Development and characterization of a z-pinch-driven hohlraum high-yield inertial confinement fusion target concept. *Phys. Plasmas*, 8:2257, 2001.

[5] J. H. Hammer, M. Tabak, S. C. Wilks, J. D. Lindl, D. S. Bailey, P. W. Rambo, A. Toor, G. B. Zimmerman, and J. L. Porter, Jr. High yield inertial confinement fusion target design for a z-pinch-driven hohlraum. *Phys. Plasmas*, 6:2129, 1999.

[6] R. A. Vesey, M. E. Cuneo, G. R. Bennett, J. L. Porter, Jr., R.G. Adams, R. A. Aragon, P. K. Rambo, L. E. Ruggles, W.W. Simpson, and I.C. Smith. Demonstration of radiation symmetry control for inertial confinement fusion in double z-pinch hohlraums. *Phys. Rev. Lett.*, 90:035005, 2003.

[7] T. J. Nash, M. S. Derzon, G. A. Chandler, R. Leeper, D. Fehl, J. Lash, C. Ruiz, G. Cooper, J. F. Seaman, J. McGurn, S. Lazier, J. Torres, D. Jobe, T. Gilliland,

M. Hurst, R. Mock, P. Ryan, D. Nielsen, J. Armijo, J. McKenney, R. Hawn, D. Hebron, J. J. MacFarlane, D. Petersen, R. Bowers, W. Matuska, and D. D. Ryutov. High-temperature dynamic hohlraums on the pulsed power driver Z. *Phys. Plasmas*, 6:2023, 1999.

[8] S. A. Slutz, M. R. Douglas, J. S. Lash, R. A. Vesey, G. A. Chandler, T. J. Nash, and M. S. Derzon. Scaling and optimization of the radiation temperature in dynamic hohlraums. *Phys. Plasmas*, 8:1673, 2001.

[9] J. E. Bailey, G. A. Chandler, S. A. Slutz, G. R. Bennett, G. Cooper, J. S. Lash, S. Lazier, R. Lemke, T. J. Nash, D. S. Nielsen, T. C. Moore, C. L. Ruiz, D. G. Schroen, R. Smelser, J. Torres, and R. A. Vesey. X-ray imaging measurements of capsule implosions driven by a z-pinch dynamic hohlraum. *Phys. Rev. Lett.*, 89:095004, 2002.

[10] M. K. Matzen, M. A. Sweeney, R. G. Adams, J. R. Asay, J. E. Bailey, G. R. Bennett, D. E. Bliss, D. D. Bloomquist, T. A. Brunner, R. B. Campbell, G. A. Chandler, C. A. Coverdale, M. E. Cuneo, J.-P. Davis, C. Deeney, M. P. Desjarlais, G. L. Donovan, C. J. Garasi, T. A. Haill, C. A. Hall, D. L. Hanson, M. J. Hurst, B. Jones, M. D. Knudson, R. J. Leeper, R. W. Lemke, M. G. Mazarakis, D. H. McDaniel, T. A. Mehlhorn, T. J. Nash, C. L. Olson, J. L. Porter, P. K. Rambo, S. E. Rosenthal, G. A. Rochau, L. E. Ruggles, C. L. Ruiz, T. W. L. Sanford, J. F. Seamen, D. B. Sinars, S. A. Slutz, I. C. Smith, K. W. Struve, W. A. Stygar, R. A. Vesey, E. A. Weinbrecht, D. F. Wenger, and E. P. Yu. Pulsed-power-driven high energy density physics and inertial confinement fusion research. *Phys. Plasmas*, 12:055503, 2005.

[11] M. K. Matzen. Z pinches as intense x-ray sources for high-energy density physics applications. *Phys. Plasmas*, 4:1519, 1997.

[12] D. D. Ryutov, M. S. Derzon, and M. K. Matzen. The physics of fast z pinches. *Rev. Mod. Phys.*, 72:167, 2000.

[13] R. F. Heeter, J. E. Bailey, M. E. Cuneo, J. Emig, M. E. Foord, P. T. Springer, and R. S. Thoe. Plasma diagnostics for x-ray driven foils at Z. *Rev. Sci. Instrum.*, 72:1224, 2001.

[14] S. V. Lebedev, J. P. Chittenden, F. N. Beg, S. N. Bland, A. Ciardi, D. Ampleford, S. Hughes, M. G. Haines, A. Frank, E. G. Blackman, and T. Gardiner. Laboratory astrophysics and collimated stellar outflows: The production of radiatively cooled hypersonic plasma jets. *Astrophys. J.*, 564:113, 2002.

[15] D. J. Ampleford, A. Ciardi, S. V. Lebedev, S. N. Bland, S. C. Bott, J. P. Chit-

tenden, G. N. Hall, A. Frank, and E. Blackman. Jet deflection by a quasi-steady-state side wind in the laboratory. *Astrophys. Space Sci.*, 307:29, 2007.

[16] J. E. Bailey, G. A. Chandler, D. Cohen, M. E. Cuneo, M. E. Foord, R. F. Heeter, D. Jobe, P. W. Lake, J. J. MacFarlane, T. J. Nash, D. S. Nielson, R. Smelser, , and J. Torres. Radiation science using z-pinch x rays. *Phys. Plasmas*, 9:2186, 2002.

[17] S. Ramo, J. R. Whinnery, and T. Van Duzer. *Fields and Waves in Communication Electronics*. John Wiley & Sons, Inc., 3rd edition, 1994.

[18] J. D. Douglass. *An Experimental Study of Tungsten Wire-Array Z-Pinch Plasmas using Time-Gated Point-Projection X-Ray Imaging*. PhD thesis, Cornell University, 2008.

[19] D. Mosher, S. J. Stephanakis, I. M. Vitkovitsky, C. M. Dozier, L. S. Levine, and D. J. Nagel. X radiation from high-energy-density exploded-wire discharges. *Appl. Phys. Lett.*, 23(8):429–430, 1973.

[20] M. Friedman and I. M. Vitkovitsky. Implosion of an unneutralized drifting relativistic electron beam. *Appl. Phys. Lett.*, 25(5):259–260, 1974.

[21] C. Stallings, K. Nielsen, and R. Schneider. Multi-wire array load for high-power pulsed generators. *Appl. Phys. Lett.*, 29:404, 1976.

[22] M. Gersten, J. E. Rauch, W. Clark, R. D. Richardson, and G. M Wilkinson. Plasma temperature measurements from highly ionized titanium imploding wire plasmas. *Appl. Phys. Lett.*, 39(2):148–149, 1981.

[23] R. F. Benjamin, J. S. Pearlman, E. Y. Chu, and J. C. Riordan. Measurements of the dynamics of imploding wire arrays. *Appl. Phys. Lett.*, 39(10):848–850, 1981.

[24] W. Clark, M. Gersten, J. Katzenstein, J. Rauch, R. Richardson, and M. Wilkinson. Aluminum, calcium, and titanium imploding plasma experiments on the BLACKJACK 5 pulse generator. *J. Appl. Phys.*, 53(6):4099–4104, 1982.

[25] N. R. Pereira and J. Davis. X rays from z-pinches on relativistic electron-beam generators. *J. Appl. Phys.*, 64:R1, 1988.

[26] F. S. Felber and N. Rostoker. Kink and displacement instabilities in imploding wire arrays. *Phys. Fluids*, 24:1029, 1981.

[27] T. W. L. Sanford, G. O. Allshouse, B. M. Marder, T. J. Nash, R. C. Mock, R. B. Spielman, J. F. Seamen, J. S. McGurn, D. Jobe, T. L. Gilliland, M. Vargas, K. W. Struve, W. A. Stygar, M. R. Douglas, and M. K. Matzen. Improved symmetry greatly increases x-ray power from wire-array z-pinches. *Phys. Rev. Lett.*, 77:5063, 1996.

[28] J. Porter. The ICF and high-energy-density science programs on the refurbished Z facility. In *Proceedings of the 7th International Conference on Dense Z-Pinches, 17–21 August 2008, Alexandria, VA*, Melville, New York, 2008. American Institute of Physics.

[29] M. E. Savage, K. R. LeChien, R. W. Lemke, K. W. Struve, and W. A. Stygar. Commissioning of the ZR driver: status and goals. In *Proceedings of the 7th International Conference on Dense Z-Pinches, 17–21 August 2008, Alexandria, VA*, Melville, New York, 2008. American Institute of Physics.

[30] C. L. Ruiz, G. W. Cooper, S. A. Slutz, J. E. Bailey, G. A. Chandler, T. J. Nash, T. A. Mehlhorn, R. J. Leeper, D. Fehl, A. J. Nelson, J. Franklin, and L. Ziegler. Production of thermonuclear neutrons from deuterium-filled capsule implosions driven by z-pinch dynamic hohlraums. *Phys. Rev. Lett.*, 93(1):015001, 2004.

[31] G. A. Rochau, J. E. Bailey, G. A. Chandler, G. Cooper, G. S. Dunham, P. W. Lake, R. J. Leeper, R. W. Lemke, T. A. Mehlhorn, A. Nikroo, K. J. Peterson, C. L. Ruiz, D. G. Schroen, S. A. Slutz, D. Steinman, W. A. Stygar, and W. Varnum. High performance capsule implosions driven by the z-pinch dynamic hohlraum. *Plasma Phys. Control. Fusion*, 49:B591B600, 2007.

[32] J. P. Chittenden, S. V. Lebedev, B. V. Oliver, E. P. Yu, and M. E. Cuneo. Equilibrium flow structures and scaling of implosion trajectories in wire array z pinches. *Phys. Plasmas*, 11:1118, 2004.

[33] S. N. Bland, S. V. Lebedev, J. P. Chittenden, G. N. Hall, F. Suzuki-Vidal, D. J. Ampleford, S. C. Bott, J. B. A. Palmer, S. A. Pikuz, and T. A. Shelkovenko. Implosion and stagnation of wire array z pinches. *Phys. Plasmas*, 14:056315, 2007.

[34] J. D. Douglass and D. A. Hammer. COBRA-STAR, a five frame point-projection x-ray imaging system for 1 MA scale wire-array z pinches. *Rev. Sci. Instrum.*, 79:033503, 2008.

[35] S. A. Pikuz, T. A. Shelkovenko, M. D. Mitchell, K. M. Chandler, J. D. Douglass, R. D. McBride, D. P. Jackson, and D. A. Hammer. Extreme luminosity imaging conical spectrograph. *Rev. Sci. Instrum.*, 77:10F309, 2006.

[36] D. B. Sinars, G. R. Bennett, D. F. Wenger, M. E. Cuneo, D. L. Hanson, J. L. Porter, R. G. Adams, P. K. Rambo, D. C. Rovang, and I. C. Smith. Monochromatic x-ray imaging experiments on the Sandia National Laboratories Z facility (invited). *Rev. Sci. Instrum.*, 75:3672, 2004.

[37] C. A. Coverdale, C. Deeney, M. R. Douglas, J. P. Apruzese, K. G. Whitney, J.W. Thornhill, and J. Davis. Optimal wire-number range for high x-ray power in long-implosion-time aluminum z pinches. *Phys. Rev. Lett.*, 88:065001, 2002.

[38] V. V. Alexandrov, E. V. Grabovsky, G. G. Zukakishvili, M. V. Zurin, N. N. Komarov, I. V. Krasovsky, K. N. Mitrofanov, S. L. Nedoseev, G. M. Oleinik, I. Yu. Porofeev, A. A. Samokhin, P. V. Sasorov, V. P. Smirnov, M. V. Fedulov, I. N. Frolov, and A. A. Chernov. Current-induced implosion of a multiwire array as a radial plasma rainstorm. *JETP*, 97:745, 2003.

[39] E. V. Grabovsky, K. N. Mitrofanov, S. L. Nedoseev, G. M. Oleinik, I. Yu. Porofeev, A. A. Samokhin, and I. N. Frolov. Heterogeneous plasma-producing structures at current implosion of a wire array. *Contrib. Plasma Phys.*, 45:553, 2005.

[40] S. V. Lebedev, D. J. Ampleford, S. N. Bland, S. C. Bott, J. P. Chittenden, J. Goyer, C. Jennings, M. G. Haines, G. N. Hall, D. A. Hammer, J. B. A. Palmer, S. A. Pikuz, T. A. Shelkovenko, and T. Christoudias. Physics of wire array z-pinch implosions: experiments at imperial college. *Plasma Phys. Control. Fusion*, 47:A91, 2005.

[41] V. V. Ivanov, V. L. Kantsyrev, V. I. Sotnikov, D. A. Fedin, A. L. Astanovitskiy, B. Le Galloudec, V. Nalajala, I. Shrestha, T. E. Cowan, B. Jones, C. A. Coverdale, C. Deeney, and P. D. LePell. Investigation of regimes of wire array implosion on the 1 MA Zebra accelerator. *Phys. Plasmas*, 13:012704, 2006.

[42] V. L. Kantsyrev, L. I. Rudakov, A. S. Safronova, A. L. Velikovich, V. V. Ivanov, C. A. Coverdale, B. Jones, P. D. LePell, D. J. Ampleford, C. Deeney, A. S. Chuvatin, K. Williamson, I. Shrestha, N. Ouart, M. F. Yilmaz, G. Osborne, A. Haboub, S. Batie, A. Astanovitsky, B. LeGalloudec, V. Nalajala, W. McDaniel, V. Shlyaptseva, T. Adkins, and C. Meyer. Properties of a pla-

nar wire arrays z-pinch source and comparisons with cylindrical arrays. *High Energy Density Phys.*, 3:136, 2007.

[43] T. A. Shelkovenko, D. A. Chalenski, K. M. Chandler, J. D. Douglass, J. B. Greenly, D. A. Hammer, B. R. Kusse, R. D. McBride, and S. A. Pikuz. Diagnostics on the COBRA pulsed power generator. *Rev. Sci. Instrum.*, 77:10F521, 2006.

[44] S. A. Pikuz, J. D. Douglass, T. A. Shelkovenko, D. B. Sinars, and D. A. Hammer. Wide band focusing x-ray spectrograph with spatial resolution. *Rev. Sci. Instrum.*, 79:013106, 2008.

[45] J. D. Douglass, S. A. Pikuz, T. A. Shelkovenko, D. A. Hammer, S. N. Bland, S. C. Bott, and R. D. McBride. Structure of the dense cores and ablation plasmas in the initiation phase of tungsten wire-array z pinches. *Phys. Plasmas*, 14:012704, 2007.

[46] S. V. Lebedev, F. N. Beg, S. N. Bland, J. P. Chittenden, A. E. Dangor, M. G. Haines, K. H. Kwek, S. A. Pikuz, and T. A. Shelkovenko. Effect of discrete wires on the implosion dynamics of wire array z pinches. *Phys. Plasmas*, 8:3734, 2001.

[47] D. B. Sinars, M. E. Cuneo, E. P. Yu, D. E. Bliss, T. J. Nash, J. L. Porter, C. Deeney, M. G. Mazarakis, G. S. Sarkisov, and D. F. Wenger. Mass-profile and instability-growth measurements for 300-wire z-pinch implosions driven by 14–18 MA. *Phys. Rev. Lett.*, 93:145002, 2004.

[48] J. B. Greenly, J. D. Douglas, D. A. Hammer, B. R. Kusse, S. C. Glidden, and H. D. Sanders. A 1 MA, variable risetime pulse generator for high energy density plasma research. *Rev. Sci. Instrum.*, 79(7):073501, 2008.

[49] J. D. Douglass, J. B. Greenly, D. A. Hammer, B. R. Kusse, J. T. Blanchard, L. M. Maxson, R. D. McBride, and H. Wilhelm. Capabilities of the reconfigured COBRA accelerator. In *Proceedings of the 15th IEEE International Pulsed Power Conference, 13–17 June 2005, Monterey, CA*, page 273, New York, 2005. IEEE.

[50] I. H. Hutchinson. *Principles of Plasma Diagnostics*. Cambridge University Press, 2nd edition, 2002.

[51] S. N. Bland, D. J. Ampleford, S. C. Bott, S. V. Lebedev, J. B. A. Palmer, S. A. Pikuz, and T. A. Shelkovenko. Extreme ultraviolet imaging of wire array z-pinch experiments. *Rev. Sci. Instrum.*, 75:3941, 2004.

[52] W. H. Bennett. Magnetically self-focussing streams. *Phys. Rev.*, 45(12):890–897, Jun 1934.

[53] R. S. Pease. Equilibrium characteristics of a pinched gas discharge cooled by bremsstrahlung radiation. *Proc. Phys. Soc. London Sect. B*, 70:11, 1957.

[54] S. I. Braginskiĭ. The behavior of a completely ionized plasma in a strong magnetic field. *Sov. Phys. JETP*, 6:494, 1958.

[55] J. D. Jackson. *Classical Electrodynamics*. John Wiley & Sons, Inc., 3rd edition, 1999.

[56] D. R. Nicholson. *Introduction to Plasma Theory*. John Wiley & Sons, Inc., 1983.

[57] F. F. Chen. *Introduction to Plasma Physics and Controlled Fusion*. Plenum Press, 2nd edition, 1984.

[58] N. R. Pereira. A simple derivation of the Pease-Braginskiĭ current. *Phys. Fluids B*, 2(3):677, 1990.

[59] J. Shiloh, A. Fisher, and N. Rostoker. Z pinch of a gas jet. *Phys. Rev. Lett.*, 40:515, 1978.

[60] P. J. Turchi and W. L. Baker. Generation of high-energy plasmas by electromagnetic implosion. *J. Appl. Phys.*, 44:4936, 1973.

[61] W. L. Baker, M. C. Clark, J. H. Degnan, G. F. Kiuttu, C. R. McClenahan, and R. E. Reinovsky. Electromagnetic-implosion generation of pulsed high-energy-density plasma. *J. Appl. Phys.*, 49:4694, 1978.

[62] D. B. Sinars, Min Hu, K. M. Chandler, T. A. Shelkovenko, S. A. Pikuz, J. B. Greenly, D. A. Hammer, and B. R. Kusse. Experiments measuring the initial energy deposition, expansion rates and morphology of exploding wires with about 1 kA/wire. *Phys. Plasmas*, 8:216, 2001.

[63] T. A. Shelkovenko, S. A. Pikuz, J. D. Douglass, I. C. Blesener, J. B. Greenly, R. D. McBride, D. A. Hammer, and B. R. Kusse. Wire core and coronal plasma expansion in wire-array z pinches with small numbers of wires. *Phys. Plasmas*, 14:102702, 2007.

[64] S. C. Bott, S. V. Lebedev, D. J. Ampleford, S. N. Bland, J. P. Chittenden, A. Ciardi, M. G. Haines, C. Jennings, M. Sherlock, G. Hall, J. Rapley, F. N. Beg, and J. Palmer. Dynamics of cylindrically converging precursor plasma flow in wire-array z-pinch experiments. *Phys. Rev. E*, 74:046403, 2006.

[65] J. B. Greenly, M. R. Martin, I. Blesener, D. Chalenski, P. Knapp, and R. McBride. The role of current advection in the development of the ablation streams and precursors of wire array z-pinches. In *Proceedings of the 7th International Conference on Dense Z-Pinches, 17–21 August 2008, Alexandria, VA*, Melville, New York, 2008. American Institute of Physics.

[66] D. B. Sinars. private communication, 2007.

[67] C. Deeney, T. J. Nash, R. B. Spielman, J. F. Seaman, G. C. Chandler, K. W. Struve, J. L. Porter, W. A. Stygar, J. S. McGurn, D. O. Jobe, T. L. Gilliland, J. A. Torres, M. F. Vargas, L. E. Ruggles, S. Breeze, R. C. Mock, M. R. Douglas, D. L. Fehl, D. H. McDaniel, M. K. Matzen, D. L. Peterson, W. Matuska, N. F. Roderick, and J. J. MacFarlane. Power enhancement by increasing the initial array radius and wire number of tungsten z pinches. *Phys. Rev. E*, 56:5945, 1997.

[68] D. B. Sinars, R.W. Lemke, M. E. Cuneo, S.V. Lebedev, E. M. Waisman, W. A. Stygar, B. Jones, M. C. Jones, E. P. Yu, J. L. Porter, and D. F. Wenger. Radiation energetics of ICF-relevant wire-array z pinches. *Phys. Rev. Lett.*, 100:145002, 2008.

[69] V. L. Kantsyrev. private communication, 2007.

[70] B. Jones, C. Deeney, C. A. Coverdale, P. D. LePell, J. L. McKenney, J. P. Apruzese, J. W. Thornhill, K. G. Whitney, R. W. Clark, A. L. Velikovich, J. Davis, Y. Maron, V. Kantsyrev, A. Safronova, and V. I. Oreshkin. K-shell radiation physics in low- to moderate-atomic-number z-pinch plasmas on the Z accelerator. *J. Quant. Spectrosc. Radiat. Transfer*, 99:341, 2006.

[71] F. N. Beg, S. V. Lebedev, S. N. Bland, J. Chittenden, A. E. Dangor, and M. G. Haines. The dynamics of single and nested nickel wire array z pinch implosions. *IEEE Trans. Plasma Sci.*, 30:552, 2002.

[72] M. Haines. Viscous heating at stagnation in z pinches. In *Proceedings of the 7th International Conference on Dense Z-Pinches, 17–21 August 2008, Alexandria, VA*, Melville, New York, 2008. American Institute of Physics.

[73] D. B. Sinars, M. E. Cuneo, E. P. Yu, S. V. Lebedev, K. R. Cochrane, B. Jones, J. J. MacFarlane, T. A. Mehlhorn, J. L. Porter, and D. F. Wenger. Measurements and simulations of the ablation stage of wire arrays with different initial wire sizes. *Phys. Plasmas*, 13:042704, 2006.

[74] A. S. Safronova, V. L. Kantsyrev, A. A. Esaulov, N. D. Ouart, M. F. Yilmaz, K. M. Williamson, I. Shrestha, G. C. Osborne, J. B. Greenly, K. M. Chandler, R. D. McBride, D. A. Chalenski, D. A. Hammer, B. R. Kusse, and P. D. LePell. Spectroscopy and implosion dynamics of low wire number nested arrays on the 1 MA COBRA generator. *Phys. Plasmas*, 15:033302, 2008.

[75] J. M. Lerner and A. Thevenon. The optics of spectroscopy - a tutorial. Retrieved October 16, 2008, from `http://www.jobinyvon.com/`.

[76] M. G. Mazarakis, C. E. Deeney, M. R. Douglas, W. A. Stygar, D. B. Sinars, M. E. Cuneo, J. Chittenden, G. A. Chandler, T. J. Nash, K. W. Struve, and D. H. McDaniel. Tungsten wire number dependence of the implosion dynamics at the Z-accelerator. *Plasma Devices Oper.*, 13(2):157, 2005.

[77] M. Gersten, W. Clark, J. E. Rauch, G. M Wilkinson, J. Katzenstein, R. D. Richardson, J. Davis, D. Duston, J. P. Apruzese, and R. Clark. Scaling of plasma temperature, density, size, and x-ray emission above 1 keV with array diameter and mass for aluminum imploding-wire plasmas. *Phys. Rev. A*, 33(1):477, 1986.

[78] T. A. Shelkovenko, S. A. Pikuz, D. B. Sinars, K. M. Chandler, and D. A. Hammer. Time-resolved spectroscopic measurements of ~1 keV, dense, subnanosecond x-pinch plasma bright spots. *Phys. Plasmas*, 9:2165, 2002.

[79] T. A. Shelkovenko, S. A. Pikuz, B. M. Song, K. M. Chandler, M. D. Mitchell, D. A. Hammer, G. V. Ivanenkov, A. R. Mingaleev, and V. M. Romanova. Electron-beam-generated x rays from x pinches. *Phys. Plasmas*, 12:033102, 2005.